

**Investigating the non-immune cell
mediated mechanisms of skeletal muscle
weakness in myositis; developing an
investigative platform to study human
diseases**

A THOMA

PhD 2021

**Investigating the non-immune cell mediated
mechanisms of skeletal muscle weakness in
myositis; developing an investigative platform
to study human diseases**

Anastasia Thoma

A thesis submitted in partial fulfilment of the requirements of Manchester Metropolitan
University for the degree of Doctor of Philosophy

Department of Life Sciences

Manchester Metropolitan University

2021

List of Contents	
Acknowledgements	
Publications	
List of Figures	
List of Tables	
List of Abbreviations	
Abstract	

1. CHAPTER 1: INTRODUCTION	20
1.1 Skeletal muscle structure, function, and architecture	21
1.1.1 Diseases of skeletal muscle	25
1.2 Idiopathic Inflammatory myopathies	25
1.2.1 Polymyositis (PM)	28
1.2.2 Dermatomyositis (DM)/Juvenile (JDM)	28
1.2.3 Inclusion body myositis (IBM)	30
1.2.4 Treatment	31
1.3 Disease mechanisms	34
1.3.1 Immune mediated mechanisms	34
1.3.1.1 Innate immune mechanisms	34
1.3.1.2 Adaptive immune mechanisms	36
1.3.1.3 Inflammatory mediators	40
1.3.2 Non-immune mediated mechanisms	41
1.3.2.1 ER stress	42
1.3.2.2 ER stress in myositis	44
1.3.2.3 ROS from mitochondria in skeletal muscle and other sources in skeletal muscle	45
1.3.2.4 ROS and mitochondria in muscle dysfunction	47
1.3.2.5 ROS and mitochondria in myositis	48
1.3.2.6 Skeletal muscle as an endocrine organ	51
1.3.2.7 Myokines in myositis	52
1.4 Aims	53
1.5 Hypothesis	54
2. CHAPTER 2: MATERIALS AND METHODS	55
2.1 Cell culture	56

2.1.1	Immortalised cell culture	56
2.1.2	Muscle biopsy collection, primary cell isolation and culture	58
2.1.3	Passaging, seeding, and cryopreservation	61
2.1.4	Treatment of cells	61
2.1.5	Transfection	62
2.2	Sample preparation	62
2.2.1	Plasmid preparation	63
2.2.2	Extraction of RNA from cells	63
2.2.3	Protein extraction from cells	64
2.3	SDS-PAGE, western blotting, Luminex multiplex analysis and qPCR	64
2.3.1	Bicinchonic acid assay	65
2.3.2	SDS-PAGE	65
2.3.2.1	Electrophoresis of proteins	65
2.3.3	Western blotting	65
2.3.3.1	Analysis of the PVDF membrane for specific proteins	66
2.3.4	quantitative Polymerase Chain Reaction (qPCR)	67
2.3.5	Luminex multiplex analysis	70
2.4	Analysis of mitochondrial function	72
2.4.1	Seahorse extracellular flux analysis	72
2.5	Fluorescent imaging of cells	76
2.5.1	Imaging of mitochondrial structure	76
2.5.1.1	Quantification of mitochondrial structure using ImageJ	77
2.5.2	Immunocytochemistry	78
2.5.2.1	Cell fixation and preparation	78
2.5.2.2	Fluorescent staining of immortalised human skeletal myoblast	78
2.5.2.3	Fluorescent staining of immortalised human skeletal myotubes	78
2.5.2.3.1	Quantification of differentiation parameters	78
2.5.2.4	Fluorescent staining of primary human skeletal muscle cell line	79
2.5.3	Live/Dead viability staining	79

2.6 Measurement of RONS	80
2.6.1 Amplex Red® hydrogen peroxide/peroxidase assay	80
2.6.2 MitoSOX™ Red	81
2.6.3 DHE	82
2.6.4 DCFH-DA	82
2.6.5 DAF-FM DA	83
2.6.6 Mitochondrial hydroxyl radical assay	84
2.7 Measurement of mitochondrial membrane potential and mass	84
2.7.1 JC-1	84
2.7.2 TMRM	85
2.7.3 MitoTracker Red CMXRos	86
2.7.4 MitoTracker Green FM	87
2.8 Statistical Analyses	87
3. CHAPTER 3: Mitochondrial function and ROS generation in an <i>in vitro</i> model of ER stress	88
3.1 Introduction	89
3.1.1 Aims of this chapter	90
3.2 Methods	91
3.2.1 Cell culture and treatments	91
3.2.2 Cell viability assay	91
3.2.3 Assessment of differentiation parameters	91
3.2.4 Immunostaining for ER stress marker	91
3.2.5 Real-time qPCR of ER stress and mitochondrial-associated markers	92
3.2.6 Assessment of cellular respiration using Seahorse Extracellular Flux Analyser	92
3.2.7 Assessment of mitochondrial membrane potential and mass	92
3.2.8 Measurement of RONS	92
3.2.9 Assessment of mitochondrial morphology parameters using confocal microscopy	93
3.2.10 Western blotting	93

3.2.11	Statistical analysis	93
3.3	Results	94
3.3.1	Cellular viability	94
3.3.2	Tunicamycin-induced ER stress activation	94
3.3.3	Myoblast differentiation and muscle atrophy in response to ER stress activation	97
3.3.4	Mitochondrial bioenergetic profile	101
3.3.5	Mitochondrial unfolded protein response (mtUPR)	107
3.3.6	Mitochondrial mass and membrane potential	107
3.3.7	Mitochondrial morphology: fusion and fission processes	111
3.3.8	ROS generation	115
3.4	Discussion	117
4.	CHAPTER 4: Mitochondrial function and ROS generation in an <i>in vitro</i> model of MHC-I overexpressing cells in presence or absence of Type I interferons	122
4.1	Introduction	123
4.1.1	Aims of this chapter	124
4.2	Methods	125
4.2.1	Cell culture	125
4.2.2	Plasmid preparation	125
4.2.3	Transfection and treatments	125
4.2.4	Assessment of transfection efficiency by immunostaining	125
4.2.5	Assessment of cellular respiration using Seahorse Extracellular Flux Analyser	126
4.2.6	Assessment of mitochondrial membrane potential and mass	126
4.2.7	Measurement of RONS	126
4.2.8	Statistical analysis	127
4.3	Results	128
4.3.1	Transfection optimisation	128
4.3.2	MHC-I levels following transfection with HLA-A2/K ^b vector in presence or absence of type I IFNs	135

4.3.3	Mitochondrial function in type I IFNs-treated myoblasts	137
4.3.4	Mitochondrial function following MHC-I overexpression in presence or absence of Type I IFNs	140
4.3.5	Effects on mitochondrial mass and membrane potential by MHC-I overexpression type I IFNs	145
4.3.6	RONS generation by MHC-I overexpression type I IFNs	147
4.4	Discussion	149
5.	CHAPTER 5: Mitochondrial function and ROS generation in human myositis cells derived from patient biopsy samples	152
5.1	Introduction	153
5.1.1	Aims of this chapter	154
5.2	Methods	155
5.2.1	Ethics statement	155
5.2.2	Muscle biopsy collection	155
5.2.3	Primary cell isolation and culture	155
5.2.4	Fluorescent imaging of cells	155
5.2.5	Assessment of cellular respiration using Seahorse Extracellular Flux Analyser	156
5.2.6	Assessment of mitochondrial membrane potential and mass	156
5.2.7	Measurement of RONS	156
5.2.8	Statistical analysis	156
5.3	Results	157
5.3.1	Growth of primary cells	157
5.3.2	Expression of HLA class I	158
5.3.3	Bioenergetic profile	159
5.3.4	Mitochondrial mass and membrane potential	164
5.3.5	RONS generation	165
5.4	Discussion	167
6.	CHAPTER 6: Effect of myokines secretome from myositis cells on mitochondrial function and ROS generation	171
6.1	Introduction	172

6.1.1 Aims of this chapter	173
6.2 Methods	174
6.2.1 Cell culture, conditioned media, and treatments	174
6.2.2 Immunostaining	174
6.2.3 Quantification of differentiation parameters	174
6.2.4 Assessment of cellular respiration using Seahorse Extracellular Flux Analyser	174
6.2.5 Assessment of mitochondrial membrane potential and mass	175
6.2.6 Measurement of RONS	175
6.2.7 Luminex multiplex assay	175
6.2.8 Statistical analysis	175
6.3 Results	176
6.3.1 Conditioned media optimization and assessment of differentiation parameters	176
6.3.2 Expression of HLA class I	178
6.3.3 Mitochondrial bioenergetic profile	179
6.3.4 Mitochondrial mass and membrane potential	185
6.3.5 ROS generation	186
6.3.6 Myokines secretome of IBM and DM myoblasts	187
6.4 Discussion	190
CHAPTER 7: General Discussion and Future Directions	193
7.1 Major findings and general discussion	194
7.2 Future directions	201
Appendix	203
References	205

Acknowledgments

Firstly, I would like to express my gratitude to my supervisor, Dr Adam Lightfoot, for giving me the opportunity to start my research career, for his trust, understanding, guidance, and support, both mentally and academically.

Special thanks to Dr Nasser Al-Shanti, Prof Jamie S McPhee, and Prof Hans Degens, as well as Prof Hector Chinoy and all the laboratory technicians of Manchester Metropolitan University for their invaluable help and time throughout my PhD research.

Most importantly, I would like to thank my parents, Yiannos and Skevi, and sister, Maria, and all my family and friends who always believed in me, supported me, and motivated me to keep going. Lastly, but definitely not least, great thanks to Theofanis for being by my side, helping me and encouraging me along this journey. You all made this possible!

Publications

Primary Research Paper

Thoma A., Lyon M., Al-Shanti N., Nye G., Cooper R.G. and Lightfoot A.P. (2020). Eukarion-134 attenuates endoplasmic reticulum stress-induced mitochondrial dysfunction in human skeletal muscle cells. *Antioxidants*

Review

Thoma A., Akter-Miah T., Reade R.L. and Lightfoot A.P. (2020) Mini-Review Targeting Reactive Oxygen Species (ROS) to combat the age-related loss of muscle mass and function. *Biogerontology*

Thoma A. and Lightfoot A.P. (2018). NF- κ B and Inflammatory Cytokine Signalling: Role in Skeletal Muscle Atrophy. *Muscle Atrophy*. Springer, Singapore.

Contributing Author

Parkes J., Thoma A., Lightfoot A.P., Day P., Chinoy H. and Lamb J. (2020) MicroRNA and mRNA profiling in the idiopathic inflammatory myopathies. *BMC Rheumatology*.

Lightfoot A.P., Morgan R.S., Parkes J.E., Thoma A., Iwanejko L.A. and Cooper R.G. (2018). 17-(Allylamino)-17-demethoxygeldanamycin reduces Endoplasmic Reticulum (ER) stress-induced mitochondrial dysfunction in C2C12 myotubes. *bioRxiv*. doi: <https://doi.org/10.1101/350702>.

List of Figures

Chapter 1

Figure 1.1 The hierarchical structure of a skeletal muscle.	21
Figure 1.2. The structure of a skeletal muscle fiber.	22
Figure 1.3. Skeletal muscle contraction.	24
Figure 1.4. Classification tree for IIM subgroups.	27
Figure 1.5. PM muscle biopsy histology features.	28
Figure 1.6. Examples of hallmark skin manifestations in patients with DM.	29
Figure 1.7. DM muscle biopsy histology features.	30
Figure 1.8 sIBM muscle biopsy histology features.	31
Figure 1.9 Innate immune mechanisms in myositis.	36
Figure 1.10 Adaptive immune mechanisms in myositis.	39
Figure 1.11 UPR signaling.	44
Figure 1.12 Potential sources and roles of RONS in skeletal muscle.	46

Chapter 2

Figure 1.1 Graphical presentation of the experimental procedure followed for isolating human primary skeletal muscle cells.	60
Figure 2.2 Blotting sandwich.	66
Figure 2.3 Luminex assay protocol	71
Figure 2.4. Graphical presentation of the XF Extracellular Flux Analyser basis.	73
Figure 2.5 Seahorse XF Cell Mito Stress test profile.	75
Figure 2.6 Antimycin A-induced superoxide generation presented by MitoSOX Red assessment.	82
Figure 2.7 Antimycin A-induced total cellular ROS generation presented by DCF-DA assessment.	83
Figure 2.8 FCCP-induced mitochondrial membrane depolarisation presented by JC-1 assessment.	85
Figure 2.9 FCCP-induced mitochondrial membrane depolarisation presented by non-quenching mode of TMRM.	86

Chapter 3

Figure 3.1 Cellular viability.	94
--------------------------------	----

Figure 3.2 Fold change in ER stress markers upon tunicamycin treatment with or without EUK-134.	95
Figure 3.3 Fluorescent intensity of GRP78.	96
Figure 3.4 GRP94 protein levels.	97
Figure 3.5 Myoblast differentiation.	98
Figure 3.6 Muscle atrophy assessment based on morphological and differentiation parameters.	100
Figure 3.7 Energy phenotype upon ER stress in presence or absence of EUK-134.	103
Figure 3.8 Bioenergetic profile upon ER stress in presence or absence of EUK-134.	104
Figure 3.9 Individual mitochondrial parameters calculated from the bioenergetic profile.	105
Figure 3.10 Normalised respiratory flux control ratios.	106
Figure 3.11 Mitochondrial uncoupling protein 3 (<i>UCP3</i>) gene expression.	106
Figure 3.12 Mitochondrial unfolded protein response markers.	107
Figure 3.13 Mitochondrial membrane potential.	109
Figure 3.14 Mitochondrial biogenesis.	110
Figure 3.15 Mitochondrial morphological parameters.	113
Figure 3.16 Mitochondrial dynamics.	114
Figure 3.17 ROS generation.	116
Figure 3.18 Superoxide dismutases protein expression.	116
Chapter 4	
Figure 4.1 Transfection optimisation using HLA-A EGFP-tagged plasmid.	129
Figure 4.2 Transfection optimisation using (2 µg/µL) EGFP-tagged HLA vector.	130
Figure 4.3 Transfection optimization using GFP-tagged HLA and empty vector.	130
Figure 4.4 Transfection optimisation using HLA-A EGFP-tagged plasmid.	131
Figure 4.5 TransIT-X2 effects at different ratios in skeletal muscle cells.	131
Figure 4.6 Expression of HLA class I following 6 hours of transfection.	133

Figure 4.7 Expression of HLA class I following 18 and 24 hours of transfection.	134
Figure 4.8 Expression of HLA class I by transIT-X2.	135
Figure 4.9 Expression of HLA class I following 18 hours of transfection in presence or absence of IFN α / β .	136
Figure 4.10 Mitochondrial function parameters of myoblasts treated with IFN α .	138
Figure 4.11 Mitochondrial function parameters of myoblasts treated with IFN α .	139
Figure 4.12 Energy phenotype of MHC-I overexpressing cells with or without type I IFNs treatment.	142
Figure 4.13 Bioenergetic profile of MHC-I overexpressing cells with or without type I IFNs treatment.	143
Figure 4.14 Individual mitochondrial parameters calculated from the bioenergetic profile.	144
Figure 4.15 Normalised respiratory flux control ratios.	145
Figure 4.16 Mitochondrial membrane potential and mass.	147
Figure 4.17 RONS generation.	148
Chapter 5	
Figure 5.1 Growth of human primary myoblast at passage 0.	157
Figure 5.2 Myogenic cells isolated from human muscle biopsy samples.	158
Figure 5.3 Expression of HLA class I.	159
Figure 5.4 Energy phenotype of IBM and DM-derived cells.	161
Figure 5.5 Bioenergetic profile of IBM and DM-derived cells.	162
Figure 5.6 Individual mitochondrial parameters calculated from the bioenergetic profile.	163
Figure 5.7 Normalised respiratory flux control ratios.	163
Figure 5.8 Mitochondrial membrane potential and mass.	165
Figure 5.9 RONS generation.	166
Chapter 6	
Figure 6.1 Muscle differentiation upon 25% conditioned media.	177

Figure 6.2 Muscle differentiation upon 50% conditioned media.	177
Figure 6.3 Muscle differentiation upon 100% conditioned media.	178
Figure 6.4 Expression of HLA class I upon 100% conditioned media.	179
Figure 6.5 Energy phenotype of immortalised human skeletal myoblasts incubated with IBM and DM conditioned media	181
Figure 6.6 Bioenergetic profile of immortalized human skeletal myoblasts incubated with IBM and DM conditioned media.	182
Figure 6.7 Individual mitochondrial parameters calculated from the bioenergetic profile.	183
Figure 6.8 Normalised respiratory flux control ratios.	184
Figure 6.9 Mitochondrial membrane potential and mass.	186
Figure 6.10 ROS generation.	187
Figure 6.11 IBM and DM myokines secretome.	189

List of Tables

Table 1.1 2017 EULAR/ACR classification criteria for IIM	26
Table 1.2 Features of the main types of IIMs	33
Table 1.3 Myositis specific autoantibodies	38
Table 2.1 Reagents for cell culture	56
Table 2.2 Growth media for immortalised human skeletal muscle cells	57
Table 2.3 Differentiation media for immortalised human skeletal muscle cells	57
Table 2.4 Relaxing Buffer (10×, pH 7.0) prepared in distilled water	58
Table 2.5 Muscle Tissue Digestion Solution prepared in low-glucose DMEM	59
Table 2.6 Growth media for primary human skeletal muscle cells	59
Table 2.7 Reagents for sample preparation	62
Table 2.8 Reagents	64
Table 2.9 Constituents of western blotting buffers	65
Table 2.10 Constituents of reagents used for protein detection	66
Table 2.11 List of antibodies (1 ^{ry} and 2 ^{ry})	67
Table 2.12 Incubation protocol for RNA reverse transcription	68
Table 2.13 Incubation protocol for RNA reverse transcription	68
Table 2.14 The sequences and annealing temperature of mitochondrial-associated primers.	69
Table 2.15 The sequences and annealing temperature of endoplasmic reticulum stress-associated primers.	70
Table 2.16 Reagents for mitochondrial function analysis	72
Table 2.17 Compound preparation and injection	74
Table 2.18 Equations for mitochondrial parameters derived from the bioenergetic profile	75
Table 2.19 Normalised respiratory flux control ratios	76
Table 2.20 Reagents for fluorescent imaging of cells	76
Table 2.21 Mitochondrial morphology parameters	77
Table 2.22 Myoblast differentiation parameters	79
Table 2.23 Reagents	80
Table 2.24 Amplex Red Assay kit solutions preparation	81
Table 2.25 Reagents	84

List of Abbreviations

2-OH-E ⁺	2-hydroxyethidium
AMPK	AMP-activated protein kinase
APCs	Antigen-presenting cells
ATF	Activating transcription factor
AZA	Azathioprine
CCL	Chemokine ligand
CHOP	cholesterol oxidase-peroxidase C/EBP homologous protein
COX	Cytochrome c oxidase
COX	Cytochrome oxidase
CsA	Cyclosporine A
CTL	Cytotoxic T cells
CYC	Cyclophosphamide
DAF-FM DA	4-amino-5-methylamino-20,70-difluorofluorescein diacetate
DAMPs	Damage-associated molecular patterns
DAPI	4',6'-diamidino-2-phenylindole dihydrochloride
DCFH-DA	2',7'-dichlorodihydrofluorescein diacetatediacetate
ddH ₂ O	double distilled water
DHE	Dihydroethidium
DM	Dermatomyositis
DMEM	Dulbecco's modified Eagle's medium
DMSO	Dimethyl sulfoxide
DRP1	Dynamin-related protein 1
ECAR	Extracellular acidification rate
EGFP	Enhanced green fluorescent protein
eIF2 α	Eukaryotic translation initiation factor-2 α
ER	Endoplasmic reticulum
ERAD	ER-associated degradation
ERK	extracellular signal-regulated kinase
EUK-134	Eukarion-134
EULAR/ACR	European League Against Rheumatism/ American College of Rheumatology
FCCP	Carbonyl cyanide-4 (trifluoromethoxy) phenylhydrazone
FIS1	Fission protein 1
GFP	Green fluorescent protein
GRP	glucose-regulated protein
GS	Glucocorticosteroids
H ₂ O ₂	Hydrogen peroxide
HLA	Human leukocyte antigen
HRP	horseradish peroxidase
HSP	Heat shock protein

IBM	Inclusion body myositis
IFN	Interferon
IIMs	Idiopathic inflammatory myopathies
IL	Interleukin
IMNM	Immune-mediated necrotizing myopathy
InsI6	Insulin-like 6
IRE1	Inositol requiring enzyme 1
IVIG	Intravenous immunoglobulin G
JC-1	5,5',6,6'- tetrachloro-1,1',3,3'-tetraethylbenzimidazolylcarbocyanine iodide
JDM	Juvenile DM
JNK	c-Jun N-terminal kinase
MAPK	mitogen-activated protein kinase
MCP1	Monocyte chemotactic protein-1
mDCs	Myeloid dendritic cells
MFN2	Mitofusin 2
MHC	Major histocompatibility complex
MIP1	Macrophage inflammatory protein 1
MMF	Mycophenolate mofetil
mtDNA	mitochondrial DNA
mtUPR	Mitochondrial unfolded protein response
MTX	Methotrexate
MyD88	myeloid differentiation response gene 88
Mφ	Macrophages
NAM	Necrotising autoimmune myopathies
NADPH	Nicotinamide adenine dinucleotide phosphate
NF-κB	Nuclear factor- κB
NMJ	Neuromuscular junction
nNOS	neuronal nitric oxide synthase
NO	Nitric oxide
NOS	Nitrogen oxygen species
O ₂ ^{•-}	Superoxide
OCR	oxygen consumption rate
ONOO ⁻	Peroxynitrite
Opa1	Optic atrophy 1
PBMCs	peripheral blood mononuclear cells
pDCs	Plasmacytoid dendritic cells
pDNA	Plasmid DNA
PERK	PKR-like eukaryotic initiation factor 2α kinase
PGC-1α	peroxisome proliferator-activated receptor-γ coactivator-1 protein-α
PM	Polymyositis

qPCR	Quantitative polymerase chain reaction
RANTES	Regulated upon Activation, Normal T-cell Expressed, and Secreted
RCR	Respiratory control ratio
RONS	reactive oxygen and nitrogen species
ROS	Reactive oxygen species
RTX	Rituximab
RyR1	ryanodine receptor 1
sIBM	Sporadic IBM
SOD	Superoxide dismutase
SR	Sarcoplasmic reticulum
SRP	Signal recognition particle
Tc	T cytotoxic
Th	T helper
TIR	Toll-IL-1 receptor
TLRs	Toll-like receptors
TMRM	tetramethylrhodamine, methyl ester
TNF- α	tumor necrosis factor- α
Tregs	T regulatory cells
TRIF	TIR domain-containing adaptor-inducing IFN- γ
UCP3	uncoupling protein 3
UPR	Unfolded protein response
XBP1	X box-binding protein 1
XO	xanthine oxidase
$\Delta\Psi_m$	mitochondrial membrane potential

Abstract

Idiopathic inflammatory myopathies, collectively termed as myositis, are a group of heterogeneous rare autoimmune muscle diseases, described by muscle weakness and fatigue leading to poor quality of life. Widely recognised by its immune mediated features, its current treatment focuses on immunosuppressive therapies, which however, seem to be ineffective in treating muscle weakness. Growing evidence support the involvement of non-immune mediated mechanisms including ER stress and mitochondrial impairments, as well as myokines up- or down-regulation, with major histocompatibility complex class I (MHC-I), a prominent myositis feature, being suggested to initiate those events. Thus, there is a great necessity for investigating the non-immune mediated mechanisms underlying myositis pathophysiology, providing the foundation for developing novel targeted therapeutic approaches.

This thesis investigated the non-immune mediated mechanisms, focusing on mitochondrial bioenergetics and biodynamics, and reactive oxygen species generation, in three human *in vitro* models of myositic muscle: **(a)** pharmacological cell model of ER stress; **(b)** genetically modified cell model of MHC-I overexpression in presence or absence of type I interferons (IFNs); and **(c)** clinical cell model of primary human myositis skeletal muscle cell line. Lastly, the downstream mechanisms of the myokines secretome derived from the primary myositis cell line was assessed.

Tunicamycin-induced ER stress activation led to an overall increase in mitochondrial respiration, potentially as an adaptive response to stress; however, mitochondrial dysfunction was evident by decreases in respiratory flux control ratios and mitochondrial membrane potential. A similar trend of mitochondrial changes was seen in IBM and DM primary cells, with effects being more drastic in DM compared to IBM primary cells. MHC-I overexpression caused significant depletion in mitochondrial respiration, accompanying by reduced respiratory flux control ratios and mitochondrial membrane potential. Interestingly, those effects seemed to exacerbate in presence of type I IFNs, suggesting the strong combinational effects of MHC-I and type I IFNs. MHC-I-induced effects were similar to those following exposure to myositic conditioned media, where DM conditioned media collected from DM primary cells showed greater mitochondrial respiratory deficiency compared to IBM primary cells-derived conditioned media. An

interesting finding was that antioxidant intervention, using Eukarion-134, was able to amend aspects of mitochondrial dysfunction in those models, highlighting the potential role of ROS accumulation in myositis.

Overall, this thesis has provided numerous models that can be used for further investigating the mechanisms involved in myositis pathogenesis and identify potential therapeutic targets. The findings suggest the involvement of multiple mechanisms that can be overlapping, but also act independently in inducing mitochondrial impairments, leading to muscle weakness in myositis. Lastly, these studies have indicated a possible role of ROS generation in mediating aspects of ER stress and mitochondrial abnormalities, suggesting that targeting ROS accumulation could be a promising therapeutic strategy for the persistent muscle weakness in individuals with myositis.

Chapter 1

Introduction

1.1 Skeletal muscle structure, function and architecture

Skeletal muscle is a robust and plastic organ, evolved to provide mobility, stability and metabolic support. As the largest organ in the human body, accounting for 40% total body weight and 50% total body protein, muscle plays a crucial role in multiple homeostatic mechanisms. Skeletal muscle has an elegant hierarchical structure, ensheathed by a layer of connective tissue, the epimysium. Skeletal muscle is composed of bundles of muscle fibers (muscle cells) arranged in parallel along the length of the muscle. Each bundle of muscle fibers, termed a fascicle, is wrapped by a connective tissue layer, called perimysium, and is located within a loose connective tissue, the endomysium (**Figure 1.1**) (Jones, Round and De Haan, 2004).

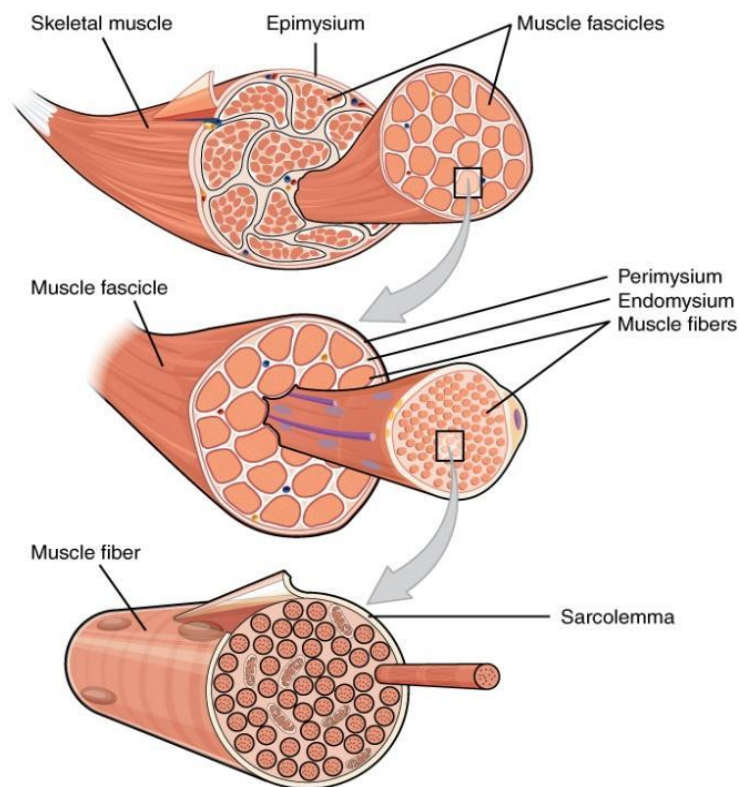


Figure 1.1 The hierarchical structure of a skeletal muscle. Skeletal muscle, encapsulated by epimysium, is composed of bundles of muscle fascicles that are surrounded by perimysium. Each muscle fascicle contains bundles of muscle fibers. Muscle fibers are in turn, ensheathed by endomysium, covered by sarcolemma. Image

“1007_Muscle_Fibes_(large).jpg” OpenStax, Skeletal Muscle. OpenStax CNX. 4 Jun 2013 <http://cnx.org/contents/6df8aab3-1741-4016-b5a9-ac51b52fade0@3.>, licenced under Creative Commons Attribution 4.0 International

A muscle fiber is surrounded by a plasma membrane, the sarcolemma, and is comprised of multiple myofibrils. The myofibrils are composed of the contractile machinery of muscle, the actin and myosin filaments (Jones, Round and De Haan, 2004). The actin and myosin filaments are arranged into sequential units, along the length of the myofibril – forming the sarcomere (the force generating unit of muscle) and giving skeletal muscle its characteristic striated appearance (Huxley and Hanson, 1954; Huxley and Niedergerke, 1954). The sarcomere is defined by Z discs placed at its borders, and contains dark and light areas that are called A and I bands, respectively. Actin filaments project from a Z disc at each end towards the M line located in the H zone, where they interact with myosin filaments (**Figure 1.2**) (Jones, Round and De Haan, 2004).

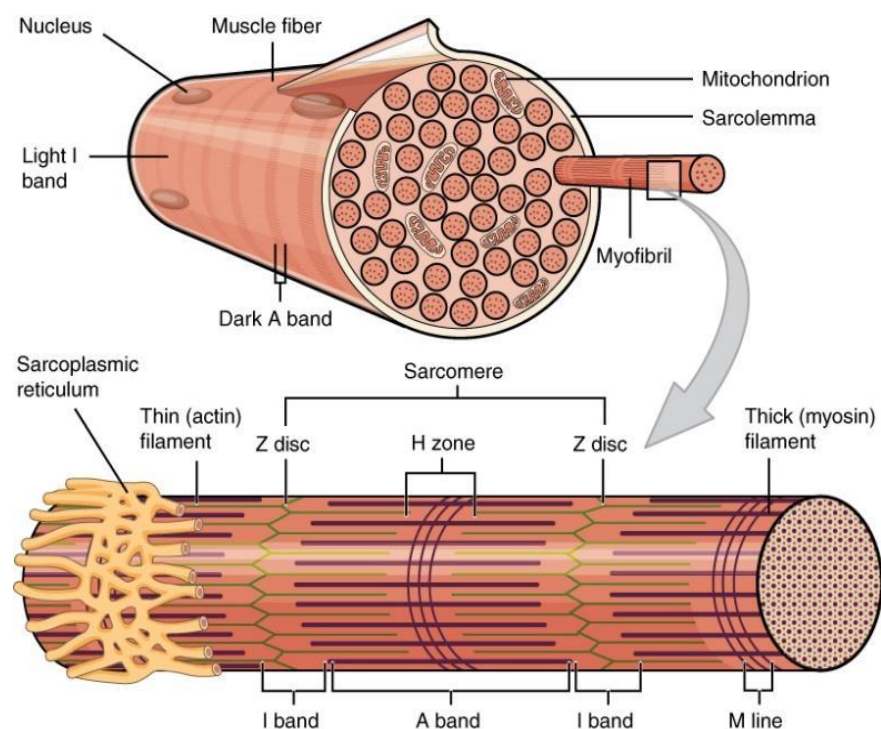


Figure 1.2 The structure of a skeletal muscle fiber. A muscle fiber is composed of myofibrils, which in turn are comprised of thin (actin; green line) and thick (myosin; purple line) filaments, constituting the sarcomere. The sarcomere consists of dark and

light areas, presenting A and I bands, respectively. The A band, an area of both thin and thick filaments, contains the H zone in the middle (thick filaments only). The I band consist of thin filaments and contains the Z disc, defining the sarcomere. Image “1022_Muscle_Fibers_(small).jpg” OpenStax, Skeletal Muscle. OpenStax CNX. 4 Jun 2013 <http://cnx.org/contents/6df8aab3-1741-4016-b5a9-ac51b52fade0@3.>, licenced under Creative Commons Attribution 4.0 International

The contraction of skeletal muscle involves a complex cascade initiated from the central nervous system. Projects from the anterior horn cells of the spinal cord arrive at the muscle fibre membrane, forming the neuromuscular junction (NMJ) – each fibre has a single NMJ. An action potential arrives at the NMJ, inducing opening of the Na^+/K^+ channels and an influx of Na^+ resulting in a net positive charge propagating across the muscle fibre. This charge differential allows transfer of the action potential down the t-tubules, which induces the release of Ca^{2+} from the sarcoplasmic reticulum (SR). Calcium ions (Ca^{2+}) released from the SR interacts with the inhibitory troponin-tropomyosin complex upon the actin filament. Calcium ions induce an allosteric change in the troponin-tropomyosin complex, freeing up the myosin binding site, allowing the formation of the cross-bridge. The cyclical process of cross-bridge formation and detachment termed cross-bridge cycling is the cyclical process of force generation, termed the power stroke. The actin and myosin filaments slide past each other, resulting in a shortening of the sarcomere at the Z disks (**Figure 1.3**) (Jones, Round and De Haan, 2004).

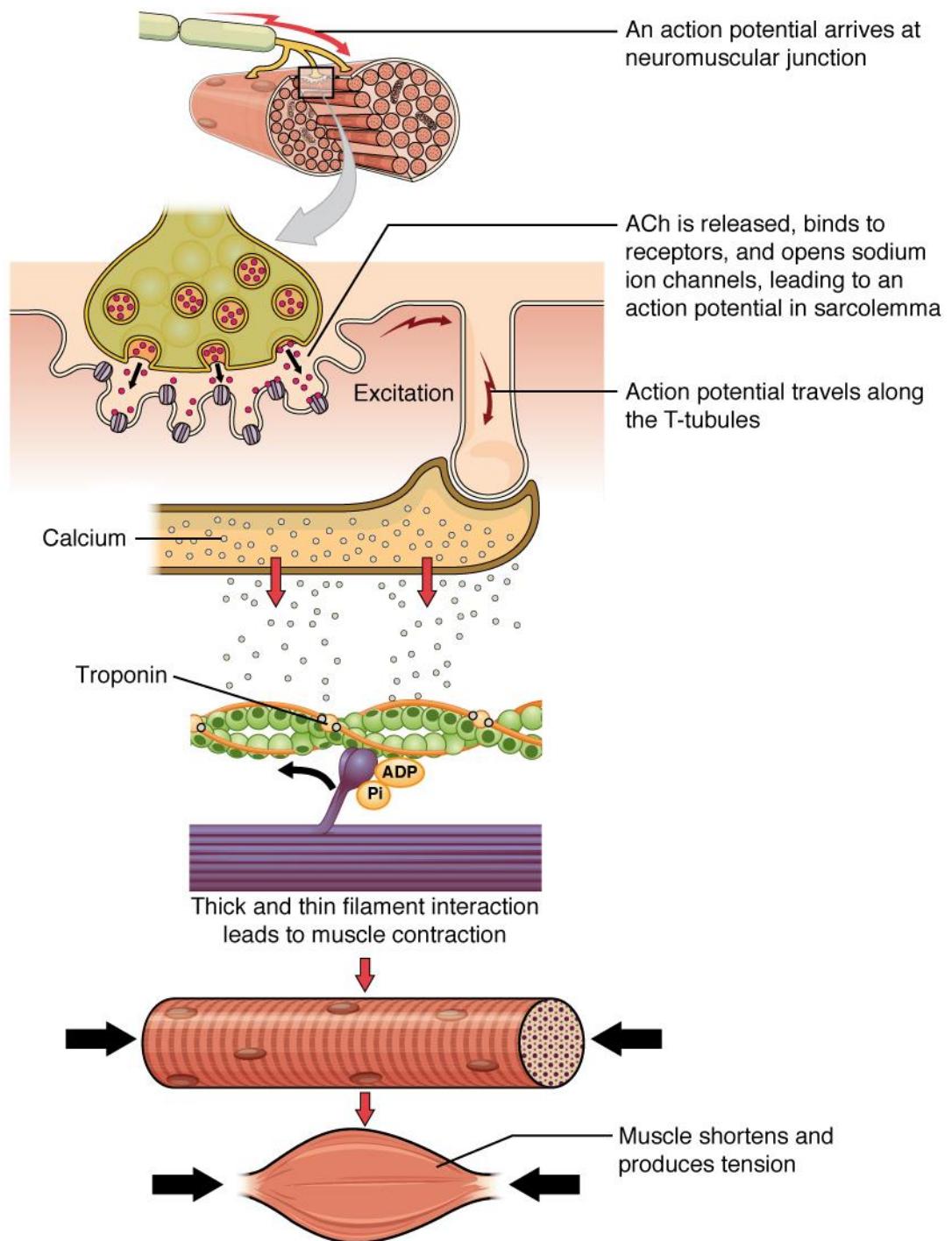


Figure 1.3 Skeletal muscle contraction. A cross-bridge formation between actin and myosin upon action potential and calcium release into the cytosol of muscle fibers, enabling muscle contraction. Image “1010a_Contraction_new.jpg” OpenStax, Skeletal Muscle. OpenStax CNX. 4 Jun 2013 <https://openstax.org/books/anatomy-and-physiology>

1.1.1 Diseases of skeletal muscle

Skeletal muscle is a crucial organ for ambulation and homeostatic regulation, and a significant factor in quality of life. Based on this, diseases which affect skeletal muscle, result in loss of muscle mass and function, weakness and disability, leading to poor quality of life. Muscle diseases are termed as 'myopathies' and are categorised into acquired and inherited. Muscular dystrophies are inherited and genetically heterogeneous muscle diseases, which are mostly well genetically determined. X-linked dystrophinopathies, such as Duchenne and Becker, and myotonic dystrophy are some examples of inherited muscular dystrophies. Acquired myopathies are less understood and can be characterized as endocrine, metabolic, and inflammatory (Chad, 2003).

1.2 Idiopathic inflammatory myopathies

Idiopathic inflammatory myopathies (IIMs) are an example of rare acquired myopathies that are collectively known as myositis. IIMs are characterised by chronic muscle weakness and inflammation of the muscle. Within IIMs, polymyositis (PM), dermatomyositis/juvenile dermatomyositis (DM/JDM), and inclusion body myositis (IBM) are the most common subgroups, with other IIMs including necrotising autoimmune myopathies (NAM), immune-mediated necrotizing myopathy (IMNM) and amyotrophic DM. Its reported prevalence ranges from 15 to 17.4 cases per 100,000 individuals in the USA (Cavazzana *et al.*, 2017). IIMs classification has been challenging because of the heterogeneity of the disease, therefore, diagnostic/classification criteria has been continuously updating. Even though IIMs share several common features, each subgroup presents a number of unique findings that enable their diagnosis. Their identification relies on histopathological findings in the muscle biopsy, clinical features, and other laboratory findings, such as myositis specific autoantibodies and myositis associated autoantibodies (**Table 1.3**). The last update of IIMs classification criteria was established by the European League Against Rheumatism/ American College of Rheumatology (EULAR/ACR) in 2017, as described in **Table 1.1**; a total score is calculated based on each variables' weighted score, which is converted into a probability of IIM. Following IIM

probability identification, IIMs subclassification is established using a classification tree (Figure 1.4) (Lundberg *et al.*, 2017).

Table 1.1 2017 EULAR/ACR classification criteria for IIM

	Score Without Muscle Biopsy	Score With Muscle Biopsy
CLASSIFICATION CRITERIA		
Age of onset of first symptom assumed to be related to the disease \geq 18 years and $<$ 40 years	1.3	1.5
Age of onset of first symptom assumed to be related to the disease \geq 40 years	2.1	2.2
MUSCLE WEAKNESS		
Objective symmetric weakness, usually progressive, of the proximal upper extremities	0.7	0.7
Objective symmetric weakness, usually progressive, of the proximal lower extremities	0.8	0.5
Neck flexors are relatively weaker than neck extensors	1.9	1.6
In the legs proximal muscles are relatively weaker than distal muscles	0.9	1.2
SKIN MANIFESTATIONS		
Heliotrope rash	3.1	3.2
Gottron's papules	2.1	2.7
Gottron's sign	3.3	3.7
OTHER CLINICAL MANIFESTATIONS		
Dysphagia or esophageal dysmotility	0.7	0.6
LABORATORY MEASUREMENTS		
Anti-Jo-1 (anti-histidyl-tRNA synthetase) autoantibody present	3.9	3.8
Elevated serum levels of creatine kinase* <i>or</i> lactate dehydrogenase* <i>or</i> aspartate aminotransferase* <i>or</i> alanine aminotransferase*	1.3	1.4
MUSCLE BIOPSY FEATURES- PRESENCE OF:		
Endomysial infiltration of mononuclear cells surrounding, but not invading, myofibres	NA	1.7
Perimysial and/or perivascular infiltration of mononuclear cells	NA	1.2

Perifascicular atrophy	NA	1.9
Rimmed vacuoles	NA	3.1

* Serum levels above the upper limit of normal

Probable IIM: Total score ≥ 5.5 , total score ≥ 6.7 if biopsy data is available.

Definite IIM: Total score ≥ 7.5 or more without muscle biopsy and ≥ 8.7 with muscle biopsy.

Possible IIM: Total score ≥ 5.3 , total score ≥ 6.5 if biopsy data is available

Table was adapted from Lundberg *et al.* (2017)

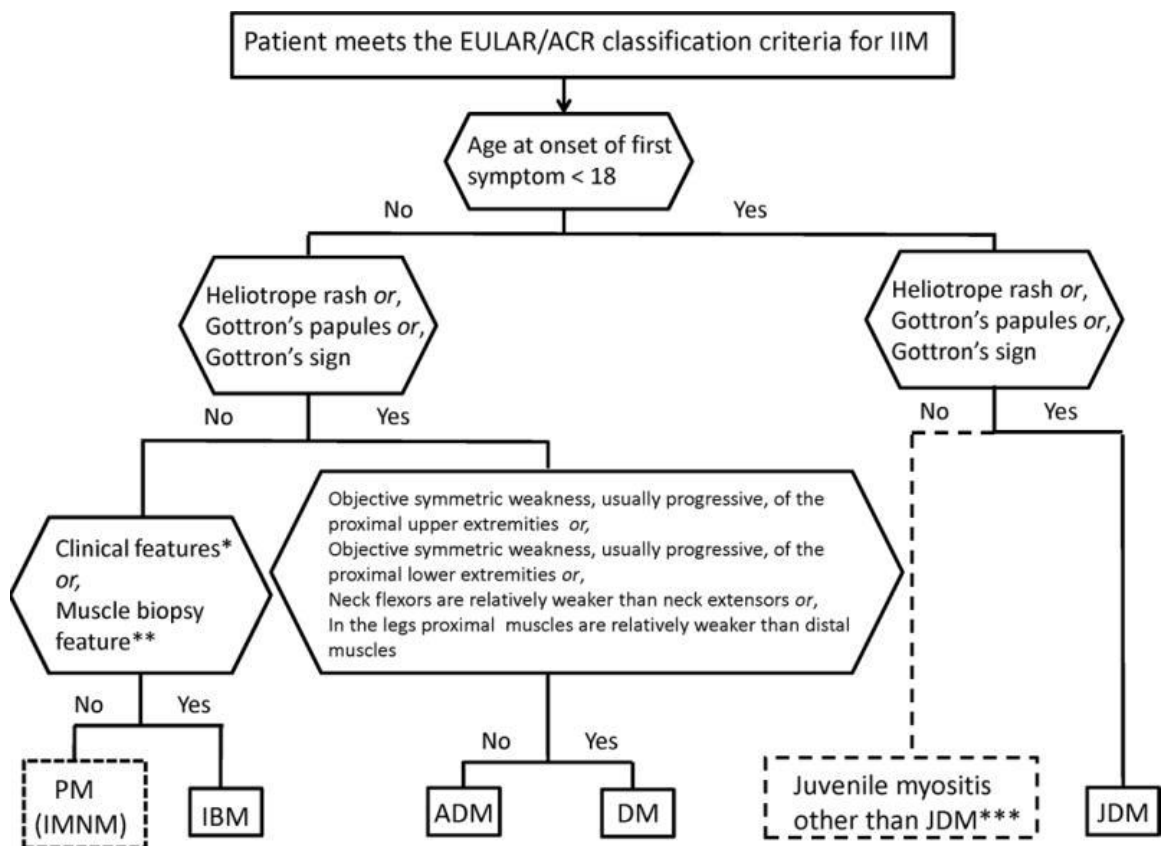


Figure 1.4 Classification tree for IIM subgroups. Patients who meet EULAR/ACR classification criteria are classified into IIM subgroups using the classification tree. *Finger flexor weakness and response to treatment: not improved. ** rimmed vacuoles, is required for diagnosis. ***Juvenile myositis other than JDM was developed based on expert opinion. Obtained from Lundberg *et al.*, 2017.

1.2.1 Polymyositis (PM)

PM and DM share several common clinical features that involve proximal, symmetrical muscle weakness, and other systemic features, such as interstitial lung disease, arthritis, and Raynaud's phenomenon (Cavazzana *et al.*, 2017). Controversy exists in the prevalence of PM, ranging from the largest rate defined in the USA population (~10 per 100,000 individuals) to the least common IIM that its diagnosis is made following exclusion of any other IIM (Schmidt, 2018).

In PM muscle biopsy, CD8+ T cells are predominantly seen in the endomysium (**Figure 1.5A**), and to a lesser degree macrophages in the perimysium (Cavazzana *et al.*, 2017). A cell-mediated cytotoxicity is considered to be a chief pathological mechanism in PM with muscle biopsies representing cytotoxic CD8+ T cells invasion on morphologically normal-appearing muscle fibers, expressing major histocompatibility complex (MHC) class I antigen on their sarcolemma (**Figure 1.5C**), and release of cytotoxic perforin and granzymes, further explained in **Section 1.3.1.2**. Other histological features include scattered necrosis and regeneration of muscle fibers (**Figure 1.5B**) (Vattemi *et al.*, 2014).

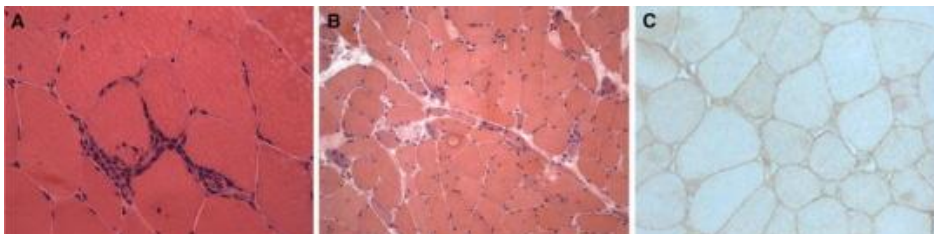


Figure 1.5 PM muscle biopsy histology features. Hematoxylin and eosin staining showing **(A)** endomysial inflammatory infiltrate in a healthy appearing muscle fiber and **(B)** scattered necrotic and regenerating muscle fibers. **(C)** MHC class I-expressing muscle fibers on the sarcolemma. Obtained from Vattemi *et al.* (2014).

1.2.2 Dermatomyositis (DM)/Juvenile (JDM)

DM can be differentiated from PM by its distinct clinical features of cutaneous lesions that worsen when exposed to sun (Oldroyd, Lileker and Chinoy, 2017). Those features include Gottron's papules over the finger joints (metacarpophalangeal and interphalangeal joints) (**Figure 1.6A**) and heliotrope rash around the eyes (**Figure 1.6B**)

that represent the hallmark feature of DM. Other features are confluent erythema overlying the lower anterior neck and upper anterior chest (V-sign rash) and over the upper back, posterior neck, and shoulders (shawl sign), as well as Mechanic's hands that refers to thickened, cracked, and fissured hyperkeratosis skin on the lateral and palmar sides of the fingers (Marvi, Chung and Fiorentino, 2012). Less common features are Gottron's sign referring to erythematous areas of skin over the elbows and/or knees, and erythroderma that is described by erythema covering over 50% of the body surface. Individuals with DM also present an increased risk (6-fold) of developing cancer (cancer-associated myositis), with diagnosis occurring in parallel with or within 1 year of dermatomyositis diagnosis (Jakubaszek, Kwiatkowska and Maślińska, 2015; Marvi, Chung and Fiorentino, 2012). JDM and adult DM share similar clinical features, with some distinct JDM features being cutaneous ulcerations, calcinosis cutis, and vasculopathy (Oldroyd, Lileker and Chinoy, 2017).

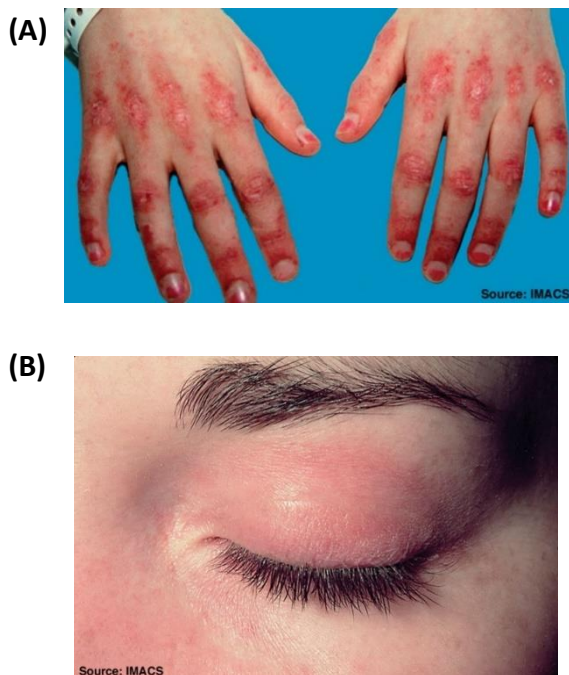


Figure 1.6 Examples of hallmark skin manifestations in patients with DM. (A) Gottron's papules over metacarpophalangeal and interphalangeal joints. **(B)** Heliotrope rash around the eye. Obtained from Dugan *et al.* (2009), licensed under the Creative Commons Attribution-Share Alike 3.0 Unported license.

A muscle biopsy of an individual with DM shows perivascular or perimysial, and rarely endomysial, inflammatory infiltration by predominantly B cells, along with CD4+ T helper (Th) cells, plasmacytoid dendritic cells and macrophages, while CD8+ T cells are rarely seen (**Figure 1.7A**). Perifascicular atrophy of 2–10 layers of both type 1 and type 2 muscle fibers is a pathognomonic feature of DM that indicates DM diagnosis even in the absence of inflammatory cells infiltration (**Figure 1.7B**). DM is also considered as a complement-mediated microangiopathy based on the observed muscle biopsy evidences of complement membrane attack complex deposition of endomysial capillaries and small blood vessels, resulting in endothelial hyperplasia and reduced capillary density (Vattemi *et al.*, 2014).

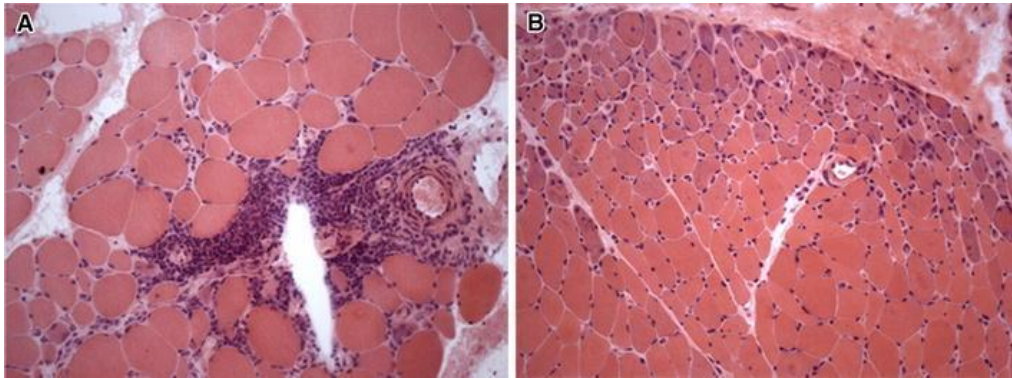


Figure 1.7 DM muscle biopsy histology features. Hematoxylin and eosin staining showing **(A)** perivascular inflammatory cell infiltration and **(B)** prominent perifascicular atrophy. Obtained from Vattemi *et al.* (2014).

1.2.3 Inclusion Body Myositis (IBM)

In contrast to PM and DM, IBM mostly occurs in an older and predominantly male population, with an age of onset of usually over 50 years, with only 20% of IBM cases developing symptoms between 40-50 years (Greenberg, 2019). Muscle weakness can be presented to be both proximal and distal, as well as both symmetrical and asymmetrical (Malik *et al.*, 2016). One of the most common and early clinical features are muscle weakness in finger flexors, knee extensors and/or ankle dorsiflexors. Frequent falls and grip weakness are some of the causes of the observed disability in patients with IBM,

with dysphagia being also a symptom in more than 50% of IBM cases (Oldroyd, Lileker & Chinoy, 2017).

Muscle biopsy of sIBM presents similar histopathology features to PM muscle biopsy, characterised by invasion of predominantly CD8+ T cells and macrophages in non-necrotic, MHC class I-expressing muscle fibers. Distinct sIBM diagnosis is made based on the presence of rimmed vacuoles, which are irregular and various in-size, mostly containing basophilic granular deposits, as well as of β -amyloid deposits, eosinophilic cytoplasmic inclusions, and cytochrome c oxidase (COX)-negative fibres (**Figure 1.8**) (Vattemi *et al.*, 2014), which are further described in **Section 1.3.2.5**. Considering the slow progression of IBM and its similar histopathological features to PM, IBM is commonly misdiagnosed as PM at early stages (Greenberg, 2019).

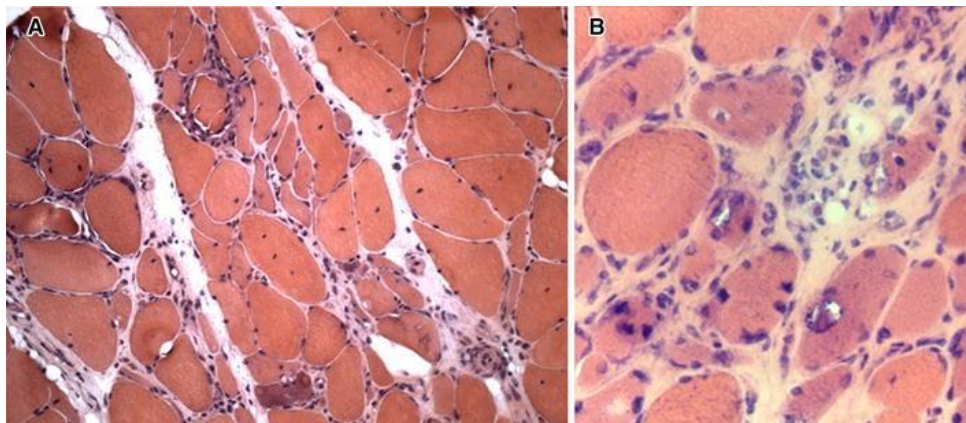


Figure 1.8 sIBM muscle biopsy histology features. Hematoxylin and eosin staining showing (A, B) rimmed vacuoles and eosinophilic inclusions. Obtained from Vattemi *et al.* (2014).

1.2.4 Treatment

The heterogeneity of IIMs and the involvement of various extramuscular manifestations requires a variation of therapeutic approaches. Overall, myositis management involves numerous immunosuppressive, immunomodulatory, and/or biologic agents. In particular, first-line therapy involves glucocorticoids, supplemented with the immunosuppressants, methotrexate or azathioprine. Second-line therapeutic approach involves

mycophenolate mofetil (immunosuppressant), tacrolimus or ciclosporin (calcineurin inhibitors) that are taken in combination with azathioprine and methotrexate. Calcineurin inhibitors or topical glucocorticoids are also used in DM to manage skin manifestation, alongside with avoidance of sunlight exposure. A third-line therapy includes supplementation of biologic agents that directly target immune cells or cytokines, such as rituximab, cyclophosphamide, and repository corticotropin injection (**Table 1.2**) (Oddis and Aggarwal, 2018). Other biologic agents, which have been in clinical trials, are further described in **Section 1.3.1.3**. An alternative or additional treatment to immunosuppressants that are not tolerated or are ineffective, is intravenous immunoglobulin G. Its efficacy and safety as a first-line treatment has been recently investigated by Lim *et al.* (2021); however, the study showed that nearly half of participants (patients with DM, IMNM, overlap myositis, and antisynthetase syndrome) showed clinically relevant improvement, while three serious adverse effects occurred, suggesting that IVIg efficacy should be further examined as an add-on treatment in combination with glucocorticoids (Lim *et al.*, 2021).

For IBM, there is no current effective treatment as patients show resistance to glucocorticosteroids and immunosuppressants, with skeletal muscle weakness persisting (Oddis and Aggarwal, 2018). Dysphagia, a common and progressive condition in IBM, has been shown to be improved by transient pharyngoesophageal dilatation or cricopharyngeal myotomy (Oh *et al.*, 2008). The efficacy of local injections of botulinum toxin has also been proved to be high in several IBM case series (**Table 1.2**) (Oddis and Aggarwal, 2018).

Besides pharmacological treatment, physiotherapy, including fatigue resistance exercise, has been a critical aspect in IIM management (Oddis and Aggarwal, 2018). Endurance training has been found to be efficient in promoting muscle growth and suppressing inflammation- and endoplasmic reticulum (ER) stress-associated genes in patients with PM and DM (Munters *et al.*, 2016). Even though a randomised controlled trial on the effect of blood-restricted resistance training in sIBM showed no improvement in physical function, the authors stated that a protective effect might be possible on mechanical muscle function, i.e., decline in leg muscle strength, which can be proven beneficial in the long-term in terms of physical function enhancement (Jørgensen *et al.*, 2018).

Table 1.2 Features of the main types of IIMs

	DM	PM	IBM
Prevalence	~1-6 per 100,000 (USA) ¹ 31% in Euromyositis group ¹	~10 per 100,000 (USA) ¹ 27% in Euromyositis group ¹	~14 per 100,000,000 ¹
Gender preponderance	Female ²	Female ²	Male ²
Clinical Features			
Muscle weakness	Proximal symmetrical muscle weakness ³	Proximal symmetrical muscle weakness ³ Neck flexor weakness	Proximal, distal, asymmetrical muscle weakness ³ Wrist/finger flexors; knee extensors and/or ankle dorsiflexors ²
Skin manifestations²	<ul style="list-style-type: none"> • Gottron’s papules • Gottron’s signs • Heliotrope rash • V-sign rash • Mechanic’s hands • Shawl sign rash • Erythroderma 		
Muscle biopsy features	B cells, along with CD4 ⁺ T cells, plasmacytoid dendritic cells, and macrophages in muscle fibers ⁴ Complement membrane attack complex deposition of endomysial capillaries ⁴	CD8 ⁺ T cells and macrophages in MHC class I-expressing muscle fibers ⁴	CD8 ⁺ T cells and macrophages in non-necrotic, MHC class I-expressing muscle fibers ⁴ Rimmed vacuoles, β -amyloid deposits, eosinophilic cytoplasmic inclusions, and cytochrome c oxidase (COX)-negative fibres ⁴
Creatine kinase levels	Normal or ~10–50 fold high ¹	~10–50 fold high ¹	Normal to 15 fold high ¹
Treatment	Basic: GS, AZA/MTX/MMF	Basic: GS, AZA/MTX/MMF	No basic immunosuppression; Probatory IVIG in

	Skin & JDM: IVIG; Lung/ Escal.: RTX, CYC, IVIG, (CsA) ¹	Escal.: RTX, CYC, IVIG ¹	selected patients justifiable; Severe dysphagia: local botulinum toxin or myotomy, percutaneous feeding tube ¹
--	--	--	---

GS = glucocorticosteroids ; AZA = azathioprine; MTX = methotrexate; MMF = mycophenolate mofetil; IVIG = intravenous immunoglobulin G; RTX = rituximab; CYC = cyclophosphamide; CsA = cyclosporine A

¹Schmidt, 2018; ²Oldroyd, Lileker and Chinoy, 2017; ³Cavazzana *et al.*, 2017; ⁴Vattemi *et al.*, 2014;

Needs of further research

Current therapeutic approaches seem to have poor efficacy, highlighting the need of further understanding the mechanisms underlying IIM pathology in order to identify potential therapeutic targets.

1.3 Disease mechanisms

1.3.1 Immune mediated mechanisms

1.3.1.1 Innate immune mechanisms

Toll-like receptors (TLRs) are expressed in capillaries and innate immune cells, such as macrophages and dendritic cells, and link innate and adaptive immunity. Innate immune response against pathogens and endogenous ligands from dead and damaged cells is initiated through the recognition of pathogen-associated molecular patterns and damage-associated molecular patterns (DAMPs), respectively (Akira, Takeda, and Kaisho, 2001). Upon ligand binding, pro-inflammatory cytokines and chemokines are released, which, in addition to DAMPs, are recognised by the corresponding receptors in muscle fibers. This leads to activation of the nuclear factor- κ B (NF- κ B) signalling pathway, a chief inflammation regulator, and therefore, a self-sustaining autoinflammatory response, involved in chronic inflammation of the targeted tissue (**Figure 1.9**) (Rayavarapu *et al.*, 2013).

In the context of myositis, it is suggested that high creatine kinase levels and other molecules released by the injured tissue represent DAMPs (Rayavarapu *et al.*, 2013). Increased expression of a number of TLRs, including TLR2, TLR3, TLR4, TLR7, and TLR9, has been observed in muscle biopsy samples from various IIMs patients, including DM, PM, and IBM, which however are expressed in differential pattern (Kim *et al.*, 2010; Tournadre, Lenief, and Miossec, 2010; Baraka and Ahmed, 2015; Schreiner *et al.*, 2006; Brunn *et al.* 2012). Interestingly, TLRs expression has been found to be correlated with disease activity and clinical features in IIMs (Brunn *et al.* 2012; Baraka and Ahmed, 2015; Torres-Ruiz *et al.*, 2020). A strong link has been also suggested to exist between cytokines and TLRs expression in myositis. TLR4 and TLR9 have been found to be significantly correlated with the release of type II interferon- γ (IFN γ), interleukin (IL)-4, IL-17, and tumor necrosis factor- α (Kim *et al.*, 2010), and TLR3 with IL-8, IL-17, and IL-6 (Tournadre, Lenief, and Miossec, 2010; Schreiner *et al.*, 2006). A more recent study has also showed that TLR7/8 agonist R-848 was able to exacerbate myositis phenotype in a murine histidyl-transfer RNA synthetase-induced autoimmune myositis (EAM) model, including MHC class I upregulation, in a type I IFN, but not type II IFN, -dependent manner (Sciorati *et al.*, 2018). In turn, TLR4 antagonist TAK-242 alleviated type II IFN γ and IL17A expression in a mice EAM model (Zhang *et al.*, 2017). Further, Brunn *et al.* (2012) highlighted a chief role of TLR4 in IIMs pathogenesis, which was predominantly expressed in different IIMs subtypes. Compared to TLR2 and TLR9, TLR4 has been found to induce NF- κ B pathway activation and subsequent expression of IL-12 and IFN γ , through the classical myeloid differentiation response gene 88 (MyD88)-dependent signaling pathway and the MyD88-independent, Toll-IL-1 receptor (TIR) domain-containing adaptor-inducing IFN- γ (TRIF)-dependent signaling pathway (Brunn *et al.*, 2012).

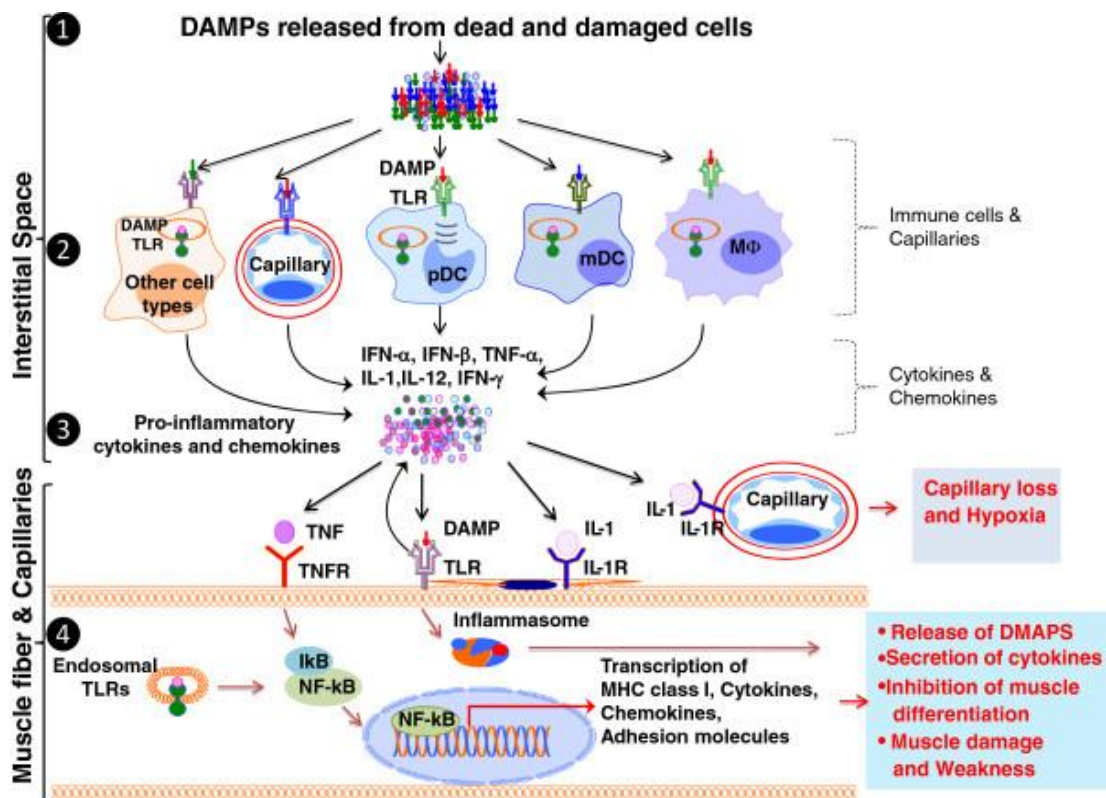


Figure 1.9 Innate immune mechanisms in myositis. **Step 1:** Physiological and pathological insults in skeletal muscle lead to the release of danger-associated molecular patterns (DAMPs) from dead and damaged cells. **Step 2:** Innate immune cells, including macrophages (M ϕ), myeloid dendritic cells (mDCs), plasmacytoid DCs (pDCs), as well as capillaries recognise danger-associated molecular patterns (DAMPs) through surface or endogenous toll-like receptors (TLRs) in the interstitial space. **Step 3.** This leads to the release of pro-inflammatory cytokines and chemokines, such as interferons (IFNs) and interleukins (ILs). **Step 4.** In muscle fibers and capillaries, cytokines, chemokines, and DAMPs are recognised by their respective receptors leading to NF- κ B signalling activation. Obtained from (Rayavarapu *et al.*, 2013).

1.3.1.2 Adaptive immune mechanisms

Innate and adaptive immune responses seem to be closely linked via DAMP signaling, leading to antigen processing and presentation by dendritic cells and consequently, activation of the adaptive immune response. T cells, subdivided into CD8+ T cytotoxic (Tc) cells and CD4+ Th cells, recognise MHC-I and MHC-II, respectively presenting antigenic

peptides of pathogens on the surface of innate immune cells (the antigen-presenting cells, APC). In combination with cytokines release, this leads to Tc cells activation and Th cells differentiation into effector Th1, Th2, and Th17 cells. Upon activation, Th cells stimulate innate immune defense through the release of cytokines. Moreover, activated Th cells are capable of stimulating the production of B cells-derived antibodies, which are discussed later in this section (**Figure 1.10**) (Rayavaparu *et al.*, 2013).

Evidence of B cells, plasma cells and immunoglobulin gene transcripts in the muscle of individuals with DM, IBM, and PM (Greenberg *et al.*, 2005; Salajegheh *et al.*, 2010; Bradshaw *et al.*, 2007) have changed the initial hypothesis that IIM pathology is mainly T cell mediated (Arahata *et al.*, 1984). B cells have been specifically described to locally mature into antibody-producing plasma cells within the myositic muscle (Salajegheh *et al.*, 2010). Autoantibodies, classified as myositis specific autoantibodies, exclusively detected in myositis, and myositis associated autoantibodies, also detected in other connective tissue disorders, are found in the serum of 50% of individuals with IIMs, and represent a vital tool in myositis diagnosis (Betteridge and McHugh, 2016). With autoantibodies being correlated with clinical features, Extended Myositis Antibody panel has been developed to facilitate the decision-making process for myositis-related diagnosis and treatment (O'Connor *et al.*, 2016; 2017). **Table 1.3**, which was readapted from Oldroyd, Lileker & Chinoy (2017), summarises myositis specific autoantibodies and their prevalence in IIMs subtypes, highlighting their diagnostic significance. The most frequent myositis specific autoantibody is anti-Jo-1 antibody that targets histidyl tRNA synthetase, classified as an antisynthetase antibody, with a prevalence of approximately 20% in patients with myositis. For this reason, anti-Jo-1 is included in 2017 EULAR/ACR classification criteria and has the highest score of probability among all the parameters (**Table 1.1**) (Lundberg *et al.*, 2017). Specifically, antisynthetase antibodies have been correlated with specific clinical features of myositis, interstitial lung disease, non-erosive arthritis, and mechanic's hands, collectively termed as antisynthetase syndrome (Lundberg, 2016).

Table 1.3 Myositis specific autoantibodies

Antibody	Prevalence
Antisynthetase antibodies (Jo-1, Zo, OJ, PL12, KS, PL7, EJ, Ha)	Jo-1 9–24% in adult DM/PM 75% of antisynthetase antibodies are Jo-1 Non-Jo-1 <5% in adult DM/PM 2–4% in JDM
MDA5	10–48% in Asian adults with DM 0–13% in Caucasian adults with DM 7–38% in JDM
SAE1	Exclusive to DM
Mi2	9–24% adult IIM 4–10% JDM
NXP2	1–17% adult PM/DM 23–25% JDM
TIF1	13–31% adult PM/DM 22–29% JDM
SRP	5% Caucasian adults PM/DM 8–13% Asian/African adult PM/DM < 2% JDM
HMGCR	6% adult PM/DM < 1% JDM
cN1A	33–34% IBM 36% Sjogren’s syndrome 20% SLE 0–5% adult DM/PM

MDA5 = melanoma differentiation-associated protein; SAE1 = SUMO-activating enzyme subunit 1; NXP2 = nuclear matrix protein 2; TIF1 = transcriptional intermediary factor 1; SRP = signal recognition particle; HMGCR = 3-hydroxy-3-methyl-glutaryl-coenzyme A reductase; cN1A = cytosolic 5’nucleotidase 1A

Table was readapted from Oldroyd, Lileker and Chinoy (2017)

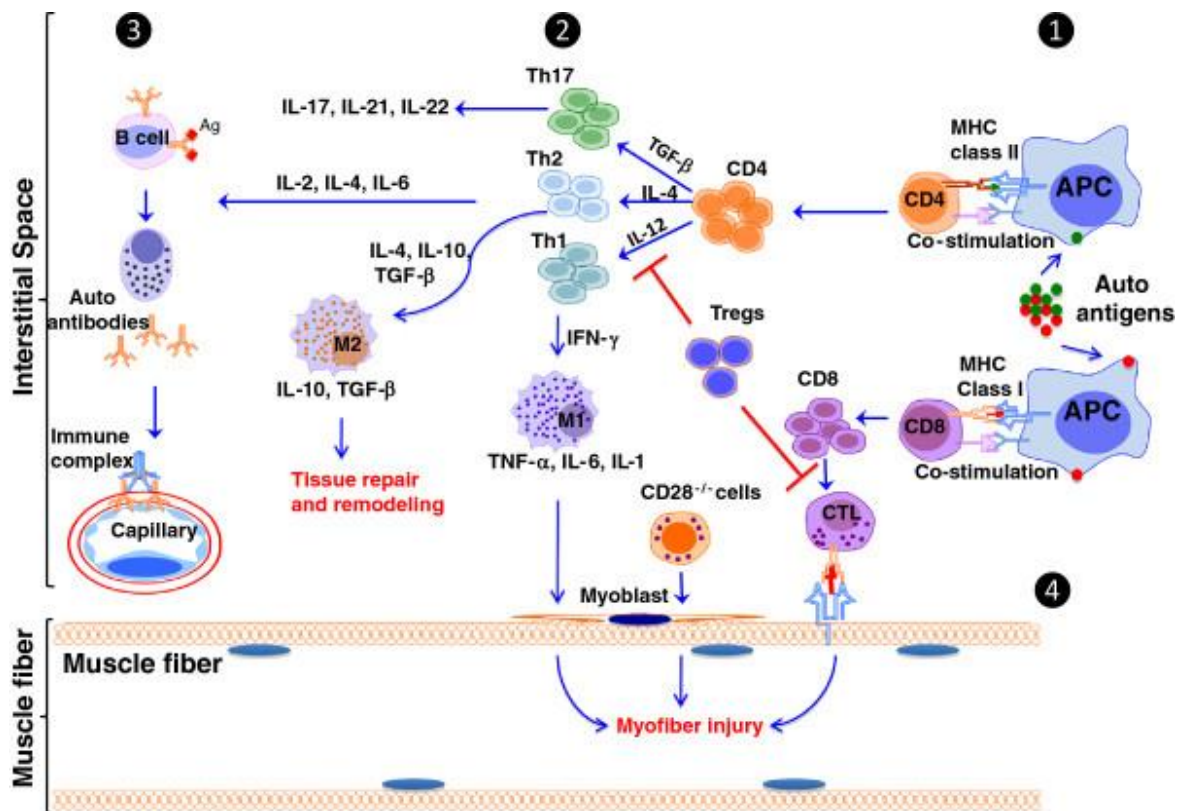


Figure 1.10 Adaptive immune mechanisms in myositis. Step 1: Antigen-presenting cells (APCs) are activated by DAMP signaling in innate immune cells, initiating adaptive immune response. **Step 2:** Major histocompatibility complex (MHC) class I and class II present an antigen to CD8+ and CD4+ T cells, respectively. Activated CD4+ T cells differentiate into Th-17,-2, and -1 effector T cells in presence of specific cytokines, producing a number of further cytokines, while activated CD8+ T cells produce cytotoxic T cells (CTL). **Step 3:** In turn, Th cells-induced cytokines activate B cells to differentiate into autoantibodies-producing plasma cells, activating complement complex and downstream damage to capillaries. **Step 4:** CTLs produce granzymes and perforin, potentially contributing to myofiber injury in myositis. Instead, T regulatory cells (Tregs) are involved in the prevention of inflammation and muscle damage. Obtained from Rayavarapu *et al.*, 2013.

1.3.1.3 Inflammatory mediators

Interferons (IFNs) are among the well-studied cytokines for both their potential use as a diagnostic marker and therapeutic target. In the past years, distinct IFN signatures have been identified allowing stratification of myositis subtypes. According to Rigolet *et al.* (2019), type I IFN α and IFN β signature is a characteristic hallmark of DM, type II IFN γ signature is specifically detected in IBM and ASM, while neither type I nor type II signature is evident in NAM. Various studies have reported increased levels of type I IFN-inducible genes in blood samples from patients with either DM or PM, but not in IBM, which was positively correlated with disease activity (Walsh *et al.*, 2007; Greenberg *et al.*, 2012). Intriguingly, controversy has been reported in the degree of type I IFN-inducible genes between DM and PM, with Walsh *et al.* (2007) describing similar magnitude of type I IFN-inducible genes expression in the two conditions, whereas Greenberg *et al.* (2012) highlighted higher magnitude in DM compared to PM. Ladislau *et al.* (2018) suggested that type I IFN may be responsible for vascular damage induction, as seen in DM pathophysiology, based on the observed strong correlation between the level of transcripts for type I IFN-stimulated genes and the angiogenesis-related genes, as well as vascular damage. Besides vascular damage, type I IFN pathway activation seemed to affect muscle differentiation and repair, and induce muscle atrophy as defined by myosin heavy chain immunofluorescence image analysis and muscle atrophy gene expression. Toll-like receptor 7 and 9 agonists-induced activation of plasmacytoid dendritic cells (pDCs) has been suggested to be involved in type I IFNs production in DM and PM patients. In turn, type I IFNs bind to IFN α receptor, existing in most human cells, initiating the JAK/STAT complex pathway. In particular, the transcription factor, IFN-stimulated gene factor 3 is activated, which upon nuclear translocation, reacts with IFN-stimulated response elements leading to the transcription of various genes and proteins production, involved in inflammation, including type I IFN cytokines (Arshanapalli *et al.*, 2015). Further to these evidence, ruxolitinib (a JAK1/2 inhibitor) was tested in 4 adult patients with DM who showed improved muscle strength and facial skin rash, accompanying by decreased serum levels of IFN (Ladislau *et al.*, 2018). A number of other research letters and primary articles have been published reporting their research on tofacitinib (a JAK1/3 inhibitor) efficacy in a small study cohort of adult individuals with refractory DM (maximum number

of 9 participants), with results mainly showing improved clinical efficacy (Kurtzman *et al.*, 2016; Kurasawa *et al.*, 2018; Paik *et al.*, 2021). In regards to juvenile DM, 2 case reports and a research letter on 25 refractory cases further recommend the potential use of JAK inhibitors as efficacious and well-tolerated therapeutic intervention (Aeschlimann *et al.*, 2018; Papadopoulou *et al.*, 2019; Ding *et al.*, 2021). Less is known about type II IFN γ in sIBM though, with an early study by Raju *et al.* (2003) showing increased levels of type II IFN γ -inducible chemokines, including CXCL9/Mig and CXCL10/IP10 in sIBM, which are involved in activated T cells recruitment, leading to self-sustained endomysial inflammation.

Among other cytokines, interleukin (IL)-6 has been commonly detected to be elevated in serum of myositis patients by ELISA and multiplex immunoassays and proved to be positively correlated with disease activity in DM and PM patients (Lundberg *et al.*, 1997; Bilgic *et al.*, 2009; Yang *et al.*, 2013; Gono *et al.*, 2014). Furthermore, in an established PM mouse model, in which a myosin-binding protein, C protein, is used to induce PM pathologic processes, IL6 blockade by anti-IL-6 receptor antibodies presented a strong therapeutic effect (Okiyama *et al.*, 2009). These findings support a previous study showing that IL-6-deficiency in a myosin-induced experimental myositis model led in absence of any clinical or histological symptoms of muscle damage as normally seen in the myositis model, including muscle fiber inflammation (Scuderi *et al.*, 2006). Given the established contribution of IL-6 in myositis-associated muscle damage, tocilizumab, a humanised anti-IL-6 receptor antibody that blocks IL-6-associated signal transduction, has been investigated in the treatment of refractory PM and DM. Even though tocilizumab administration has showed decreased serum creatine kinase levels and muscle inflammatory signs in two refractory Jo-1-positive PM patients (Narazaki *et al.*, 2011), as well as clinical improvement in a patient with an overlap syndrome with DM and systemic sclerosis (Kondo *et al.*, 2014), a phase IIb double-blind randomised controlled trial showed that tocilizumab was not adequately efficient (Aggarwal *et al.*, 2020).

1.3.2 Non-immune mediated mechanisms

Even though the involvement of innate and adaptive immune responses has been widely recognised as a mechanism of muscle weakness in myositis, a number of evidences

strongly suggest the involvement of other non-immune mediated alterations. These evidences include: **(1)** the degree of infiltration of inflammatory cells is independent of subjective clinical symptoms of myodiyid, including muscle weakness and pain (Dorph *et al.*, 2006); **(2)** muscle weakness precedes muscle inflammation (Coley *et al.* 2012; Frenette *et al.*, 2002); and **(3)** there is lack of response to immunosuppressive therapies with muscle weakness persisting despite the complete elimination of inflammatory cells (Lundberg *et al.*, 2000). A striking finding in different studies though has been the persistent expression of MHC class I antigens on muscle fibers accompanying with muscle weakness in absence of inflammatory infiltrates or following immunosuppressive treatment (Englund *et al.*, 2001; Li *et al.*, 2004; Lundberg *et al.*, 2000; Dorph *et al.*, 2006; Nyberg *et al.*, 2000). These observations highlight the potential role of MHC class I in initiating and maintaining myositis pathology through non-immune mediated mechanisms. In an attempt to investigate the role of MHC-I in myositis, it has been suggested that overexpression of the MHC-I molecules could itself mediate muscle cell death, independently of their involvement in the adaptive immune response, via activation of the ER stress response pathway and the generation of a self-sustained loop (Nagaraju *et al.*, 2005; Fréret *et al.*, 2013). In addition to ER stress activation, mitochondrial damage and reactive oxygen species (ROS) generation have also been proposed as non-immune-mediated mechanisms involved in myositis pathogenesis (Lightfoot *et al.*, 2015); however, their association to MHC-I overexpression remains to be revealed.

1.3.2.1 ER stress

The ER is a complex, membranous organelle within all eukaryotic cells, responsible for maintaining homeostasis in protein folding mechanism. Newly synthesised proteins in ribosomes bound to the ER membrane are transferred into the ER via signal recognition particle (SRP). The SRP binds the amino *N*-terminal signal sequence of the secretory proteins, as well as the ribosome, entering them into the ER via SRP receptor and membrane translocation complex binding. Once the signal sequence enters the ER, it is cleaved, releasing the polypeptide into the ER lumen, where it undergoes pro-translational modification and is correctly fold into its biologically active three-dimensional conformation (Cooper, 2000; Adams, 2019). In turn, failure of correct

polypeptide folding, leading to the accumulation of misfolded or aggregated proteins within the ER, activates the ER stress adaptive response, the unfolded protein response (UPR) that reduces protein load, restores homeostasis, and achieves cell survival. Three ER transmembrane sensors, inositol requiring enzyme 1 (IRE1), PKR-like eukaryotic initiation factor 2 α kinase (PERK), and activating transcription factor (ATF) 6, are activated in presence of misfolded proteins and stimulate UPR downstream cascades via the activation of specialised transcription factors (Senft and Ze'ev, 2015). IRE1 autophosphorylation leads to X box-binding protein 1 (XBP1) splicing that induces ER-associated degradation (ERAD), enabling ubiquitylation and degradation of misfolded proteins via the ubiquitin proteasome pathway (26S proteasome) (Adams, 2019). UPR also attenuates protein assembly via translation inhibition as controlled by PERK autophosphorylation and its downstream phosphorylation of eukaryotic translation initiation factor-2 α (eIF2 α). eIF2 α activation also leads to upregulation of ATF4 and subsequent cholesterol oxidase-peroxidase C/EBP homologous protein (CHOP) activation, involved in apoptosis initiation, when protein homeostasis cannot be restored. ATF6 ER sensor travels to the Golgi apparatus where it undergoes cleavage, releasing its cytosolic side. Once entering the nucleus, it stimulates the release of chaperones such as glucose-regulated protein 78 kDa and 94 kDa; GRP78 and GRP94, respectively, contributing to the increase of protein folding capacity (**Figure 1.11**) (Senft and Ze'ev, 2015; Adams, 2019).

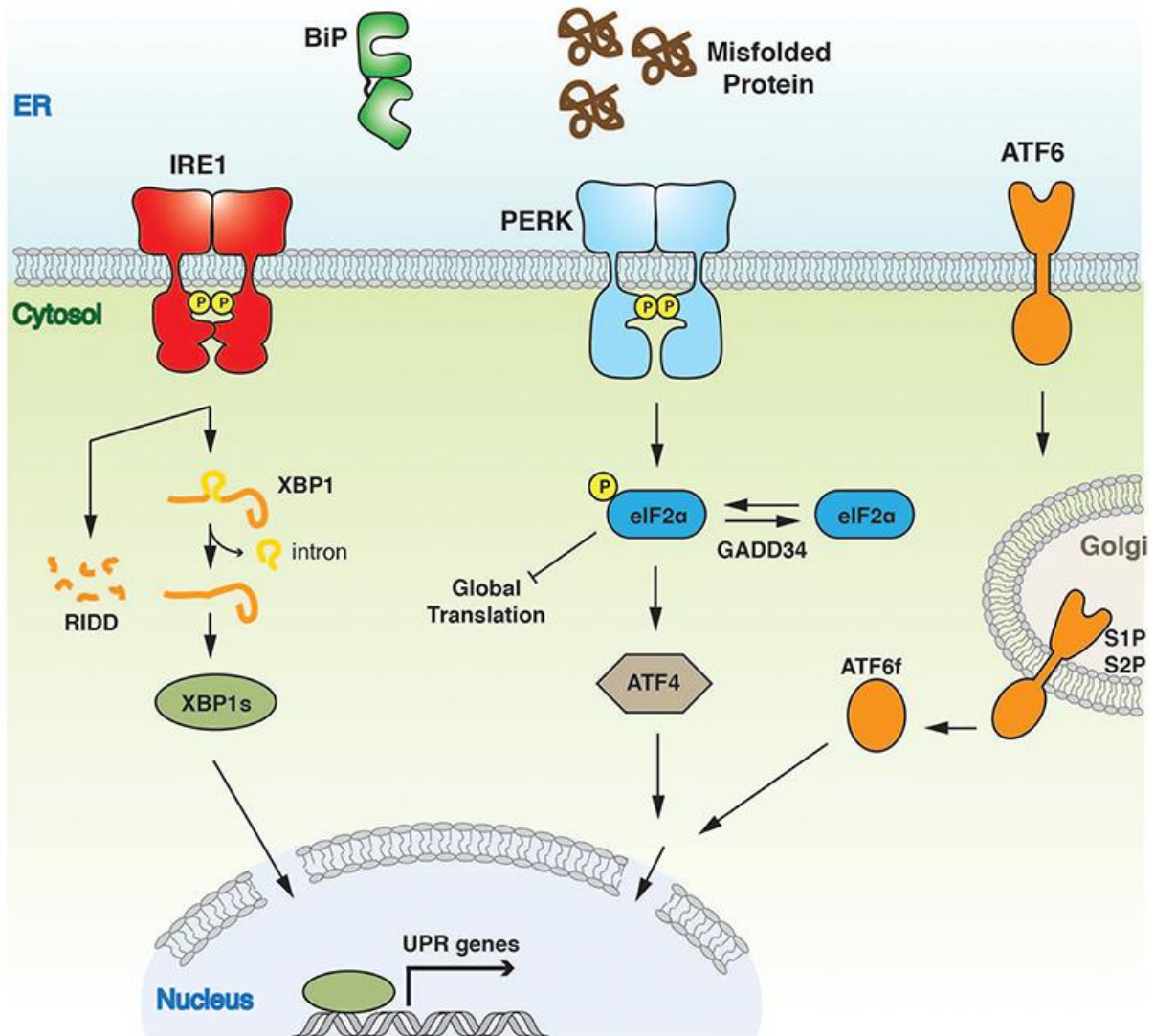


Figure 1.11 UPR signaling. Molecular mechanisms downstream the three ER transmembrane sensors IRE1, PERK, ATF6 activated upon accumulation of misfolded proteins, to retain protein homeostasis. Obtained from Adams *et al.*, 2019.

1.3.2.2 ER stress in myositis

A number of studies have revealed the implication of ER stress in myositis pathology. Increased protein expression of ER chaperones, such as GRP94, GRP78, ERp72, calnexin, and calreticulin, and chaperone-associated proteins, has been detected in sporadic IBM muscle fibers (Güttsches *et al.*, 2020; Vattemi *et al.*, 2004; Li *et al.*, 2006; 2014), with immunofluorescence analysis showing chaperones in the form of inclusions that are co-localised with amyloid- β (Vattemi *et al.*, 2004). Nogalska *et al.* (2006 and 2015) provided

a more in-depth analysis of the protein and gene expression of the three arms of UPR, demonstrating upregulation of ATF4 and its downstream target CHOP, spliced XBP-1, as well as ATF6 cleavage and GRP78 expression in muscle biopsies of sporadic IBM, but also reported the upregulation of homocysteine-induced ER protein, a common ER stress-induced protein, potentially downstream to ATF4 overexpression, and its co-localisation with amyloid- β , GRP78, and 20S proteasome subunit. Impairments in the autophagosomal-lysosomal pathway and clearance of misfolded proteins have also been reported as an ER stress-associated pathogenic mechanism in sporadic IBM (Nogalska *et al.*, 2010; D'Agostino *et al.*, 2011; Girolamo *et al.*, 2013).

1.3.2.3 ROS from mitochondria and other sources in skeletal muscle

Skeletal muscle is a key site of reactive oxygen and nitrogen species (RONS or ROS/RNS) generation through diverse endogenous and exogenous sources. ROS/RNS constitute free radicals and non-radical reactive species that are oxygen- and nitrogen-centered, respectively; however, RNS are also entirely oxygen-, besides nitrogen-containing species (Li, Jia, and Trush; 2016). Free radicals are capable of existing independently, have short half-life and are highly and rapidly reactive species with any surrounding molecules as they contain at least one unpaired electron that can be donated or abstract another electron from other compounds to attain stability, turning the other compound a free radical itself (Phandiendra, Jestadi, and Perivasamy, 2015). Non-radical ROS/NOS are derivatives of oxygen and nitrogen, respectively, with long half-life that can transport within the cell, react with various cellular molecules, and contribute to numerous signaling pathways (Barbieri and Sestili, 2012).

RONS are constantly generated by skeletal muscle at rest and during contractile activity, with the primary radical species generated being superoxide and nitric oxide (NO), which can readily react leading to the formation of a wide range of other RONS (Sakellariou *et al.*, 2014). **Figure 1.12** illustrates the potential sources of RONS as reported by Nemes *et al.* (2018). Mitochondrial electron transport chain, particularly from Complex I and Complex III, is considered as the main source of ROS generation in skeletal muscle, with numerous studies in both mice and human showing increased mitochondria-derived ROS generation during contraction and exercise (Saborido *et al.*, 2011; Vasilaki *et al.*, 2006; Sahlin *et al.*, 2010). However, other non-mitochondrial sources within muscle and

satellite cells, as well as their surrounding cells such as fibro-adipogenic precursors, macrophages, endothelial cells and other vascular cells, serve as another source of RONS generation, including during skeletal muscle regeneration (Le Moal *et al.*, 2017). Myostatin has been also found to induce ROS generation via tumor necrosis factor- α (TNF- α) and nicotinamide adenine dinucleotide phosphate (NADPH) oxidase, with myostatin depletion leading to muscle atrophy and mimicking aging (Sriram *et al.*, 2011). In addition, xanthine oxidase (XO) in endothelium lining skeletal muscle, reacts with oxygen to generate superoxide, while NADPH oxidase in sarcolemma and other enzymes in the cytoplasm, such as phospholipase A2, are also involved in further ROS generation. Last but not least, in skeletal muscle, NO is generated by the neuronal NO synthase isoform (type I or nNOS) (Michaelson, Iler and Ward, 2013).

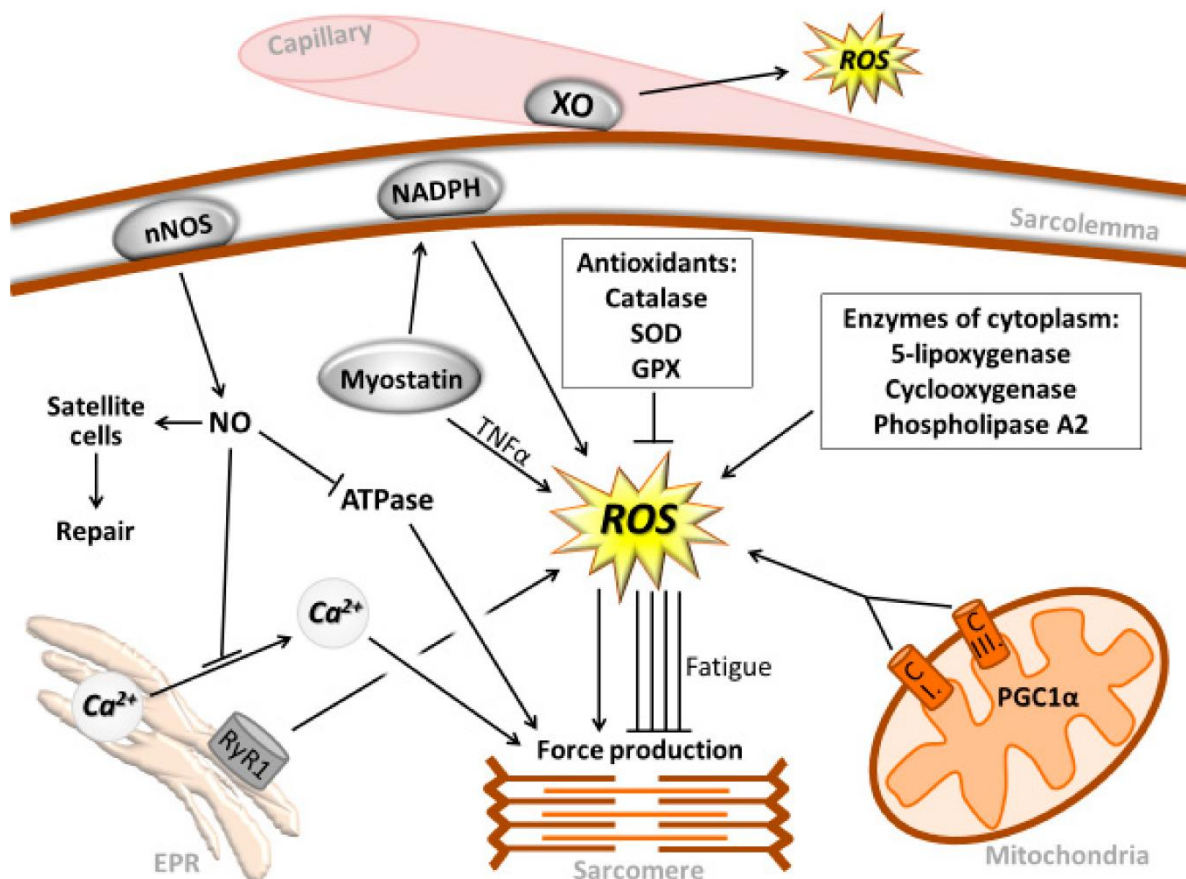


Figure 1.12 Potential sources and roles of RONS in skeletal muscle. ROS can be generated through mitochondrial electron transport chain, mainly from Complex I and III,

myostatin through TNF- α and NADPH oxidase, and activation of ryanodine receptor 1 (RyR1) in the SR of skeletal muscle, as well as XO located in the endothelial cells, in generation is also induced via different enzymatic activities in the cytoplasm. Obtained from Nemes *et al.*, 2018.

RONS play a dual role in skeletal muscle, and other tissues, depending on the magnitude and period of RONS generation. Beneficial effects that allow cellular adaptation to and protection against stress are seen under physiological conditions described by low/moderate levels over a short period of time, while harmful effects, leading to cell death are induced under pathophysiological conditions of high/aberrant levels longer period (Ji *et al.*, 2006). Early studies have identified the importance of muscle-derived ROS in producing force in unfatigued muscle, with endogenous ROS depletion resulting in reduced force production in both single fibers and fiber bundles isolated from frog limb muscle and rat diaphragm, respectively (**Figure 1.12**) (Regnier *et al.*, 1992; Reid, Khawli and Moody, 1993). ROS also present a chief role on the ER of the muscle (SR), with basal redox states exerting oxidative and nitrosative modifications of the ryanodine receptor (RyR) calcium release channels, leading to activation of calcium signaling pathways in the cell (Hidalgo, Donoso and Carrasco, 2005). Additionally, ROS can activate various protein kinases, including AMP-activated protein kinase (AMPK) and mitogen-activated protein kinase (MAPK) family members – c-Jun N-terminal kinase (JNK), p38 MAPK, and extracellular signal-regulated kinase (ERK) – inducing phosphorylation of redox-sensitive transcription factors and subsequent synthesis of proteins associated with cellular adaptation (Powers *et al.*, 2010). Additional evidence of ROS-mediated cellular adaptation is the activation of peroxisome proliferator-activated receptor- γ coactivator-1 protein- α (PGC-1 α) in response to exogenous hydrogen peroxide treatment in mouse skeletal muscle myotubes (Irrcher, Ljubcic and Hood, 2009). In particular, PGC-1 α is a chief mediator of mitochondrial biogenesis, which is suggested to be stimulated during exercise downstream to the aforementioned kinases activity (Mason and Wadley, 2014).

1.3.2.4 ROS and mitochondria in muscle dysfunction

It is undoubtable that low-level ROS play a crucial role in normal muscle functioning; nevertheless, aberrant high ROS levels have been highly contributed to muscle wasting and dysfunction, and therefore widely studied in such instances, including ageing and

muscle diseases. Numerous studies have proven the involvement of oxidative damage, induced by the imbalance between oxidants and antioxidants, to contractile proteins, including myosin heavy chain proteins and troponin C (Coirault *et al.*, 2007; Plant, Lynch and Williams, 2000). Increased ROS contributes to muscle protein synthesis inactivation through enhancement of proteolysis processes (Hyatt and Powers, 2021). This occurs via calpain and caspase-3 activation, and further ubiquitin proteasome system stimulation, also leading to impaired mitochondrial regulatory proteins, such as mitochondrial fission and fusion-associated dynamin related protein 1 (DRP1) and mitofusin (MFN)1, respectively (Hyatt *et al.*, 2021). Furthermore, as previously mentioned, ROS mediate RyR-derived calcium; however, continuous ROS-associated calcium leak from oxidised and nitrosylated RyR1 in aged mice muscle has been positively correlated with depressed muscle-specific force and exercise capacity. RyR calcium leak has also led to mitochondrial membrane depolarisation, as well as further mitochondrial superoxide and cellular NO production (Andersson *et al.*, 2011). Based on this evidence, a recent review by Hyatt and Powers (2021) has listed three interdependent manners through which mitochondrial dysfunction induces skeletal muscle wasting, as **(a)** elevated mitochondrial ROS generation, **(b)** proapoptotic factors release, and **(c)** mitochondrial respiratory deficiency.

1.3.2.5 ROS and mitochondria in myositis

Mitochondrial abnormalities have been extensively detected in IIMs using histological and histochemical analysis; however, less is known at a molecular level. Specifically, the presence of cytochrome c oxidase (complex IV, COX) (deficient fibres, as well as increased mitochondrial DNA (mtDNA) deletions, have been an early and consistent feature of mitochondria-associated abnormalities involved in sIBM pathophysiology (Santorelli *et al.*, 1996; Oldfors *et al.*, 1995; Chariot *et al.*, 1996; Blume *et al.*, 1997; Lindgren *et al.*, 2015). Using histochemical and immunohistochemical analyses, Rygiel *et al.* (2015) demonstrated different stages of mitochondrial abnormalities as described by different respiratory-deficient sIBM muscle fibres, which showed higher propensity to muscle atrophy compared to normal respiratory fibres. The study described three types of deficient fibres, as follows: (a) COX-deficient fibres with absent COX enzymatic activity, loss of expression of complex I and complex IV subunits I and IV (COX-I and COX-IV,

respectively); (b) COX-intermediate fibres with decreased COX enzymatic activity, preserved COX-IV expression, and loss of complex I expression; and (c) complex I-deficient fibres with normal COX enzymatic activity, but loss of complex I protein expression. Furthermore, complex I-deficient fibres seemed to be present in a higher percentage compared to COX-deficient fibres in the specific cohort. Overall, these findings indicate a progressive mitochondrial dysfunction in sIBM that initiates with deficits in complex I (Rygiel *et al.*, 2015). These results are consistent with another clinical study established by Joshi *et al.* (2014) that proposed COX-deficient fibres in sIBM, with decreased COX activity and increased citrate synthase activity, but also investigated their functional effects, showing decreased oxygen desaturation and increased lactate production during exercise.

Aiming to extend IBM research on mitochondrial abnormalities, Catalán-García *et al.* (2016, 2020) examined mitochondrial phenotype of sIBM muscle biopsies and blood samples using genetic, molecular, and functional techniques. Initially, reduced mtDNA content was seen specifically in the IBM muscle tissue, which was positively correlated with mtDNA deletions, as well as downregulated mitochondrial fusion protein MFN2. Even though mitochondrial respiratory complex assembly analysis showed no statistically significant changes, attenuated complex IV activity was found in muscle and peripheral blood mononuclear cells (PBMCs). Interestingly, mitochondrial content was increased as described by changes in citrate synthase activity, and mitochondrial protein synthesis presented a trend of increase in sIBM muscle, all suggesting mitochondrial biogenesis involvement as a compensation mechanism for mitochondrial defects in muscle, but not in PBMCs. It should also be noted that in the specific study cohort of sIBM patients, no lipid peroxidation was evident (Catalán-García *et al.*, 2016). Downregulated mitochondrial dynamics were also found in another study involving 2 human skeletal muscle samples of sIBM, described by reduced protein content of the fusion, MFN2 and Optic atrophy 1 (OPA1), and fission, DRP1, associated molecules (Shabrokh *et al.*, 2014).

Besides their distinct presence in the disease pathology, only a few studies have been established on mitochondrial respiration in myositis, which mostly focused on sIBM. A recent study has reported diminished mitochondrial respiration in sIBM fibroblasts confirming the involvement of mitochondrial abnormalities in peripheral tissues, besides

its target tissue (muscle) (Catalán-García *et al.*, 2020). This change was accompanying by increased serum lactate levels indicative of anaerobic metabolism, potentially to compensate for deficits in cellular oxidative phosphorylation. To examine the ability of mitochondria to respond to increased energetic output in response to glucose deprivation, mitochondrial respiration was observed under low-glucose growth conditions (5 mM glucose) in order to prevent Crabtree effect – switch to glycolytic metabolism because of high glucose availability in growth media (Catalán-García *et al.*, 2020; Basualto-Alarcón *et al.*, 2020). Results showed inability of sIBM fibroblasts to activate mitochondria, while decreased respiration and COX activity, as well as increased proton leak were seen (Catalán-García *et al.*, 2020). Real-time measurements of mitochondrial oxygen consumption in skeletal muscle cells derived from IIMs biopsy samples, were established for the first-time last year by Basualto-Alarcón *et al.* (2020) and Oikawa *et al.* (2020). As seen in sIBM fibroblasts (Catalán-García *et al.*, 2020), mitochondrial respiratory deficits as described by diminished basal, maximal, and ATP-linked oxygen consumption rate (OCR), accompanying by decreased cellular ATP levels, were found in myoblasts derived from three cases of sIBM compared to healthy control. As previously described, no changes were seen in the expression levels of mitochondrial respiratory chain complexes I-V. Changes in mitochondrial morphology and dynamics were also reported in the form of decreased mitochondrial area and length/width ratio, and reduced mitochondrial mobility, as well as downregulation in the expression of mitochondrial fission Drp1 and fusion Opa1 proteins in sIBM myoblasts, while expression of mitochondrial fusion MFN1 and MFN2 proteins remained unaffected (Oikawa *et al.*, 2020). The study performed by Basualto-Alarcón *et al.* (2020) used a cohort of 2 patients with DM, 2 patients with IMNM, and 1 patient with IMNM or DM, and results were presented altogether as IIMs samples. Similar to sIBM myoblasts, DM/IMNM myoblasts showed diminished overall OCR, including ATP-linked respiration, and mitochondrial hyperpolarisation in standard high-glucose growth conditions, with no changes in total intracellular oxidative phosphorylation-linked ATP levels. However, in glucose-free and galactose supplemented growth media, IIMs myoblasts showed their ability to increase mitochondrial respiration to normal levels as seen in healthy myoblasts, suggesting that mitochondria in DM/IMNM muscle retain their ability to reach functionality. The study showed though that highly functional mitochondrial can be detrimental to the cells as

they presented higher propensity to die after an oxidative insult (Basualto-Alarcón *et al.*, 2020).

Oxidative stress has also been spotulated to be involved in myositis pathogenesis. In the previously mentioned study of Catalán-García *et al.* (2020), oxidative stress was reported in sIBM fibroblasts in response to reduced glucose levels, while elevated total antioxidant capacity levels seen in sIBM under normal glucose conditions (25 mM glucose). Consistently with this study in regards to antioxidant capacity in sIBM, Shabrokh *et al.* (2014) demonstrated a trend toward catalase upregulation in human skeletal muscle biopsy samples from 2 sIBM patients. In contrast, reduced antioxidant status was observed in a large cohort of PM and DM patients compared to healthy controls, as described by bilirubin and uric acid serum concentrations – no differences were seen between the two IIMs types (Chen *et al.*, 2017). Increased ROS generation, specifically intracellular superoxide levels, was also noticeable in DM/IMNM muscle cells in both absence and presence of glucose (Basualto-Alarcón *et al.*, 2020).

The role of NO signalling in myositis remains poorly understood. An early study by Schmidt *et al.* (2012) on the expression of NOS in different types of myositis, showed that inducible NOS was overexpressed in the muscle fibres of 5 out of 10 sIBM samples, while less was seen in DM (2 out of 11) and PM (3 out of 8) samples, similarly to the levels of intracellular NO production. Interestingly, NO production was seemed to be correlated with β -amyloid accumulation and inflammation in skeletal muscle (Schmidt *et al.*, 2012; Baron *et al.*, 2000).

1.3.2.6 Skeletal muscle as an endocrine organ

Skeletal muscle is a dynamic organ that is responsible for a variety of functions in the human body, which are not limited to locomotion and power generation. Instead, skeletal muscle has been known to be able to communicate with other tissues through active secretion of various factors. Those include cytokines, chemokines, and peptides, termed as myokines, that are synthesised and released by skeletal muscle, with muscle contraction being considered as the main mediator of their expression and secretion (Ostrowski *et al.*, 1998). Myokines exert autocrine, paracrine, and endocrine effects on other organs, setting skeletal muscle as an endocrine organ (Schnyder and Handschin,

2015). The last decade a wide range of myokines have been detected, composing the skeletal muscle secretome. Specifically, in-depth proteomic analysis of the human skeletal muscle secretome has revealed over 600 myokines, which however have not all been fully characterised (Lee and Jun, 2019). Since then, myokines research has emerged in the context of their association with skeletal muscle mass and function, with more and more studies also examining their role in diseased muscle, such as in cancer cachexia, and muscular dystrophy, while a few are focusing on myokines in myositis pathology (Mageriu *et al.*, 2020).

1.3.2.7 Myokines in myositis

MHC-I upregulation, as a prominent feature in myositis pathophysiology, has been previously assessed in the aspect of myokines secretome, with related studies though being limited. Following Nagaraju *et al.* (2005) early suggestion of MHC-I-induced ER stress and NF- κ B pathway activation, and its potential involvement in inflammatory myokines release in absence of inflammation, Lightfoot *et al.* (2015) provided some evidence of a correlation between MHC-I upregulation, ER stress, and the release of IL-6, as well as chemokine ligands (CCLs), CCL2 (or monocyte chemotactic protein-1, MCP-1), CCL4 (or Macrophage inflammatory protein 1b, MIP1b), and CCL5 (or Regulated upon Activation, Normal T-cell Expressed, and Secreted, RANTES) in a murine skeletal muscle cell line. Multiple other studies also supported a role of myokines secretome in IIMs, showing the upregulation of IL-6, IL-15, IL-18, as well as chemokine ligands (CCLs), CCL2, (or monocyte chemotactic protein-1, MCP-1), CCL4 (or Macrophage inflammatory protein 1b, MIP1b), and CXCL10 in IIMs (Civatte *et al.*, 2005; Sanner *et al.*, 2014; De Paepe *et al.*, 2005; Helmers *et al.*, 2018; Sugiura *et al.*, 2002).

Most of the studies have focused on myokines that are overexpressed in the myositic muscle secretome, while less is known on the potential downregulated myokines and their role in IIMs pathology. Insulin-like 6 (Insl6), a member of the insulin-like/relaxin family is one of the limited myokines that have been proposed to be deficient in PM and DM. In particular, decreased gene expression of Insl6 was observed in human skeletal muscle biopsy samples compared to control samples, which were correlated with disease severity, as defined by muscle atrophy. Intriguingly, this is in contrast to murine models of myositis and cardiotoxin injury that have shown upregulated Insl6. This suggests that

in those short-term injury models, Insl6 might be stimulated as an adaptive response to immune-mediated tissue damage, while in chronic human disease, the reduced Insl6 activity might contribute to IIMs development. Therefore, this study highlights the importance of investigating the muscle secretome in human myositic samples. Further investigation into the role of Insl6 showed that Insl6 deficiency in a mouse experimental model of autoimmune myositis led to a worsened myositis phenotype, described by CD5 and CD8 T-cells infiltration and upregulated expression of inflammatory cytokines TNF α and IFN γ , which were rescued by Insl6 overexpression (Zeng *et al.*, 2014).

Needs of further research

A greater understanding of the non-immune mediated mechanisms in IIM pathology is required. In particular, *in vitro* studies on the molecular and functional changes in mitochondrial function associated with ER stress, MHC class I, and myositic muscle secretome are needed.

1.4 Aims

1. Develop human *in vitro* models of myositic muscle:
 - a) pharmacological cell model of ER stress using tunicamycin
 - b) genetically modified cell model of an immortalised human skeletal muscle transfected cell line that overexpresses MHC-I, in presence or absence of type I IFNs
 - c) clinical cell model of primary human myositis skeletal muscle cell line derived from patient biopsy samples.
2. Characterise mitochondrial function in the *in vitro* models.
3. Assess the role of ROS generation in myositis related mitochondrial abnormalities.
3. Assess the impact of myokines secretome derived from myositis cells on mitochondrial function and ROS generation.

1.5 Hypothesis

Multiple intrinsic mechanisms that can be overlapping and interdependent lead to impaired ROS-dependent mitochondrial bioenergetics that can potentially underly persistent muscle weakness in myositis disease.

Chapter 2

Materials and Methods

2.1 Cell Culture

Table 2.1 Reagents for cell culture

Reagents	Supplier	Catalogue #
High-glucose (4.5 g/L) Dulbecco's modified Eagle's medium (DMEM)	Lonza	12-914F
Medium-199 with Earle's balanced salt solution mixture	Sigma Aldrich	12-119F
Heat-inactivated foetal bovine serum	Gibco	10500-064
Penicillin/streptomycin	Lonza	17-602E
Gentamicin	Sigma Aldrich	G1397
L-glutamine	Lonza	17-605E
Fetuin from foetal bovine serum	Sigma Aldrich	F3004
Dexamethasone	Sigma Aldrich	D4902
Recombinant human insulin	Sigma Aldrich	
Recombinant human basic fibroblast growth factor	Gibco	PHG0026
Recombinant human epidermal growth factor	Gibco	PHG0311
Recombinant human hepatocyte growth factor	Gibco	PHG0254
DPBS	Lonza	17-512F
Trypsin-EDTA	Sigma Aldrich	T4049
Trypan Blue	Lonza	17-942E
Dimethyl sulfoxide (DMSO)	Fisher BioReagents	10103483
Ham's F-12 Nutrient Mix	Gibco	21765029
KCL	Merck	7447-40-7
Imidazol	Sigma-Aldrich	I5513
MgCl ₂	Sigma-Aldrich	255777
EGTA	Merck	67-42-5
Dispase II	Sigma-Aldrich	D4693
250 mM CaCl ₂	Sigma-Aldrich	449709
Collagenase D	Roche	11088882001
Laminin	Sigma-Aldrich	114956-81-9
OPTI-MEM	Gibco	31985062
TransIT-X2	Mirus	MIR 6003

2.1.1 Immortalised cell culture

An immortalised human skeletal muscle cell line (donor age, 25 years; sex, male) was provided as a gift from the laboratory of Professor Vincent Mouly, Institute of Myology, Paris. Primary myoblasts were isolated from the semitendinosus muscle of a 25-year-old healthy man and immortalised by transduction of human telomerase reverse transcriptase and cyclin-dependent kinase 4-expressing vectors, retaining significant

characteristics of *in vivo* human skeletal muscle (Mamchaoui *et al.*, 2011). Skeletal muscle cells were retrieved from liquid nitrogen in cryovials were transferred into 15 mL tubes containing growth media, centrifuged at 1,000 RPM for 5 min, resuspended and cultured in growth media (**Table 2.2**) in tissue culture flasks (T75), and incubated at 37°C in a humidified atmosphere of 5% CO₂. Cells were passaged once reaching approximately 80% confluency, using conventional trypsin-EDTA detachment. To induce differentiation, growth media was replaced with differentiation media (**Table 2.3**) when cells reached 90-100% confluency and incubated for 72–96 hours.

Table 2.2 Growth media for immortalised human skeletal muscle cells

Reagents	Concentration
High-glucose (4.5 g/L) DMEM and Medium-199 with Earle's balanced salt solution mixture	1:5 v/v
Heat-inactivated foetal bovine serum	20% (v/v)
Penicillin/streptomycin	1% (v/v)
Gentamicin	10 µg/mL
L-glutamine	1% (v/v)
Fetuin from foetal bovine serum	25 ng/mL
Dexamethasone	0.2 µg/mL
Recombinant human insulin	5 µg/mL
Recombinant human basic fibroblast growth factor	0.5 ng/mL
Recombinant human epidermal growth factor	5 ng/mL
Recombinant human hepatocyte growth factor	2.5 ng/mL

Table 2.3 Differentiation media for immortalised human skeletal muscle cells

Reagents	Concentration
DMEM	
Heat-inactivated foetal bovine serum	2% (v/v)
Penicillin/streptomycin	1% (v/v)
Gentamicin	10 µg/mL
L-glutamine	1% (v/v)
Recombinant human insulin	10 µg/mL

2.1.2 Muscle Biopsy Collection, Primary Cell Isolation and Culture

The study was approved by the Myositis Research Tissue Bank and donors provided written informed consent to participate in this study. Human skeletal muscle samples were collected from Salford Royal NHS Foundation Trust in ice-cold 10× relaxing solution (pH 7.0) and transferred on ice to Manchester Metropolitan University laboratory (**Table 2.4**). Tissue digestion was performed on the same day of collection according to Soriano-Arroquia *et al.* (2017). Firstly, the biopsy sample was immersed in 70% ethanol, washed with sterile DPBS, and placed on a Petri dish containing 10× relaxing solution. Connective and fat tissue was removed using sterile tweezers and minced into small pieces using sterile scalpels under Zeiss Stereoscope. The sample was then transferred into a 50 mL tube and incubated in 2 mL (already warmed to 37°C) enzymatic digestion solution prepared in low-glucose (1 g/L) DMEM (**Table 2.5**) for 30–40 minutes at 37°C. The tube was gently inverted every 5–10 minutes. After incubation, digestion was neutralised with 4 mL (2 volumes) of passage 0 Growth Media (**Table 2.6**). After pipetting up and down a few times, the digestion solution was filtered twice through a 70 µm cell strainer over a 50 mL tube. Then, cells were pelleted for 5 minutes at 443× g at room temperature. The supernatant was discarded, and cell pellet was resuspended in 5 mL passage 0 Growth Media, and cells were plated in laminin-coated T25 flasks. Specifically, laminin was prepared at a 10 µg/mL working solution in DPBS. T25 flasks were coated and incubated with 1 mL laminin solution at 37°C for 1 hour. Excess solution was removed, and flasks were left to air dry at least 2 hours before adding the cells. Flasks prepared a previous day were wrapped in parafilm and stored at 4°C for maximum 1 week.

Table 2.4 Relaxing Buffer (10×, pH 7.0) prepared in distilled water

Reagents	Stock Concentration	Volume (mL)
KCL	2.5 M	20
Imidazol	0.5 M	10
MgCl ₂	0.1 M	5
EGTA	0.1 M	10

Table 2.5 Muscle Tissue Digestion Solution prepared in low-glucose DMEM

Reagents	Concentration
Dispase II	4.8 mg/mL
250 mM CaCl ₂ in 1× DPBS	2.5 mM
Collagenase D	10 mg/mL

Cells in laminin-coated flasks were incubated in a humidified incubator (5% CO₂) at 37°C. Following 2 days of incubation, and every 2-3 days, media was changed to fresh passage 0 Growth Media. Primary skeletal muscle cells retrieved from liquid nitrogen in cryovials were transferred into 15 mL tubes containing growth media, centrifuged at 1,000 RPM for 5 min, resuspended and cultured in passage 1-5 Growth Media in T75 flasks (**Table 2.6**).

Table 2.6 Growth media for primary human skeletal muscle cells

Reagents	Concentration
<i>Passage 0 Growth Media</i>	
Ham's F-12 Nutrient Mix	
Heat-inactivated foetal bovine serum	20%
L-glutamine	1%
Penicillin/streptomycin	1%
Recombinant human basic fibroblast growth factor	2.5 ng/mL
<i>Passage 1-5 Growth Media</i>	
High-glucose DMEM	
Heat-inactivated foetal bovine serum	30%
L-glutamine	1%
Penicillin/streptomycin	1%

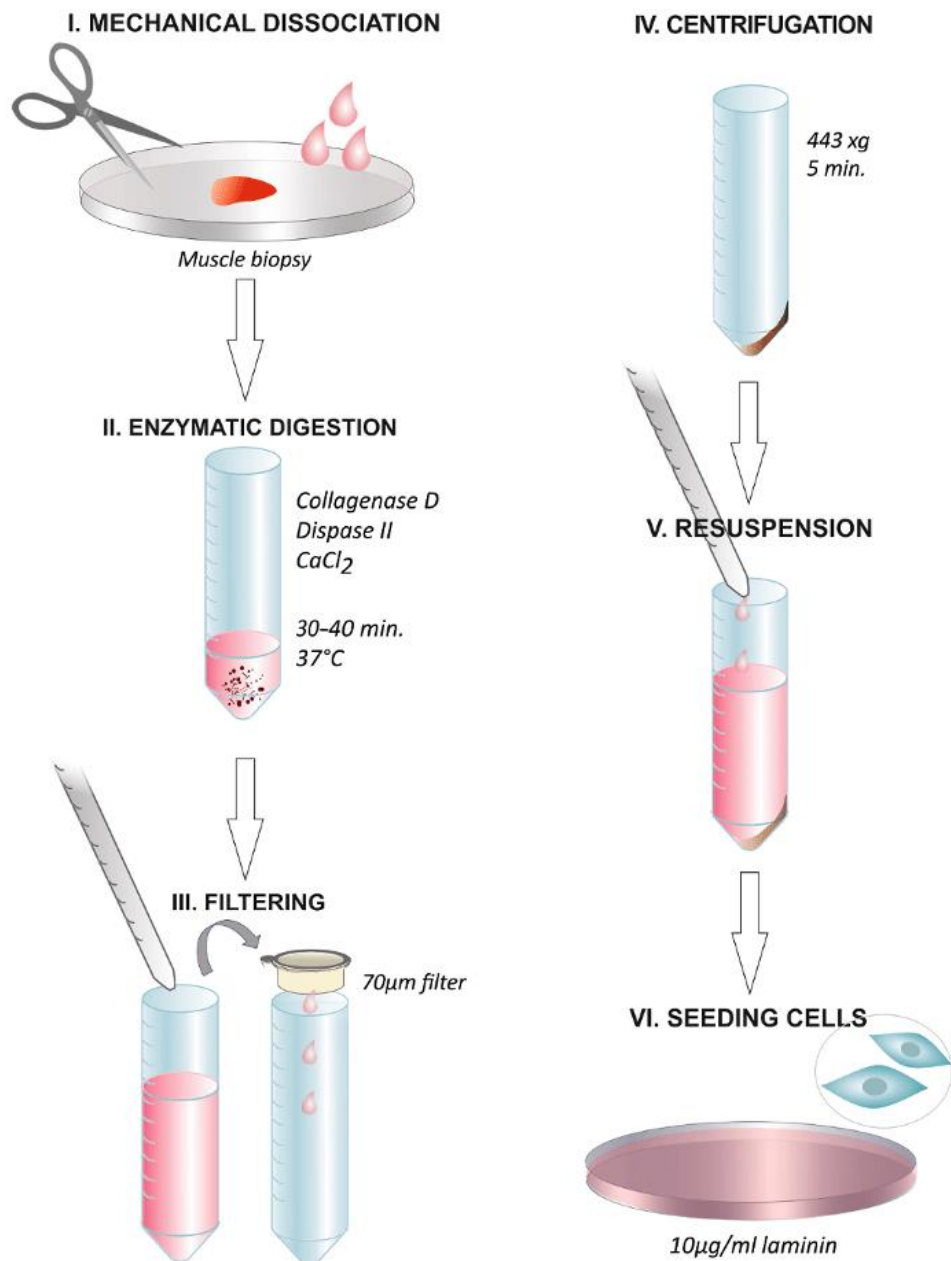


Figure 1.1 Graphical presentation of the experimental procedure followed for isolating human primary skeletal muscle cells. Skeletal muscle biopsy sample is dissociated (I) and then introduced to enzymatic solution to enable tissue digestion (II). Neutralised enzymatic digestion is filtered twice through a 70 µm membrane filter into a 50 mL tube (III) and centrifuged (IV). Cell pellet is resuspended in growth media (V) and cells are plated in a T25 flask (VI). Obtained from Soriano-Arroquia *et al.* (2017).

2.1.3 Passaging, seeding, and cryopreservation

Skeletal muscle cells were passaged when reached 80% confluency. Growth medium was removed, and cells were washed once with 1× DPBS (T75 flask, 5 mL; T175 flask, 10 mL). Immortalised human skeletal muscle cells were incubated at 37°C with 0.05% Trypsin/0.53 mM EDTA (1×) for 5 min to detach the adherent cells. For primary human skeletal muscle cells passaging, 0.05% Trypsin/0.53 mM EDTA (1×) was added to the cells for 10 seconds at room temperature; following Trypsin/EDTA removal, cells were incubated at 37°C for 3–5 minutes. Trypsin/EDTA activity was inhibited by the addition of equal volume of growth media, cells solution was centrifuged at 1,000 RPM for 5 minutes, and cell pellet was resuspended in growth medium. Cells were transferred into tissue culture flasks or counted to be cryopreserved or seeded into plates for experimental use. Cell suspension was mixed 1:1 with Trypan Blue (50 µL) and viable cells (unstained cells) were counted using a haemocytometer. The following formula was used to determine the number of viable cells/mL: (Average number of viable cells in 8 corner squares) × (dilution factor (2)) × (10⁴). Following cell counting, cell solution was diluted in growth media and transferred into plates. For cryopreservation, cell solution was centrifuged at 300 × g for 10 min, supernatant was aspirated, and cell pellet was resuspended in ice-cold freezing media containing 90% foetal bovine serum and 10% Dimethyl sulfoxide (DMSO) in a concentration of 1×10⁶ cells per cryovial. The cryovials were stored into a Mr. Frosty freezing container at –80°C overnight and then transferred to liquid nitrogen (196°C) tank.

2.1.4 Treatment of cells

Tunicamycin was prepared as a 5 mg/mL stock solution in DMSO and stored at 4°C. Immortalised human myoblasts were exposed to 0.1 µg/mL diluted in growth media for 24 hours (**Table 2.2**), while control cells remained untreated.

Eukarion-134 (EUK-134) was reconstituted in sterile double distilled water (ddH₂O) at a stock concentration of 2 mg/mL and stored at –20°C. EUK-134 was used at a final concentration of 10 µM diluted in tunicamycin-containing growth media (**Chapter 3**) or primary human skeletal muscle cells growth media (**Chapter 5 and 6**).

Recombinant human IFNβ protein carrier-free formulation was prepared as a 200 µg/mL stock solution in sterile ddH₂O and stored at –20°C. Recombinant human IFN Alpha A

(IFN α) protein was supplied frozen at 0.05 mg/mL in PBS. Both IFN α and IFN β were generally used at a final concentration of 100 ng/mL for 18 hours, unless otherwise stated, prepared in complete growth media or transfection solution.

2.1.5 Transfection

Immortalised human skeletal muscle cells were seeded in 24-well plates and grown to 70–90% confluency. Transfection complexes were initially prepared by combining transIT-X2 and plasmid DNA (pDNA) (1 μ g/ μ l stock) at different ratios in Opti-MEM; **Section 2.2.1** describe how specific plasmids were handled and how pDNA was isolated. Following 15–30 minutes incubation at room temperature to facilitate complexes formation, 50 μ L of transfection complexes solution was added drop-wise to each well and cells were incubated for different time points (6, 18, 24 hours) prior evaluation for green fluorescent protein (GFP) or human leukocyte antigen (HLA) expression.

2.2. Sample Preparation

Table 2.7 Reagents for sample preparation

Reagents	Supplier	Catalogue #
Plasmid preparation		
HLA-A2/K ^b plasmid	Addgene	14906
pSV2-neo control plasmid	ATCC	37149
EGFP-tagged control plasmid	VectorBuilder	Ecoli (VB181226-1397jaz)-P
HLA-A/EGFP-tagged plasmid	VectorBuilder	E. coli (VB191105-1259dmg)
LB agar powder	Sigma-Aldrich	L2897
LB Broth	Sigma-Aldrich	L3022
Ampicillin Sodium Salt	Fisher Scientific	BP17605
100% Glycerol	Fisher Scientific	BP2291
QIAprep spin miniprep	Qiagen	27104
RNA extraction		
EZ-RNA Total RNA Isolation Kit	Biological Industries	20-400-100
Isopropanol		278475
Ethanol	Sigma-Aldrich	51976
DEPC-treated water	Invitrogen	750023
Protein extraction		
RIPA buffer	Sigma-Aldrich	R0278
Protease and phosphatase inhibitor	Abcam	ab201119

2.2.1 Plasmid preparation

Psv2-neo plasmid containing HLA-A2/K^b was a gift from Linda Sherman (Addgene, USA) (Irwin *et al.*, 1989), and its control plasmid, pSV2-neo empty vector was purchased from ATCC (UK). HLA-A expression plasmid tagged with EGFP and its relevant EGFP-tagged control plasmid vector were designed and prepared by order from VectorBuilder (USA). Plasmids were sent in *Escherichia coli* as agar stab. The bacteria were then streaked onto sterile agar plates, which were prepared with LB agar and a selection antibiotic, ampicillin (100 µg/mL), and incubated overnight at 37°C. Single colonies were picked using a sterile pipette tip and transferred into 5 mL LB Broth media (20 g LB broth in 1 L of H₂O, autoclave at 121°C), supplemented with ampicillin. Liquid bacterial culture was incubated at 37°C for 16–18 hours in a shaking incubator (200 rpm). For future experiments, bacteria were stored at 37°C in 50% glycerol solution prepared in distilled water.

The pDNA was extracted and purified using QIAprep spin miniprep kit. Firstly, the liquid bacterial culture was centrifuged at 6800 ×g for 3 minutes at room temperature. The bacterial cell pellet was resuspended in Buffer P1, containing RNase solution A, and transferred to a fresh microcentrifuge tube. Bacterial cells were lysed with 250 µL Buffer P2 by inversion and neutralised with 250 µL Buffer N3. Following 10 minutes centrifugation at 13000 rpm, the supernatant was transferred to a QIAprep spin column placed in a fresh microcentrifuge tube and centrifuged for 60 seconds to enable DNA binding to the column. The flow-through was discarded and the spin column was then washed with 500 µL Buffer PB and centrifuged for 60 seconds. A second washing step was followed using 750 Buffer PE. Lastly, the pDNA was eluted by adding 50 µL Buffer EB to the center of the spin column. The buffer was led to stand at room temperature for a minute and the spin column was centrifuged to transfer the pDNA into a fresh Eppendorf tube. pDNA concentration and purity were determined on a Nanodrop 2000 spectrophotometer (Thermo). pDNA with absorbance ratio of 260/280 > 1.80 and 260/230 > 2.0 was used.

2.2.2 Extraction of RNA from cells

RNA was isolated using EZ-RNA isolation kit. Cells cultured in 6-well plates were washed once with ice-cold DPBS. Then, cells were scraped in fresh DPBS and centrifuged at 12,000

×g for 5 minutes. The cell pellet was resuspended in 500 µL Denaturing Solution containing guanidine thiocyanate and stored for 5 minutes at room temperature. Equal volume of Extraction Solution was added to the homogenate, agitated vigorously for 15 seconds, and stored for 10 minutes at room temperature. The samples were then centrifuged at 12,000 ×g for 15 minutes at 4°C to enable phase separation of the lysate as following: organic phase (lower pink solution) containing protein and lipids; interphase (middle solution) containing DNA; and aqueous phase (upper colourless solution) containing RNA. The aqueous phase was transferred into a fresh Eppendorf tube and the RNA was precipitated from the aqueous phase by adding 500 µL isopropanol. The sample was stored for 10 minutes at room temperature and then centrifuged at 12,000 ×g for 8 minutes at 4°C. After centrifugation, the RNA pellet was washed with 70% ethanol and centrifuged at 7,500 ×g for 5 minutes at 4°C. Ethanol was removed and the sample was left to air-dry at room temperature for 5 minutes. Lastly, the RNA pellet was dissolved in 20 µL of DEPC-treated water and heated for 15 minutes at 55°C. RNA purity and quantity was assessed using Nanodrop 2000 spectrophotometer. Samples were stored at –80°C.

2.2.3 Protein extraction from cells

Cells cultured in 6-well plates or T25 flasks were washed once with ice-cold DPBS. Then, cells were scraped in fresh DPBS and the cell solution was transferred to a pre-cooled 1.5 mL Eppendorf tube and centrifuged at 10,000 rpm for 5 minutes at 4°C. Following centrifugation, supernatant was removed, and cell pellets were used immediately for further experiments or stored at –80°C. For western blotting, cells pellets were resuspended in 30 µL RIPA buffer containing 1:100 protease and 1:100 phosphatase inhibitors until complete dissociation was ensured.

2.3 SDS-PAGE, western blotting, Luminex multiplex analyses and qPCR

Table 2.8 Reagents

Reagents	Supplier	Catalogue #
SDS-PAGE, western blotting		
Ponceau S stain	Fisher BioReagents	6226-79-5
Tween-20	Sigma-Aldrich	P1379
Trizma HCl	Sigma-Aldrich	T-3253
NaCl	Sigma-Aldrich	S7653
Chemiluminescence substrate	Thermo Scientific	32109

Luminex Multiple Analysis		
BPX Pro HU Immunotherapy Panel 20- Plex kit	Bio-Rad	12007975
qPCR		
iScript cDNA synthesis kit	Bio-Rad	1708890
QuantiNova SYBR Green PCR Kit	Qiagen	1054575

2.3.1 Bicinchonic Acid Assay

The Pierce™ BCA Protein Assay and Bovine Gamma Globulin standards (125, 250, 500, 750, 1000, 1500, 2000 µg/ml) were used to determine protein concentration in each sample. Cell lysates in RIPA lysis buffer were diluted 1:20 with dH₂O to a final volume of 20 µL per well. BCA working reagent was prepared by mixing BCA solution with copper sulphate in a 50:1 ratio. Each standard or unknown protein cell samples were added into a microplate in duplicates, followed by the addition of 200 µL of the BCA working reagent to each well. Plate was incubated at 37°C for 30 minutes and absorbance was measured at 562 nm on a Synergy HTX Multi-mode microplate reader (BioTek).

2.3.2 SDS-PAGE

2.3.2.1 Electrophoresis of proteins

Based on protein concentration, cell lysates were diluted in dH₂O to yield a 20 µg of protein per sample and an equal volume of loading dye Laemmli was added. Protein samples were boiled at 95°C for 5 minutes and allowed to cool for around 15 minutes while kept on ice. Samples and protein ladder were then loaded to a 4–15% Mini-PROTEAN TGX Precast Gel (PAGE) placed in an electrophoresis tank filled with 1× running buffer (Tris/Glycine buffer supplemented with 0.1% SDS). The gel electrophoresis power was set to 20 mA per gel until the lowest ladder reaches the line at the bottom of the gel.

2.3.3 Western Blotting

Table 2.9 Constituents of western blotting buffers

Buffers	Constituents
Anode 1 buffer	0.3 M Tris Base in 20% MetOH (pH 10.4)
Anode 2 buffer	0.025 M Tris Base in 20% MetOH (pH 10.4)
Cathode buffer	40 mM 6-amino n hexanoic acid, 20% MetOH pH 9.4

Once electrophoresis of proteins was completed, proteins were transferred from the gel to a nitrocellulose membrane using the semi-dry Tans-Blot Turbo transfer system (Bio Rad, UK). The membrane and the gel were first equilibrated in Anode 2 for 10 minutes, while Whatmann filter papers were soaked in Anode 1 (×4), Anode 2 (×2), and Cathode (×2) buffers. Then, the gel was placed on the nitrocellulose membrane and sandwiched in between layers of the filter papers (blotting sandwich) on the cassette base (anode) of the Trans-Blot Turbo machine, as shown in **Figure 2.2**. The current was set to 1.A (25 V) for 30 minutes.

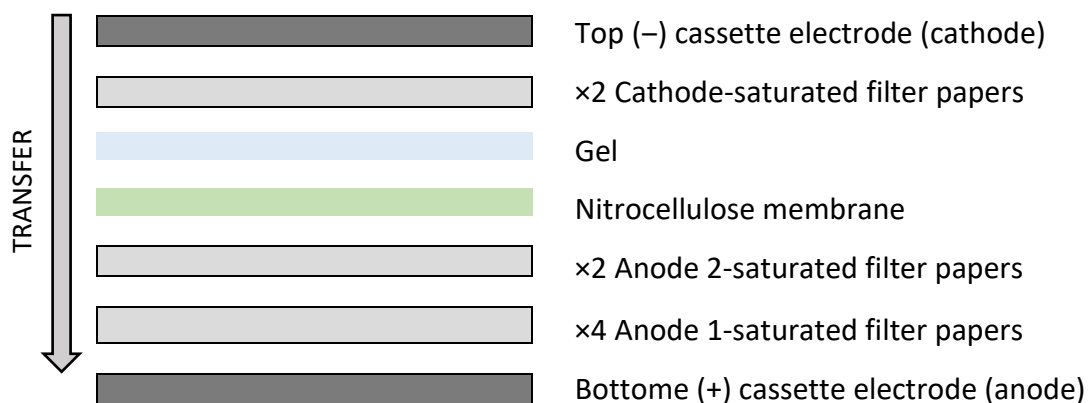


Figure 2.2 Blotting sandwich. Schematic representation of the arrangement of blotting sandwich for transferring proteins from the SDS-PAGE gel to a nitrocellulose membrane using the semi-dry transfer technique.

2.3.3.1 Analysis of the PVDF membrane for specific proteins

Table 2.10 Constituents of reagents used for protein detection

Reagents	Constituents
Ponceau S stain	0.1% Ponceau S, 5% Acetic acid
TBST solution	0.05% Tween-20, TBS (Trizma HCl/NaCl) 1×, in dH ₂ O
Blocking solution	5% Marvel dried skimmed milk in TBST
Primary antibody (1 ^{ry} Ab) solution	1% Marvel dried skimmed milk in TBST
Secondary antibody (2 ^{ry} Ab) solution	3% Marvel dried skimmed milk in TBST

Nitrocellulose membranes were stained with Ponceau S stain (5-minute incubation) to confirm protein transfer. The membranes were then incubated into blocking solution for 1 hour at room temperature on a shaker (gentle shaking, 20 RPM), followed by a 3× 5-minute wash with TBST. Primary antibodies were diluted in 1^{ry} Ab solution, as detailed in **Table 2.11**. Each membrane was incubated with 10 mL 1^{ry} Ab solution overnight at 4°C on shaker. Following 3× 5-minute wash with TBST, membranes were exposed to the appropriate 2^{ry} Ab diluted in 2^{ry} Ab solution, as shown in **Table 2.11**, for 1 hour under agitation at room temperature. Finally, the membranes were washed 3× for 5 minutes with TBST, exposed to a chemiluminescence substrate, and imaged using LI-COR Odyssey Fc imaging system (LI-COR, UK). Analysis of the intensity of the bands on the membranes was performed using ImageJ software (National Institutes of Health, USA).

Table 2.11 List of antibodies (1^{ry} and 2^{ry})

Ab	Supplier	Catalogue #	Species	Dilution
1^{ry} Ab				
GRP94	Abcam	ab3674	Rabbit (polyclonal)	1:1000
MFN2	Abcam	ab56889	Mouse (monoclonal)	1:1000
SOD1	Abcam	ab13498	Rabbit (polyclonal)	1:1000
SOD2	Abcam	ab13522	Rabbit (polyclonal)	1:1000
B-ACTIN	Abcam	ab8226	Mouse (monoclonal)	1:5000
2^{ry} Ab				
Anti-Mouse IgG H&L (HRP)	Abcam	ab97023	Goat	1:1000
Anti-Rabbit IgG H&L (HRP)	Abcam	ab6721	Goat	1:1000

2.3.4 quantitative Polymerase Chain Reaction (qPCR)

Isolated RNA, as described in **Section 2.2.2**, was reversed transcribed to cDNA using iScript cDNA synthesis kit. To prepare 10 ng of cDNA in a total volume of 20 µL, the appropriate volume of RNA, based on RNA quantification data (**Section 2.2.2**), was diluted in RNase-free dH₂O and mixed with 1 µL reverse transcriptase enzyme and 4 µL reaction mix. The complete reaction mix was incubated in a thermal cycler (Q Cycler II, Biotron Healthcare, India) using the protocol shown in **Table 2.12**. The cDNA samples were then stored at –20°C for further analysis.

Table 2.12 Incubation protocol for RNA reverse transcription

Priming	5 minutes at 25°C
Reverse transcription	20 minutes at 46°C
Reverse transcription inactivation	1 minute at 95°C

QuantiNova SYBR Green PCR kit was used for real-time qPCR analyses. cDNA samples were diluted 1:10 in RNA-ase free water (10 ng/μL) and were used in a total volume of 10 μL PCR reaction mixture (5 μL SYBR Green PCR Master Mix, 1 μL ROX Reference Dye, 2 μL Primer mix, 1 μL nuclease free water). A no-cDNA template control was also used as a negative qPCR control to examine genomic contamination or primer dimers. Following loading of reaction mixture and samples, plates were tightly sealed with an optical film and the qPCR was performed on a StepOnePlus™ real-time PCR system (Applied Biosystems, UK) with the experimental cycles showing in **Table 2.13**. The sequences and optimal annealing temperature of each primer, previously defined using endpoint PCR, are presented in **Table 2.14** and **Table 2.15**. The annealing temperature for the housekeeping gene 18S, which has been widely used in muscle samples, was set at 55.7°C (Zygmunt *et al.*, 2017; Wang *et al.*, 2018; Debaud *et al.*, 2017). Once completion of the PCR reaction (40 cycles), a melting curve was also produced, according to manufacturer's instructions, to enable assessment of the specificity of the primer annealing and amplification process; single product amplification was an indication of primer affinity and was further analysed.

Table 2.13 Incubation protocol for RNA reverse transcription

PCR initial heat inactivation – Hot Start	2 minutes at 95°C
Denaturation	20 seconds at 95°C
Annealing	°20 seconds at optimal temperature
Extension	20 seconds at 72°C
Number of Cycles	40
Meting curve	
Step 1	15 seconds at 95°C
Step 2	1 minute at 50°C
Step 3	15 seconds at 95°C

StepOne software allows the determination of Ct (the endpoint of real-time qPCR, cycle threshold) values for genes of interest and 18S. The Ct values for each target gene were normalised to the Ct values of 18S (ΔCt) and the relative difference to control (fold change) was determined using the $2^{-\Delta\Delta Ct}$, using the equations below:

$$\Delta\Delta Ct = \Delta Ct \text{ of experimental sample} - \Delta Ct \text{ of control sample}$$

where $\Delta Ct = Ct \text{ of target gene} - Ct \text{ of housekeeping gene}$

Table 2.14 The sequences and annealing temperature of mitochondrial-associated primers.

Target mRNA	Annealing Temperature (°C)	Forward Primer Sequence (5'-3')	Reverse Primer Sequence (5'-3')
<i>MFN2</i>	58	AGTTGGAGCGGAGACTTAGC	ATCGCCTTCTTAGCCAGCAC
<i>HSP60</i>	58	GAACAGCTAACTCCAAGTCAGA	CAGCCGCTCTGAGAACTTCA
<i>TFAM</i>	58	CTGCACTCTGTCCCTCACTC	GGGTAACCGAAGCATTCTGC
<i>DRP1</i>	58	TCACCCGGAGACCTCTCATT	TCTGCTTCCACCCCATTTTCT
<i>Citrate Synthase</i>	58	TGATGAGGGCATCCGTTTCC	GTTCTTCCCCACCCTTAGCC
<i>FIS1</i>	58	AGGCCTTAAAGTACGTCCGC	TGCCACGAGTCCATCTTTC
<i>UCP3</i>	55.7	GGGTCAACCTGGGATGTAGC	TCCCTAACCCCTCCCCATCAG
<i>HSPA9</i>	58	AGAAGACCGGCGAAAGAAGG	TGTTGCACTCATCAGCAGGT

Abbreviations: MFN1, mitofusin 2; HSP60, heat shock protein 60; TFAM, transcription factor A, mitochondrial precursor; DRP1, dynamin-related protein 1; FIS1, fission 1; UCP-3, uncoupling protein 3; and HSPA9, heat shock protein family A member 9.

Table 2.15 The sequences and annealing temperature of endoplasmic reticulum stress-associated primers.

Target mRNA	Annealing Temperature (°C)	Forward Primer Sequence (5'-3')	Reverse Primer Sequence (5'-3')
<i>GRP78</i>	59.3	TGACATTGAAGACTTCAA AGCT	CTGCTGTATCCTCTTCACCAGT
<i>Total XBP1</i>	59.3	GGCATCCTGGCTTGCCTC CA	GCCCCCTCAGCAGGTGTTCC
<i>ERDJ4</i>	59.3	TCGGCATCAGAGCGCCAA ATCA	ACCACTAGTAAAAGCACTGTGT CCAAG
<i>CHOP</i>	59.3	GGAGCATCAGTCCCCCAC TT	TGTGGGATTGAGGGTCCACATC
<i>GADD34</i>	59.3	CCCAGAAACCCCTACTCAT GATC	GCCCAGACAGCCAGGAAAT

Abbreviations: GRP78, glucose-regulated protein 78 kDa; total XBP1, total X-box-binding protein 1; ERDJ4, ER-DnaJ-like 4; CHOP, cholesterol oxidase-peroxidase C/EBP homologous protein; and GADD34, growth arrest and DNA damage-inducible gene 34.

2.3.5 Luminex multiplex analysis

Luminex multiplex bead analysis technique was used to measure the concentration of various human premixed cytokines, chemokines, and growth factors in cell culture media from the various *in vitro* myositis models. The Luminex assay principle involves mixing the samples with colour-coded beads, pre-coated with analyte-specific capture antibodies, which the bind to the analytes of interest (**Figure 2.3** Step 1). Then, antibody-antigen sandwich is formed by adding biotinylated detection antibodies specific to the analytes. Phycoerythrin (PE)-conjugated streptavidin, which binds to the biotinylated detection antibodies, is also added (**Figure 2.3** Step 2). Lastly, Luminex 200 apparatus uses dual-laser flow-cytometry based technology. Briefly, the primary laser identifies each bead based on the colour (bead-region) assigned for each analyte, and the secondary laser

quantifies the mean PE-derived fluorescence intensity (MFI), which is proportional to the amount of analyte bound (**Figure 2.3** Step 3).

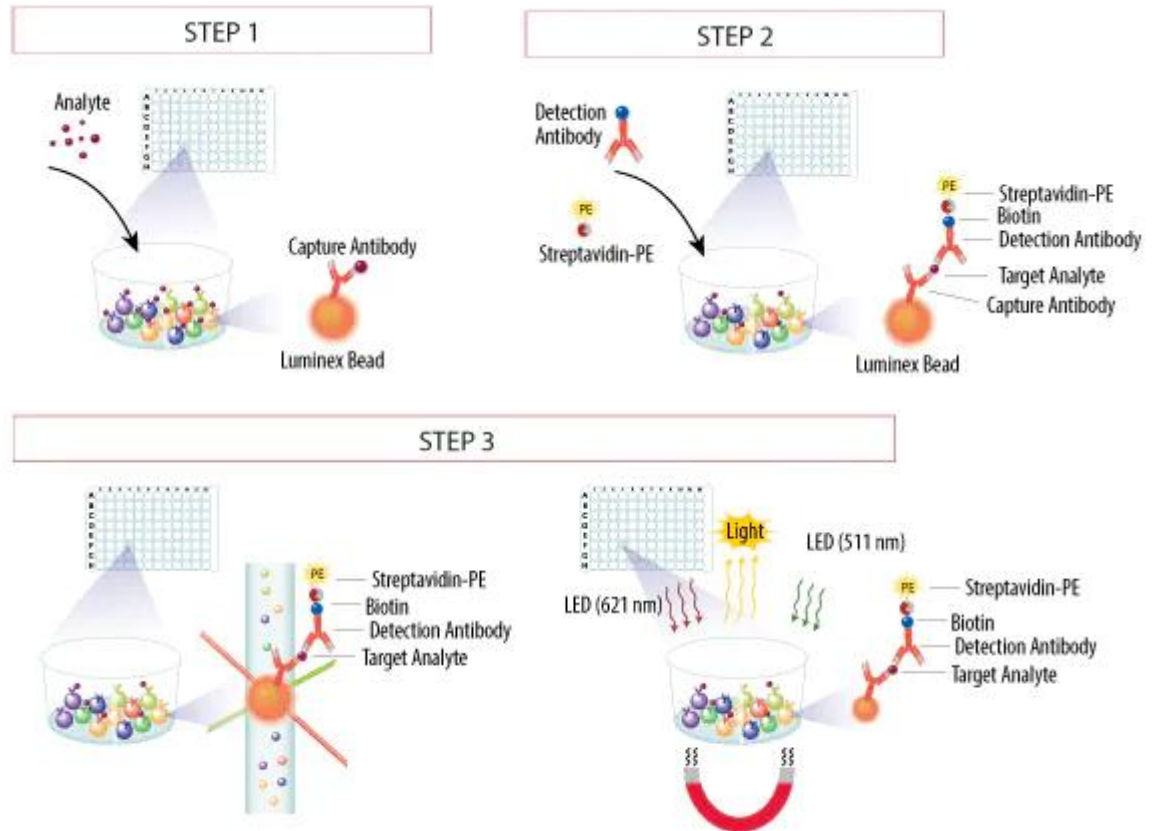


Figure 2.3 Luminex assay principle. Obtained from R&D Systems (2021) website: <https://www.rndsystems.com/resources/technical/luminex-assay-principle>

A 96-well filter plate was prewet with 100 μ L assay buffer, which was then aspirated. Coupled beads were diluted from 20 \times stock to 1 \times in Assay buffer and were transferred to the 96-well plate (50 μ L per well). Following two washing steps with 100 μ L Bio-Plex wash buffer using Bio-Tek microplate magnetic washing system with a suction pressure of 1-3 mmHg, 50 μ L of samples and standards of known lyophilised human cytokines were added to each well and incubated on a shaker at 850 rpm at room temperature for 30 minutes in the dark. After incubation of the samples and standards with the beads, the plate was washed three times with 100 μ L Bio-Plex wash buffer. Detection antibodies previously diluted in detection antibody diluent to 1 \times , were then added to the plate (25

µL per well) and incubated on the shaker as before. Following three further washing steps, samples and standards were incubated with the streptavidin-phycoerythrin fluorophore, previously diluted from 100× stock to 1×, for 10 minutes at room temperature in the dark. A final washing was performed three times, and samples and standards were resuspended in 125 µL assay buffer for 30 seconds on the shaker, and analysed using a Luminex 200 Multiplex analyser (Luminex xMAP Technology, 0135027).

2.4 Analysis of mitochondrial function

Table 2.16 Reagents for mitochondrial function analysis

Reagents	Supplier	Catalogue #
Cell Mito Stress Test kit	Agilent Technologies	103015-100
XF DMEM Medium, pH 7.4	Agilent Technologies	103575-100
XF calibrant	Agilent Technologies	103022-100

2.4.1 Seahorse extracellular flux analysis

XFp Extracellular Flux Analyser and the Cell Mito Stress Test kit were used to measure key parameters of the bioenergetic function of human skeletal muscle cells in real time. This assay is based on its integrated drug delivery system through a sensor cartridge placed on top of an 8-well cell culture microplate. Each well of the cartridge contains sensor probes with integrated fluorophores that can detect oxygen and protons released by the cells in the culture media (**Figure 2.4**). Therefore, this enables the simultaneous measurement of OCR and extracellular acidification rate (ECAR), defined as the rate of reduction in oxygen concentration and the rate of increase in proton concentration (or pH decrease), which are indicators of mitochondrial respiration and glycolysis, respectively. For each measurement cycle, the culture media is initially mixed, and the probes lower into the culture media to create a transient microchamber to enable measurement of OCR and ECAR with increased sensitivity and signal to noise. Furthermore, cartridge wells have four ports for sequentially injecting compounds into the culture media at defined intervals to change cell conditions and measure acute responses to them (**Figure 2.4**).

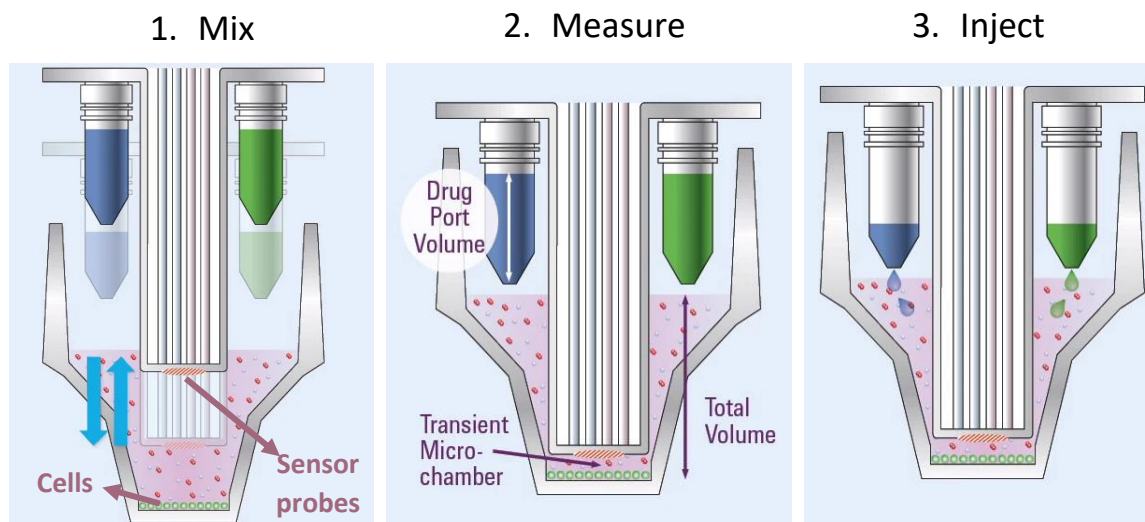


Figure 2.4 Graphical presentation of the XF Extracellular Flux Analyser basis. The sensor cartridge probes are lowered into each microplate well to mix the culture medium and then create a transient microchamber to minimise diffusion. This enables the measurement of the levels of oxygen consumed or protons excreted from the cells through the fluorophores embedded in the sensor cartridge probes. After basal measurements occur, drug ports surrounding the sensor probes can inject up to four compounds into the culture medium. Adapted from Agilent Seahorse XF (2021) website: www.agilent.com/en/product/cell-analysis/real-time-cell-metabolic-analysis/xf-sensor-cartridges-cell-culture-microplates/seahorse-fluxpaks-740883?fbclid=IwAR3keKR5l65QPADjIKnNUQpYTPkdwIqs2n87cyarBlml5CGsijLV7qU_Js0

Cells were seeded in the 8-well cell culture microplate at a density of 7×10^3 cells/well, in 100 μ l of growth medium, unless otherwise stated, leaving wells A and H blank for background measurement. Following cell attachment, cells were exposed to different treatments as described in **Section 2.1.4**. On the day prior the assay, 200 μ l per well XF Calibrant were added in the sensor cartridge to hydrate overnight at 37°C in a non-CO₂ incubator. On the day of the assay, growth medium was replaced with 180 μ l per well Seahorse XF DMEM medium supplemented with 1 mM pyruvate, 2 mM L-glutamine, and 10 mM glucose and adjusted to 7.4 pH using 0.1 M NaOH solution (assay medium). The plate was equilibrated for 1 hour at 37°C in the non-CO₂ incubator. Oligomycin, (Carbonyl cyanide-4 (trifluoromethoxy) phenylhydrazine) FCCP, and rotenone/antimycin A mixture

were prepared in assay medium and added into each port of the sensor cartridge as presented in **Table 2.17**.

Table 2.17 Compound preparation and injection

Port	Compound	Stock concentration (μM)	Volume added to port (μL)	Final Well Concentration (μM)
A	Oligomycin	100	20	1
B	FCCP	100	22	2
C	Rotenone/ Antimycin A	50	25	0.5

OCR and ECAR values were automatically calculated by Seahorse XFp software version 2.2.0 (Seahorse Bioscience) and presented as pmol of oxygen/min and mpH/min, respectively. Following measurement of the OCR values at basal conditions, representing **basal respiration**, Oligomycin, an ATP synthase inhibitor, is injected to enable measurement of **ATP-linked respiration**, as well as **proton leak**, as the basal respiration that is not used for ATP production. Then, the uncoupling agent FCCP is added to disrupt mitochondrial membrane potential and measure the oxygen consumed when mitochondria need to operate at maximum capacity, indicative of **maximal respiration**. FCCP is also used to measure **spare respiratory capacity** as the difference between maximal and basal respiration. Finally, a mixture of rotenone, a complex I inhibitor, and antimycin A, a complex III inhibitor, is added to block mitochondrial respiration and allow the measurement of **non-mitochondrial respiration (Figure 2.5)**. Each of those parameters were calculated using the Seahorse XF Cell Mito Stress Test Report Generator, a Microsoft Excel Macro file, as shown in **Table 2.18**. In addition, respiratory flux control ratios, including **coupling efficiency (%)**, **respiratory control ratio**, and **phosphorylating respiration**, which are further normalised to enable more accurate comparisons, were calculated using the previously mentioned parameters, as described by Dott *et al.* (2014); the relevant calculations are presented in **Table 2.19**. In particular, coupling efficiency refers to the fraction of oxygen used for ATP production compared with that used for proton leak. Respiratory control ratio presents the potential for substrate oxidation and

ATP turnover, and phosphorylating respiration shows the proportion of oxygen consumption used under basal conditions to synthesise ATP (Dott *et al.*, 2014).

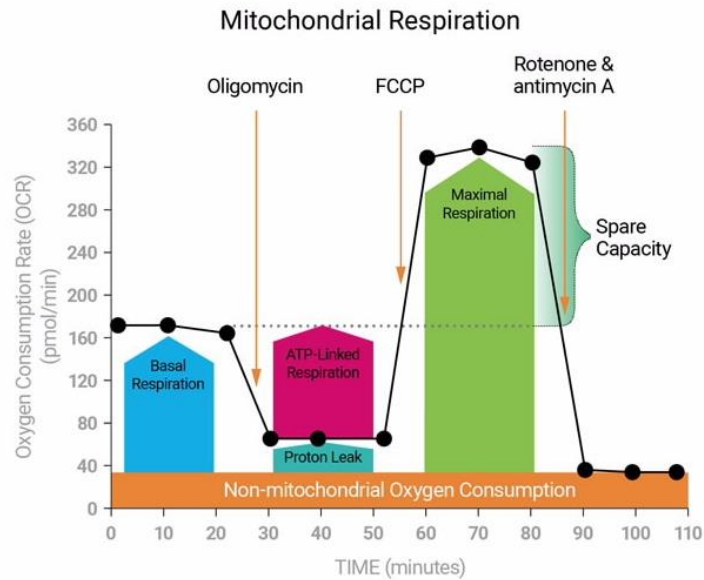


Figure 2.5 Seahorse XF Cell Mito Stress test profile. From Agilent Seahorse XFp Cell Mitochondrial Stress Test kit, User Guide Kit #103015-100

Table 2.18 Mitochondrial parameters calculation

Parameter	Equation
Non-mitochondrial Respiration	Lowest OCR measurement after Rotenone/Antimycin A injection
Basal Respiration	Last OCR measurement before Oligomycin injection – Non-mitochondrial respiration
Maximal Respiration	Highest OCR measurement after FCCP injection – Non-mitochondrial respiration
Proton Leak	Lowest OCR measurement after Oligomycin injection – Non-mitochondrial respiration
ATP Production	Last OCR measurement before Oligomycin injection – Last OCR measurement after Oligomycin injection
Spare Respiratory Capacity	Maximal Respiration – Basal Respiration

Table 2.19 Normalised respiratory flux control ratios

Parameter	Equation
Coupling Efficiency	$(\text{ATP Production} / \text{Basal Respiration}) \times 100$
Respiratory Control Ratio	Maximal Respiration / Proton Leak
Phosphorylating Respiration	ATP Production / Maximal Respiration

2.5 Fluorescent imaging of cells

Table 2.20 Reagents for fluorescent imaging of cells

Reagents	Supplier	Catalogue #
MitoTracker Red CMXRos	Invitrogen	M7512
Paraformaldehyde	Sigma-Aldrich	P6148
Triton X-100	Sigma-Aldrich	T8787
Goat serum	Sigma-Aldrich	G9023
Horse serum	Sigma-Aldrich	H014
BD Perm/Wash buffer	BD Biosciences	554723
1^{ry} Ab		
Anti-HLA class I antibody	Abcam	ab23755
Anti-MyOD antibody	Cell Signaling Technology	13812P
2^{ry} Ab		
Goat anti-mouse IgG (H+L) Alexa Fluor 488	Abcam	ab150113
Goat anti-rabbit IgG (H+L) Alexa Fluor 647	Abcam	ab150115
Myosin 4 monoclonal antibody Alexa Fluor 488	Invitrogen	53-6503-82
4',6'-diamidino-2-phenylindole dihydrochloride (DAPI)	Sigma-Aldrich	MBD0015
Live and Dead Cell Assay	Abcam	Ab115347

Following fluorescent staining, cells were maintained in DPBS and images were acquired using LEICA DMI6000 B inverted microscope (CTR6000 laser, Leica Microsystems) at room temperature at 20× magnification, unless otherwise stated.

2.5.1 Imaging of mitochondrial structure

Immortalised human skeletal myoblasts seeded on a 35 mm glass bottom μ -Dish (ibidi®, Germany) and treated as described in **Section 2.1.4**, were stained with MitoTracker Red CMXRos. MitoTracker Red CMXRos is a cell-permeable fluorophore that selectively labels living mitochondria red. The specific fluorophore was used to stain mitochondria as it is

well retained following fixation, and therefore, confocal microscopy could be performed in absence of live-cell conditions. MitoTracker Red CMXRos was reconstituted in DMSO to a final concentration 1 mM. Following washing with DPBS, 5 μ M MitoTracker Red CMXRos and DAPI (1:5000) solution, prepared in phenol red-free DMEM, was added to the cells for 30 minutes at 37°C). Cells were washed with DPBS and fixed with 4% (v/v) paraformaldehyde solution (**Section 2.5.2.1**). Imaging was performed on a Leica TCS SP5 confocal microscope (Leica Microsystems, UK), using a 63 \times /1.4 oil immersion objective.

2.5.1.1 Quantitation of mitochondrial structure using ImageJ

Mitochondrial structure parameters were algorithmically quantified using a macro on NIH ImageJ software version 1.46, created by Dagda *et al.* (2009). This macro is publicly available and can be downloaded from the ImageJ Wiki site (https://imagejdocu.tudor.lu/plugin/morphology/mitochondrial_morphology_macro_plugin/start). Initially, background fluorescence was subtracted, and local contrast was enhanced equally for every image. Then, the area of interest (individual cell) was selected using the polygon selection tool, and macro was activated to threshold mitochondria and converts images into binary. The macro outlines each mitochondrion and calculate the different mitochondrial parameters, as described in **Table 2.21**.

Table 2.21 Mitochondrial morphology parameters

Parameter	
Mitochondrial Content	% of cytosol occupied by mitochondrial
Mitochondrial Interconnectivity	Average area to perimeter ratio of mitochondria
Mitochondrial Elongation	Average circularity of mitochondria
Mitochondrial Area	Average area of mitochondria analysed
Mitochondrial Perimeter	Average perimeter of mitochondria analysed

2.5.2 Immunocytochemistry

2.5.2.1 Cell fixation and preparation

For fixation, the medium was aspirated and cells were washed twice with DPBS. The cells were then fixed with ice-cold 4% (v/v) paraformaldehyde solution, prepared in PBS, for 10-15 minutes at room temperature. The cells were then washed twice with DPBS and maintained in DPBS for up to 7 days at 4°C. Alternatively, MitoTracker Red-stained cells were imaged immediately, or immunocytochemistry was performed in non-stained cells.

2.5.2.2 Fluorescent staining of immortalised human skeletal myoblast

Fixed immortalised cells were permeabilised in 0.5% (v/v) Triton X-100 for 15 minutes at room temperature and washed three times with DPBS. Following permeabilisation, cells were incubated with 3% (v/v) goat serum in DPBS, supplemented with 0.05% (v/v) Tween-20 (blocking solution) for 1 hour at room temperature, to block non-specific antibody binding. Cells were washed as before and incubated with anti-HLA class I antibody at 4°C overnight. Following incubation with primary antibody, Alexa Fluor 488 (goat anti-mouse IgG; 1:1000) was added in presence of DAPI (1:5000) for 1 hour at room temperature in the dark. Both primary and secondary antibodies were prepared in blocking solution.

2.5.2.3 Fluorescent staining of immortalised human skeletal myotubes

Differentiated immortalised human skeletal myotubes were fixed as described in **Section 2.5.2.1**. Following fixation, cells were permeabilised using 1× BD Perm/Wash buffer, supplemented with 10% (v/v) goat serum to block non-specific antibody binding. Cells were washed three times with DPBS, and myosin heavy chains and nuclei were visualised by using Myosin 4 monoclonal antibody Alexa Fluor 488 (MF20; 1:400) and DAPI (1:5000), respectively.

2.5.2.3.1 Quantification of differentiation parameters

Differentiation parameters, including fusion index, myotube area, and aspect ratio, were quantified using NIH ImageJ, as described in **Table 2.22** (Al-Dabbagh *et al.*, 2015). Among those, myotube length, myotube width, number of nuclei in myotubes per field and number of nuclei per myotube were defined. To calculate the width of each myotube, myotubes were measured at 3 different points along their width and the average value

was calculated. Three images were taken per well for each individual experiment (Ono and Sakamoto, 2017).

Table 2.22 Myoblast differentiation parameters

Parameter	Equation
Aspect ratio	length of myotubes containing ≥ 2 nuclei / their average width
Myotube area	(total area of MF20-positive myocytes in the field / the entire field of view) $\times 100$
Fusion index	(number of nuclei in each myotube containing ≥ 2 nuclei / the total number of nuclei in the field) $\times 100$

2.5.2.4 Fluorescent staining of primary human skeletal muscle cell line

Following fixation, primary cells were immunostained according to Soriano-Arroquia *et al.* (2017). Block 1 solution containing 10% (v/v) horse serum and 0.1% (v/v) Triton X-100 in DPBS, was added to the cells for 1 hour at room temperature. Following three times washing with DPBS, cells were incubated with primary antibody solution (anti-HLA class I antibody and/or anti-MyOD antibody; 1:1000), prepared in block 2 solution consisting of 10% (v/v) horse serum with 0.05% (v/v) Triton X-100 in DPBS, overnight at 4°C. Corresponding secondary antibodies (goat anti-mouse IgG (H+L) Alexa Fluor 488 and/or goat anti-rabbit IgG (H+L) Alexa Fluor 648; 1:1000, also prepared in block 2 solution, containing DAPI (1:5000), were added to the cells for 1 hour at room temperature.

2.5.3 Live/Dead viability staining

The Live and Dead Cell Assay kit was used to assess cell viability in response to tunicamycin treatment (**Chapter 3**). This assay uses two highly fluorescent dyes: **(1)** a membrane permeable non-fluorescent molecule that reacts with ubiquitous intracellular esterases within intact, viable cells, producing a green fluorescence; and **(2)** a membrane impermeable dye that binds to DNA of cells with compromised membranes (dead cells), staining their nuclei red. Therefore, live cells are labelled green and dead cells are labelled red.

Cells cultured in a 12-well plate and treated as described in **Section 2.1.4**, were washed once with DPBS and exposed to 5× Live and Dead dye, diluted in DPBS (5 µL 1000× Live and Dead dye added to 1 mL DPBS) for 10 minutes at room temperature. Images of live cells maintained in the staining solution were rapidly acquired after staining using LEICA DMI6000 B inverted microscope.

2.6 Measurement of RONS

Table 2.23 Reagents

Reagents	Supplier	Catalogue #
Amplex Red hydrogen peroxide/peroxidase assay	Invitrogen	A22188
MitoSOX™ Red	Invitrogen	M36008
DHE	Sigma-Aldrich	104821-25-2
DCFH-DA	Sigma-Aldrich	4091-99-0
DAF-FM DA	Abcam	ab145295
Mitochondrial hydroxyl radical assay	Abcam	ab219931

Skeletal muscle cells were cultured in black-sided, clear-bottom, microplate (96-well) and treated as explained in **Section 2.1.4**, unless otherwise stated. Hydrogen peroxide, mitochondrial superoxide, cellular superoxide, total cellular ROS, NO, and mitochondrial hydroxyl radical release were assessed using specific fluorophores. Dyes were prepared in phenol red-free DMEM media, unless otherwise stated. Endpoint fluorescence was measured using a Synergy™ multi-detection microplate reader (BioTek Instruments, UK). All measurements were corrected for background fluorescence and normalised to total protein content per sample as described in **Section 2.3.1**.

2.6.1 Amplex Red® hydrogen peroxide/peroxidase assay

Amplex™ Red hydrogen peroxide/peroxidase assay was used according to the manufacturer's protocol for the detection of extracellular hydrogen peroxide. Amplex Red reagent (N-acetyl-3,7-dihydroxyphenoxazine) is a non-fluorescent compound that, in presence of horseradish peroxidase (HRP), reacts with hydrogen peroxide in a 1:1 stoichiometry, leading to the formation of the red-fluorescent resorufin. Hydrogen peroxide and cell culture media stored at -80°C were serially diluted in 1× Reaction Buffer (**Table 2.24**). Hydrogen peroxide standards of 1, 2, 4, 6, 8, and 10 µM were also prepared in 1× Reaction Buffer. Fifty microlitres per sample, hydrogen peroxide standards, and

positive and negative controls were added in individual wells of a black 96-well, clear bottom microplate. Then, 50 μL of 100 μM Amplex™ Red reagent and 0.2 U/mL HRP solution (**Table 2.24**) was added to each well and incubated in the dark for 30 minutes at room temperature. Fluorescence was measured using a microplate reader (HT synergy) at 530/25 and 590/35 nm. Measurements were normalized to total protein content (**Section 2.3.1**).

Table 2.24 Amplex Red Assay Kit solutions preparation

Reagent	Volume/ Amount of Reagent	Volume of Solvent	Final Concentration of Working Solutions
Amplex Red	1 vial	60 μL DMSO	10 mM
5X Reaction Buffer	4 mL	16 mL dH ₂ O	1×
HRP	1 vial	1 mL 1X Reaction Buffer	10 U/mL
Hydrogen Peroxide	22.7 μL	977 μL 1X Reaction Buffer	20 mM

2.6.2 MitoSOX™ Red

Release of mitochondrial superoxide was measured using MitoSOX™ Red mitochondrial superoxide indicator. MitoSOX™ Red is a mitochondrial-targeted hydroethidine that in presence of superoxide, it is oxidised into 2-hydroxyetgidium (2-OH-Mito-E+) exhibiting red fluorescence. A final concentration of 5 μM of MitoSOX™ Red was added to live cells for 30 minutes at 37°C. Furthermore, the complex III inhibitor, antimycin A prepared in MitoSOX™ Red staining solution, was used as a positive control (150 μM , 30 minutes)

(Figure 2.6). Cells were washed with DPBS and maintained in phenol red-free media. Endpoint fluorescence was measured at 530/25 nm excitation and 590/35 nm emission.

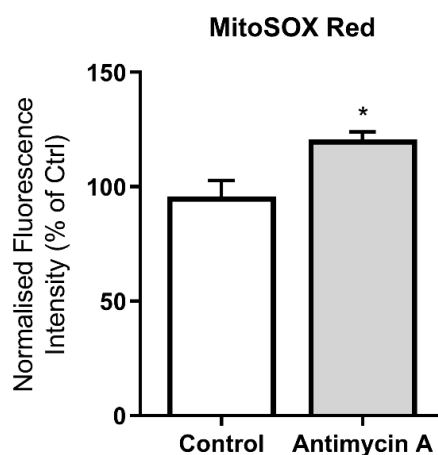


Figure 2.6 Antimycin A-induced superoxide generation presented by MitoSOX Red assessment. Increased MitoSOX Red fluorescence intensity indicative of superoxide generation as induced by Antimycin A treatment. Data were normalised to total protein content and represent mean relative to control (%) \pm S.E.M. ($n=3$), * $p\leq 0.05$ compared to control.

2.6.3 DHE

Intracellular superoxide levels were detected using DHE (dihydroethidium) that enters the cell where it is oxidised by superoxide form a red fluorescent compound 2-hydroxyethidium (2-OH-E⁺). This compound is superoxide-specific and is detected at excitation and emission 360/40 and 460/40 nm, respectively, as previously suggested by Pearson *et al.* (2014). DHE was used at 5 μ M for 20 min at 37°C. Following incubation with the dye, cells were wash with DPBS and read in phenol red-free media.

2.6.4 DCFH-DA

DCFH-DA (2',7'-dichlorodihydrofluorescein diacetatediacetate) is a cell-permeable dye used for the detection of total cellular ROS. DCFH-DA is diacetylated to the non-fluorescent DCFH (2',7'-dichlorodihydrofluoresce), which in turn, is oxidized into the fluorescent compound DCF (2',7'-dichlorofluorescein) by ROS. A final concentration of 10

μM of DCFH-DA was added to the cells for 30 minutes at 37°C . Antimycin A was also used as a positive control, as previously mentioned (**Section 2.6.2**) (**Figure 2.7**). Following a washing step with DPBS, cells were maintained in phenol red-free media and endpoint fluorescence measurements were performed with excitation wavelength at 530/25 nm and emission wavelength at 590/35 nm.

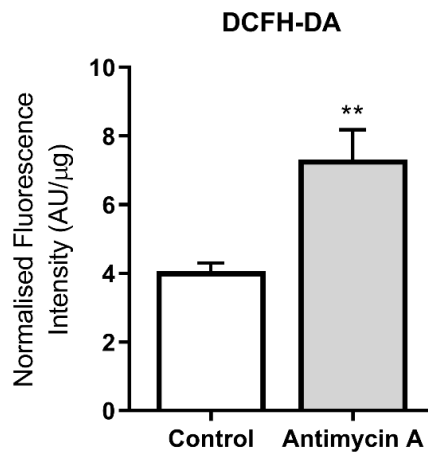


Figure 2.7 Antimycin A-induced total cellular ROS generation presented by DCF-DA assessment. Increased DCFH-DA fluorescence intensity indicative of total cellular ROS generation as induced by Antimycin A treatment. Data were normalised to total protein content and represent mean \pm S.E.M. ($n=3$), ** $p<0.002$ compared to control.

2.6.5 DAF-FM DA

DAF-FM DA (4-amino-5-methylamino-20,70-difluorofluorescein diacetate) was used for the quantification of cellular NO generation. Specifically, DAF-FM DA is a fluorinated DAF-2 (the first-generation compound) diacetate derivative with increased NO sensitivity and pH stability. Upon inside the cell, the non-fluorescent DAF-FM DA is hydrolysed to DAF-FM by esterases, which is non-membrane permeable, and therefore it accumulates within the cell. In turn, DAF-FM reacts with NO to form a fluorescent triazole (DAF-FM-T) (Cortese-Krott *et al.*, 2012). DAF-FM DA was added to the cells at $10 \mu\text{M}$ in presence of relevant treatments for 30 minutes at 37°C . Following wash with DPBS, cells were maintained in phenol red-free media in presence of treatments, and endpoint fluorescence was read at 485/20 nm excitation and 528/20 nm emission.

2.6.6 Mitochondrial hydroxyl radical assay

Generation of mitochondrial hydroxyl radical was measured using OH580 probe (250× stock solution), according to the manufacturer's instructions. OH580 stain working solution was prepared in Assay Buffer and added to live cells for 1 hour at 37°C. Cells were washed with DPBS and maintained in Assay Buffer. Endpoint fluorescence was measured at 530/25 nm excitation and 590/35 nm emission.

2.7. Measurement of mitochondrial membrane potential and mass

Table 2.25 Reagents

Reagents	Supplier	Catalogue #
JC-1	Abcam	Ab113850
TMRM	Invitrogen	T668
MitoTracker Red CMXRos	Invitrogen	M7512
MitoTracker Green FM	Invitrogen	M7514

Skeletal muscle cells were cultured in black-sided, clear-bottom, 96-well plate and treated as described in **Section 2.1.4**. Cells were exposed to different fluorophores, prepared in phenol red-free DMEM, to assess mitochondrial membrane potential. All measurements were taken using Synergy™ multi-detection microplate reader, corrected for background fluorescence and normalised to total protein content per sample as described in **Section 2.3.1**.

2.7.1 JC-1

JC-1 (5,5',6,6'- tetrachloro-1,1',3,3'-tetraethylbenzimidazolylcarbocyanine iodide) is a lipophilic, cationic fluorophore that at low concentrations, it exists as monomers (JC-1 monomers), exhibiting green fluorescence. The positively charged JC-1 is able to enter and accumulate in energised negatively charged mitochondria with high mitochondrial membrane potential, where at high concentrations, it forms red fluorescent polymers/aggregates (JC-1 polymers). In contrast, JC-1 enters to a lesser degree in depolarised mitochondria and therefore, it is unable to trigger JC-1 polymers formation. The red to green fluorescence (JC-1 polymers/JC-1 monomers) ratio is used to define mitochondrial membrane potential with mitochondrial membrane depolarisation indicated by a decrease in the red to green fluorescence ratio (Sivandzade *et al.*, 2019).

Live cells were exposed to 5 μM JC-1 for 30 minutes at 37°C. The uncoupling agent FCCP, prepared in DMSO, was used as a positive control (10 μM , 4 hours) (**Figure 2.8**). Following incubation with JC-1, cells were washed with DPBS and maintained in phenol red-free media. Endpoint fluorescence from JC-1 polymers and monomer forms was measured at excitation 530/25 and 485/20 nm, respectively, and emission 590/35 nm.

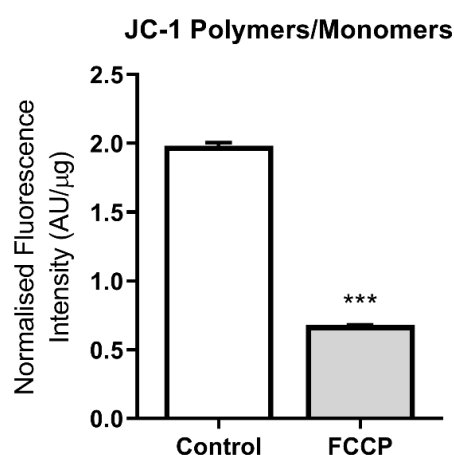


Figure 2.8 FCCP-induced mitochondrial membrane depolarisation presented by JC-1 assessment. Decreased JC-1 polymers/monomers ratio indicative of mitochondrial membrane depolarisation as induced by FCCP treatment. Data were normalised to total protein content and represent mean \pm S.E.M. ($n=3$), *** $p<0.001$ compared to control.

2.7.2 TMRM

TMRM (tetramethylrhodamine, methyl ester) is another commonly used cationic fluorophore that enters and accumulates in negatively charged mitochondria, producing red fluorescence. Unlike JC-1, TMRM is a single-excitation/emission dye. This means that TMRM signal is affected by changes in mitochondrial volume. In this study, TMRM was used at non-quenching mode to produce more reliable estimate of slow changes in mitochondrial membrane potential, as previously suggested (Connolly *et al.*, 2018; Perry *et al.*, 2011). The non-quenching mode involves low concentration of the dye (<30 nM) that prevents aggregation and quenching of the fluorophore in mitochondria. Therefore, decreases in the fluorescence signal are indicative of mitochondrial depolarisation (less negative mitochondria) (Connolly *et al.*, 2018; Perry *et al.*, 2011). Live cells were treated with 10 nM TMRM for 30 minutes at 37°C. FCCP was used as a positive control as

previously described (**Section 2.7.1**) (**Figure 2.9**). TMRM fluorescence was normalised to MitoTracker Green FM, used as explained in **Section 2.7.4**. Endpoint fluorescence for TMRM was read in the presence of staining solution at 530/25 nm excitation and 590/35 nm emission.

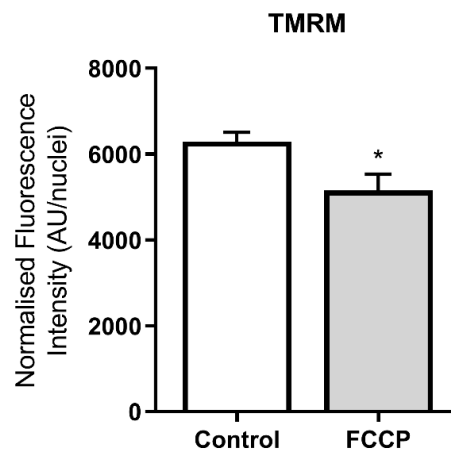


Figure 2.9 FCCP-induced mitochondrial membrane depolarisation presented by non-quenching mode of TMRM. Decreased TMRM fluorescence signal indicative of mitochondrial membrane depolarisation as induced by FCCP treatment. Data were normalised to total protein content and represent mean \pm S.E.M. ($n=3$), $*p\leq 0.05$ compared to control.

2.7.3 MitoTracker Red CMXRos

MitoTracker Red CMXRos was also used to determine mitochondrial membrane potential as it is a mitochondria-targeted fluorophore, exhibiting red fluorescence, that is sequestered by negatively charged functioning mitochondria. Therefore, increases of MitoTracker Red CMXRos red fluorescence intensity reflects increases in mitochondrial membrane potential and *vice versa*. Live myoblasts were stained in 5 μ M MitoTracker Red CMXRos solution (30 min, 37 $^{\circ}$ C), as previously described (**Section 2.5.1**), and endpoint fluorescence was measured in cells maintained in phenol red-free media at excitation 590/20 and emission 645/40 nm.

2.7.4 MitoTracker Green FM

MitoTracker Green FM is a green fluorescent dye that accumulates in mitochondria independent to mitochondrial membrane potential. Therefore, it can be used for reliably quantifying mitochondrial volume. MitoTracker Green FM was prepared at 100 nM in presence or absence of other fluorophores, including MitoSOX Red and TMRM, and incubated for 30 minutes at 37°C. Measurements of endpoint fluorescence for MitoTracker Green were taken at 485/20 nm excitation and 528/20 nm emission.

2.8 Statistical Analyses

Statistical analysis was performed and graphs were created using GraphPad Prism version 8. Firstly, data were assessed for normality of distribution using Shapiro-wilk test. Normally distributed data were analysed using one-way ANOVA with Tukey's post-hoc test. Non-normally distributed data were analysed using Dunn's post-test following a Kruskal-Wallis test. A p -value ≤ 0.05 was considered to be statistically significant.

CHAPTER 3

Mitochondrial function and ROS generation in an *in vitro* model of ER stress

3.1 INTRODUCTION

The ER is a specialised, pleiomorphic organelle representing the main site of folding and maturation of newly synthesised proteins into their biological active three-dimensional state, events facilitated by its reducing environment (Walter and Ron, 2011; Ellgaard *et al.*, 2018). Its correct functioning is fundamental for cell survival. Various environmental and pathological insults can result in the aggregation of unfolded and/or misfolded proteins, such as mutants or damaged proteins, within the ER, termed the ER stress. ER stress activates UPR, an ubiquitous adaptive response, to restore protein homeostasis or cell death, through autophagy or apoptosis. UPR downstream mechanisms aim increased protein folding through release of chaperones, reduced protein assembly via translational attenuation to reduce further accumulation of misfolded/unfolded proteins, and clearance of misfolded proteins via ER-associated degradation activation. Upon establishment of protein homeostasis in the ER, feedback control is activated to inhibit further UPR activity and prevent fatal cellular effects by sustained ER activation (Osowski and Urano, 2011).

ER and mitochondria crosstalk has been largely explored in various aspects based on their bi-directional crosstalk that exists via the mitochondrial-associated ER membranes and Ca²⁺ signalling. In addition, UPR is a network of cellular processes that involve the generation of ROS from both ER lumen and mitochondria. In the ER, protein folding requires thiol/disulphide exchange mechanism that results in hydrogen peroxide (H₂O₂) generation, while mitochondrial complexes I and III are a major source of superoxide (O₂^{•-}) release following Ca²⁺ influx from ER into mitochondria (Bhandary *et al.*, 2012; Cao *et al.*, 2014). In turn, O₂^{•-} can react with H₂O₂, as well as NO to produce peroxynitrite (ONOO⁻). Therefore, sustained ER stress activation can have detrimental impact on mitochondrial function, leading to abnormal ROS generation and oxidative damage (Cao *et al.*, 2014; Bravo *et al.*, 2012)

Chronic or prolonged ER stress activation is seen in various neurodegenerative diseases (e.g., Alzheimer's disease), chronic metabolic diseases (e.g., diabetes), and musculoskeletal diseases (e.g., Duchenne muscular dystrophy and IIMs) (Xiang *et al.*, 2017; Pauly *et al.*, 2017; Hotamisligil, 2010; and Nagaraju *et al.*, 2005). In an attempt to further investigate the non-immune mediated mechanisms involved in IIMs, this chapter

focuses on the understanding of the ER stress downstream mechanisms in skeletal muscle. Even though a wide range of studies have investigated the impact of acute and chronic ER stress on mitochondrial function, potential regulators of this ER-mitochondria crosstalk have not been fully defined (Bravo *et al.*, 2011; Jackisch *et al.*, 2016; Madreiter-Sokolowski *et al.*, 2019). Therefore, this chapter explores the role of ROS generation in changes in mitochondrial bioenergetics, biogenesis, and biodynamics, including mitochondrial respiration and morphology, downstream to tunicamycin-induced ER stress activation in presence or absence of the superoxide dismutase and catalase mimetic, EUK-134 (Baker *et al.*, 1998).

3.1.2 Aims of this chapter

1. Establish an *in vitro* model of ER stress in human skeletal muscle cells.
2. Characterise mitochondrial biodynamics and bioenergetics, as well as oxidative stress upon ER stress.
3. Assess the role of ROS generation on ER stress-induced changes in mitochondrial biodynamics and bioenergetics using the antioxidant EUK-134.

3.2 Methods

3.2.1 Cell culture and treatments

Immortalised human skeletal muscle cells were cultured as previously described in **Section 2.1.1** and exposed to the pharmaceutical ER stress inducer, tunicamycin (0.1 µg/mL) with or without EUK-134 (10 µM) for 24 hours (**Section 2.1.4**). Following 24-hour treatment, cells were harvested in DPBS and stored –80°C until further analysis.

For quantifying differentiation parameters, myoblasts at 70–80% confluency were differentiated into differentiation media as described in **Section 2.1.1**. Fully differentiated cells were treated with tunicamycin as described above.

3.2.2 Cell viability assay

Cellular viability in response to tunicamycin was assessed using the Live and Dead assay kit as described in **Section 2.5.3**. LEICA DMI6000 B inverted microscope at 10× magnification was used to image live (green fluorescence) and dead (red fluorescence) cells.

3.2.3 Assessment of differentiation parameters

As mentioned in Section 2X, 4% paraformaldehyde was used to fix myotubes, and PD/Perm wash supplemented with 10% (v/v) goat serum were used to permeabilised myotubes and block non-specific antibody, respectively. Then, Myosin 4 monoclonal antibody Alexa Fluor 488 (MF20) and DAPI were added to label myosin heavy chains and nuclei, respectively (**Section 2.5.2.3**). Images were acquired using LEICA DMI6000 B inverted microscope. NIH ImageJ was used to assess myotubes morphology and quantify differentiation parameters as described in **Section 2.5.2.3.1**.

3.2.4 Immunostaining for ER stress marker

Fixed cells were permeabilised with 0.5% (v/v) Triton X-100, following incubation with blocking solution. Anti-GRP78 was added to the cells overnight at 4°C. DAPI to stain nuclei, and 2nd Ab conjugated with Alexa Fluor 488 were added for 1 hour at room temperature, as described in **Section 2.5.2.2**. Cells maintained in DPBS were imaged using a LEICA DMI6000 B inverted microscope at 20× magnification.

3.2.5 Real-time qPCR of ER stress and mitochondrial-associated markers

Isolated RNA, using EZ-RNA Isolation kit (**Section 2.2.2**), was converted into cDNA, which was amplified by real-time qPCR (**Section 2.3.4**) using various ER stress and mitochondrial-associated primers. Housekeeping gene 18S was used as a control and each target gene of interest was analysed by the delta-delta ($2^{-\Delta\Delta ct}$) method).

3.2.6 Assessment of cellular respiration using Seahorse Extracellular Flux Analyser

OCR and ECAR, indicators of mitochondrial function and glycolytic activity, respectively were measured with an XFp Extracellular Flux Analyser, using the Seahorse XFp Mito Stress Test kit as explained in Section 2X. Human skeletal muscle cells were plated in XFp microplates at a density of 7×10^3 cells/well in growth media, and treated with tunicamycin in presence or absence of EUK-134 for 24 hours. Data were normalised to total protein concentration as explained in **Section 2.3.1**.

3.2.7 Assessment of mitochondrial membrane potential and mass

Human skeletal muscle myoblasts were seeded at 8×10^3 cells/well in a black-sided, clear-bottom 96-well plate, and treated for 24 hours as described above. JC-1 fluorophore, MitoTracker Red CMXRos, and TMRM were used to examine mitochondrial membrane potential ($\Delta\Psi_m$) at the excitation/emission wavelengths described in **Section 2.7**. TMRM fluorescence was also normalised to mitochondrial mass using MitoTracker Green as described in **Section 2.7.4**.

3.2.8 Measurement of RONS

Myoblasts plated in 96-well plate and incubated with tunicamycin with or without EUK-134, were exposed to the following fluorescent dyes to assess total intracellular ROS, intracellular superoxide, mitochondrial superoxide, and hydrogen peroxide, respectively: DCFH-DA (10 μ M, 30 min, 37°C), DHE (5 μ M, 20 minutes, 37°C), MitoSOX™ Red (5 μ M, 30 minutes, 37°C), and Amplex Red as described in **Section 2.6.1**. Endpoint fluorescence was measured using HT synergy microplate reader with the following excitation and emission wavelengths: DCFH-DA, 485/20 and 590/35 nm; DHE, 320/40 and 460/40 nm; MitoSOX™ Red, 360/40 and 590/35 nm; and Amplex Red, 530/25 and 590/35 nm, respectively. All

measurements were normalised to total protein content as described above in **Section 2.3.1**.

3.2.9 Assessment of mitochondrial morphology parameters using confocal microscopy

Myoblasts seeded on a 35 mm glass-bottom μ -Dish, treated with tunicamycin with or without EUK-134 were exposed to the mitochondrial-targeted MitoTracker Red CMXRos to quantify mitochondrial morphology, as described in **Sections 2.5.1**. Images were taken on a Leica TCS SP5 confocal microscope using a 63 \times /1.4 oil immersion objective, and mitochondrial morphology parameters and biodynamics were quantified using an established macro technique on NIH Image J, as explained in **Section 2.5.1.1**.

3.2.9 Western blotting

Tunicamycin-treated cells in presence or absence of EUK-134 were collected into ice-cold DPBS, centrifuged at 4°C and resuspended in lysis buffer. Total protein content was quantified using BCA protein assay as described in **Section 2.3.1**. Analysis of GRP94, MFN2, SOD1, and SOD2 protein content was established by SDS-PAGE and western blotting, as described in **Section 2.3.2 and 2.3.3**, with β -actin used as a loading control. Bands of target protein were visualised using chemiluminescent detection method in LI-COR Odyssey Fc Imaging System, as described in **Section 2.3.3.1**, and quantified using NIH Image J.

3.2.10 Statistical analysis

GraphPad Prism version 8 was used to determine normality distribution. Normally distributed data were assessed for statistical significance using one-way ANOVA followed by Tukey's test, and non-normally distributed data using Dunn's test. A p -value ≤ 0.05 was defined to be statistically significant. In all graphs, TN corresponds to tunicamycin.

3.3 Results

3.3.1 Cellular viability

Cellular viability upon 0.1 $\mu\text{g}/\text{mL}$ tunicamycin in presence or absence of EUK-134 (10 μM) for 24 hours was assessed to ensure their efficacy and the induction of ER stress-associated effects in absence of apoptosis/cell death. Live and Dead assay was used to stain viable cells green and dead cells red. As seen in **Figure 3.1**, no cell death was induced by tunicamycin or EUK-134 treatment at the specific doses and incubation time, with only green fluorescence being present. In contrast, ethanol-induced cell death was evident by red fluorescent cells.

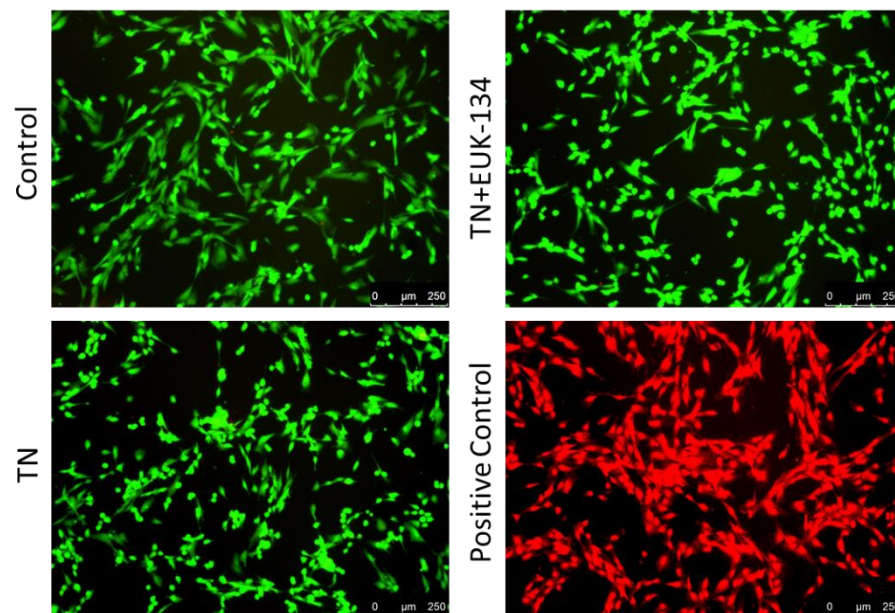


Figure 3.1 Cellular viability. Representative fluorescence images of cellular viability in control untreated cells, tunicamycin-treated cells with or without EUK-134, and positive control ethanol-treated cells. Images captured at 10 \times magnification. Scale bar = 250 μm .

3.3.2 Tunicamycin-induced ER stress activation

Treatment with 0.1 $\mu\text{g}/\text{mL}$ tunicamycin for 24 hours in human skeletal myoblasts resulted in significant elevated changes in the expression (fold change) of various UPR genes, including *GADD34* (12%, $p=0.02$), *GRP78* (40%, $p<0.001$), *CHOP* (36%, $p<0.001$), *ERDJ4*

(20%, $p < 0.001$), and *Total XBP1* (40.5%, $p < 0.001$), compared to control (). This increase was significantly attenuated by the presence of EUK-134, except of that seen in *GADD34* – although not statistical significance was reached by EUK-134 compared to tunicamycin treatment, a relative decrease in *GADD34* fold change was evident (~5%) (**Figure 3.2**).

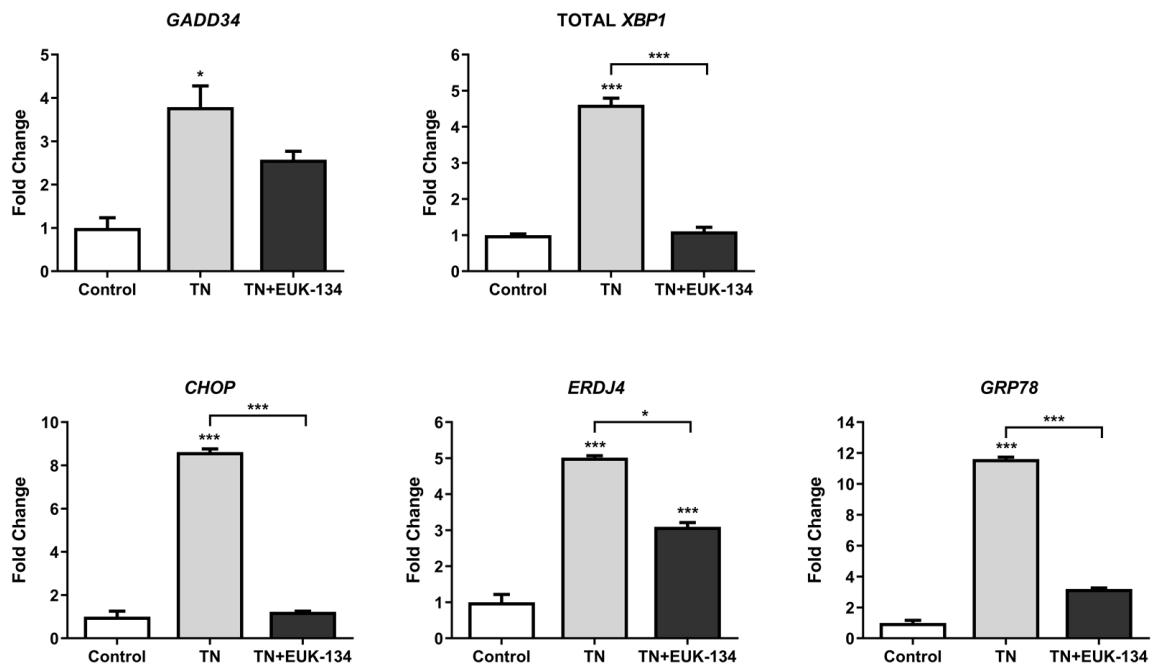


Figure 3.2 Fold change in ER stress markers upon tunicamycin treatment with or without EUK-134. Fold change in ER stress-associated gene expression following tunicamycin +/- EUK-134 treatment. Data represent mean fold change of $2^{-\Delta\Delta Ct} \pm$ S.E.M. of ΔCt values ($n=3$), * $p \leq 0.05$, *** $p < 0.001$ compared to control or as indicated.

GRP78 fluorescence intensity was also examined to assess ER stress activation upon tunicamycin and the effects of EUK-134. As expected, tunicamycin induced a significant rise in GRP78 fluorescence intensity compared to untreated control (42% of increase, $p=0.004$), quantified in the whole image area and normalised to nuclei number. Even though at mRNA levels, EUK-134 was able to decrease tunicamycin-induced increased in GRP78 fold change, no inhibitory effects were evident by immunofluorescence (**Figure 3.3**).

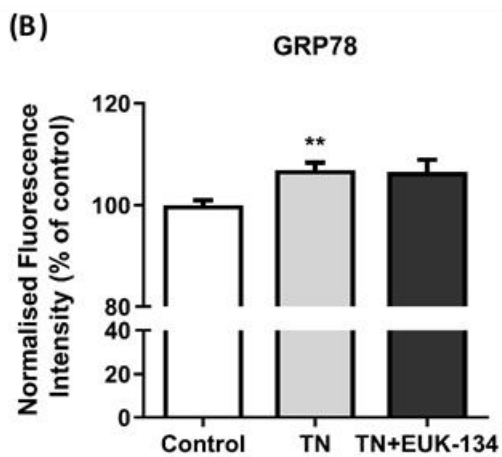
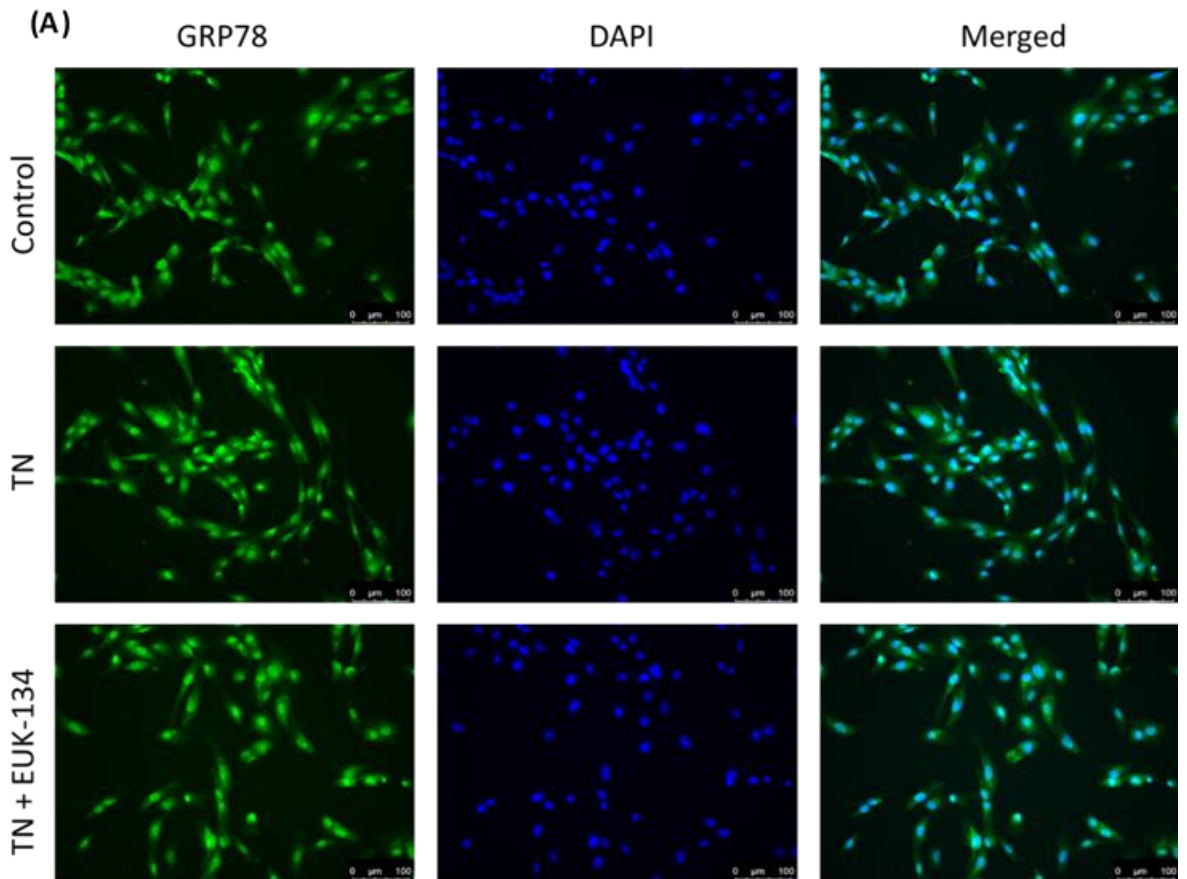


Figure 3.3 Fluorescent intensity of GRP78. (A) Representative images of tunicamycin-treated human skeletal muscle myoblasts with or without EUK-134 stained for GRP78 (green) and DAPI (blue). Images captured at 20× magnification. Scale bar = 100 μm. Brightness was adjusted equally in each image to enhance visualisation. (B) Quantification of GRP78 fluorescence intensity level normalised to nuclei number (DAPI

staining). Data represent mean \pm S.E.M. ($n=3$), $**p<0.01$ compared to untreated control. TN: tunicamycin

GRP94 is another marker of ER stress activation. Protein levels of GRP94 were examined, with results showing tunicamycin-induced significant elevation in GRP94 protein expression relative to loading control (~ 40 , $p=0.03$). However, EUK-134 was unable to attenuate this effect, with statistical significance being evident by combination treatment with tunicamycin and EUK-134, as well ($p=0.03$) (Figure 3.4).

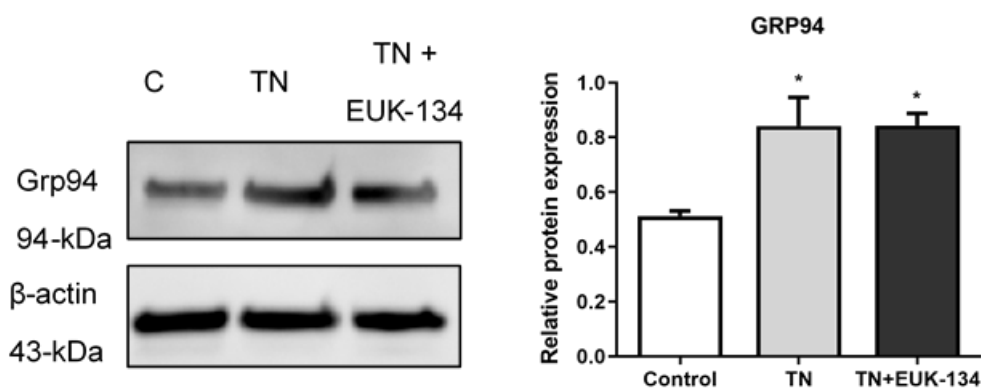


Figure 3.4 GRP94 protein levels. Representative western blot image and quantification of GRP94 protein levels relative to loading control β -actin. Data represent mean \pm S.E.M. ($n=3$) $*p\leq 0.05$ compared to control.

3.3.3 Myoblast differentiation and muscle atrophy in response to ER stress activation

Induction of myoblast differentiation into myotubes under ER stress was assessed by tunicamycin treatment in presence or absence of EUK-134 prior to exposure to differentiation media. Representative images of MF20-positive cells show inhibition of myotube formation by tunicamycin as seen by absence of elongated, branched, and multinucleated myotubes that are visible in control (Figure 3.5) (Dugdale *et al.*, 2018). Furthermore, the observed ER stress-associated inhibition of myoblast differentiation was not rescued by EUK-134 (Figure 3.5).

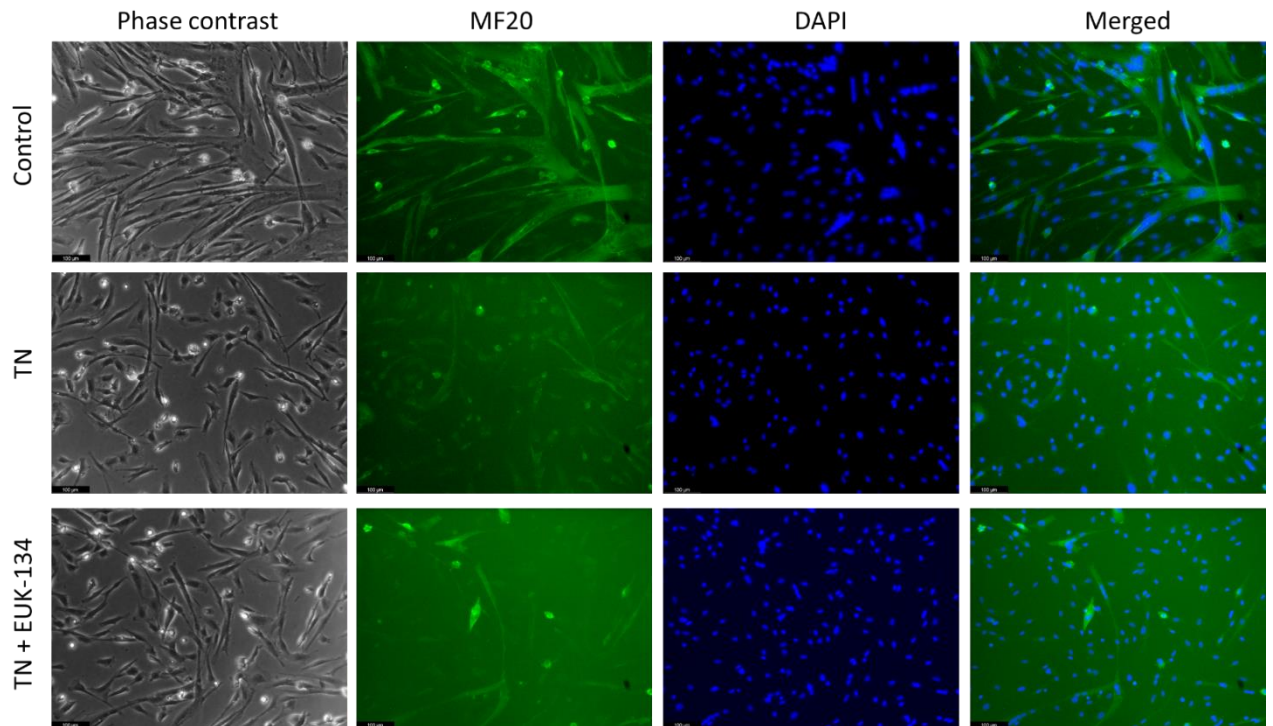
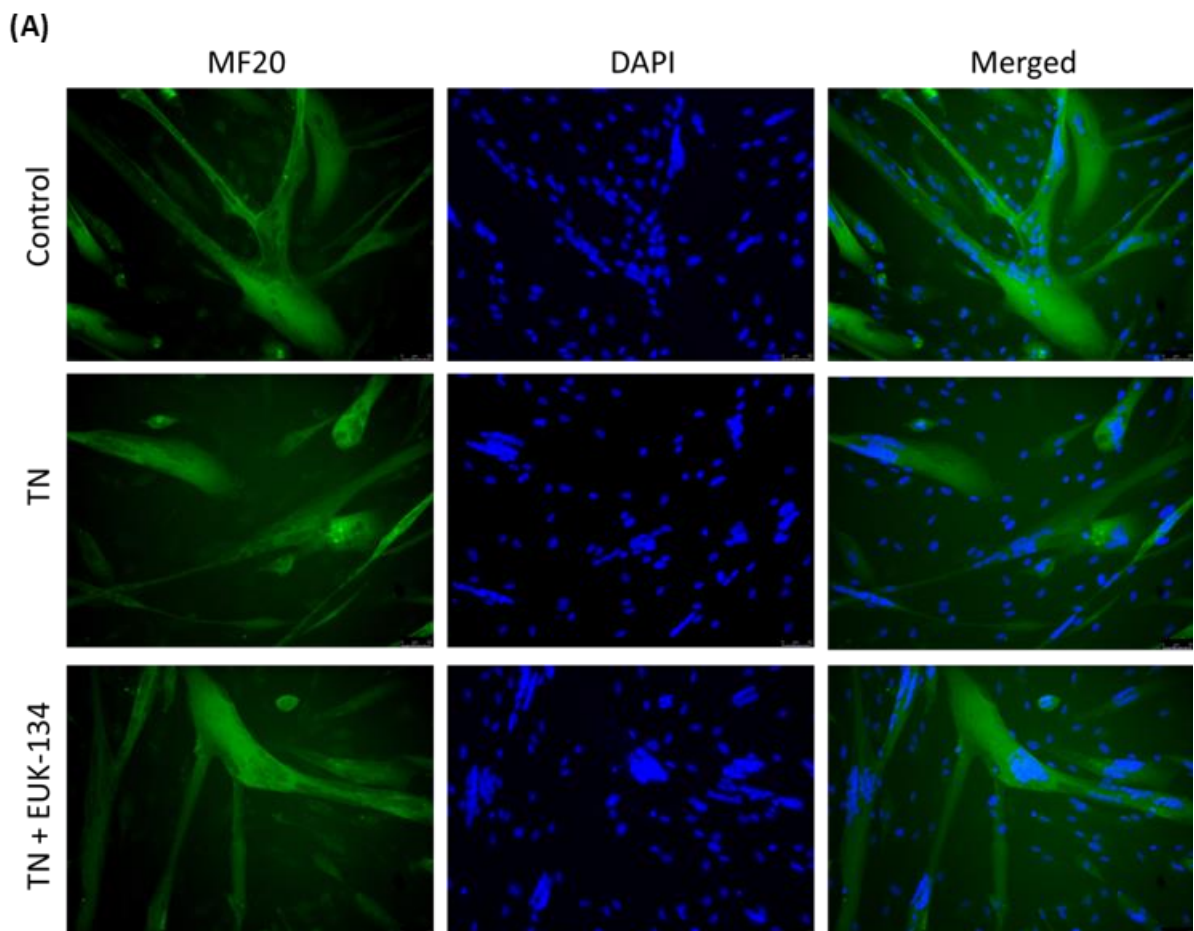


Figure 3.5. Myoblast differentiation. Representative images of myotubes stained for MF20 (green fluorescence) and counterstained with DAPI (blue fluorescence) following tunicamycin treatment with or without EUK-134 prior differentiation induction. Images captured at 20× magnification. Scale bar = 100 μm.

To further assess muscle hypertrophy/atrophy and myotubes capacity to retain differentiation processes upon ER stress, tunicamycin was added to fully differentiated cells, as well, in presence or absence of EUK-134. Tunicamycin treatment resulted in distinct myotube morphological alterations, with quantitative analysis showing significantly decreased length compared to control cells ($p=0.004$), an effect that was significantly attenuated by EUK-134 ($p=0.04$). However, no changes were observed in the width of terminally differentiated cells upon tunicamycin treatment in presence or absence of EUK-134. As a result, no statistically significant changes were seen in aspect ratio, described by the length of myotubes per width – however, a decreased trend was apparent in presence of tunicamycin (34% of decrease) that was inhibited by EUK-134. Tunicamycin-induced muscle atrophy was also suggested by the observed decrease in myotube area ($p<0.001$), representing the total area of MF20-positive cells per the entire

field of view. As it can be seen by the representative images of MF20-positive cells, tunicamycin-treated cells show smaller myotubes with less branching compared to control cells. Even though myotube area was significantly decreased in presence of EUK-134 compared to control ($p=0.02$), this decrease was smaller than that induced by tunicamycin treatment in absence of EUK-134 (33% of increase following EUK-134 compared to tunicamycin treatment). Furthermore, tunicamycin diminished myogenic differentiation potential of terminally differentiated cells compared to control cells, as presented by the fusion index (number of nuclei in each myotube per the total number of nuclei in field) ($p=0.009$). Consistent with this finding, the number of nuclei per myotube was also significantly reduced in tunicamycin-treated cells compared to untreated control cells ($p=0.02$). Both fusion index (%) and nuclei number in each myotube were restored by EUK-134 (**Figure 3.6**).



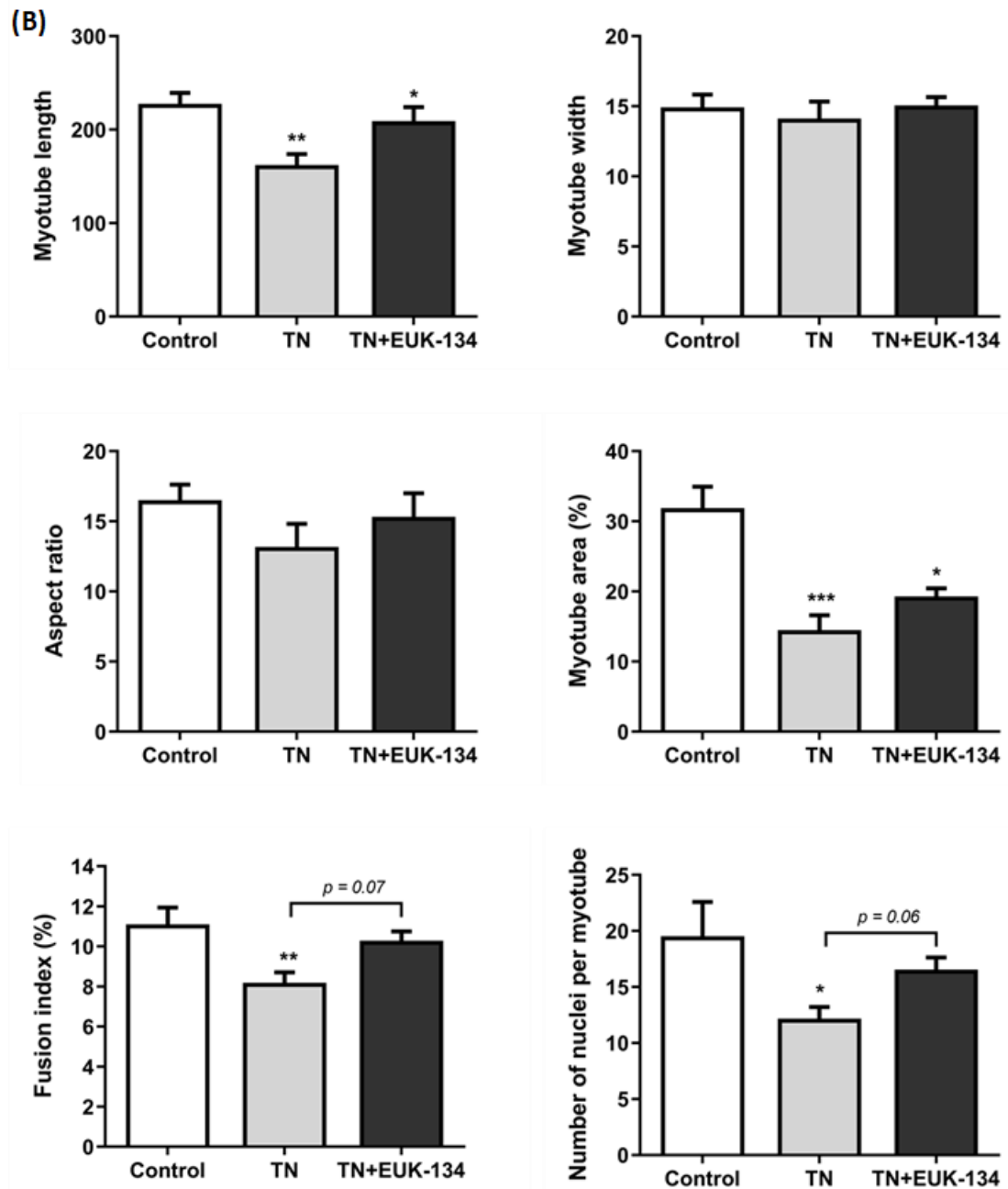
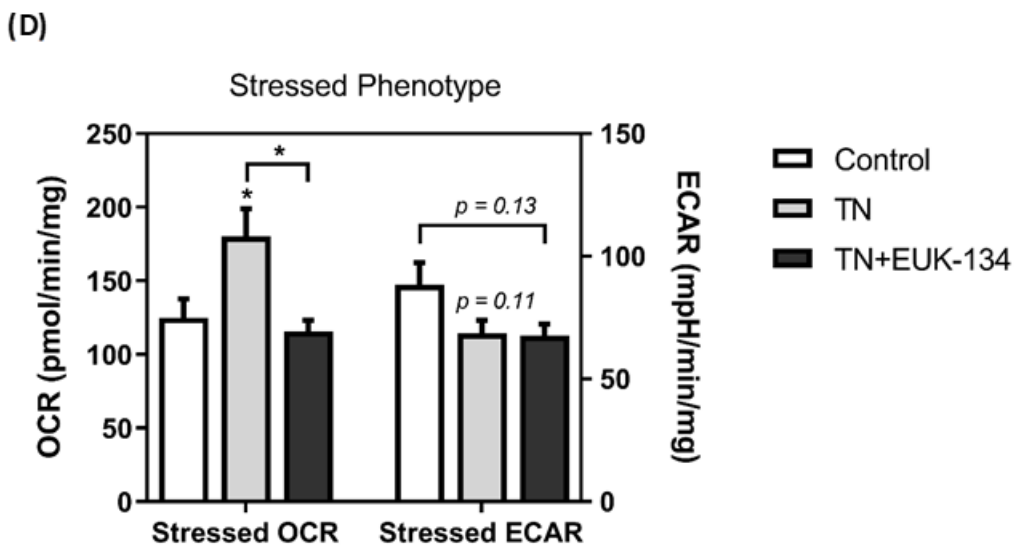
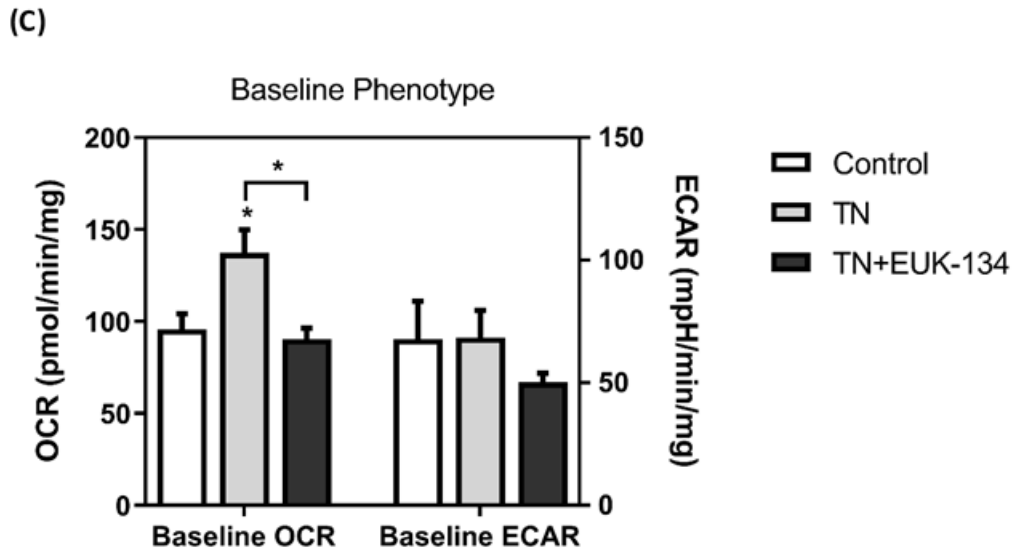
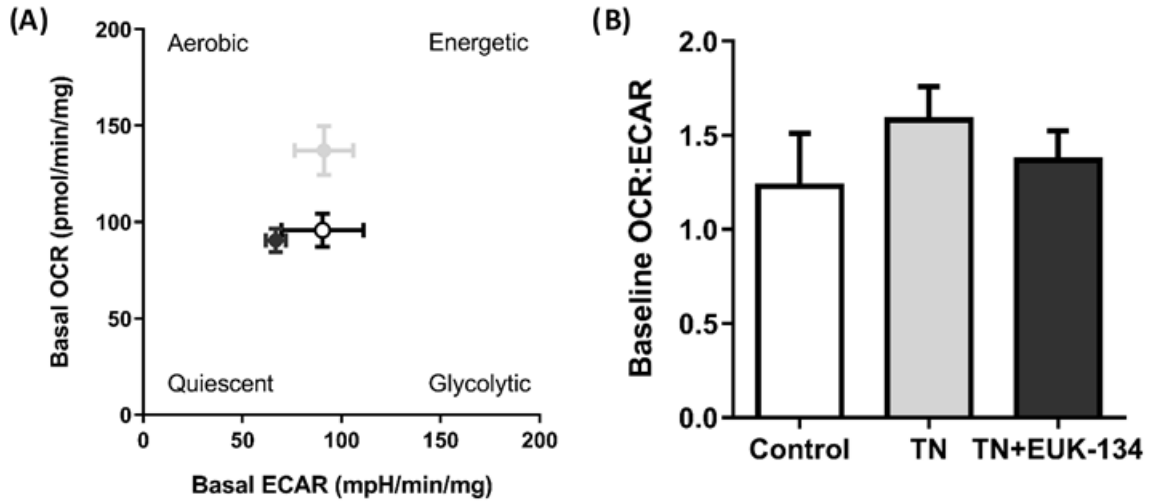


Figure 3.6 Muscle atrophy assessment based on morphological and differentiation parameters. (A) Representative images of MF20 (green fluorescence) and DAPI (blue fluorescence) stained myotubes that were exposed to tunicamycin treatment with or without EUK-134 after full differentiation was occurred. Images captured at 20 \times magnification. Scale bar = 100 μ m. Brightness was adjusted equally in each image to enhance visualisation. **(B)** Quantification of the myotubes morphological parameters, myotube length and width, and the differentiation parameters, aspect ratio, myotube

area (%), fusion index (%), and number of nuclei per myotube. Data represent mean \pm S.E.M. ($n=3$), * $p\leq 0.05$, ** $p<0.01$, *** $p<0.001$ compared to control.

3.3.4 Mitochondrial bioenergetic profile

Real-time OCR and ECAR measurements derived from the Seahorse extracellular flux analyser were used to determine the energy phenotype (**Figure 3.7A**) and individual mitochondrial respiration parameters (**Figure 3.9**) under tunicamycin-induced ER stress in presence or absence of EUK-134. In particular, a graph presenting basal OCR versus ECAR values was created to identify their metabolic status (energy phenotype) – glycolytic, oxidative/aerobic, energetic or quiescent state. Interestingly, tunicamycin-treated myocytes showed a trend towards oxidative/aerobic phenotype, whereas in presence of EUK-134, myocytes presented a similar energy phenotype with control myocytes (**Figure 3.7A**). This trend was also apparent when plotting basal OCR to ECAR ratio, showing a relative increase upon ER stress activation (**Figure 3.7B**). This indicates that tunicamycin-treated myocytes rely mostly on oxidative phosphorylation, instead of glycolysis, with OCR being significantly increased by tunicamycin compared to control under basal conditions ($p=0.02$), while ECAR remained unaffected; this OCR increase was significantly attenuated by EUK-134 ($p=0.01$) (baseline phenotype, **Figure 3.7C**). Under Mito stress by FCCP, myocytes showed similar trend of oxidative phosphorylation utilisation, while glycolytic flux was interestingly reduced by tunicamycin in both absence ($p=0.11$) and presence of EUK-134 ($p=0.13$) compared to control (**Figure 3.7D**). Further investigation on their metabolic potential, the percentage of increase of stressed ECAR over baseline ECAR was substantially reduced upon tunicamycin treatment (~25%), which was inhibited by EUK-134, indicating inability of the cells to increase glycolysis to meet energy demands; no changes were seen in metabolic potential in respect to oxidative phosphorylation (OCR) compared to control (**Figure 3.7E**).



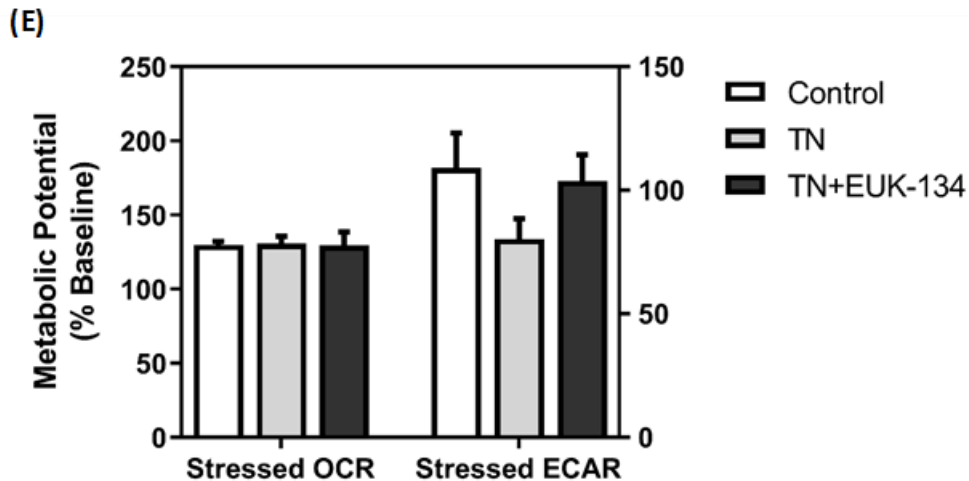


Figure 3.7 Energy phenotype upon ER stress in presence or absence of EUK-134. (A) Bioenergetic profile expressed as OCR versus ECAR measured under basal conditions. Statistical analysis of **(B)** baseline OCR to ECAR ratio, **(C)** OCR and ECAR baseline phenotype, **(D)** OCR and ECAR stressed phenotype, and **(E)** metabolic potential. Data were normalised to total protein content. Data represent mean \pm S.E.M ($n=3$), $*p\leq 0.05$.

According to the OCR trace, tunicamycin treatment resulted in an overall increase compared to control that was retained throughout the sequential addition of mitochondrial stressors, which was dropped to control levels in presence of EUK-134 (**Figure 3.8**). This increase was apparent in both non-mitochondrial (**Figure 3.9A**) and mitochondrial respiration under both basal and maximal conditions (**Figure 3.9B and C**); specifically, statistical significance was seen in basal respiration by tunicamycin, which was significantly depressed by EUK-134. EUK-134 was also able to restore tunicamycin-induced deficit in spare respiratory capacity (%) to a percentage that was significantly higher than control (**Figure 3.9D**). Consistently, reduced ATP-linked respiration was evident upon tunicamycin treatment (**Figure 3.9E**), as well as enhanced proton leak ($p = 0.07$) (**Figure 3.9F**). Importantly, proton leak induction was significantly attenuated by EUK-134 compared to tunicamycin treatment only (**Figure 3.9F**).

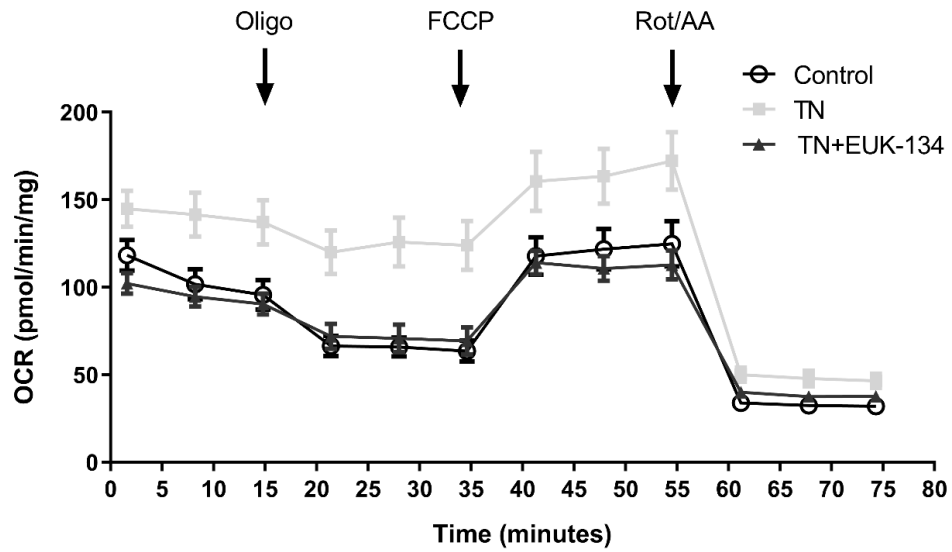
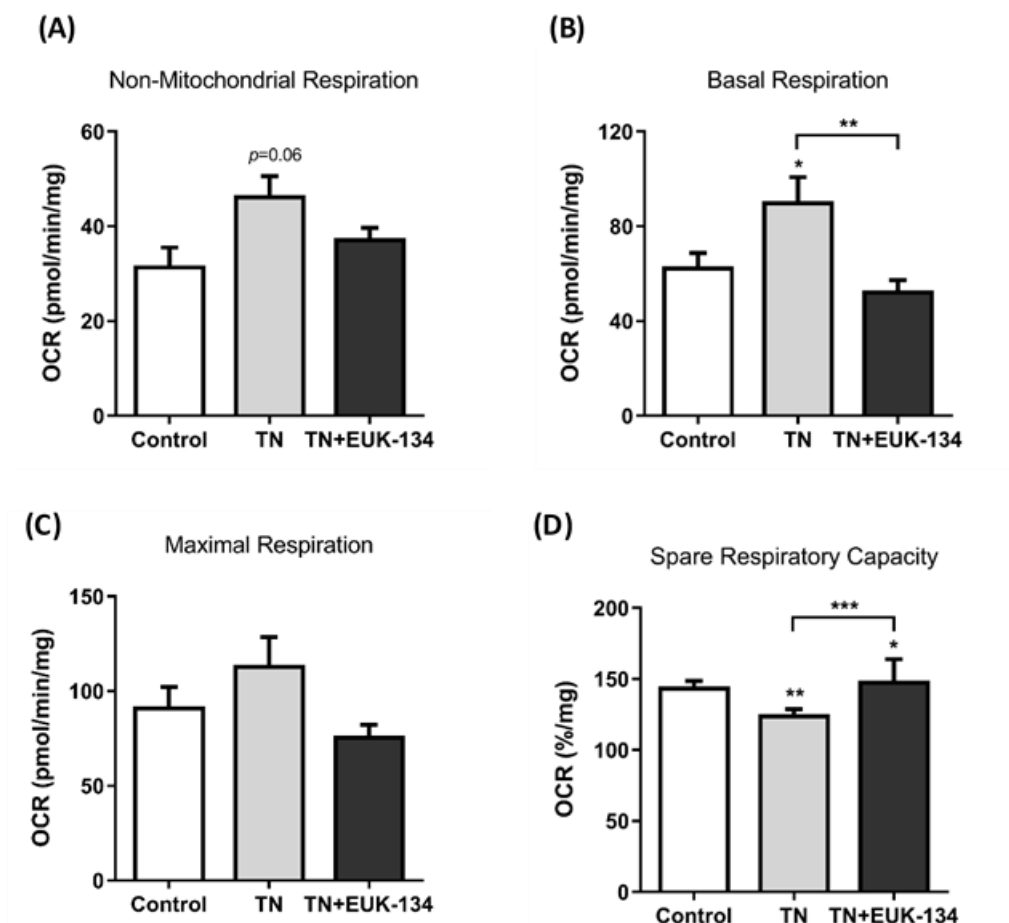


Figure 3.8 Bioenergetic profile upon ER stress in presence or absence of EUK-134. Real-time measurements of oxygen consumption rate (OCR) following the sequential injection of oligomycin, FCCP, and a mixture of rotenone/antimycin A. Data were normalised to total protein content and represent mean \pm S.E.M ($n=3$).



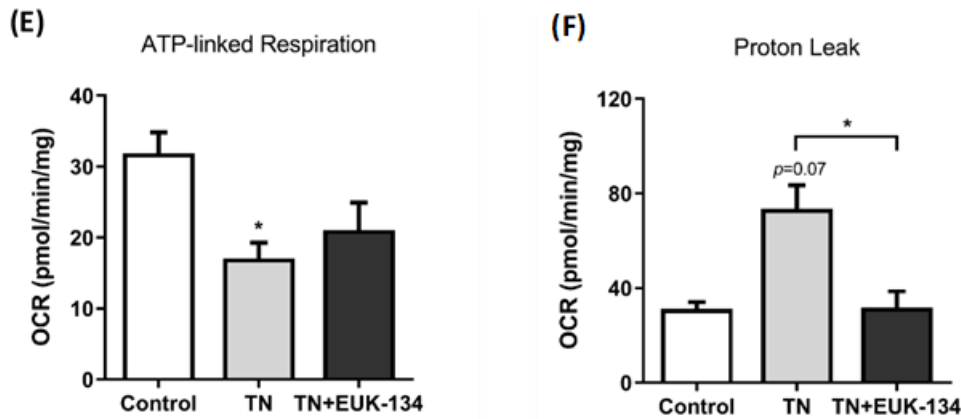
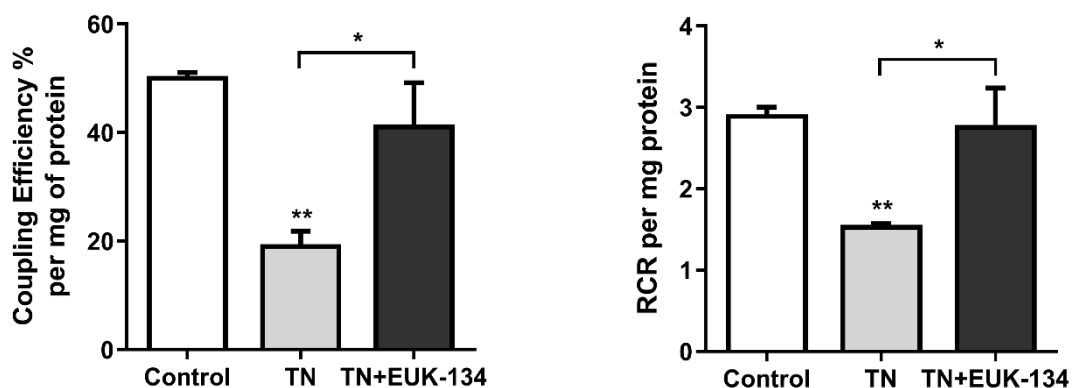


Figure 3.9 Individual mitochondrial parameters calculated from the bioenergetic profile. (A–F) Mitochondrial parameters – non-mitochondrial respiration, basal respiration, maximal respiration, spare respiratory capacity, proton leak, and ATP production – per mg of protein, in IBM and DM cells in presence or absence of EUK-134. Data represent mean \pm S.E.M. ($n=3$), * $p \leq 0.05$, ** $p < 0.01$, *** $p < 0.001$ compared to control or otherwise stated.

Normalised respiratory flux ratios, as described by Dott *et al.* (2014), were calculated to further evidence mitochondrial dysfunction downstream to ER stress activation and the beneficial impact of EUK-134. Mitochondrial respiration deficient was evident by a significant reduction in coupling efficiency ($p=0.001$), RCR ($p=0.01$), and phosphorylating respiration ($p < 0.001$). The observed decline in normalised respiratory flux ratios was inhibited by EUK-134 and restored to control levels ($p=0.02$, $p=0.02$, $p=0.03$, respectively) (Figure 3.10).



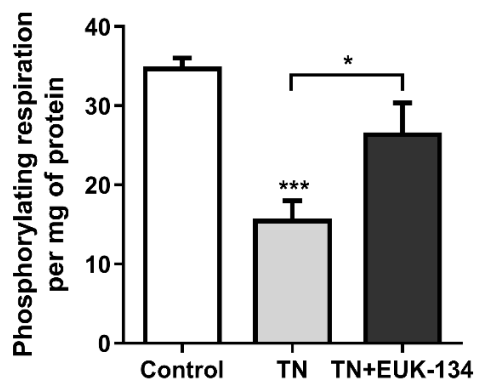


Figure 3.10 Normalised respiratory flux control ratios. Coupling efficiency (%), respiratory control ratio (RCR), and phosphorylating respiration per mg of protein in tunicamycin-treated myoblasts in presence or absence of EUK-134, calculated from individual mitochondrial parameters. Data represent mean \pm S.E.M. ($n=3$), * $p \leq 0.05$, ** $p < 0.01$, *** $p < 0.001$ compared to control or otherwise stated.

Further to the observed proton leak induced by tunicamycin, the mRNA expression of the mitochondrial uncoupling protein 3 (*UCP3*) was also assessed. As seen in **Figure 3.11**, fold change in *UCP3* was drastically increased by tunicamycin compared to control ($p < 0.001$). EUK-134 was able to significantly reduce tunicamycin-induced *UCP3* fold change, but not to control levels; instead, statistical significance was also seen by tunicamycin with EUK-134 compared to control (**Figure 3.11**).

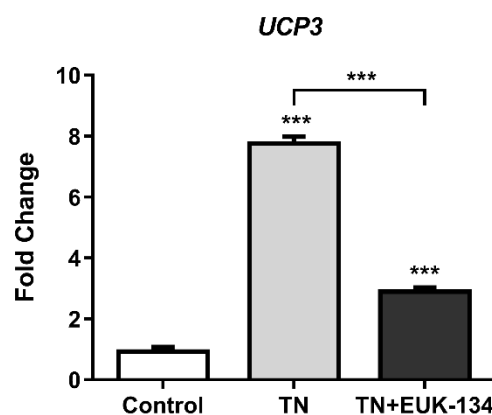


Figure 3.11 Mitochondrial uncoupling protein 3 (*UCP3*) gene expression. Relative fold change in mRNA expression of *UCP3*. Data represent mean fold change normalised to 18S

housekeeper gene \pm S.E.M. of Δ Ct values ($n=3$), *** $p<0.001$ compared to control or otherwise stated.

3.3.5 Mitochondrial unfolded protein response (mtUPR)

Activation of the mtUPR upon ER stress in presence or absence of EUK-134 was examined through assessment of the mRNA expression of two heat shock proteins. Real-time qPCR data analysis displayed significantly increased fold change in mRNA expression of both HSP Family A Member 9 (*HSPA9*) and *HSP60* by tunicamycin treatment ($p<0.001$ and $p=0.005$, respectively). Interestingly, EUK-134 was able to prevent tunicamycin-induced changes in *HSPA9* mRNA expression, reaching statistical significance compared to tunicamycin ($p<0.001$), but not in *HSP60* (Figure 3.12).

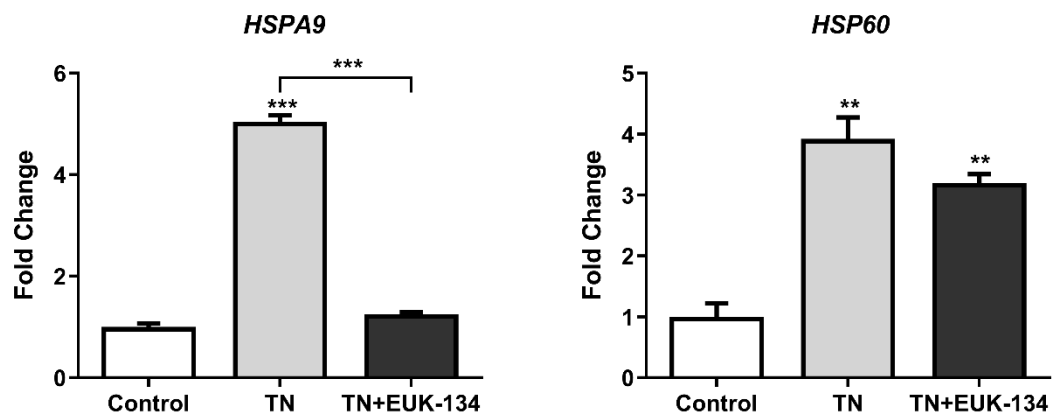
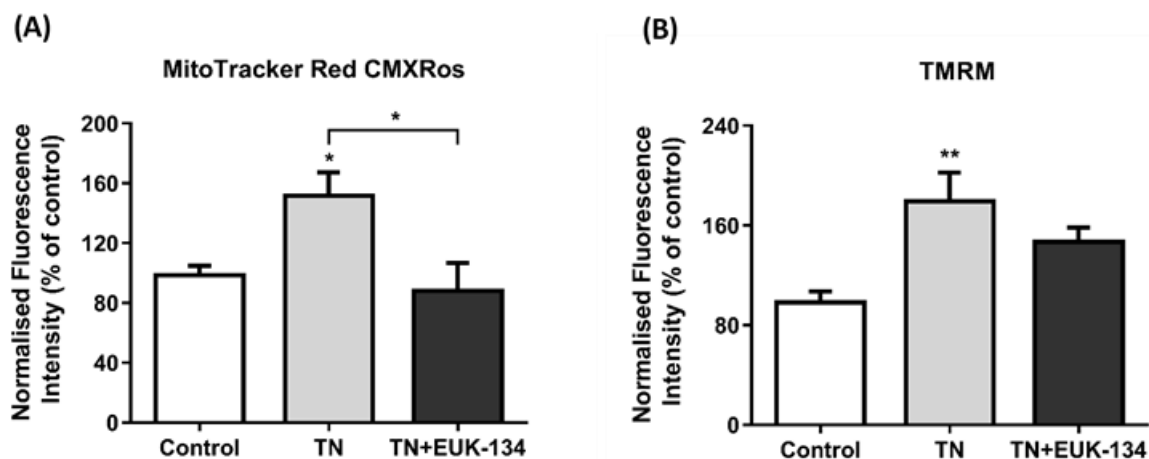


Figure 3.12 Mitochondrial unfolded protein response markers. Relative fold change in mRNA expression of *HSPA9* and *HSP60*. Data represent mean fold change normalised to 18S housekeeper gene \pm S.E.M. of Δ Ct values ($n=3$), ** $p<0.01$, *** $p<0.001$ compared to control or otherwise stated.

3.3.6 Mitochondrial mass and membrane potential

Mitochondrial membrane potential was investigated using various fluorophores to further assess mitochondrial dysfunction in the *in vitro* model of ER stress in presence or

absence of EUK-134. Mitochondrial membrane hyperpolarisation, defined by increased MitoTracker Red CMXRos fluorescence intensity, was initially seen by tunicamycin treatment, which was significantly prevented by EUK-134 (**Figure 3.13A**). Likewise, TMRM fluorescence intensity was significantly elevated following tunicamycin treatment, suggesting mitochondrial hyperpolarisation, but not in presence of EUK-134 (**Figure 3.13B**). To examine whether mitochondrial mass accounts for increased fluorescence signals upon ER stress, as previously suggested (Perry *et al.*, 2005), TMRM fluorescence intensity was normalised to MitoTracker Green fluorescence intensity, attributable to mitochondrial mass. As seen in **Figure 3.13C**, mitochondrial content normalisation resulted in a substantial decrease in fluorescence intensity ($p=0.07$) in tunicamycin-treated myoblasts, but not in presence of EUK-134, indicating mitochondrial membrane depolarisation upon ER stress. This shows that mitochondrial mass is elevated by tunicamycin that has affected the initial interpretation on mitochondrial membrane potential. JC-1 fluorophore assay allows normalised interpretation as the ratio of healthy negatively charged mitochondria with J-aggregates (polymers) and depolarised mitochondria with J-monomers is calculated (Madreiter-Sokolowski *et al.*, 2019). Indeed, JC-1 polymers to monomers ratio was significantly reduced by tunicamycin, an effect that was significantly attenuated by EUK-134 (**Figure 3.13D**).



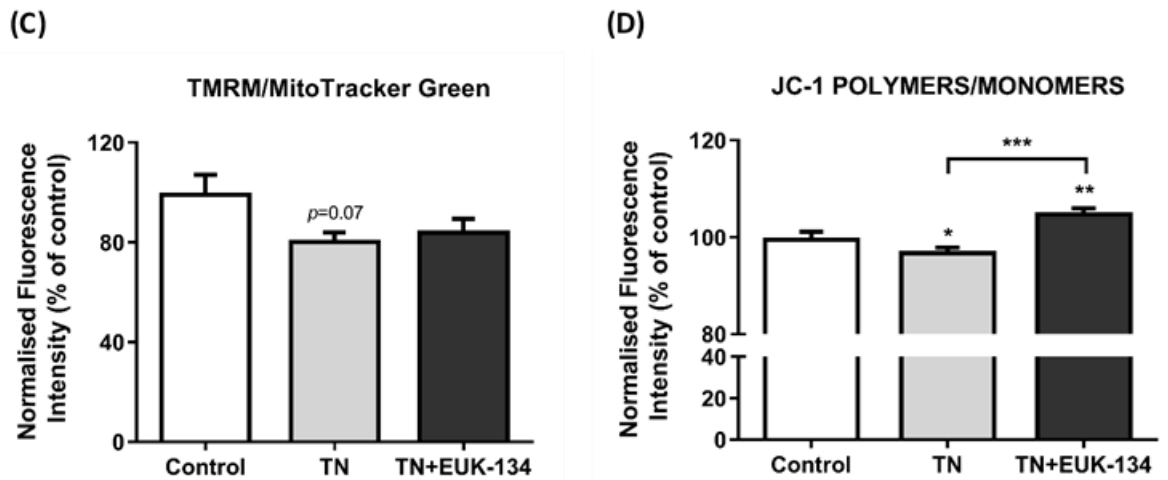


Figure 3.13 Mitochondrial membrane potential. Relative change (%) in **(A)** MitoTracker Red CMXRos fluorescence intensity, **(B)** TMRM fluorescence intensity, **(C)** TMRM per MitoTracker Green fluorescence intensity, and **(D)** JC-1 polymers to monomers ratio, normalised to protein content. Data represent mean \pm S.E.M. ($n=4$), * $p\leq 0.05$, ** $p<0.01$, *** $p<0.001$ compared to control or otherwise stated.

Changes in mitochondrial mass were further assessed by qualitative analysis of MitoTracker Green staining, with representative images showing distinct increase in MitoTracker Green staining in tunicamycin-treated cells compared to control, with less effect being noticeable in presence of EUK-134 (**Figure 3.14A**). Similarly, quantitative analysis showed significantly increased MitoTracker Green fluorescence intensity by tunicamycin that was prevented by EUK-134 (**Figure 3.14B**). Mitochondrial biogenesis was further confirmed by tunicamycin-induced increased fold change in mRNA expression of *Citrate Synthase* ($p=0.03$ compared to control), the initial enzyme of citric acid cycle, and transcription factor A and mitochondrial precursor (*TFAM*) ($p<0.001$ compared to control), a mitochondrial DNA transcription mediator, which was

significantly inhibited in presence of EUK-134 ($p=0.03$ and $p=0.006$, respectively, compared to tunicamycin treatment only) (**Figure 3.14C and D**).

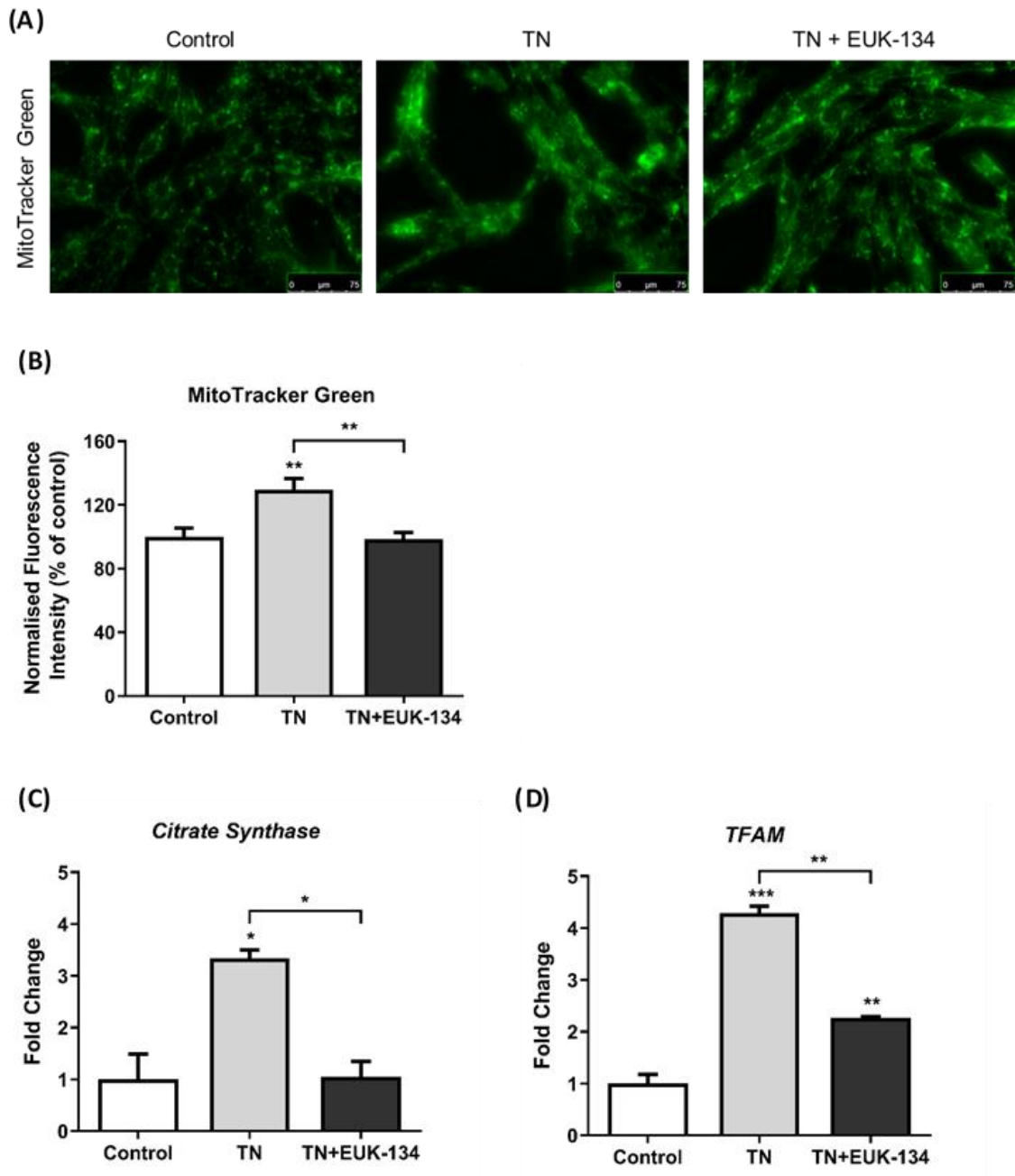


Figure 3.14 Mitochondrial biogenesis. **(A)** Representative images of live-cell mitochondrial staining in tunicamycin-treated cells with or without EUK-134 using MitoTracker Green fluorophore. Images captured at 40× magnification. Scale bar = 75 μm. Brightness was adjusted equally in each image to enhance visualisation. **(B)** Relative change (%) in MitoTracker Green fluorescence intensity, normalised to protein content.

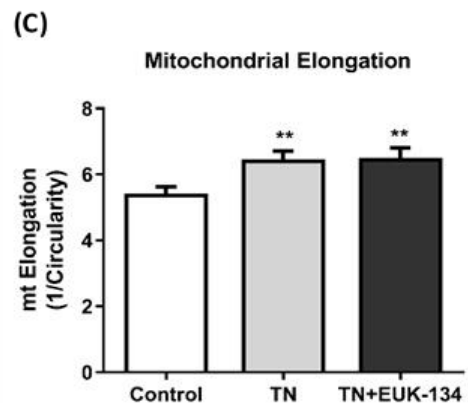
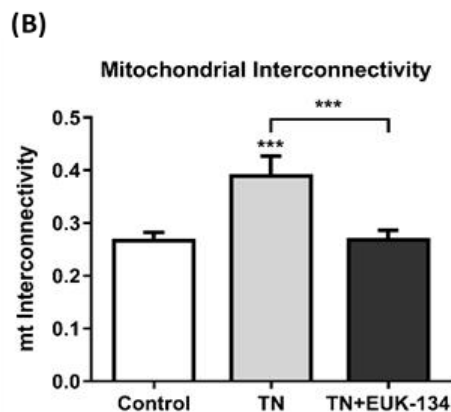
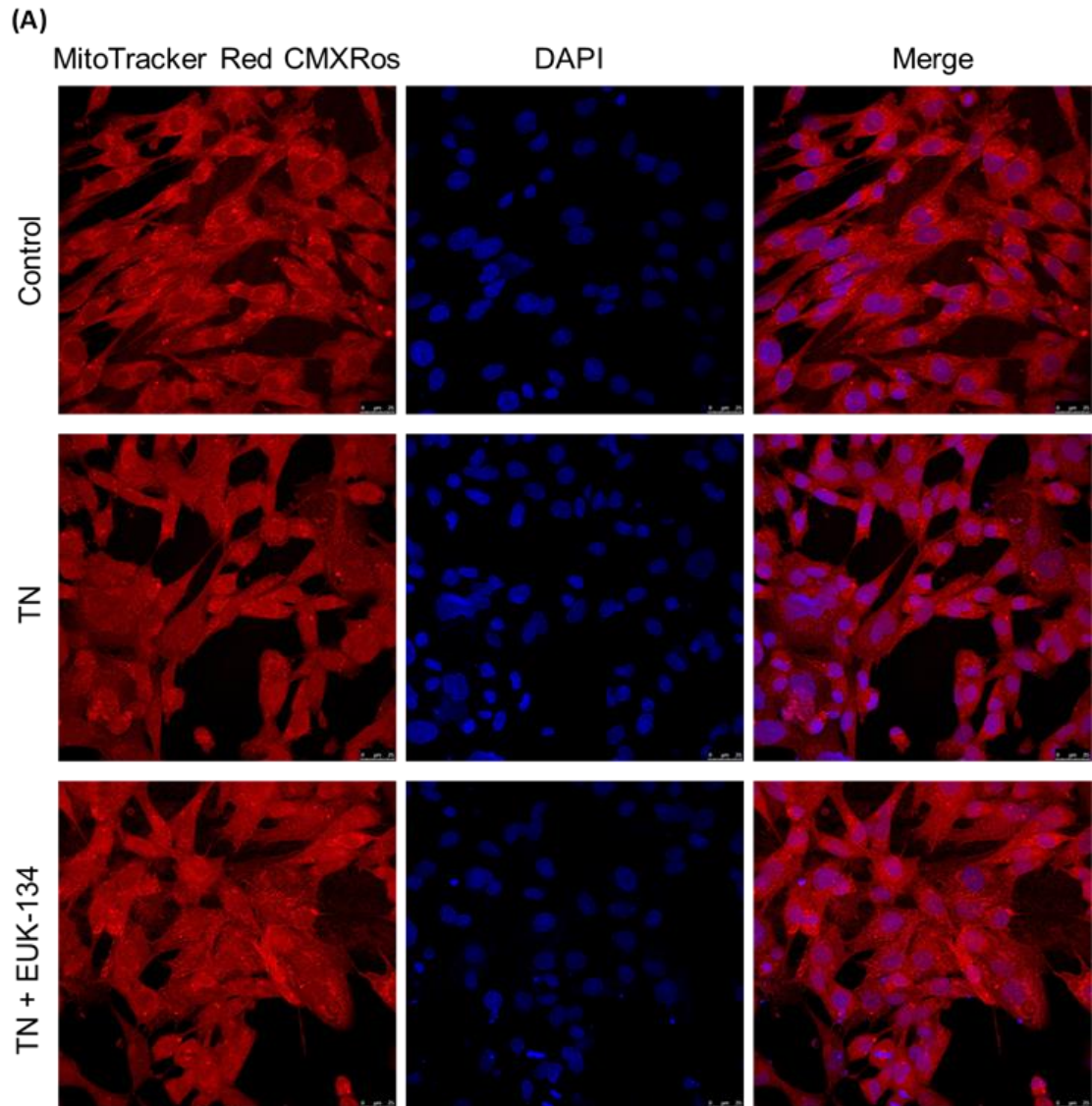
Data represent mean \pm S.E.M. ($n=4$), $**p<0.01$, compared to control or otherwise stated. Relative fold change in mRNA expression of **(C) Citrate Synthase** and **(D) TFAM**. Data represent mean fold change normalised to 18S housekeeper gene \pm S.E.M. of Δ Ct values ($n=3$), $*p\leq 0.05$, $**p<0.01$, $***p<0.001$ compared to control or otherwise stated.

3.3.7 Mitochondrial morphology: fusion and fission processes

MitoTracker Red CMXRos high-content imaging using confocal microscopy was established to assess mitochondrial network structure and their association to fusion and fission events upon ER stress and EUK-134 treatment (**Figure 3.15A**). As previously explained, mitochondrial interconnectivity and elongation are correlated with mitochondrial fusion processes, and in this study, both parameters were risen following tunicamycin treatment ($p<0.001$ and $p=0.009$, respectively, compared to control) (**Figure 3.15B and C**). These parameters can be related to increased mitochondrial content, which was evident by an increase in the percentage of cytosol occupied by mitochondria, as well ($\sim 50\%$ of increase, $p<0.001$) (**Figure 3.15D**) (Seo *et al.*, 2010; Bankapalli *et al.*, 2020). EUK-134 intervention significantly dropped tunicamycin effects in mitochondrial interconnectivity and content, but not in mitochondrial elongation (**Figure 3.15B and D**), which was also significantly risen compared to control ($p<0.005$) (**Figure 3.15C**). Mitochondrial fusion events upon ER stress were further supported by significant elevated fold change in mRNA expression of *MFN2* by tunicamycin; although EUK-134 resulted in a substantial decrease of *MFN2* fold change compared to tunicamycin, statistical significance was still observed compared to control (**Figure 3.16A**). It should also be noted that tunicamycin-induced changes in *MFN2* expression were not evident at protein level (**Figure 3.16B and C**).

Interestingly, propensity of fission events has been positively associated with mitochondrial perimeter and area (Seo *et al.*, 2010; Westrate *et al.*, 2014). Tunicamycin treatment showed increased mitochondrial perimeter and area (**Figure 3.15E and F**). However, EUK-134 treatment significantly reduced the tunicamycin-induced effect in both parameters (**Figure 3.15E and F**), suggesting ROS-mediated propensity of mitochondrial fragmentation. Increased fold change in the mRNA expression of fission-related genes fission 1 (*FIS1*) and *DRP1* was also seen in tunicamycin-treated cells

compared to control ($p < 0.001$ and $p = 0.01$, respectively) (Figure 3.16D and E). In turn, tunicamycin with EUK-134 showed significantly reduced *FIS1* fold change compared to tunicamycin, but not *DRP1* fold change (Figure 3.16D and E).



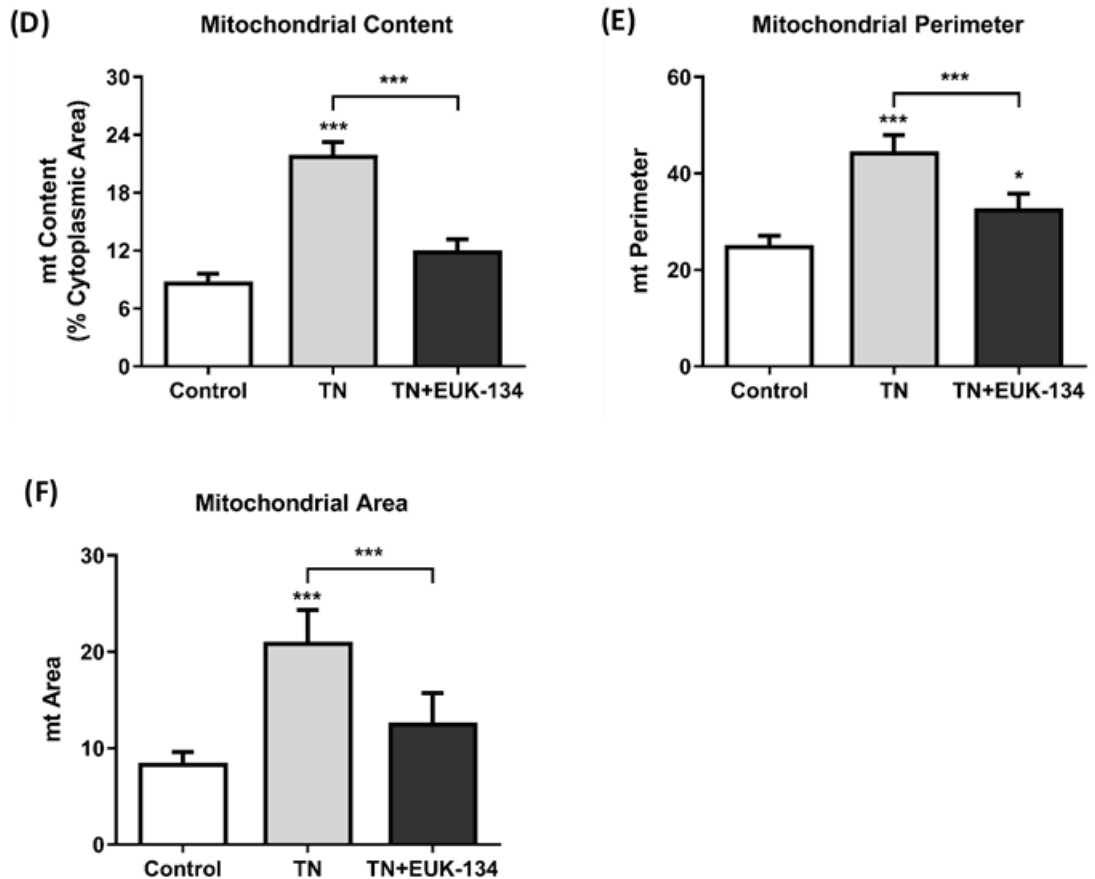


Figure 3.15 Mitochondrial morphological parameters. (A) Representative images of fixed-cell MitoTracker Red CMXRos staining in tunicamycin-treated cells with or without EUK-134 using. Images captured using 63 \times /1.4 oil immersion objective. Scale bar = 25 μ m. (B) Mitochondrial interconnectivity expressed by the ratio of mitochondrial area/perimeter, (C) mitochondrial elongation expressed by 1/circularity, (D) mitochondrial content as % of cytoplasmic area, (E) mitochondrial perimeter and (F) mitochondrial area. Data represent mean \pm SEM (n = 100 cells per group), * p \leq 0.05, ** p < 0.01, *** p < 0.001 compared to control or otherwise stated.

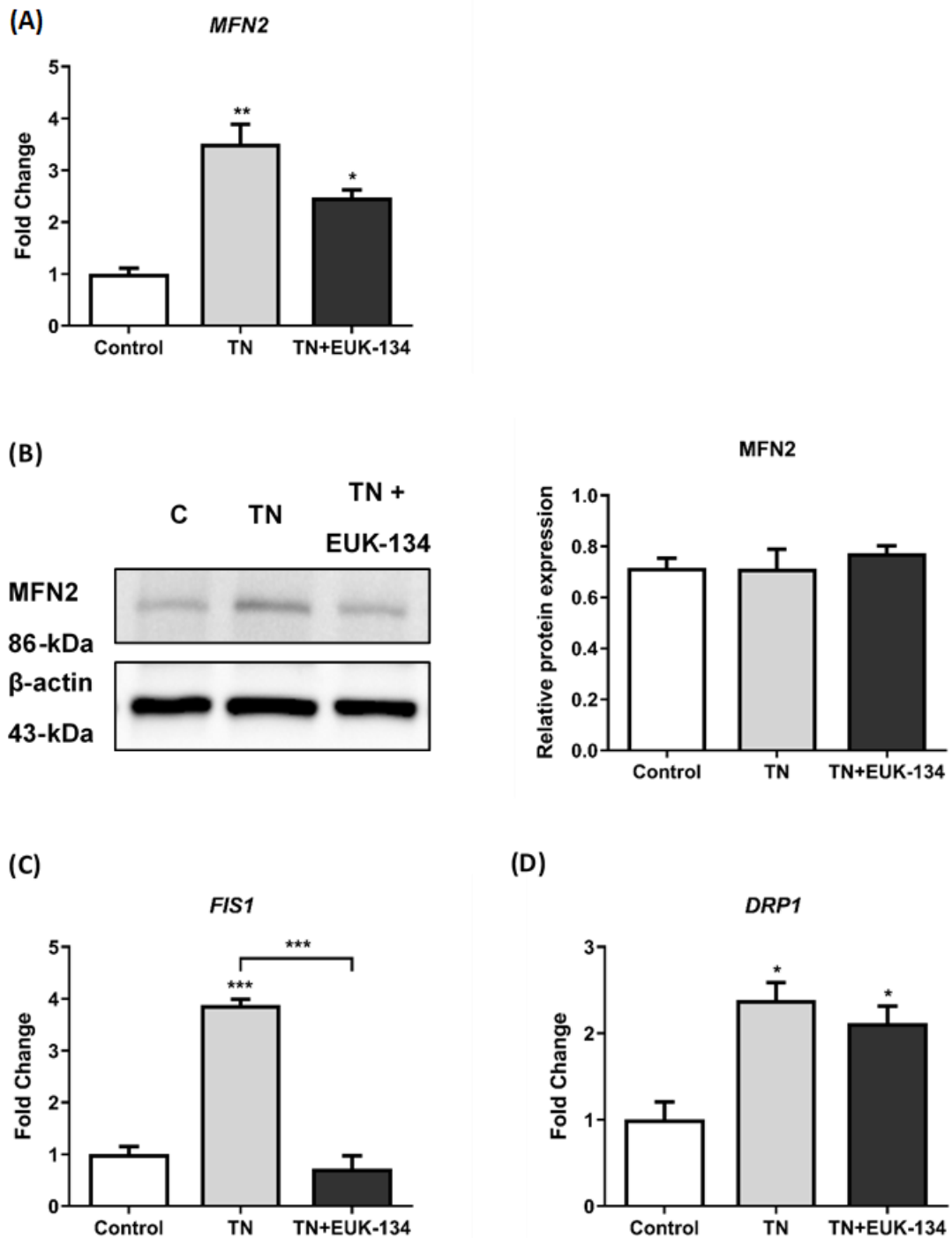
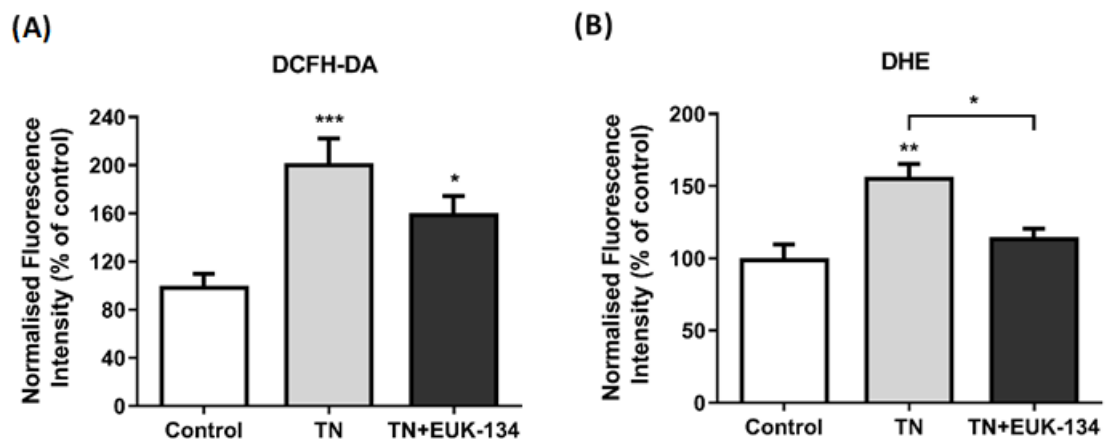


Figure 3.16 Mitochondrial dynamics. **(A)** Relative fold change in mRNA expression of *MFN2* fusion-associated gene. Data represent mean fold change normalised to 18S housekeeper gene \pm SEM of Δ Ct values ($n=3$), * $p \leq 0.05$, ** $p < 0.01$ compared to control or otherwise stated. **(B)** Cropped representative western blot image and quantification of *MFN2* protein levels relative to β -actin (loading control). Data represent mean \pm SEM

(n=3). **(C–D)** Relative fold changes in mRNA expression of *FIS1* and *DRP1* fission-associated genes. Data represent mean fold change normalised to 18S housekeeper gene \pm SEM of Δ Ct values (n=3), * $p \leq 0.05$, *** $p < 0.001$ compared to control or otherwise stated.

3.3.8 ROS generation

Based on the previous findings on the role of ROS in ER stress (tunicamycin)-induced changes in mitochondrial function, ROS generation was further assessed using different fluorophores. Tunicamycin rised DCFH-DA fluorescence intensity compared to control, indicative of total cellular ROS levels (**Figure 3.17A**). Specifically, superoxide levels, as described by DHE fluorescence intensity, were found to be elevated by tunicamycin ($p=0.002$ compared to control) and decreased in presence of EUK-134 compared to tunicamycin treatment only ($p=0.01$) (**Figure 3.17B**). However, no changes were seen in mitochondrial superoxide levels (MitoSOX Red fluorescence intensity) (**Figure 3.17C**). According to the literature, inability to see changes in mitochondrial superoxide levels might be attributable to the rapid conversion to hydrogen peroxide or peroxynitrite; however, this possibility has not been tested in this instance (Cao and Kaufman, 2014; Pearson *et al.*, 2014; Ott *et al.*, 2007). Protein levels of the antioxidants superoxide dismutase (SOD) 1 and 2 were also examined. As seen in **Figure 3.18**, a substantial increase in SOD1 protein expression levels was induced by tunicamycin (66%, $p=0.10$ compared to control), but not in SOD2 protein expression levels.



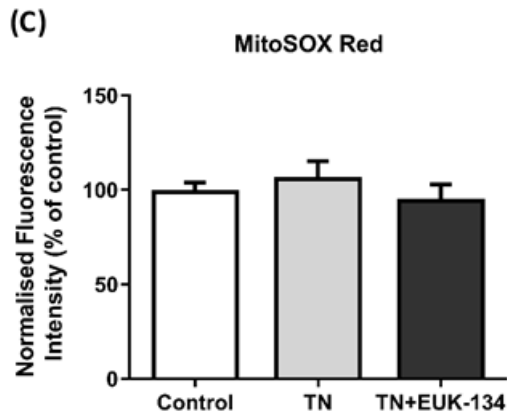


Figure 3.17 ROS generation. Relative change (%) in fluorescence intensity levels of **(A)** DCFH-DA (total cellular ROS levels, $n=3$), **(B)** DHE (total cellular superoxide levels, $n=4$), and **(C)** MitoSOX Red (mitochondrial superoxide levels, $n=4$), normalised to protein content. Data represent mean \pm SEM, * $p \leq 0.05$, ** $p < 0.01$, *** $p < 0.001$ compared to control or otherwise stated.

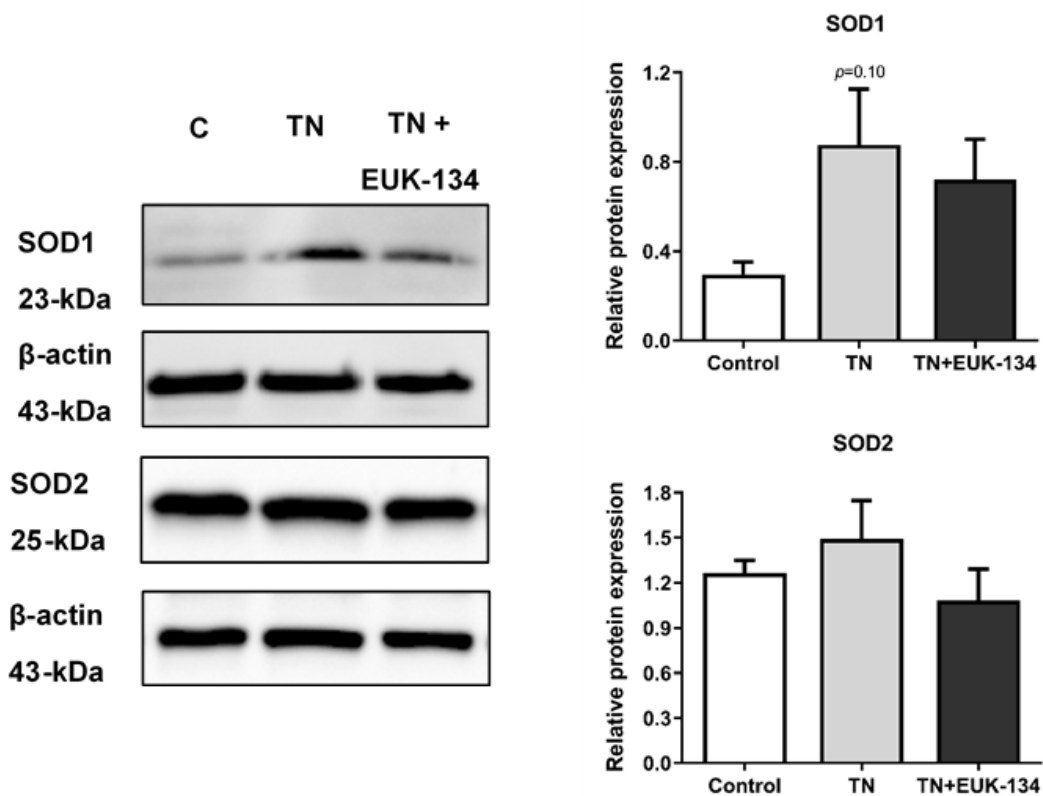


Figure 3.18 Superoxide dismutases protein expression. Cropped representative western blot image and quantification of SOD1 and SOD2 protein levels relative to β -actin (loading control). Data represent mean \pm SEM ($n=3-5$).

3.4 Discussion

ER and mitochondria associations constitute a variety of signaling pathways that mediate key cellular processes, while existing evidence also describe a strong interconnection between chronic/aberrant ER stress and mitochondrial abnormalities (Cao and Kaufman; 2014). Promising studies have suggested the involvement of ER stress activation in myositis pathogenesis and the persistent skeletal muscle weakness seen in patients (Nagaraju *et al.*, 2005). Further to this, as well as the poor knowledge on the importance of ROS generation in ER stress and mitochondria associations, this chapter sought to assess the impact of the antioxidant EUK-134 in an *in vitro* model of tunicamycin-induced ER stress in human skeletal muscle. Mitochondrial dysfunction upon ER stress activation, in presence or absence of EUK-134, was investigated in the aspects of respiration, biogenesis, and biodynamics. With EUK-134 being previously proven to be beneficial in preventing muscle atrophy and dysfunction upon oxidative stress, it has been considered as a great candidate for investigating the role of ROS in this setting (Kim and Lawler, 2012; Lawler *et al.*, 2014; Yamada *et al.*, 2015; Himori *et al.*, 2017).

Tunicamycin, an inhibitor of the *n*-glycosylation step of protein folding, inducing unfolded *n*-glycans aggregation within the ER (Duksin and Mahoney, 1982), has long been used to stimulate and study ER stress in mouse and human skeletal muscle cell lines (Win *et al.*, 2014; Quan *et al.*, 2015; Hassan *et al.*, 2012). The present study selected the use of a relatively low tunicamycin concentration (0.1 µg/mL), but with longer incubation period (24 hours) to induce later phase of ER stress and prevent compound toxicity (Bravo *et al.*, 2011; Deldicque *et al.*, 2011). Indeed, 0.1 µg/mL tunicamycin treatment for 24 hours in showed no effects on human skeletal muscle cells viability with or without EUK-134 treatment setting this condition as optimal for investigating ER stress induction in absence of apoptosis. ER stress activation following tunicamycin treatment was confirmed by upregulation of UPR pathway markers at both mRNA and protein levels, with *CHOP* mRNA upregulation, a pro-apoptotic transcription factor, enhancing the hypothesis of prolonged/maladaptive ER stress activation (Alam *et al.*, 2017). Interestingly, antioxidant treatment was able to inhibit aspects of UPR induction, with the tunicamycin-induced mRNA effects of *GRP78*, *ERDJ4*, and *total XBP1* being ameliorated by EUK-134.

With muscle atrophy being a prominent feature in myositis disease, the role of ROS generation in myoblast differentiation and muscle atrophy was initially investigated by exposing both regenerating myoblasts and fully differentiated (mature) myotubes to tunicamycin in presence or absence of EUK-134, respectively, as previously suggested (Dugdale *et al*, 2018). Distinct blockage of differentiation was seen in tunicamycin-treated myoblasts, as described by absence of elongated, branched, and multinucleated myotubes formation, as observed in control. Furthermore, EUK-134 was unable to mitigate ER stress-associated myoblast differentiation inhibition. ER stress has emerged as a crucial mediator of myogenesis (Bohnert, McMillan, and Kumar, 2018). Complementary to these findings, CHOP, which is upregulated in the present model, is known to inhibit myoblast differentiation. shRNA-mediated CHOP knockdown in mouse skeletal myoblast (C2C12) has shown early and high myogenin and MyHC expression following incubation into differentiating media, whereas exogenous CHOP upregulation caused the opposite effects (Alter and Bengal, 2011).

This study also showed a clear association between ER stress activation in fully differentiated cells and muscle atrophy, as well as differentiation potential, as presented by tunicamycin-induced reduction in myotube length, area, and aspect ratio, as well as fusion index, respectively. These results are in concordance with a study by Lightfoot *et al.*, 2014 showing muscle atrophy following tunicamycin treatment in existing myotubes. In particular, Acosta-Alvear *et al.* (2007) recommended XBP1 as a significant inhibitor of myoblast differentiation process. Furthermore, according to other studies, myostatin precursor protein, a negative regulator of muscle growth increased in sIBM, has been proved to be upregulated in *in vitro* models of ER stress, further supporting ER stress-associated muscle atrophy (Nogalska *et al.*, 2007; Sachdev *et al.*, 2018). Interestingly, EUK-134 treatment in existing myotubes under ER stress induction was able to both improve differentiation capacity and reduce muscle atrophy, supporting the importance of ROS generation in ER stress-mediated myogenesis.

Turning our attention into mitochondrial functionality, elevated mitochondrial respiration and mass have been considered as an adaptive mechanism in response to ER stress (Knupp *et al.*, 2019; Bravo *et al.*, 2011). However, unresolved ER stress and consequently chronic ER stress pathway activation, has been associated with impaired

mitochondrial function and cell death (Bankapalli *et al.*, 2020). It was interesting to see in this study that tunicamycin-induced ER stress activation led to mitochondrial abnormalities that seemed to be mediated by ROS generation; this is a crucial element in the light of novel developments for targeted therapeutic approaches in myositis.

Being unable to stimulate glycolysis, myoblasts exposed to prolonged tunicamycin treatment showed enhanced basal mitochondrial respiration, a previously seen mechanism upon ER stress (Jackisch *et al.*, 2016), explained by the potential need of the cells to compensate for increased ATP demand (Hill *et al.*, 2012). Mitochondrial dysfunction though was clearly evident as tunicamycin evoked reduced ATP-linked respiration, reserve capacity, RCR, and phosphorylating respiration. Those observations were in agreement with a previous study that demonstrated diminished total cellular levels of ATP upon sustained ER stress (tunicamycin, 0.5 µg/mL over 20 hours), compared to early ER stress (tunicamycin, 0.5 µg/mL over 1–4 hours) or control cells (Bravo *et al.*, 2011). The observed inhibitory effects of EUK-134 on tunicamycin-induced changes in mitochondrial respiration provide a rationale for considering ROS generation as an important factor in this aspect. In addition, it has been suggested that increased in mitochondrial respiration under basal conditions can be related with other sources of oxygen consumption, besides electron transport chain, such as ROS generation (Hill *et al.*, 2012). Indeed, non-mitochondrial OCR was found to be upregulated following tunicamycin treatment. This hypothesis was further supported by the induction of oxidative stress markers observed following ER stress activation. Those included elevated total cellular ROS generation, including superoxide levels, by tunicamycin, which were mitigated in presence of EUK-134. It should be noted though that mitochondrial superoxide assessment seemed to be remained unaltered in this model. According to the literature, NO generation is able to compete with superoxide dismutase and decrease superoxide availability in the model, leading to peroxynitrite production (Pearson *et al.*, 2014; Pearson, McArdle and Jackson, 2015) – an observation that can explain no noticeable effects in mitochondria superoxide in this case. Furthermore, Guha *et al.* (2017) reported that aberrant ER stress activation in prostate cancer cells, as induced by tunicamycin treatment, was associated with upregulated endothelial NOS and NO generation. The effects of EUK-134 on nitrosative stress and proximal tubular cell injury

have also been examined, showing EUK-134-associated reduction in NO levels (Chatterjee *et al.*, 2004).

Proton leak is an additional indicator of mitochondrial dysfunction, as seen in this ER stress model, and has been linked to alterations in mitochondrial membrane potential (Trnka, Elkalaf and Anděl, 2015). Considering the importance of normalising mitochondrial membrane potential to mitochondrial mass, ER stress activation in this model seemed to induce mitochondrial membrane depolarisation (Perry *et al.*, 2005), alongside with elevated mitochondrial mass, suggesting related alterations in mitochondrial biogenesis. Particularly, stimulated mitochondrial biogenesis was indicative upon ER stress in this study, a mechanism that is speculated to be induced to compensate to increased ATP demands, an effect that was not seen in presence of EUK-134. In agreement with this finding, Wredenberg *et al.* (2002) reported respiratory chain deficit leading to elevated mitochondrial mass in mitochondrial myopathy mice.

Previously seen association between ER UPR and mitochondrial UPR activation (Xiao *et al.*, 2020; Iqbal and Hood, 2014) was in consistent with this study's finding of mRNA *HSP60* and *HSPA9* mitochondrial UPR markers upregulation. Linking mitochondrial biogenesis and mitochondrial UPR, evidence exists in relation to HSP60-mediated mitochondrial biogenesis stimulation in skeletal muscle (Jadiya and Tomar, 2020). This has been specifically proved by the HSP60-induced increases in proliferator-activated receptor gamma coactivator 1 α 1 expression, which is a central regulator of mitochondrial biogenesis (Marino Gammazza *et al.*, 2018; Barone *et al.*, 2016). It should not be ignored though that the observed changes in *HSP60* and *HSPA9* mRNA expression might be induced as a response to the rise in mitochondrial mass upon ER stress in order to meet increased demands of mitochondrial protein translocation, folding, and refolding (Jadiya and Tomar, 2020).

The impact of oxidative stress has been widely studied in relation to mitochondrial structure preservation. Hydrogen peroxide treatment in C2C12 myocytes has shown to induce mitochondrial fragmentation, an effect that was preceded by mitochondrial depolarisation and deficient reserve capacity (Fan, Hussein and Brooks, 2010), which are also seen in this study's model. Other studies have particularly stated that mitochondria tend to elongate and fuse prior to mitochondrial fission processes, a response that seems

to be adaptive to cellular insults, such as ER stress and ROS generation (Bankapalli *et al.*, 2020; Lebeau *et al.*, 2018). Additionally, mitochondrial network morphology has been an important regulator of cell fate upon autophagy, with cell viability being maintained by elongated mitochondria (Gomes, Di Benedetto and Scorrano, 2011). Similarly, in this study, mitochondrial fusion processes, as described by elongated and interconnected mitochondria, were retained following tunicamycin exposure and were partially mitigated by EUK-134. The observed mitochondrial fusion events can also be positively correlated with elevated mitochondrial mass, as previously explained by Seo *et al.*, 2010. It should be noted though that protein expression levels of the fusion mediator MFN2 were unaltered, pointing out the following hypotheses: (a) mitochondrial number, interconnectivity, and elongation might be MFN1-dependent, meaning that outer mitochondrial membrane fusion takes place mainly via homotypic MFN1-MFN1 manner, or (b) other MFN2-required processes are activated, such as Parkin-mediated mitophagy (Shirihai, Song and Dorn, 2015). Overall, data recommend that maladaptive ER stress conditions evoke ROS-mediated mitochondrial fusion stimulation, which seems to be MFN2-independent, as well as accumulation of dysfunctional mitochondria.

Based on the observation of mitochondrial dysfunction preceding mitochondrial fragmentation, the propensity of mitochondria to fragment, as highlighted by Westrate *et al.* (2014), was examined under the indicated ER stress conditions. In agreement with this, tunicamycin-induced ER stress showed increased mitochondrial perimeter and mitochondrial area that are the two parameters that have been characterised to be predictive of future mitochondrial fragmentation (Westrate *et al.*, 2014). Additionally, mRNA expression of fission markers *FIS1* and *DRP1* was elevated following tunicamycin treatments. Further highlighting the role of ROS in this aspect, those effects were prevented by EUK-134 treatment.

Shedding further light on the ER stress-associated alterations in mitochondrial function, biodynamics, and biogenesis, this study also shows the protective effects of the antioxidant EUK-134 under these instances. Collectively, this study offers a rationale for considering ROS generation quenching in ER stress-related diseases, including myositis.

CHAPTER 4:

Mitochondrial function and ROS generation in an *in vitro* model of MHC-I overexpressing cells in presence or absence of Type I interferons

4.1 Introduction

The idiopathic inflammatory myopathies (IIMs) are a group of rare acquired inflammatory diseases of the muscle, collectively known as myositis. Patients with myositis share some common clinical features, including underlying muscle weakness, increased circulating muscle enzymes (e.g., creatine kinase), alongside with the presence of inflammatory infiltration of CD4⁺/CD8⁺ T-cells and B-cells into muscle fibres, muscle-specific and -associated autoantibodies, IFNs upregulation in muscle, and overexpression of MHC-I molecules upon the surface of muscle fibres (Carstens and Schmidt, 2014).

A recent study demonstrated that IFN signature facilitates stratification of IIMs, with type I IFN α and IFN β being a hallmark of dermatomyositis, allowing it to be distinguished from other IIMs such as inclusion body myositis (Rigolet *et al.*, 2019). Furthermore, type I IFN treatment of human peripheral blood mononuclear cells and skeletal muscle cells induced the expression of genes that were largely identical to the profile observed in patients with dermatomyositis (Arshanapalli *et al.*, 2015). IFN-inducible genes were also present in the blood samples of patients with dermatomyositis and polymyositis, which were correlated with disease activity. Specifically, dermatomyositis samples presented higher levels of type I IFN-inducible genes compared to polymyositis, while none were found in inclusion body myositis (Walsh *et al.*, 2007).

The distinct type I IFN signature in dermatomyositis and to a lesser degree in polymyositis, as well as the predominant overexpression of MHC-I have turned the attention on their downstream pathology-associated mechanisms. Sustained up-regulation of MHC-I in muscle has displayed a positive correlation with endoplasmic reticulum stress activation (Fréret *et al.*, 2013), which has been evident in patients with myositis (Nagaraju *et al.*, 2005). Perifascicular atrophy is a histological hallmark of dermatomyositis, studies have shown mitochondrial abnormalities are predominantly localised to these fibres undergoing atrophy (Alhatou *et al.*, 2004), while a recent study highlighted the involvement of mitochondrial damage, by the mitochondria-localised pro-apoptotic harakiri protein, in myofiber death and muscle weakness in individuals with dermatomyositis and polymyositis (Boehler *et al.*, 2019). A further study showed decreased expression of genes associated with mitochondrial biogenesis and those encoding proteins of the electron transport chain complexes, as well as reduced mitochondrial respiration and

increased ROS generation in dermatomyositis muscle fibres, as well as in muscle fibres from a murine experimental autoimmune model of myositis. Furthermore, they provided evidence of type I IFN score being correlated with mitochondrial respiratory deficiency in DM muscle, while IFN- β treatment of human myotubes showed to decrease mitochondrial respiration in a ROS-dependent manner (Meyer *et al.*, 2017).

Both type I IFN signature and MHC-I have been suggested to play an important role in dermatomyositis and polymyositis. Despite the evidences of mitochondrial abnormalities in myositis, to our knowledge, the role of MHC-I overexpression on mitochondrial function remains to be revealed, while little is known about the distinct effects of IFN α and IFN β in this context. Herein, we introduce an *in vitro* MHC-I human skeletal muscle model that overexpresses HLA class I (the so-called MHC-I system in humans) (Cruz-Tapias *et al.*, 2013). The present study brings insight not only into the role of MHC-I overexpression on mitochondrial functionality, but also presents the distinct effects of type I IFN α/β in presence or absence of MHC-I overexpression. MHC-I overexpression act synergistically in causing mitochondrial respiratory defects and in parallel present a segregated effect on reactive oxygen and nitrogen species.

4.1.2 Aims of this chapter

1. Establish an *in vitro* model of MHC-I overexpression in human skeletal muscle cells.
2. Characterise mitochondrial function and oxidative stress upon MHC-I overexpression, as well as upon combinational treatment with type I IFNs.
3. Characterise the distinct effects of type I IFNs on mitochondrial function and oxidative stress.

4.2 Methods

4.2.1 Cell culture

Immortalised human skeletal muscle cells were grown under standard cell culture conditions (37°C, 5% CO₂) as described in **Section 2.1.1**.

4.2.2 Plasmid preparation

The DNA from Psv2-neo empty vector plasmid in *Escherichia coli* and Psv2-neo plasmid containing HLA-A2/K^b were amplified by creating single colonies of the *Escherichia coli* in agar plates and incubating them in Lennox L Broth as described in **Section 2.2.1**. The pDNA were stored as glycerol stocks and purified using QIAprep spin miniprep kit. The concentration was determined before use and only pDNA with 260/280 > 1.80 and 260/230 > 2.0 was used.

4.2.3 Transfection and treatments

Human skeletal muscle myoblasts were seeded 24 hours before transfection to achieve approximately 70–90% confluence. At the time of transfection, the growth media was replaced with fresh growth medium described in **Section 2.1.5**. Cells were initially incubated with the transIT-X2: plasmid (1 µg/µl) complex at different ratio and incubation time to determine optimal transfection conditions. Two MHC-I overexpression plasmids and their relevant empty vectors were investigated for transfection conditions: (1) EGFP-tagged HLA expression plasmid and EGFP-tagged control plasmid, and (2) HLA-A2/K^b expression plasmid and pSV2-neo control plasmid. Following transfection optimisation, cells were transfected at 2:1 transIT-X2: plasmid ratio using HLA-A2/K^b plasmid and its empty vector, prepared in Opti-MEM for 18 hours. Type I IFNα or IFNβ (100 ng/mL) were also added to the culture media at the same time of transfection, as described in **Section 2.1.4**.

4.2.4 Assessment of transfection efficiency by immunostaining

Transfection efficiency was demonstrated by immunostaining. Human skeletal muscle myoblasts were fixed in 4% paraformaldehyde and permeabilised using 0.5% Triton X-100 as described in **Section 2.5.2**. Cells washed in DPBS were blocked using 3% goat serum supplemented with 0.05% Tween-20 for 1 hour at room temperature. Washed cells were

incubated with anti-HLA class I antibody at 4°C overnight and stained with goat anti-mouse IgG (H+L) Alexa Fluor 488 and 4',6'-diamidino-2-phenylindole dihydrochloride for 1 hour at room temperature protected from ambient light. Cells maintained in DPBS were imaged using a LEICA DMI6000 B inverted microscope.

4.2.5 Assessment of cellular respiration using Seahorse Extracellular Flux Analyser

Mitochondrial function and glycolytic activity were measured with an XFp Extracellular Flux Analyser. Human skeletal muscle cells were seeded in an 8-well XFp plate at a density of 7×10^3 cells/well in GM. After overnight incubation, cells were transfected with the HLA-A2/K^b overexpression vector or empty vector in the presence or absence of type I IFN α or IFN β , as described in **Section 2.1.4**. Real-time oxygen OCR and ECAR, as a measure of mitochondrial respiration and basal glycolysis, respectively (Dott *et al.*, 2014), were assessed using the Seahorse XFp Mito Stress Test as described in Section 2X. OCR and ECAR, normalised to total protein concentration using the Pierce™ BCA Protein Assay as described in **Section 2.3.1**.

4.2.6 Assessment of mitochondrial membrane potential and mass

Human skeletal muscle myoblasts were seeded at 8×10^3 cells/well in a black-sided, clear-bottom microplate (96 wells), cultured in growth media, and transfected and treated as described above. JC-1 fluorophore, MitoTracker Red CMXRos and TMRM were used to assess mitochondrial membrane potential ($\Delta\Psi_m$) as described in **Section 2.7**.

4.2.7 Measurement of RONS

To quantify mitochondrial superoxide and hydroxyl radical generation, myoblasts transfected with HLA-A2/K^b or empty vector +/- type I IFNs were washed with DPBS and incubated with MitoSOX™ Red mitochondrial superoxide indicator (5 μ M, 30 minutes, 37°C) or OH580 probe, mitochondrial hydroxyl radical indicator (1 hour, 37°C) as described in **Section 2.6**. Following incubation, cells were washed with DPBS, maintained in assay medium, and endpoint fluorescence was measured with the following excitation and emission wavelengths: MitoSOX™ Red, 360/40 and 590/35 nm; and OH580 probe, 530/25 and 590/35 nm, respectively. Measurements were normalised to total protein content as described above. To assess intracellular NO generation, DAF-

FM-DA (10 μ M) was added to the cells in the presence of transfection solution +/- type I IFNs. Following 30 minutes incubation at 37°C, cells were washed with DPBS, maintained in GM +/- type I IFNs, and endpoint fluorescence was measured at 485/20 nm excitation and 528/20 nm emission. Amplex[®] Red Hydrogen Peroxide/Peroxidase assay (Invitrogen, UK) was used to measure H₂O₂ released from cells according to the manufacturer's instructions. Briefly, cell culture media and standard curve samples of known H₂O₂ concentrations were incubated with the Amplex[®] Red reagent (100 μ M)/Horseradish peroxidase (0.2 U/mL) solution) at room temperature for 30 minutes and endpoint fluorescence was measured at 530/25 nm excitation and 590/35 nm emission.

4.2.8 Statistical analysis

Statistical analysis was performed with GraphPad Prism version 8. Data were assessed for normality of distribution using Shapiro-wilk test. Normally distributed data were analysed using one-way ANOVA followed by Tukey's test, and non-normally distributed data using Dunn's test. A *p*-value ≤ 0.05 was considered to be statistically significant. In all graphs, empty vector is abbreviated as EV, while HLA corresponds to HLA-A2/K^b transfected myoblasts.

4.3 Results

4.3.1 Transfection optimisation

When transfection technique is used to investigate the effects of a target protein, it is required that transfection efficiency is optimised to establish the most effective and sufficient delivery of pDNA expressing the target protein into cells. A common method for assessing transfection efficiency is using fluorescent proteins, such as green fluorescence protein (GFP) that are co-expressed with a target protein. Following transfection, transfected cells can be determined by quantifying GFP-positive cells.

In this study, an HLA-A enhanced GFP (EGFP)-tagged plasmid was initially used at a range of transfection conditions, including different time points, transIT-X2:pDNA ratio, and pDNA concentration, and transfection efficiency was determined by visualising EGFP-positive cells under a fluorescent microscope. Short-term transfection of 4 and 6 hours incubation with transIT-X2: HLA-A EGFP-tagged pDNA ratio of 2:1 and 3:1 showed no EGFP-positive cells (**Figure 4.1**). Long-term transfection of 22 and 24 hours at 2:1 and 3:1 showed a small amount of EGFP-positive cells that was considered insufficient to be used for future experiments (**Figure 4.1**).

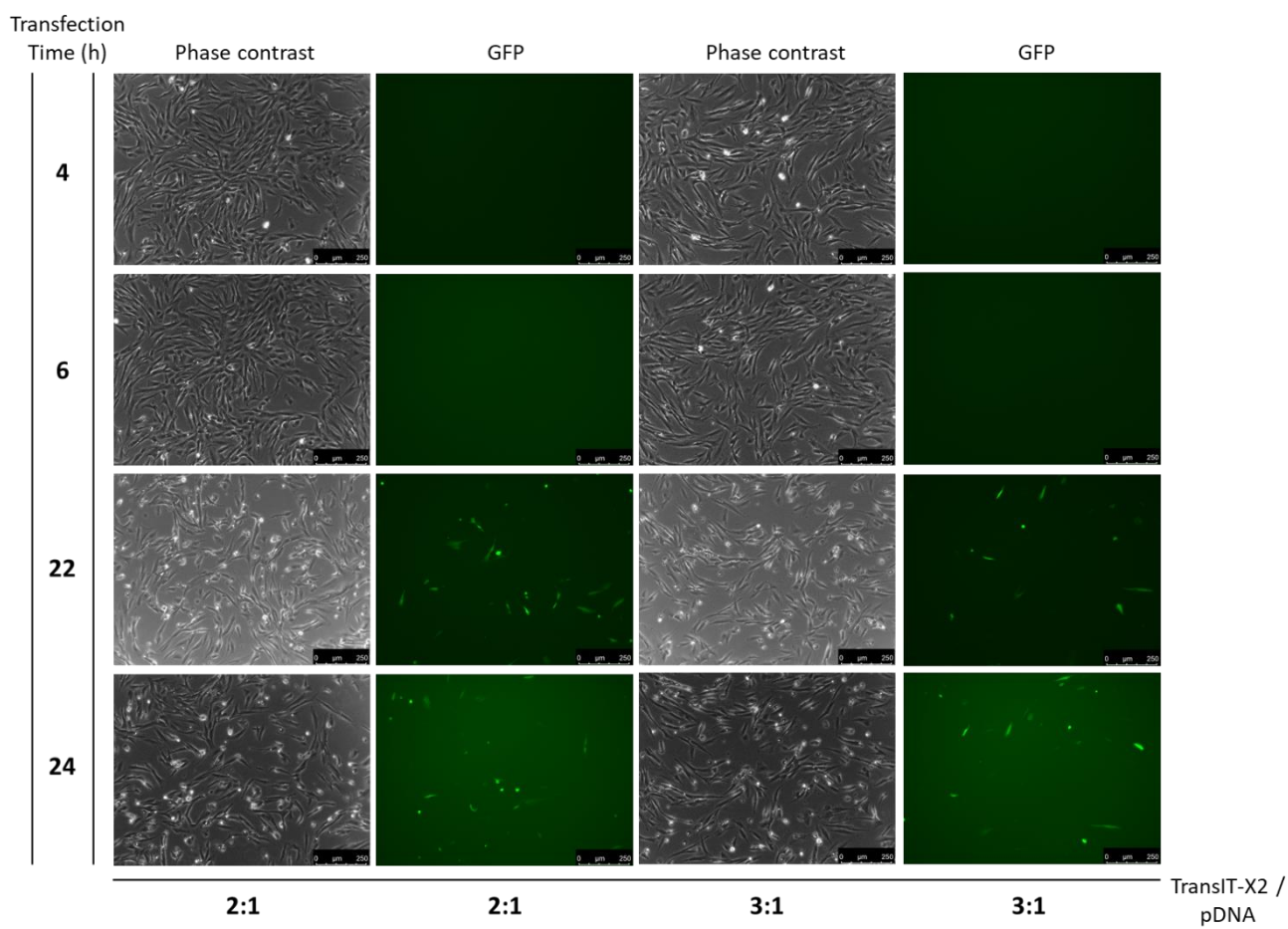


Figure 4.1 Transfection optimisation using HLA-A EGFP-tagged plasmid. Representative images of EGFP-positive cells transfected for 4, 6, 22, and 24 hours at a transIT-X2:pDNA (1 $\mu\text{g}/\mu\text{L}$) ratio 2:1 and 3:1. Images captured at 10 \times magnification. Scale bar = 250 μm

In an attempt to improve transfection efficiency, increased pDNA concentration (2 $\mu\text{g}/\mu\text{L}$) at 2:1 or 3:1 ratio transfected for 22 or 24 hours (**Figure 4.2**), as well as further 24 hour-incubation with fresh culture media following 24 hour-incubation in transfection media (**Figure 4.3**), were examined. However, none of those conditions provided higher transfection efficiency; instead, lower or similar amount of GFP-positive cells was seen (**Figure 4.2 and 4.3**). Increased transIT-X2:pDNA ratio to 4:1 or 5:1, exposed to cells for 22 or 24 hours was also examined (**Figure 4.4**). Similar to previous attempts, only a small amount of cells were GFP-positive with transIT-X2 cytotoxicity being noticeable, as well (**Figure 4.4**). This observation was also seen when having a closer look at the effect of transIT-X2 only, prepared in Opti-MEM at all the examined ratios, 2:1, 3:1, 4:1, and 5:1 in

the context of cell viability and morphology following long-term incubation, compared to Opti-MEM only, (Figure 4.5).

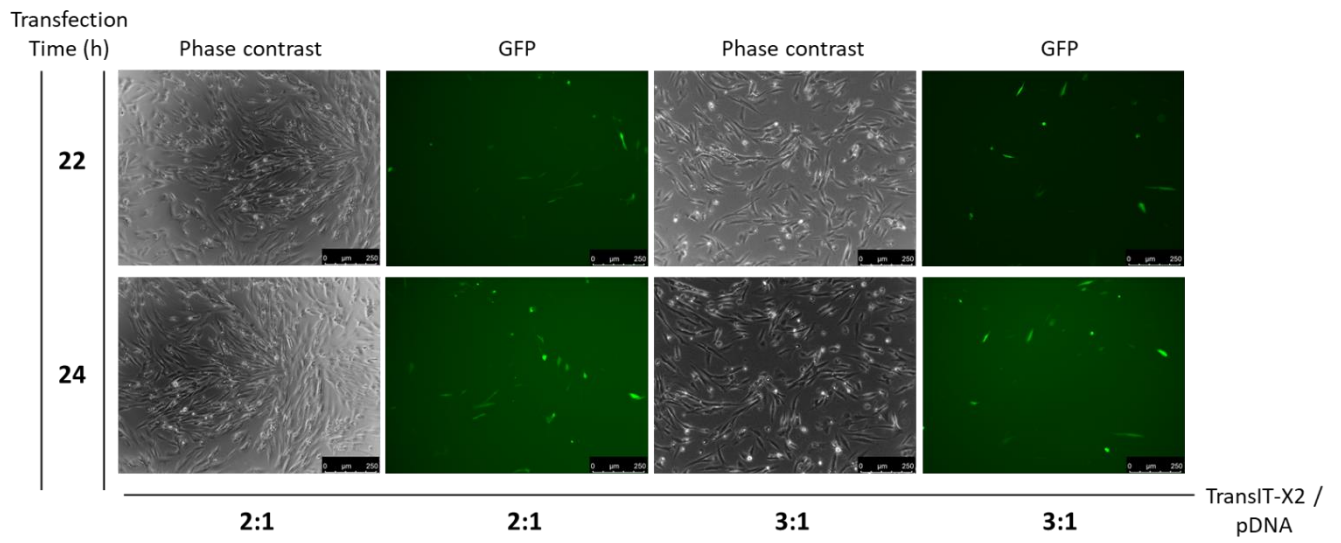


Figure 4.2 Transfection optimisation using (2 µg/µL) EGFP-tagged HLA vector. Representative images of EGFP-positive cells incubated for 22 and 24 hours at a transIT-X2:pDNA (2 µg/µL) ratio 2:1 and 3:1. Images captured at 10× magnification. Scale bar = 250 µm.

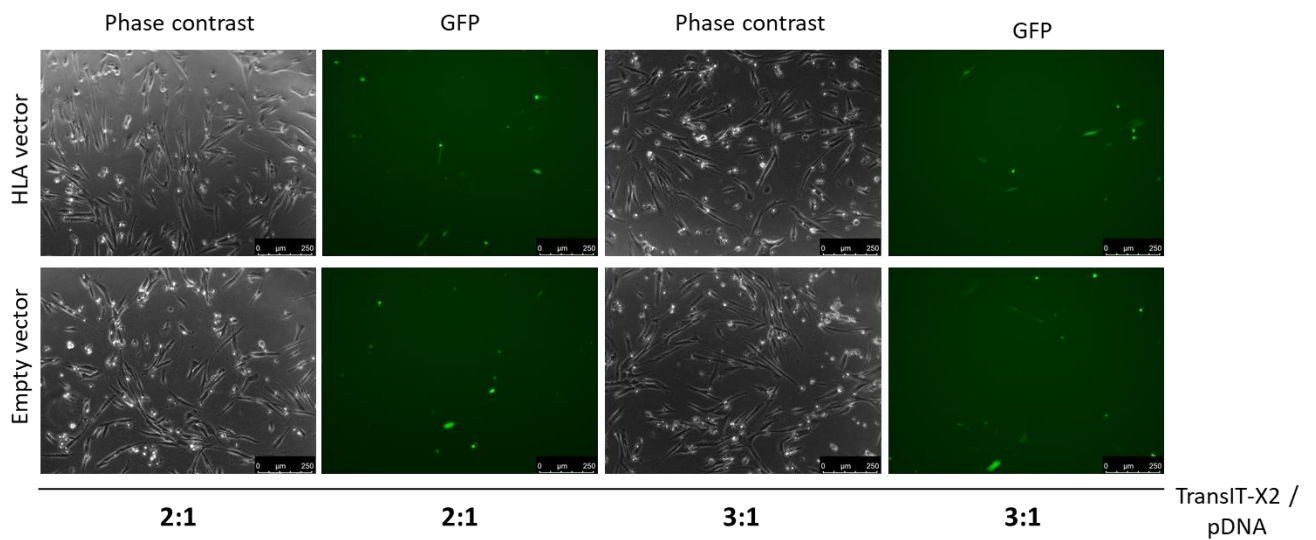


Figure 4.3 Transfection optimization using GFP-tagged HLA and empty vector. Representative images of EGFP-positive cells incubated for 24 hours post 24-hour

transfection at a transIT-X2:pDNA (1 $\mu\text{g}/\mu\text{L}$) ratio 2:1 and 3:1. Images captured at 10 \times magnification. Scale bar = 250 μm .

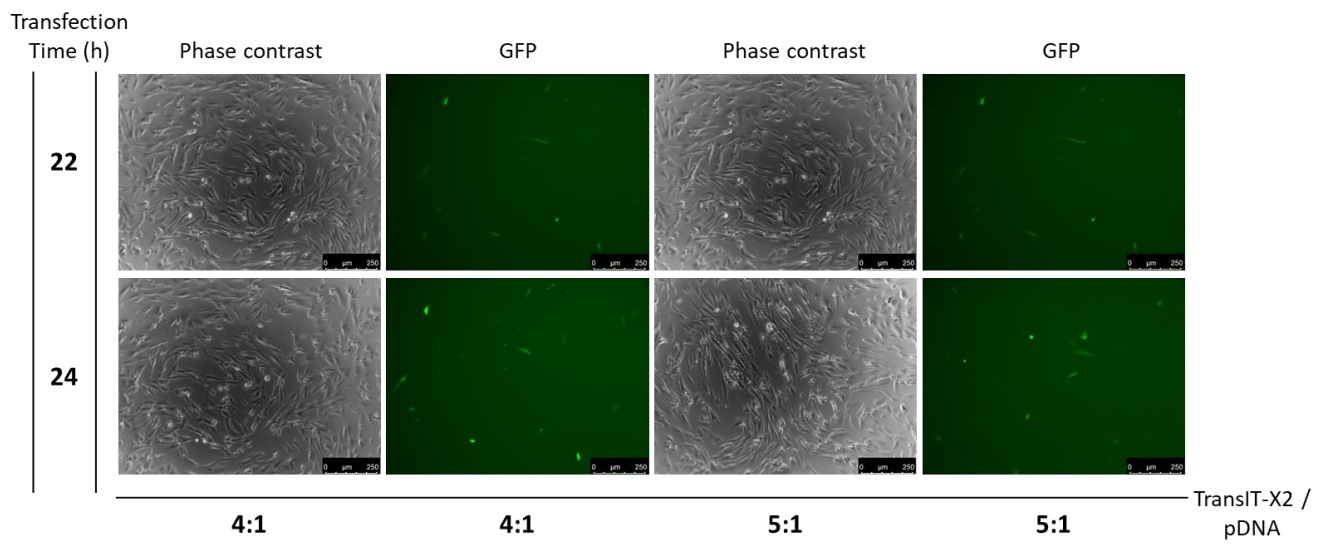


Figure 4.4 Transfection optimisation using HLA-A EGFP-tagged plasmid. Representative images of EGFP-positive cells transfected for 22 and 24 hours at a transIT-X2:pDNA ratio 4:1 and 5:1. Images captured at 10 \times magnification. Scale bar = 250 μm .

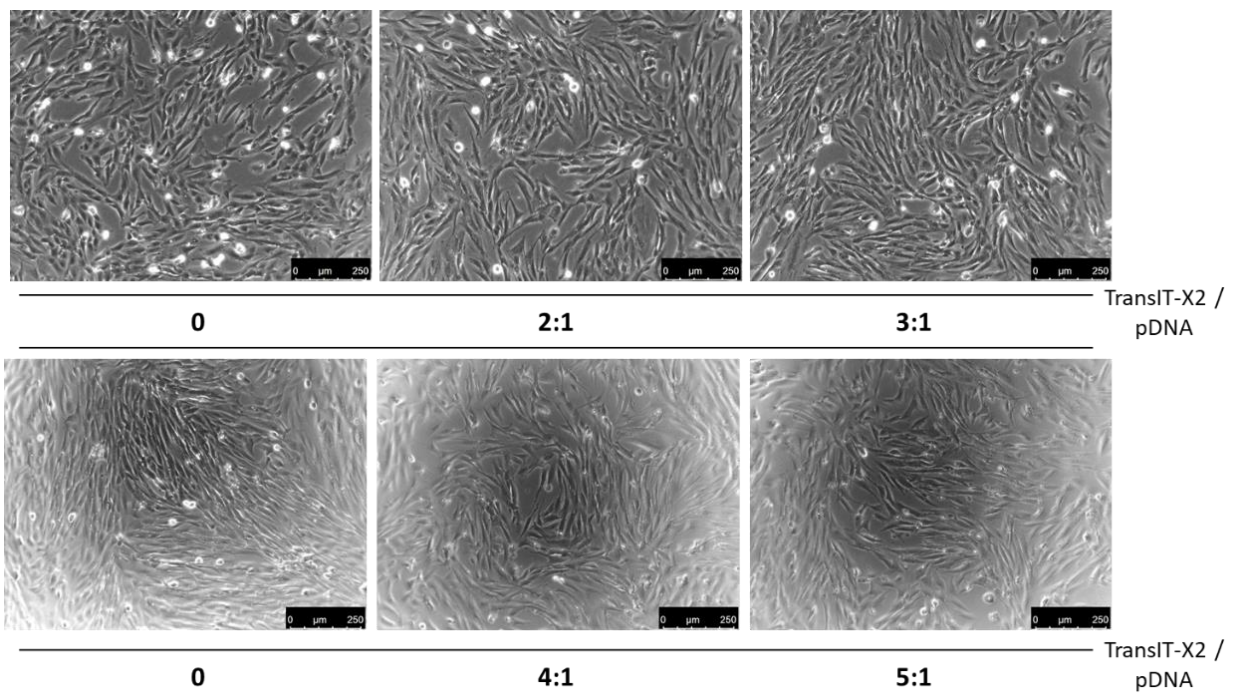


Figure 4.5 TransIT-X2 effects at different ratios in skeletal muscle cells. Representative images of skeletal muscle cells exposed to different ratios of TransIT-X2, in absence of

pDNA, or OptiMEM only, for 24 hours. Images captured at 10× magnification. Scale bar = 250 μm .

Failing to induce sufficient transfection efficiency, EGFP-tagged plasmids were not considered suitable to be used for further experiments. Instead, transfection with an HLA-A2/K^b plasmid or empty vector, in absence of fluorescent protein, was examined for transfection efficiency based on the expression of the target protein, visualised by immunostaining with an anti-HLA Class I antibody. According to manufacturer and other references, HLA-A2/K^b plasmid contains the genes encoding for α 1 and α 2 domains of HLA-A2.1 molecule, as well as the α 3 cytoplasmic and transmembrane domains of the K^b molecule (Terasawa *et al.*, 2002). A range of transfection conditions were examined again to optimise the overexpression of HLA Class I with transIT-X2. Final decision of optimal transfection conditions was made compared to empty vector, while all conditions were also examined against to a non-transfected control.

HLA overexpression was initially examined at transIT-X2:pDNA ratio of 2:1 and 3:1 following 6 hours incubation; higher transIT-X2:pDNA ratio were not used as they have been previously determined inappropriate. Based on phase contrast images, 3:1 ratio induced noticeable cell death and morphological changes, and therefore has been excluded from further transfections (**Figure 4.6**).

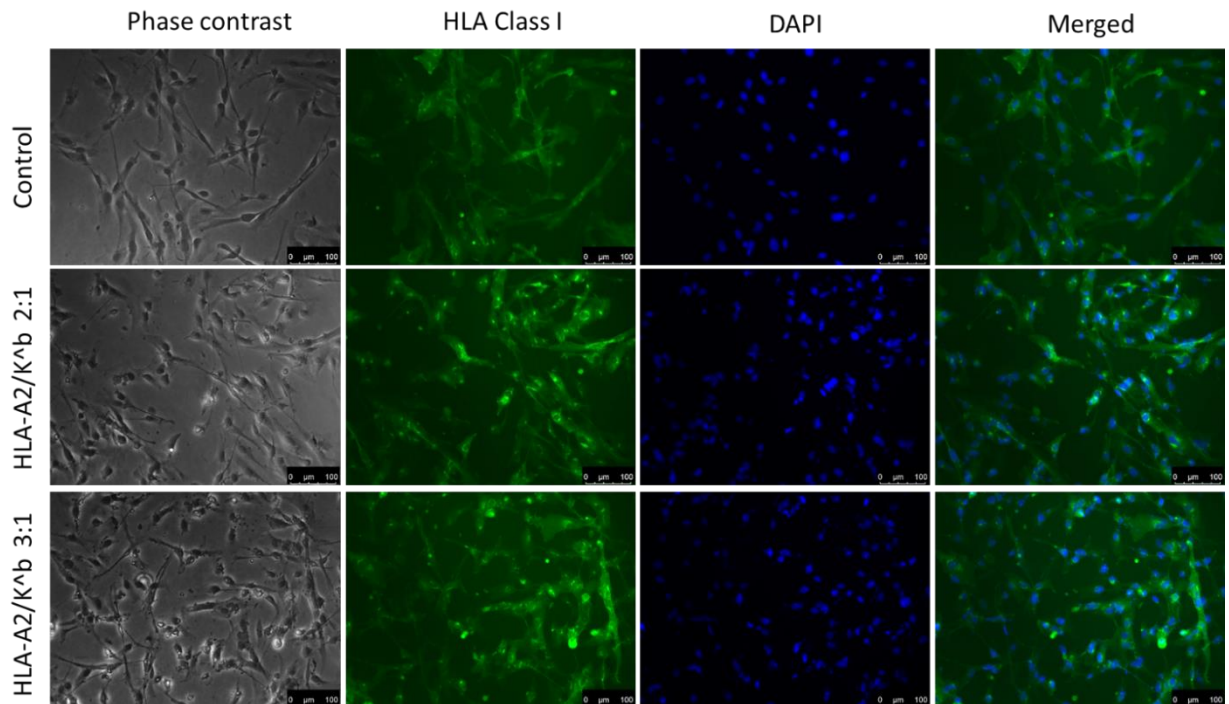


Figure 4.6 Expression of HLA class I following 6 hours of transfection. Representative images of human immortalised myoblast transfected with the transIT-X2:plasmid (EV or HLA-A2/K^b; 1 µg/µl) complex at 2:1 and 3:1 ratio for 6 hours. Transfected cells were stained with DAPI (blue) and anti-HLA class I (green). Images captured at 20× magnification. Scale bar = 100 µm.

Following examination at longer time points, 18 hours with a 2:1 transIT-X2:pDNA ratio was determined suitable for further experiments, since 24 hours incubation resulted in noticeable reduction of the cell number (**Figure 4.7**). To validate that expression of target protein was not induced by the transfection reagent, cells exposed to transIT-X2 solution only (2:1) for 18 hours were assessed for HLA class I fluorescence staining, as well. As **Figure 4.8** shows, transIT-X2-induced HLA class I was limited.

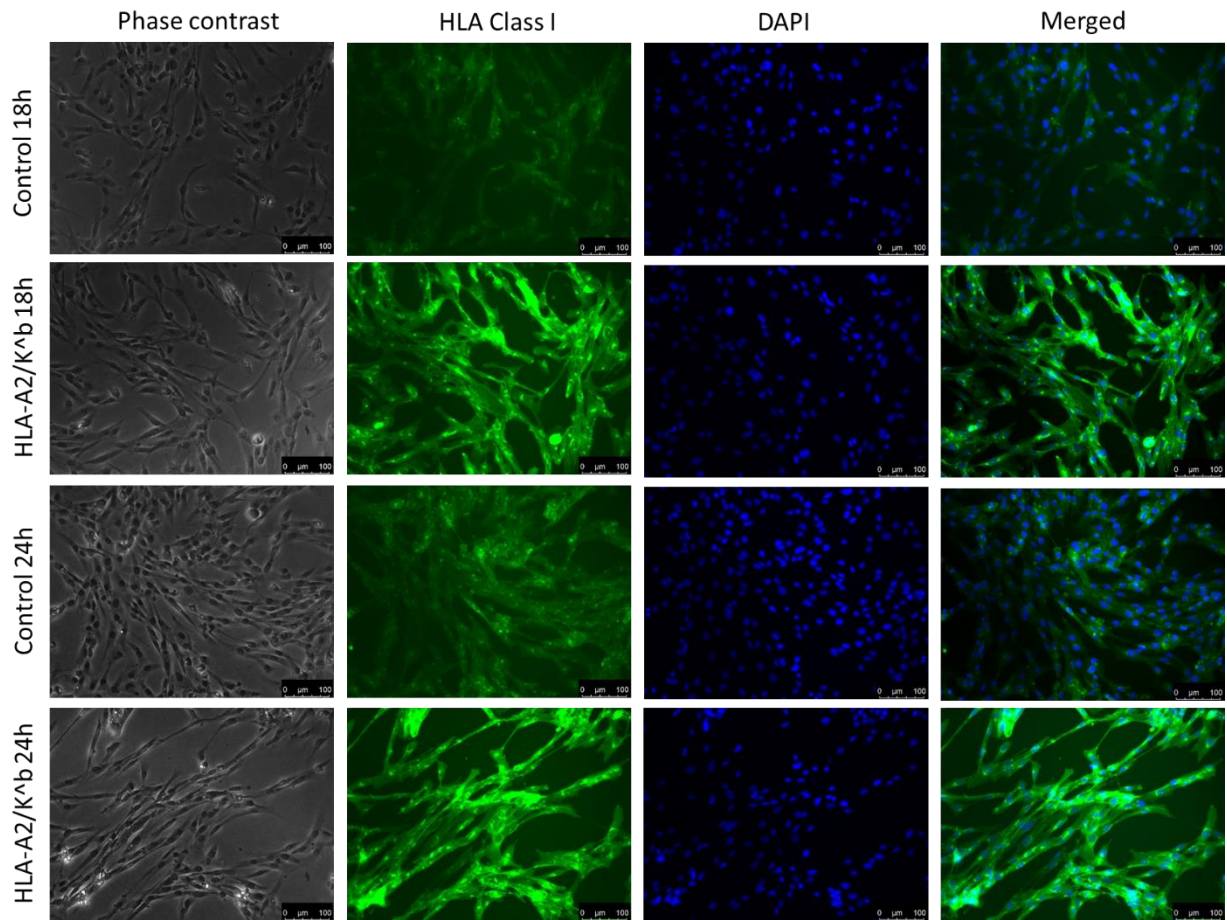


Figure 4.7 Expression of HLA class I following 18 and 24 hours of transfection. Representative images of human immortalised myoblast transfected with the transIT-X2: plasmid (EV or HLA-A2/K^b; 1 $\mu\text{g}/\mu\text{l}$) complex at 2:1 for 18 and 24 hours. Transfected cells were stained with DAPI (blue) and anti-HLA class I (green). Images captured at 20 \times magnification. Scale bar = 100 μm .

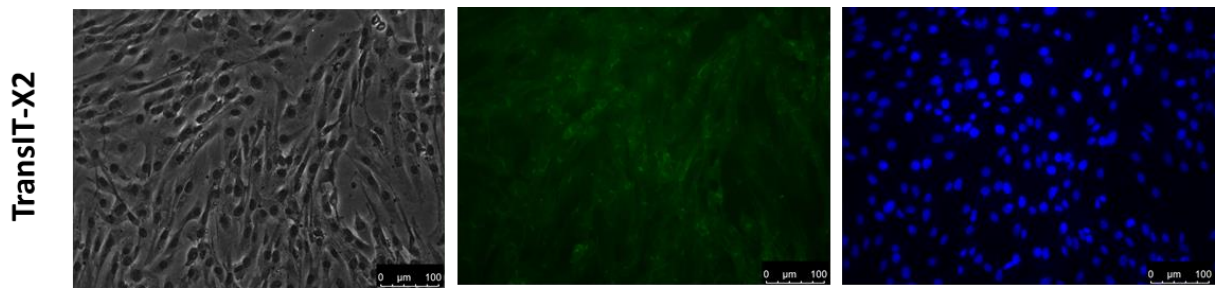


Figure 4.8 Expression of HLA class I by transIT-X2. Representative images of human immortalised myoblast exposed to transIT-X2: plasmid only (2:1) for 18 hours. Images captured at 20× magnification. Scale bar = 100 µm. Brightness was adjusted equally in each image to enhance visualisation.

4.3.2 MHC-I levels following HLA-A2/K^b vector transfection in presence or absence of type I IFNs

Fluorescence intensity levels of HLA class I normalised to nuclei number were determined following 18 hours transfection with the HLA-A2/K^b vector in presence or absence of 100 ng/mL type I IFNs. HLA-A2/K^b vector transfection resulted in significantly upregulated MHC-I expression compared to empty vector ($p < 0.001$) as described by changes in fluorescence intensity (A.U./nuclei). Interestingly, IFN α exposure in MHC-I overexpressing myoblasts induced significantly higher HLA fluorescence intensity levels, by 78.2%, compared to solely HLA-transfected myoblasts ($p < 0.001$), while IFN β exposure in MHC-I overexpressing myoblasts slightly increased fluorescence by 20.5%, compared with MHC-I expression alone (**Figure 4.9A and 4.9B**).

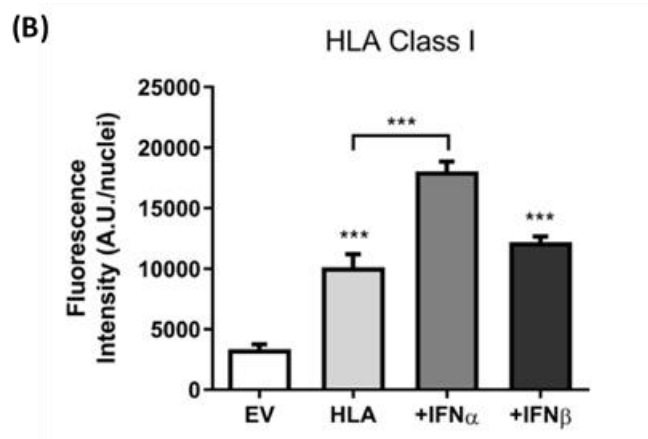
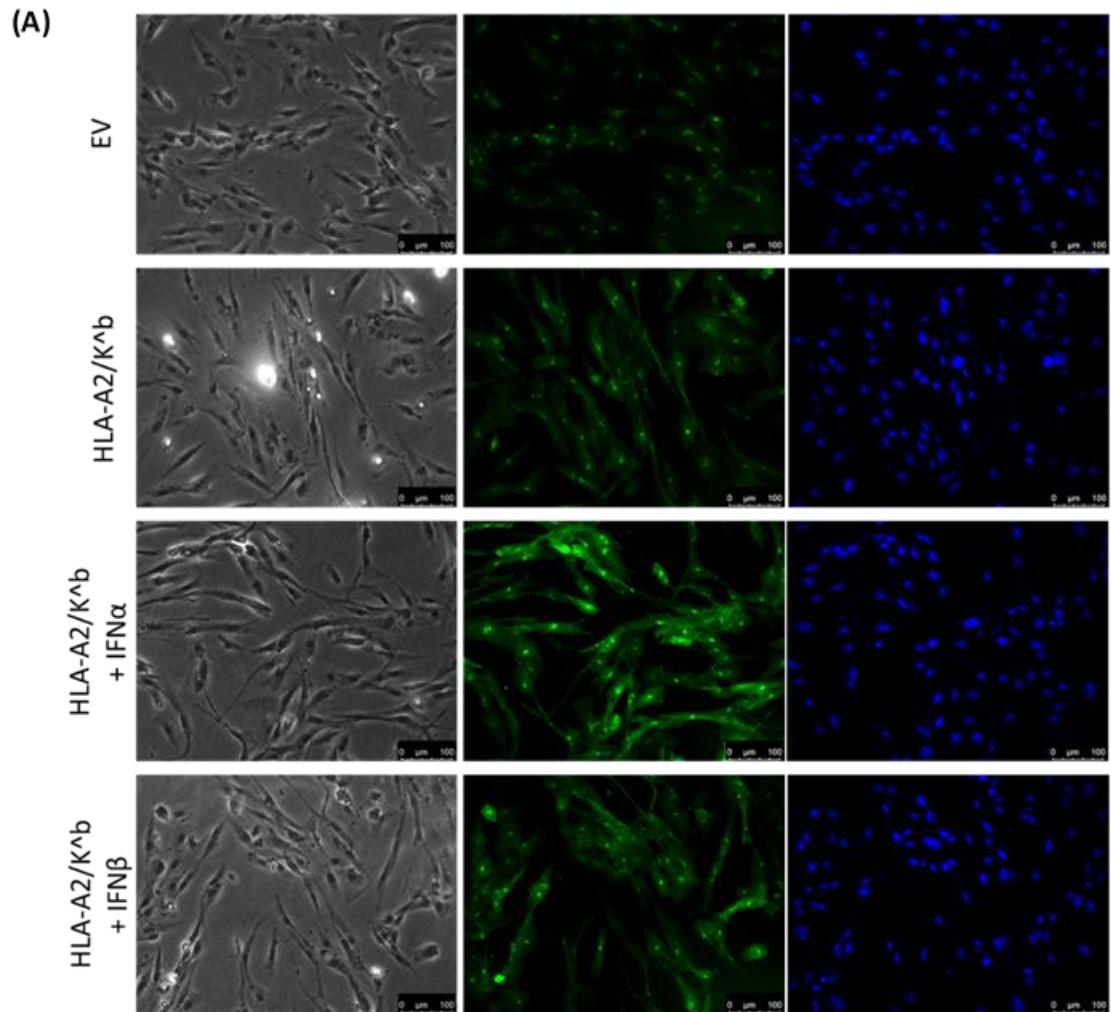
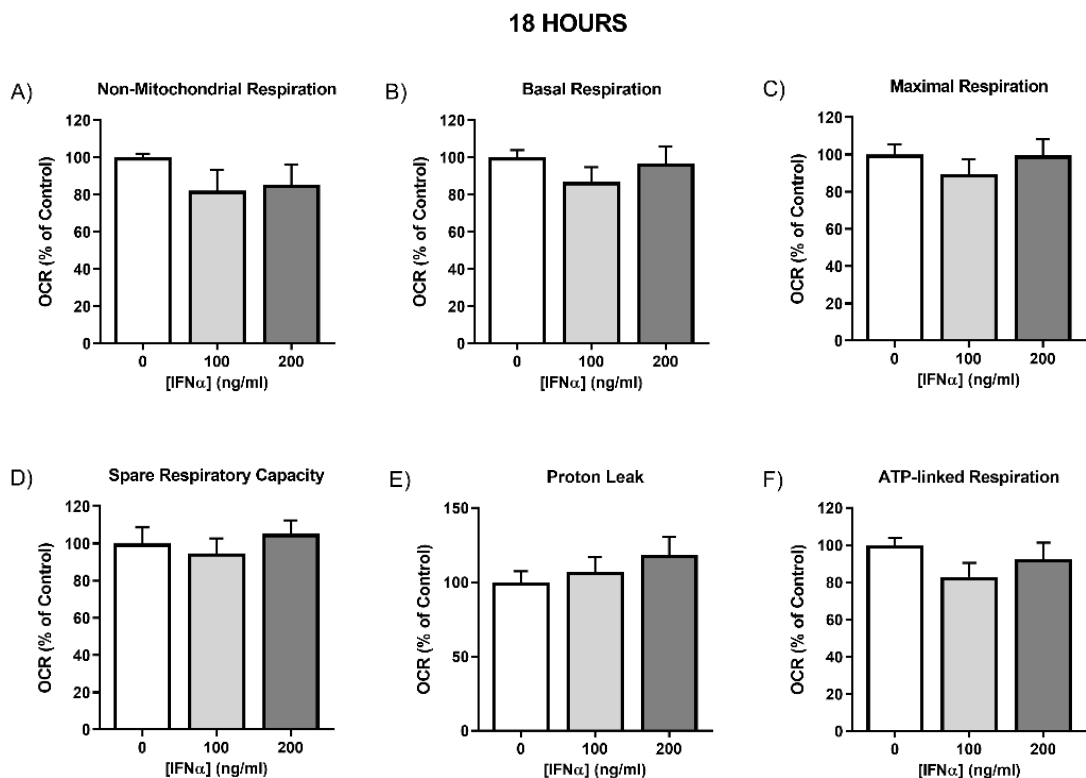


Figure 4.9 Expression of HLA class I following 18 hours of transfection in presence or absence of IFN α / β . (A) Representative images of human immortalised myoblast transfected with the transIT-X2: plasmid (EV or HLA-A2/K^b; 1 μ g/ μ l) complex at 2:1 for 18 in presence or absence of IFN α / β . Transfected cells were stained with DAPI (blue) and anti-HLA class I (green). Images captured at 20 \times magnification. Scale bar = 100 μ m. (B)

Quantification of HLA class I fluorescence intensity level normalised to nuclei number (DAPI). Data represent mean \pm S.E.M., *** $p < 0.001$ compared to control or as indicated.

4.3.3 Mitochondrial function in type I IFNs-treated myoblasts

The mitochondrial function of non-transfected myoblasts exposed to 100 ng/mL or 200 ng/mL IFN α or IFN β for 18 hours and 24 hours was evaluated using Seahorse extracellular flux analyzer. In non-transfected myoblasts, 18 hours exposure to 100 ng/mL or 200 ng/mL IFN α treatment did not induce any significant changes in mitochondrial function parameters, including spare respiratory capacity, basal, maximal, ATP-linked, and leak respiration, neither in non-mitochondrial respiration (**Figure 4.10A–F**). Mitochondrial bioenergetics remained unaffected following 24 hours treatment with 100 ng/mL IFN α , while higher IFN α concentration (200 ng/mL) significantly reduced oxygen consumed for basal and ATP-linked respiration only ($p \leq 0.05$), indicating the initiation of mild effects on mitochondrial function by longer exposure to IFN α (**Figure 4.10G–L**).



24 HOURS

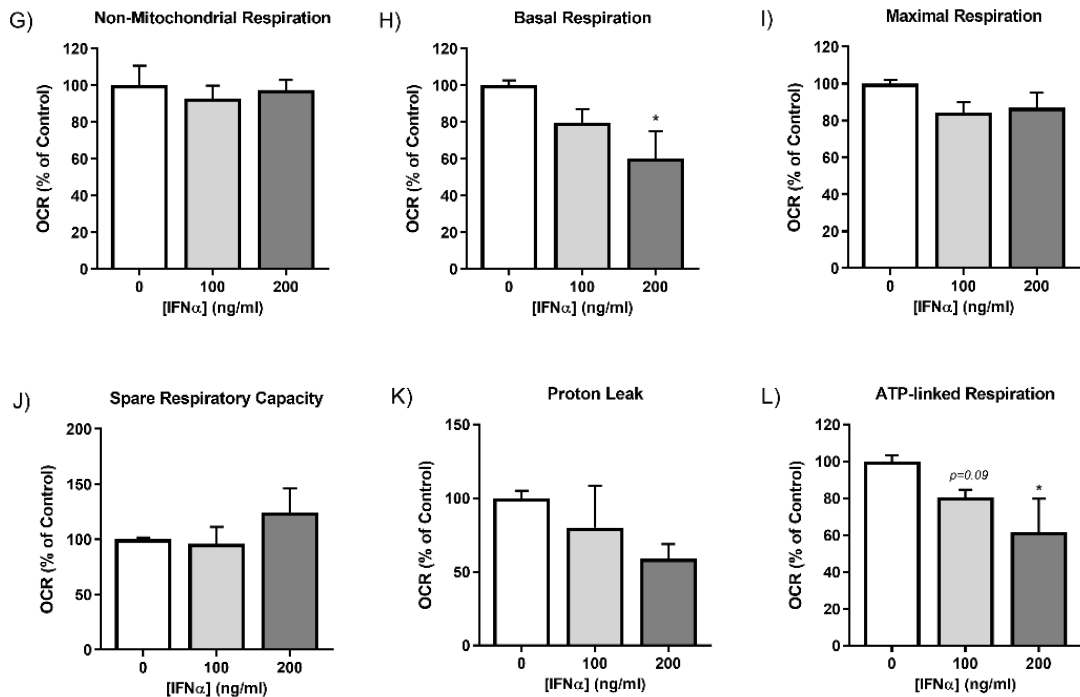
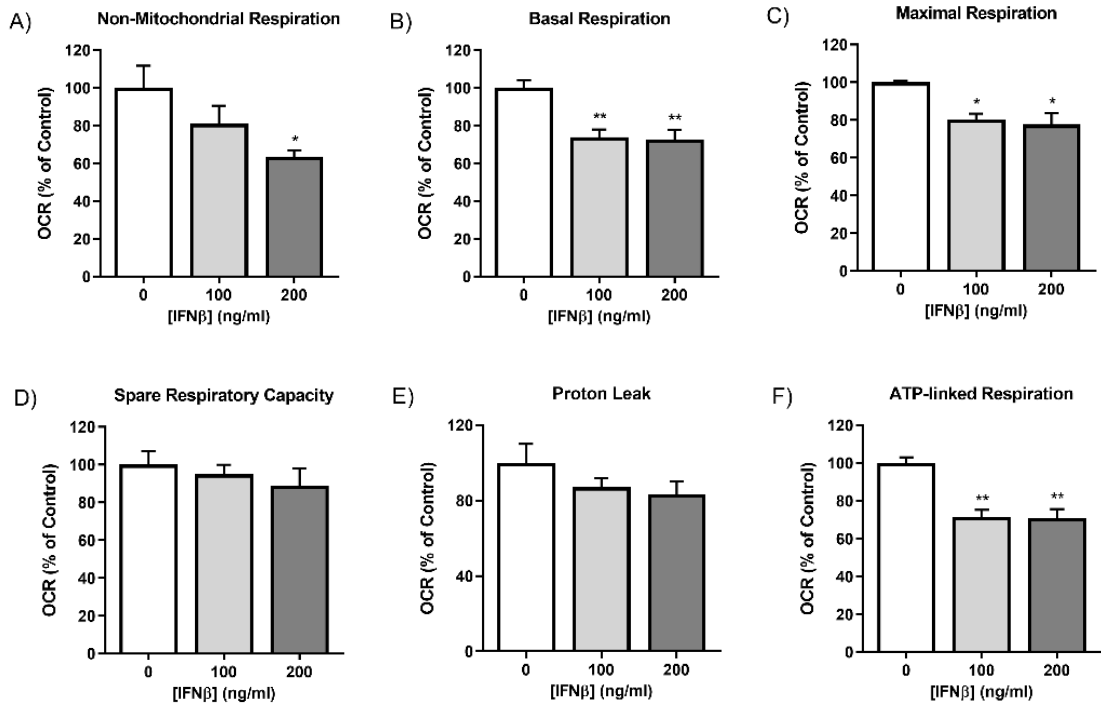


Figure 4.10. Mitochondrial function parameters of myoblasts treated with IFN α . Non-mitochondrial respiration, basal respiration, maximal respiration, spare respiratory capacity, proton leak, and ATP-linked respiration, normalised to protein content following 18 hours (A–F) and 24 hours (G–L) incubation with IFN α . Data represent mean \pm S.E.M. ($n=3$), * $p \leq 0.05$ compared to control.

In contrast to IFN α treatment, treatment of non-transfected myoblasts with both 100 ng/mL and 200 ng/mL of IFN β for 18 hours induced a significant reduction in basal, maximal and ATP-linked respiration, while defects in non-mitochondrial respiration were induced by 200 ng/mL IFN β only (Figure 4.11B–F). It should be noted though that 18 hours exposure to IFN β at any concentration did not induce any changes in spare respiratory capacity or leak respiration (Figure 4.11D and 4.11E). Interestingly, lower proton leak was sustained following 24 hours treatment with IFN β (Figure 4.11K), with no statistical changes being evident in other mitochondrial function parameter (Figure 4.11G–L).

18 HOURS



24 HOURS

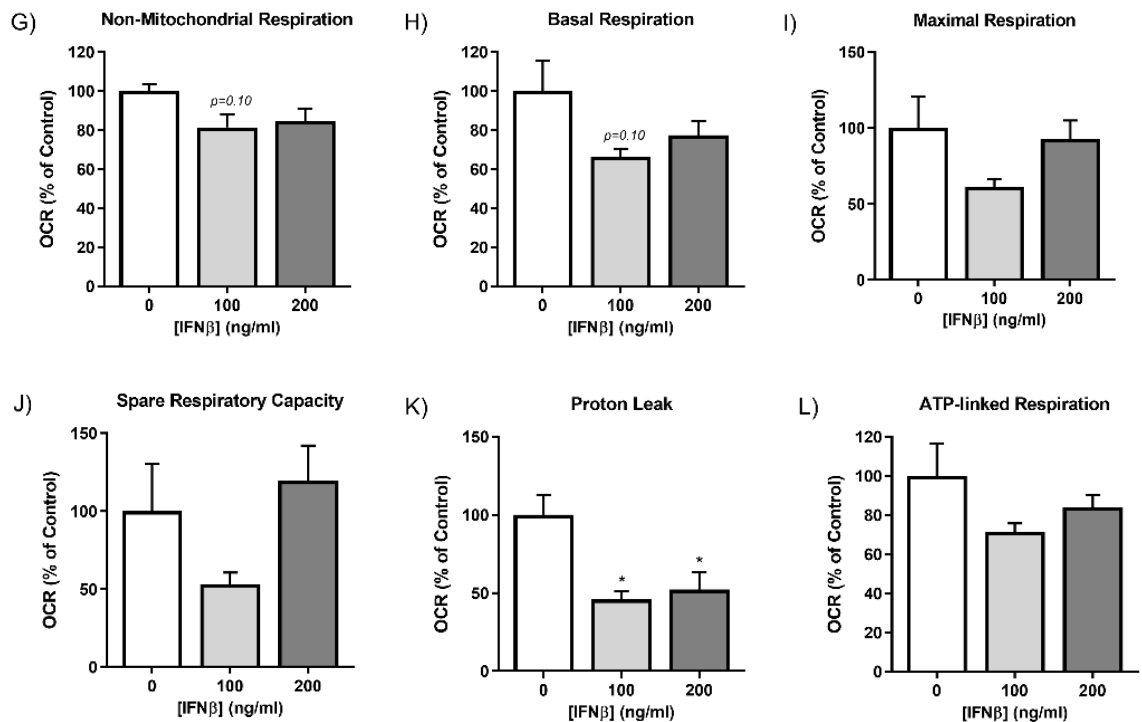
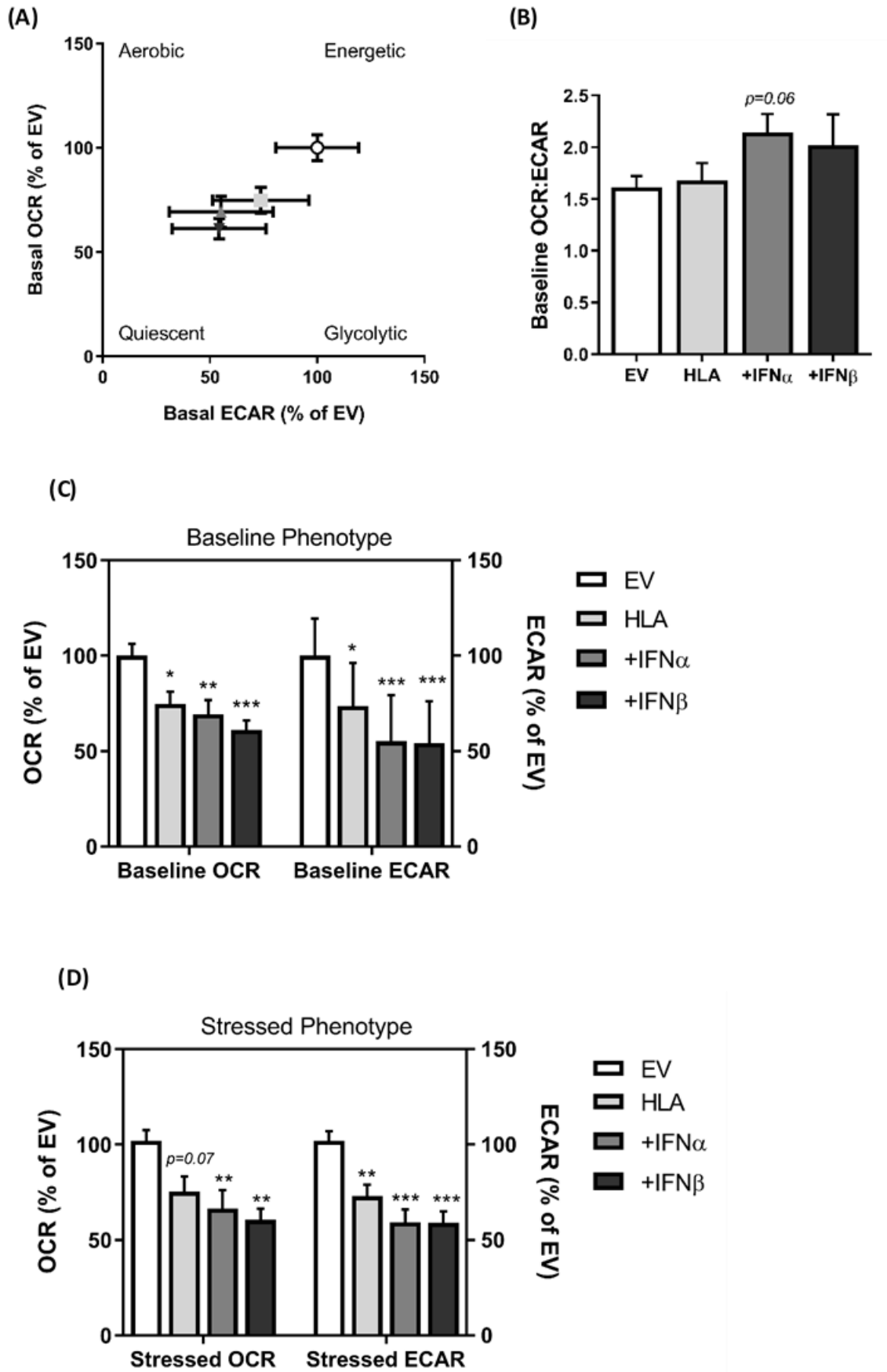


Figure 4.11. Mitochondrial function parameters of myoblasts treated with IFN α . Non-mitochondrial respiration, basal respiration, maximal respiration, spare respiratory

capacity, proton leak, and ATP-linked respiration, normalised to protein content following 18 hours (A–F) and 24 hours (G–L) incubation with IFN β . Data represent mean \pm S.E.M. ($n=3$), * $p \leq 0.05$, ** $p < 0.01$, compared to control.

4.3.4 Mitochondrial function following MHC-I overexpression in presence or absence of type I IFNs

Baseline OCR values derived from Seahorse extracellular flux analyzer were plotted against ECAR values to define the energy phenotype profile of MHC-I overexpressing cells in presence or absence of 100 ng/ml type I IFNs (IFN α and IFN β) following 18 hours of exposure (Figure 4.12A). Results showed that MHC-I overexpressing cells are plotted towards the quiescent state (Figure 4.12A). According to Figure 4.12B, showing increasing baseline OCR to ECAR ratio compared to control, especially in presence of type I IFNs, with IFN α reaching a p value of 0.06. This implies that transfected cells and specifically following type I IFNs exposure, seem to be more reliant on oxidative phosphorylation, while they are unable to utilise glycolytic flux as a compensatory machinery (Figure 4.12B). Reduced metabolic phenotypes were apparent in transfected cells, while they are unable to utilise glycolytic flux as a compensatory machinery in respect to both oxidative phosphorylation and glycolysis under both baseline and stressed conditions (Figure 4.12C and D). In particular, this reduction was exacerbated in presence of type I IFNs (Figure 4.12C and D). Interestingly, no significant effects were seen in their metabolic potential, whereas only a relative decrease in OCR was seen by IFN β exposure in MHC-I overexpressing cells compared to empty vector (Figure 4.12E).



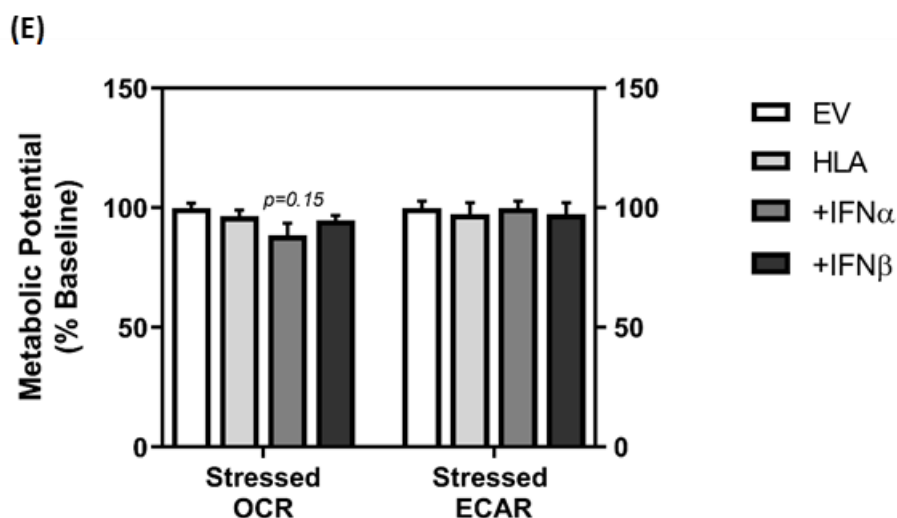


Figure 4.12 Energy phenotype of MHC-I overexpressing cells with or without type I IFNs treatment. (A) Bioenergetic profile expressed as OCR versus ECAR measured under basal conditions. Statistical analysis of (B) OCR and ECAR ratio, (C) OCR and ECAR baseline phenotype, (D) OCR and ECAR stressed phenotype, and (E) metabolic potential. Data were normalised to total protein content and are expressed as relative to empty vector. Data represent mean \pm S.E.M. ($n=3$), * $p\leq 0.05$, ** $p<0.01$, *** $p<0.001$ compared to empty vector.

Individual bioenergetic parameters (Figure 4.14) were calculated from the OCR trace, presented in Figure 4.13, following the sequential injection of oligomycin, FCCP, and rotenone/antimycin A mixture. MHC-I overexpressing myoblast showed reduced non-mitochondrial respiration that was statistically significant in presence of IFN β (Figure 4.14). Mitochondrial respiration was suppressed at both basal and maximal capacities by MHC-I overexpression, which was exacerbated in presence of IFN α or IFN β , with IFN β showing stronger effects (Figure 4.14). Decreased mitochondrial respiration was accompanied by significantly reduced ATP-linked respiration in MHC-I overexpressing myoblasts, with IFN β inducing the highest percentage of change, followed by IFN α (Figure 4.14). IFN β in MHC-I overexpressing myoblasts was also able to significantly decrease spare respiratory capacity (Figure 4.14). Lastly, leak respiration was decreased by MHC-I overexpression, with IFN α and IFN β treatments leading to higher percentage of change (Figure 4.14). Even though distinct deficits were seen in individual mitochondrial function

parameters, respiratory flux control ratios, including coupling efficiency, respiratory control ratio, and phosphorylating respiration seem not to be affected by MHC-I overexpression or type I IFNs (Figure 4.15).

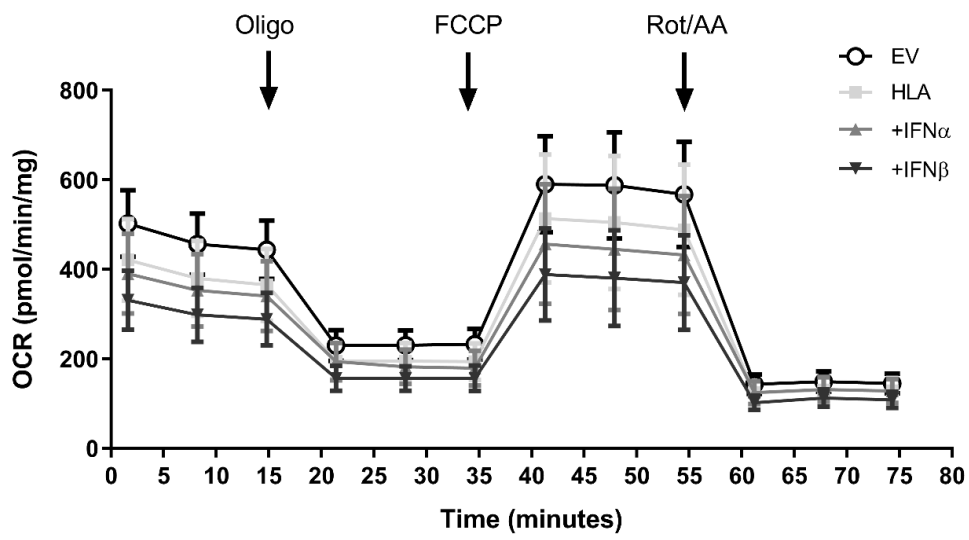
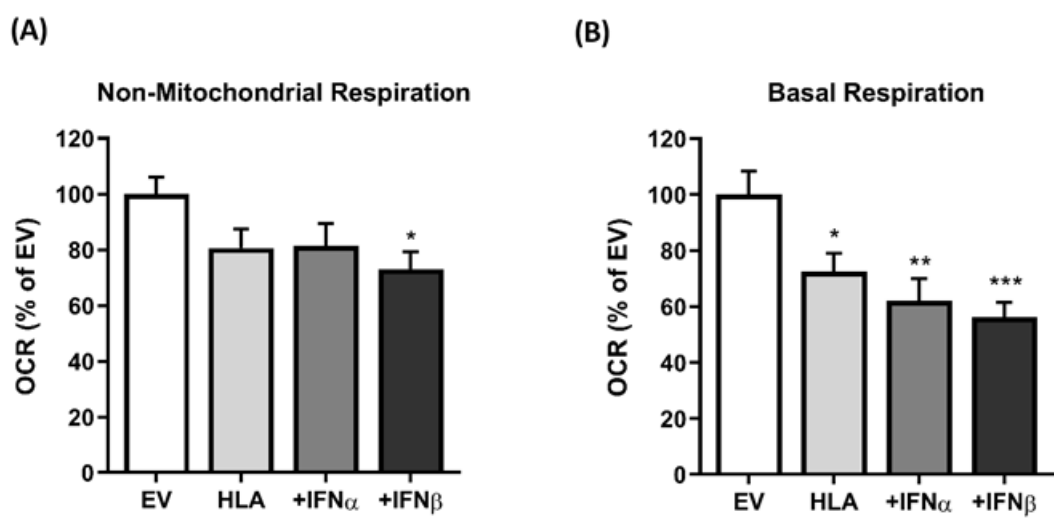


Figure 4.13 Bioenergetic profile of MHC-I overexpressing cells with or without type I IFNs treatment. Real-time measurements of oxygen consumption rate (OCR) following the sequential injection of oligomycin, FCCP, and a mixture of rotenone/antimycin A. Data were normalised to total protein content and represent mean \pm S.E.M ($n=3$).



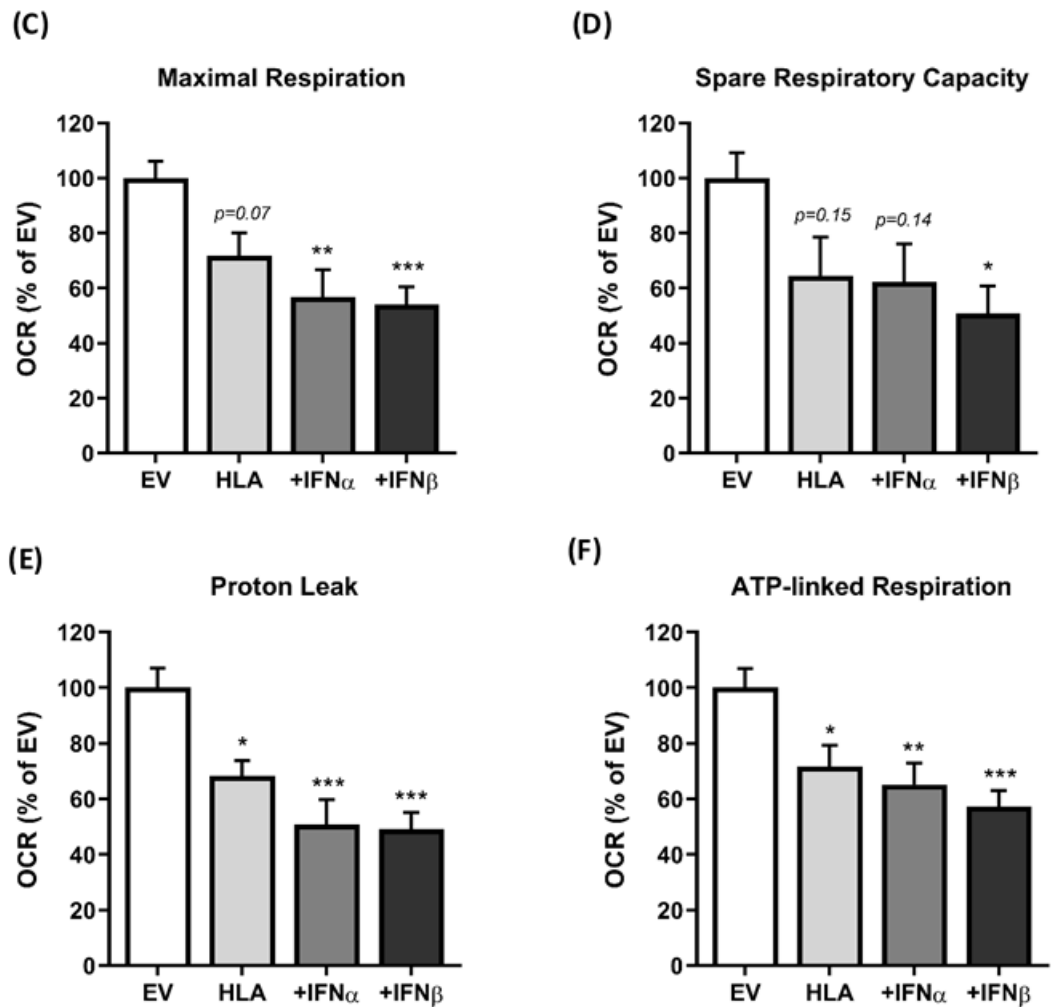


Figure 4.14 Individual mitochondrial parameters calculated from the bioenergetic profile. (A–F) Mitochondrial parameters – non-mitochondrial respiration, basal respiration, maximal respiration, spare respiratory capacity, proton leak, and ATP production – in MHC-I overexpressing cells in presence or absence 100 ng/ml type I IFNs. Data are expressed as relative to empty vector, and represent mean \pm S.E.M. ($n=3$), * $p \leq 0.05$, ** $p < 0.01$, *** $p < 0.001$ compared to empty vector.

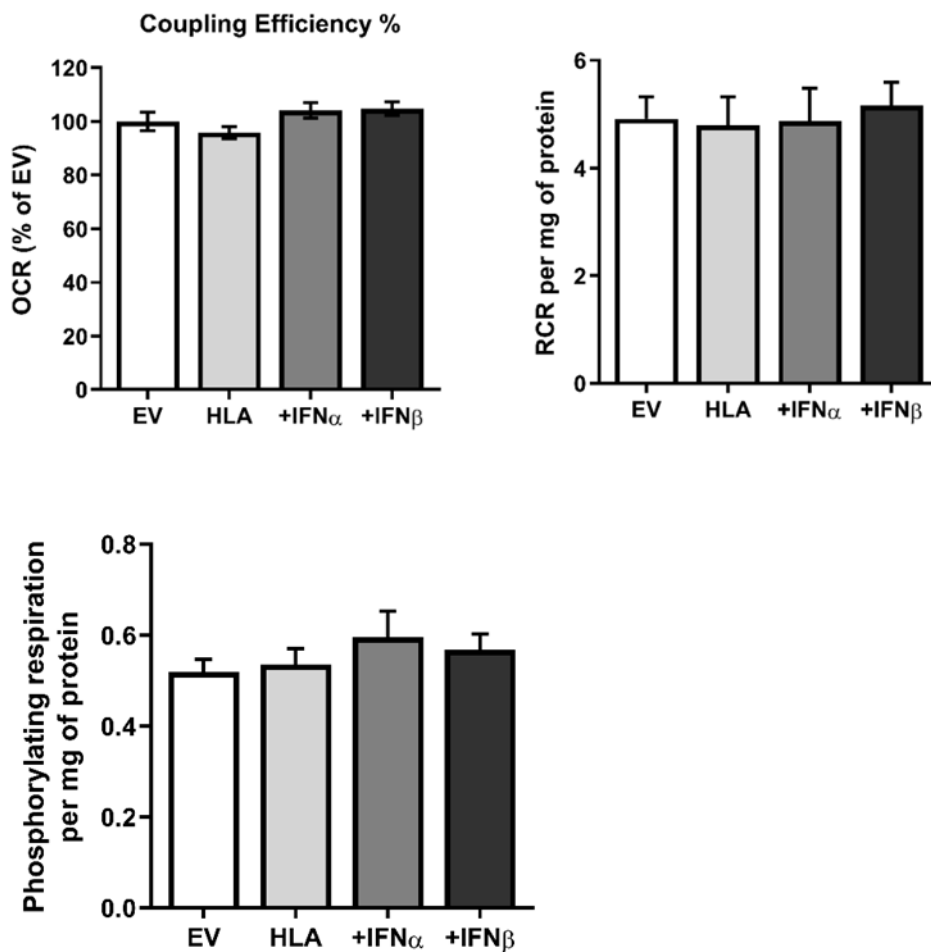
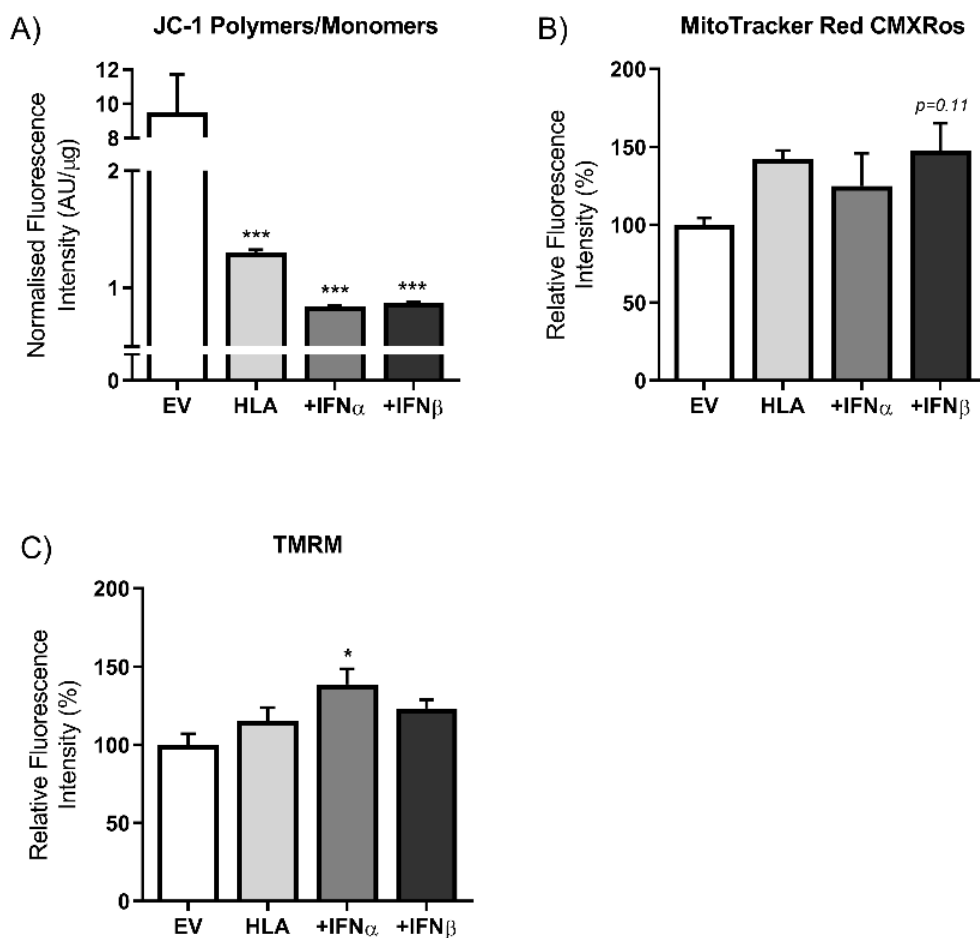


Figure 4.15 Normalised respiratory flux control ratios. Coupling efficiency (%), respiratory control ratio (RCR), and phosphorylating respiration per mg of protein MHC-I overexpressing cells in presence or absence 100 ng/ml type I IFNs, calculated from individual mitochondrial parameters. Data represent mean \pm S.E.M. ($n=3$).

4.3.5 Effects on mitochondrial mass and membrane potential by MHC-I overexpression type I IFNs

Different fluorophores were used to describe changes in mitochondrial membrane potential in response to MHC-I overexpression in presence or absence of type I IFNs. JC-1 polymers to monomers ratio, referring to J-aggregates formed in healthy negatively charged mitochondria and J-monomers that are present in depolarised mitochondria (Madreiter-Sokolowski *et al.*, 2019) was significantly decreased in MHC-I overexpressing cells, with type I IFNs inducing higher percentage of decrease by approximately 35%

compared to MHC-I overexpressing cells only (**Figure 4.16A**). Interestingly, MitoTracker Red CMXRos showed no significant changes in its fluorescence intensity between treatments, while an increased trend in response to MHC-I overexpression was noticeable (**Figure 4.16B**). Likewise to MitoTracker Red CMXRos assay, TMRM assay showed a significant rise in TMRM fluorescence by MHC-I overexpression + IFN α , with an increased trend being presented upon MHC-I overexpression in presence or absence of IFN β . (**Figure 4.16C**). However, MHC-I overexpression induced increases in MitoTracker Green FM fluorescence intensity in presence of type I IFNs (**Figure 4.16D**) and therefore, when TMRM was normalised to mitochondrial mass using MitoTracker Green FM, decreased TMRM fluorescence intensity was noticeable in MHC-I overexpressing cells with IFN β and not IFN α (**Figure 4.16E**), results that were relatively consistent with those seen with JC-1 assay.



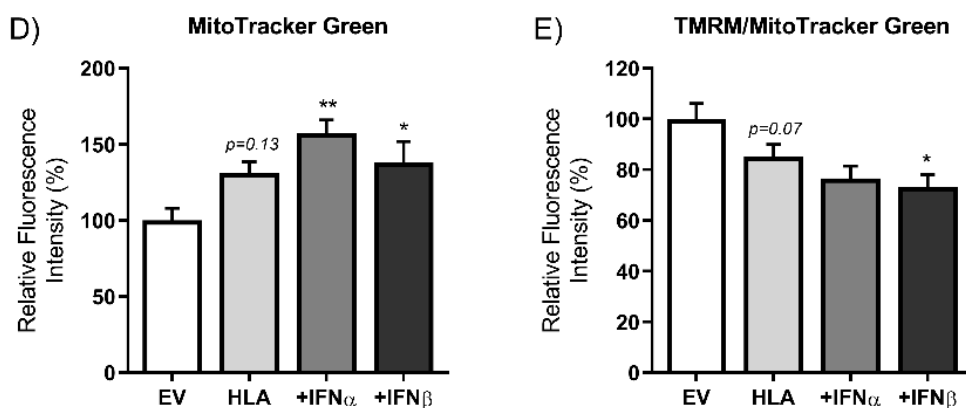


Figure 4.16 Mitochondrial membrane potential and mass. (A) Mitochondrial membrane potential expressed as JC-1 aggregates (red fluorescence) to JC-1 monomers (green fluorescence) ratio normalised to protein content. **(B–C)** Fluorescence intensity changes of MitoTracker Red CMXRos and TMRM, relative to empty vector, indicative of changes in mitochondrial membrane potential, as well as of MitoTracker Green, representing changes in mitochondrial mass. **(E)** Relative fluorescence intensity of TMRM normalised to MitoTracker Green. Data represent mean \pm S.E.M. ($n=3-4$), * $p \leq 0.05$, ** $p < 0.01$, *** $p < 0.001$ compared to empty vector.

4.3.6 RONS generation by MHC-I overexpression type I IFNs

Type I IFNs induced a significant increase in mitochondrial superoxide compared to control (**Figure 17A**), while no change was observed in MHC-I-overexpressing myoblasts in the absence of type I IFNs (**Figure 17B**). However, MHC-I overexpression + IFN β induced a significant increase in mitochondrial superoxide compared to both empty vector and MHC-I overexpressing myoblast, while no significant change was observed in the case of IFN α (**Figure 17B**). Overexpression of MHC-I promoted intracellular NO generation compared to those transfected with the EV, indicated by the increased DAF-FM DA fluorescence intensity (**Figure 17C**). This change was also substantially increased compared to MHC-I overexpression + IFN β ($p=0.07$) (**Figure 17C**). In contrast, MHC-I-overexpressing cells treated with type I IFNs showed no changes in NO generation. Lastly,

there was no change in H₂O₂ levels following MHC-I overexpression in the absence or presence of type I IFNs compared to empty vector (**Figure 17D**).

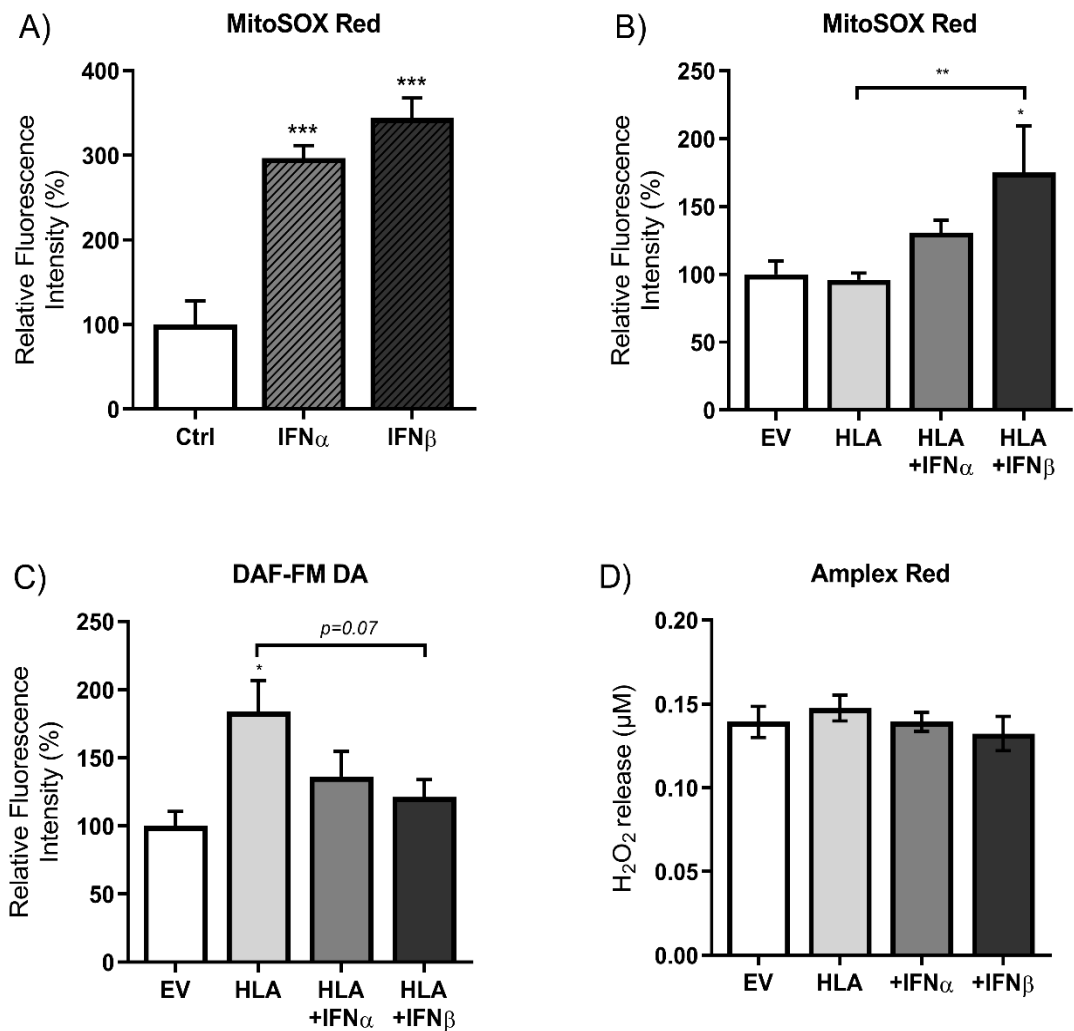


Figure 4.17 RONS generation. (A–B) Fluorescence intensity levels of MitoSOX Red, an indicator of mitochondrial superoxide generation induced by type I IFNs or MHC-I overexpressing cells with or without type I IFNs, and (C) DAF-FM DA, showing cellular NO generation ($n=4$), normalised to protein content. (D) Release of hydrogen peroxide as measured by Amplex Red assay. Data represent mean \pm S.E.M. ($n=3-4$), * $p \leq 0.05$, ** $p < 0.01$, *** $p < 0.001$ compared to empty vector or otherwise stated.

4.4 Discussion

Early research has shown that MHC-I overexpression can induce ER stress, potentially driving skeletal muscle weakness in myositis in the absence of inflammatory infiltrates in muscle fibres (Li *et al.*, 2009; Englund *et al.*, 2001). Furthermore, distinct IFN signatures have been suggested to act as biomarkers of different IIMs, with type I IFNs being predominantly seen in dermatomyositis and to a lesser degree in polymyositis (Greenberg *et al.*, 2010). Given the bi-directional crosstalk between ER and mitochondria, as well as the strong evidence of mitochondrial abnormalities in myositic muscle (Alhatou *et al.*, 2004; Boehler *et al.*, 2019; Meyer *et al.*, 2017; Thoma *et al.*, 2020), this study aimed to assess the effects of MHC-I overexpression in human skeletal muscle in the presence or absence of type I IFNs on mitochondrial functionality. The major findings of the present research are that the negative impact of MHC-I overexpression on mitochondrial function is aggravated by the presence of in particular IFN α , and to a greater extent by IFN β .

In this study, we observed that IFN α further induced MHC-I upregulation in the HLA-transfected model. This finding is consistent with previous studies showing IFN α -induced long-lasting MHC-I overexpression in human beta cells (de Brachène *et al.*, 2018; Marroqui *et al.*, 2017). Moreover, a study in human primary skeletal muscle cells found that type I IFN pathway activation inhibited myoblast differentiation and induced myotube atrophy in the context of diabetes, as reflected by upregulated levels of HLA-ABC (Ladislau *et al.*, 2018). Here we were able to specify that it is IFN α , rather than IFN β , that induces enhanced expression in MHC-I overexpressing cells, highlighting the differential effects of IFN α and IFN β on MHC class I regulation in human skeletal myoblast.

Where IFN α enhances the expression of MHC-I, IFN β induced stronger defects on mitochondrial function compared to IFN α , independent of MHC-I overexpression. More specifically, IFN α induced mild mitochondrial respiratory defects, specifically seen in basal and ATP-linked respiration, that only became evident after 24 hours incubation at a concentration of 200 ng/ml, while such effects were already evident after 18 hours incubation in the presence of 100 ng/ml IFN β . This corresponds with IFN β -induced mitochondrial damage reported in previous studies of brown adipose tissue (Kissig *et al.*,

2017) and skeletal muscle (Meyer *et al.*, 2017). However, the IFN β -induced mitochondrial dysfunction can be considered moderate, as IFN β seems to decrease basal, maximal, and ATP-linked respiration, but not reserve capacity, effects that were abolished with longer exposure (24 hours).

Our data show the direct effects of MHC-I overexpression on mitochondrial respiration, as well as basal glycolysis, in human skeletal muscle cells; interestingly, these effects were exacerbated in presence of type I IFNs. Mitochondrial impairments were also evident by mitochondrial membrane depolarisation in response to MHC-I overexpression with or without type I IFNs. Further, a combinational effect of MHC-I overexpression and IFN β increased mitochondrial mass, which may be an attempt by the cells to compensate for respiratory deficits. It should be noted though that the Kissig *et al.* (2017) study in brown adipocytes reported no IFN α -induced changes in mitochondrial biogenesis. Thus, the observed increase in mitochondrial mass may be MHC-I-driven; however, no conclusive statements can be made as the effects of IFN only have not been examined in this matter. Altogether, these findings imply a strong combinational impact of MHC-I overexpression and type I IFNs on mitochondrial function.

ROS have been reported to play a role in the pathogenesis of several myopathological conditions other than myositis, it is possible that ROS are involved in myositis-associated muscle weakness (Lightfoot *et al.*, 2015). However, the role of ROS in myositis is overall poorly understood. The present study showed that both IFN α and IFN β contribute to mitochondrial ROS generation, as observed by increases in mitochondrial superoxide. This observation is consistent with a previous study showing IFN β -induced ROS generation in a dose dependent manner (Meyer *et al.*, 2017). Mitochondrial superoxide generation was also highly induced by MHC-I overexpression in presence of type I IFNs, with IFN β -treated MHC-I overexpressing cells reaching statistical significance. It was surprisingly though that IFN α -treated MHC-I overexpressing cells showed no significant change in mitochondrial superoxide generation, considering the drastic elevations observed by IFN α treatment alone. Similarly, IFN β -treated MHC-I overexpressing cells showed a lower percentage of change in mitochondrial superoxide compared to IFN β -treated cells only. In addition to this, MHC-I overexpression alone showed no effects on mitochondrial superoxide generation. These findings raised several questions regarding

the availability of mitochondrial superoxide in MHC-I overexpressing cells or the involvement of hydrogen peroxide generation (Pearson *et al.*, 2014; Ott *et al.*, 2007). Further investigation of ROS generation reported no changes in the release of hydrogen peroxide in MHC-I overexpressing cells in presence or absence of type I IFNs. Nevertheless, significant evidence reports that NO can react with superoxide producing peroxynitrite, which may result in an overall decreased superoxide availability (Pearson *et al.*, 2014). In the present study, no changes were observed in mitochondrial superoxide levels following MHC-I overexpression, which may be linked to increased levels of NO, as observed in the present study. The involvement of NO in inflammatory myopathies has been early reported by Tews and Goebel (1998) who showed inducible and nNOS up-regulation in the muscle fibres of 21 patients with myositis. Another study has also shown overexpressed inducible NOS and elevated NO levels, as described by nitrated tyrosine residues staining, in the muscle fibres of sporadic inclusion body myositis and to a lower degree in DM (Schmidt *et al.*, 2012). In contrast, MHC-I overexpression in presence of type I IFNs was unable to promote nitric oxide generation. Therefore, the absence NO generation allows the availability of mitochondrial superoxide under type I IFNs and MHC-I overexpression conditions, leading to increased MitoSOX Red fluorescence intensity. Further supporting these findings, both IFN α and IFN β showed inhibitory effects on NO production in endothelial cells (Buie *et al.*, 2017; Jia *et al.*, 2018).

The present findings provide some novel differential effects between IFN α and IFN β , on mitochondrial respiration and ROS generation. This study also sheds light on the strong combinational effects of MHC-I overexpression and type I IFNs specifically on mitochondrial function, acting synergistically in inducing drastic respiratory defects and loss of mitochondrial membrane potential. However, it is of great interest that MHC-I and type I IFNs exert distinct segregated effects on reactive oxygen and nitrogen species, with MHC-I overexpression contributing to NO generation but type I IFNs showing inhibitory effects.

CHAPTER 5:

**Mitochondrial function
and ROS generation in
human myositis cells
derived from patient
biopsy samples**

5.1. Introduction

IIMs are a group of autoimmune muscle diseases characterized by progressive muscle weakness leading to poor quality of life. Even though diagnosis is still challenging, requiring numerous specialists and examinations, IBM and DM are two of the main types of IIMs that present distinct differential characteristics in epidemiological, clinical and physiological aspects. IBM occurs commonly in men (women to men ratio, 1:2) aged over 50 years, whereas DM is seen in both adults (peak age of onset 40–50 years) and children (JDM) and is predominantly developed in women (women to men ratio, 2:1) (Oldroyd *et al.*, 2017). Compared to other forms of IIMs, patients with IBM present mild elevation of creatine kinase levels (up to 10–15 fold increase), both proximal and distal asymmetrical muscle weakness that progresses in a much slower rate, making diagnosis even harder.

In contrast, patients with DM present a significant elevation of creatine kinase levels (10–50 fold increase), and proximal and symmetrical muscle weakness (Schmidt, 2018). The clinical course of DM is rapidly progressive, with however, muscle atrophy not being evident early in the course (Khadilkar and Dhamne, 2020). Furthermore, in DM, skeletal muscle is not the only organ that is affected, with a characteristic symptom being its skin manifestations, including Gottron's papules and signs, heliotrope, shawl (posterior neck) and v-sign (anterior upper chest) rash, mechanic's hands and erythoderma (Oldroyd *et al.*, 2017). Those two types differ extremely histologically as well, with DM muscle biopsies showing perifascicular, perimysial or perivascular infiltrates, while histological examination of IBM shows endomysial infiltrates and rimmed vacuoles that are selective to IBM (Lundberg *et al.*, 2016). Last but not least, a characteristic feature of all IIMs is the upregulation of MHC-I, with IBM though also presenting significant upregulation of MHC-II (Rigolet *et al.*, 2019; Das *et al.*, 2013).

Despite inflammation of the muscle is a common feature in IIMs, the pathophysiological mechanisms that underly muscle weakness and dysfunction remain to be fully determined. Numerous studies have reported the involvement of mitochondrial abnormalities. The majority of those studies though have focused on histological and histochemical examination of mitochondria as seen in muscle biopsies collected from various myositis types. Decreased or absence of COX (complex IV) activity and mtDNA deletions have been a common histological feature in IIMs (Rygiel *et al.*, 2015).

Interestingly, different respiratory-deficient muscle fibres (both slow and fast twitch fibres), including COX-deficient/intermediate fibres and NADH dehydrogenase (complex I)-deficient fibers, have been identified in sIBM, indicative of progressive mitochondrial dysfunction initiated by complex I deficiency, with complex II levels not being affected (Rygiel *et al.*, 2015; Joshi *et al.*, 2014). In another study where histochemical staining for mitochondrial complexes in DM, it was found that COX-negative fibres were 30-fold higher in DM than in controls, with other myositis patients (including PM and IBM) presenting less amount of COX-negative fibres. In contrast, an irregular increased complex I staining was seen especially in the perimysial region of DM fibres (Meyer *et al.*, 2017). Overall, these findings suggest a different pattern of mitochondrial abnormalities between DM and IBM.

Introducing functional analysis of mitochondrial respiration into the role of mitochondria in myositis, Catalán-García *et al.* (2020) and Oikawa *et al.* (2020) recently showed decreased respiration in both sIBM fibroblasts and myoblasts, showing that those abnormalities are not only restricted to the target disease tissue (muscle). Another study on DM showed decreased mitochondrial respiration in myoblasts (Basualto-Alarcón *et al.*, 2020) and muscle fibres that also presented increased total superoxide levels and hydrogen peroxide in response to diminished mitochondrial substrates and maximal respiration conditions (Meyer *et al.*, 2017). In an attempt to further determine the involvement of mitochondrial respiratory defects and ROS generation in IIMs, this study aimed to investigate those mechanisms at a functional level in primary cells derived from newly diagnosed DM and IBM patients.

5.1.1 Aims of this chapter

1. Establish a clinical cell model of primary human myositis skeletal muscle cell line derived from patient biopsy samples with IBM and DM.
2. Characterise mitochondrial function and oxidative stress in IBM and DM cells.
3. Assess the role of ROS generation on IBM and DM-associated changes in mitochondrial function using the antioxidant EUK-134.

5.2 Methods

5.2.1 Ethics statement

This study was undertaken with ethical approval from The Myositis Research Tissue Bank and The Manchester Metropolitan University. All participants provided written, informed consent before surgical procedure for collecting the muscle biopsy sample for research purposes.

5.2.2 Muscle biopsy collection

Muscle biopsy took place at Salford Royal NHS Foundation Trust. After surgical excision, muscle biopsy samples were placed in ice-cold Relaxing Buffer, as explained in **Section 2.1.2**, and transported to Manchester Metropolitan University laboratory. Muscle biopsy samples were collected from two female individuals diagnosed with IBM and DM, and a healthy male individual.

5.2.3 Primary cell isolation and culture

The biopsy sample of muscle tissue was dissociated in digestion solution (Collagenase D/Dispase II/ CaCl₂ mixture in low-glucose DMEM) for 30 - 40 minutes at 37 °C, with gentle agitation every 5 - 10 minutes, as described in **Section 2.1.2**. Briefly, after filtration and centrifugation at 443 ×g for 5 minutes, cell pellet was resuspended in passage 0 Growth Media (**Section 2.1.2**), transferred in laminin-coated T25 flasks, and maintained at standard culture conditions.

5.2.4 Fluorescent imaging of cells

As described in **Section 2.5**, primary cells were seeded and cultured in a 12-well plate, fixed using 4% (w/v) paraformaldehyde (10 minutes, room temperature), and incubated in block 1 solution for 1 hour at room temperature. Primary antibodies, anti-MyoD and anti-HLA class I, prepared in block 2 solution, were added to the cells and incubated overnight at 4°C. Secondary antibodies conjugated with Alexa Fluor 648 (goat anti-mouse IgG; 1/1000) and Alexa Fluor 488 (goat anti-rabbit IgG; 1:1000) and DAPI (1/5000) were added to the cells for 1 hour at room temperature in the dark. Cells were maintained in DPBS and images were acquired using a LEICA DMI6000 B inverted microscope.

5.2.5 Assessment of cellular respiration using Seahorse Extracellular Flux Analyzer

Seahorse XFp Cell Mito Stress Test kit was used to measure real-time OCR and ECAR in primary myositis cells exposed to EUK-134 for 24 hours, as described in **Section 2.4.1**. OCR and ECAR measurements were normalised to total protein using the Pierce™ BCA Protein Assay as described in **Section 2.3.1**.

5.2.6 Assessment of mitochondrial membrane potential and mass

Primary skeletal muscle cells seeded at 8×10^3 cells/well in a black-sided, clear-bottom 96-well plate and treated with or without EUK-134, were incubated with TMRM, as described in **Section 2.7.2**, to measure mitochondrial membrane and normalised to mitochondrial mass as measured by MitoTracker Green.

5.2.7 Measurement of RONS

To quantify reactive oxygen and nitrogen species, as well as mitochondrial hydroxyl radical generation, primary myositis cells seeded at 8×10^3 cells/well in a black-sided, clear-bottom 96-well plate, were incubated with or without EUK-134. Following 24 hours incubation, cells were exposed to different fluorophores as described in **Section 2.6**, including: MitoSOX™ Red mitochondrial superoxide indicator, OH580 mitochondrial hydroxyl radical probe, DAF-FM-DA NO indicator, Amplex® Red reagent/Horseradish peroxidase solution (total cellular hydrogen peroxide indicator), and DHE total cellular superoxide fluorophore.

5.2.8 Statistical analysis

Graph Pad Prism 8 software was used to statistically analyse the data. Following normality of distribution using Shapiro-wilk test, normally distributed data were analysed using one-way ANOVA with Tukey's post-hoc test, while non-normally distributed data were analysed using Dunn's test. Statistical significance was defined as a p -value ≤ 0.05 .

5.3 Results

5.3.1 Growth of primary cells

Isolated cells were attached 24 hours after seeding and had a small and circular shape up to the 5th day of incubation in growth media supplemented with recombinant human basic fibroblast growth factor, while they adopted a spindle-like shape after approximately a week of incubation, and elongated after 11 days (**Figure 5.1A**). At the first passage, spindle-like shaped myoblasts were seen from day 1 (**Figure 5.1B**). Isolation of myoblast was confirmed by MyoD expression, as examined by immunofluorescent staining (**Figure 5.2**).

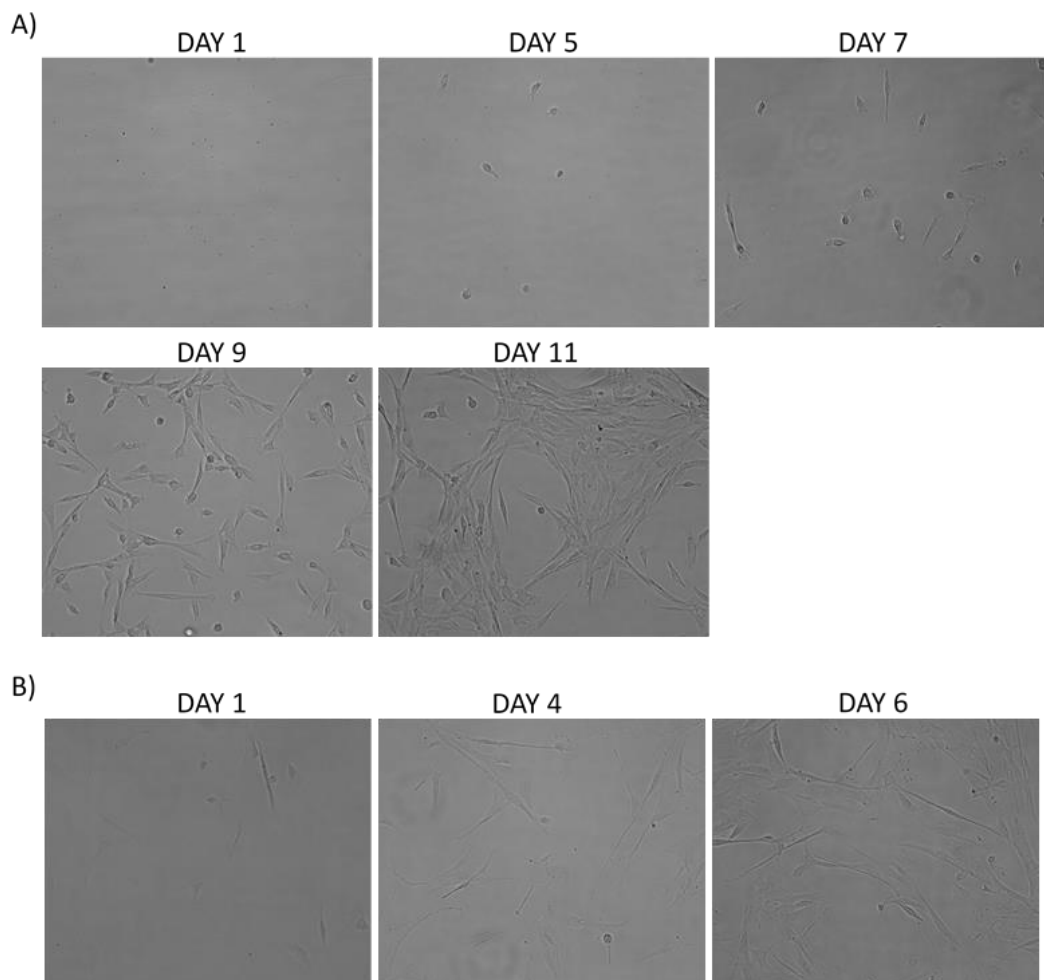


Figure 5.1 Growth of human primary myoblast at passage 0. (A) Representative images of passage 0 myoblasts isolated from *tibialis anterior* of dermatomyositis patient taken

after 1, 5, 7, 9, and 11 days of incubation under a phase contrast microscope, and **(B)** of passage 1 myoblasts after 1, 4, and 6 days.

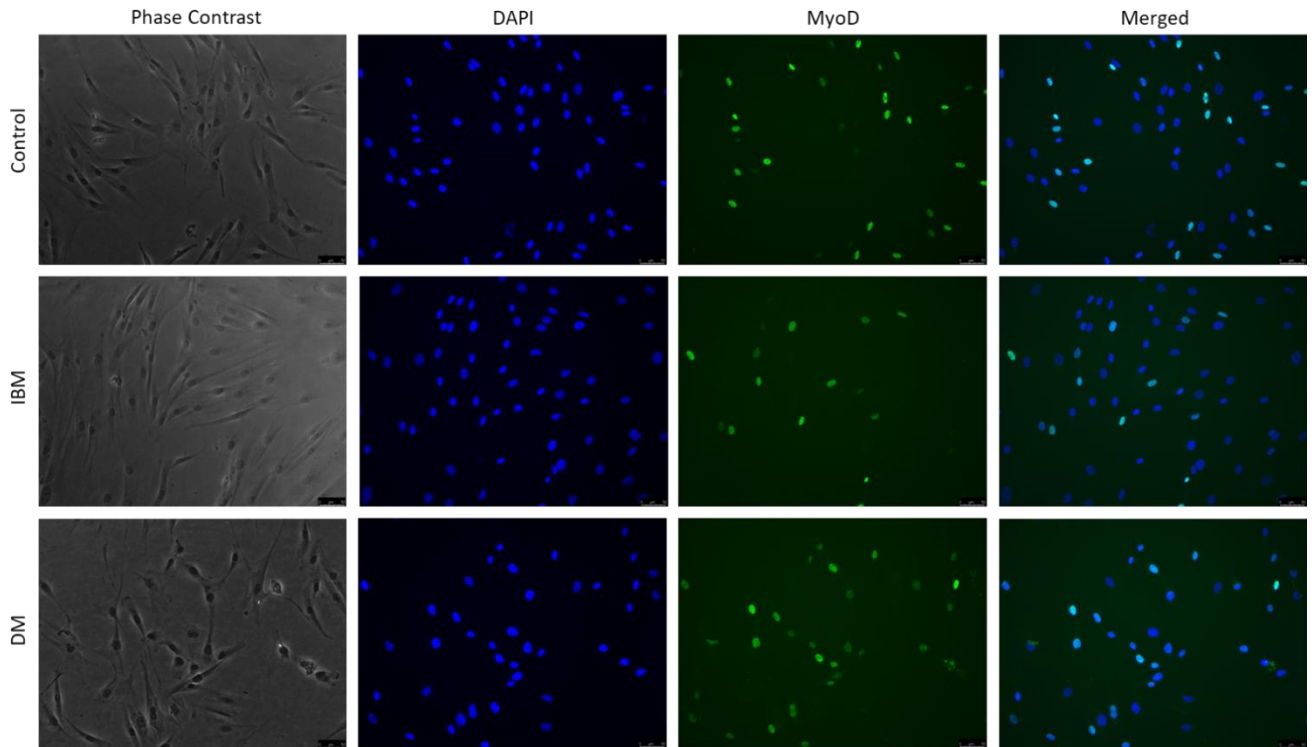


Figure 5.2 Myogenic cells isolated from human muscle biopsy samples. Representative images of MyoD-positive cells (green fluorescence) isolated from three different human muscle biopsy samples, a healthy (Control) individual, IBM patient, and a DM patient. Images captured at 20× magnification. Scale bar = 50 μm .

5.3.2 Expression of HLA class I

MHC-I expression in myositis cells was defined by staining with anti-HLA class I. As expected, qualitative analysis showed that HLA class I fluorescence intensity was elevated in myositic cells compared to control, with DM cells showing a relatively more intense HLA class I intensity compared to IBM cells (**Figure 5.3**).

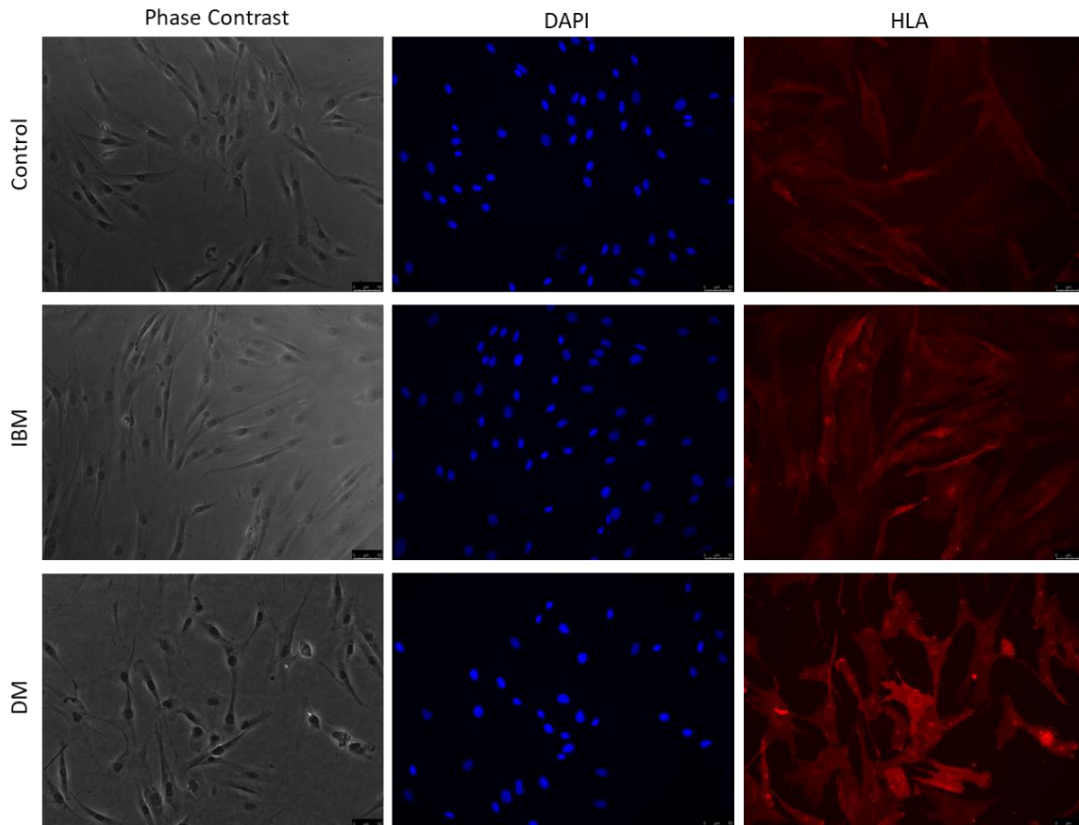
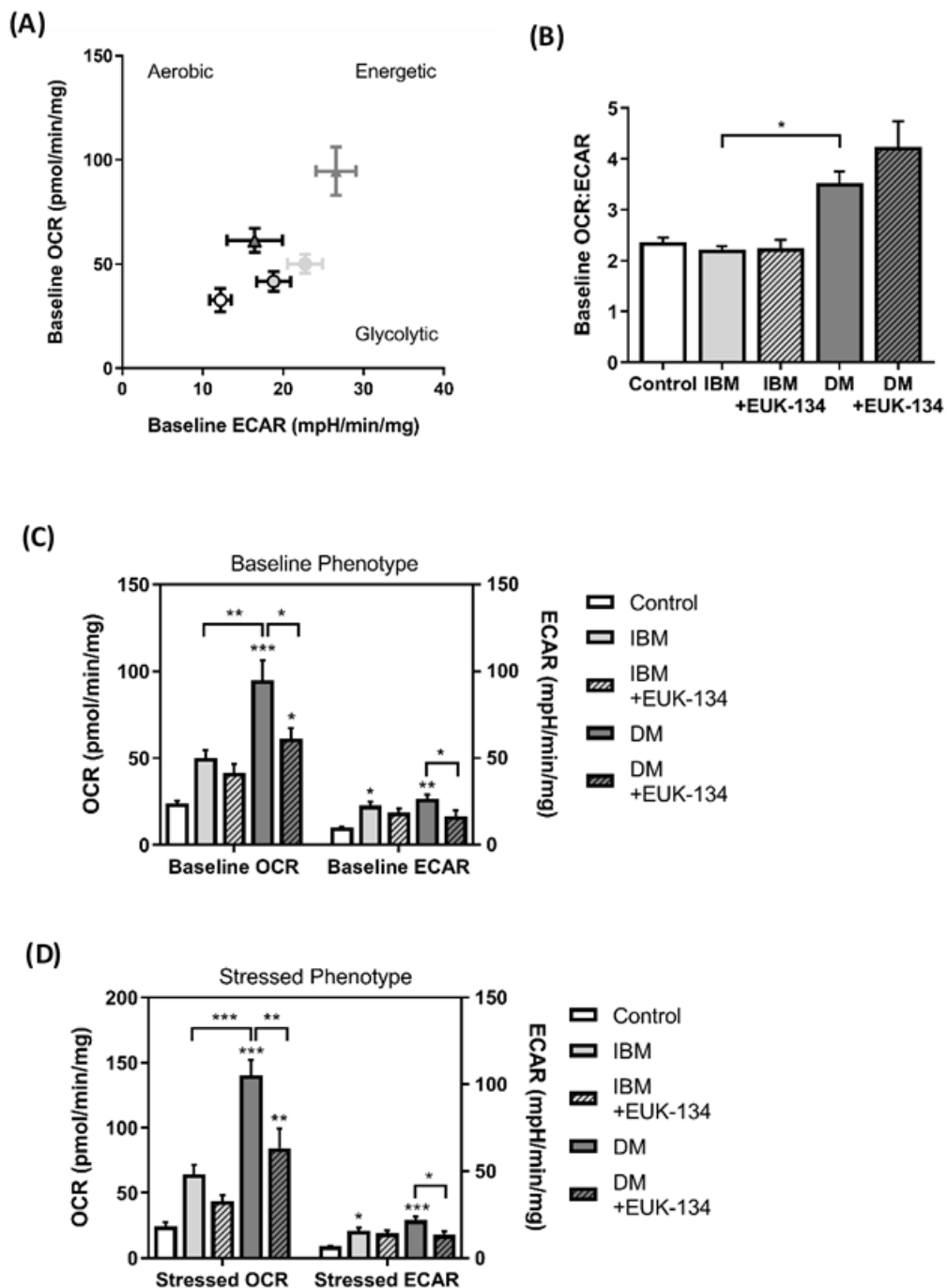


Figure 5.3 Expression of HLA class I. Representative images of human primary myoblast isolated from three different human muscle biopsy samples, a healthy (Control) individual, IBM patient, and a DM patient, stained with DAPI (blue) and anti-HLA class I (red). Images captured at 20× magnification. Scale bar = 50 μ m.

5.3.3. Bioenergetic profile

Seahorse extracellular flux analysis was used to evaluate the bioenergetic status of the IBM and DM primary cells. Basal OCR values were plotted versus ECAR values to depict whether samples are at a glycolytic, aerobic, energetic or quiescent state. Both IBM and DM samples showed higher OCR and ECAR compared to healthy cells, with DM cells showing a highly energetic profile that is reduced in presence of EUK-134 towards the bioenergetic status seen in healthy cells (**Figure 5.4A**). This means that DM cells increase both oxidative phosphorylation (OCR) and glycolysis (ECAR) under basal conditions to meet high energetic demands, as suggested by their baseline phenotype (**Figure 5.4C**). It should be noted though that DM cells seem to rely mostly on oxidative phosphorylation as shown by increased baseline OCR to ECAR ratio (55% of increase, $p=0.27$), a ratio that

was unchanged in presence of EUK-134 (**Figure 5.4B**). Furthermore, DM cells show the largest % of increase of OCR when mitochondrial function was impaired (stressed OCR) following inhibition of ATP synthase and mitochondrial membrane depolarization (**Figure 5.4D**), while no significant changes are seen in ECAR from basal to stressed conditions; this indicates that DM cells exhibit high metabolic potential that is more reliant on oxidative metabolism (**Figure 5.4E**). In contrast, even though IBM cells show an increased trend in OCR under both basal and stressed conditions (52% and 62% of increase, respectively) (**Figure 5.4C and D**), they seem to predominantly utilise glycolysis.



(E)

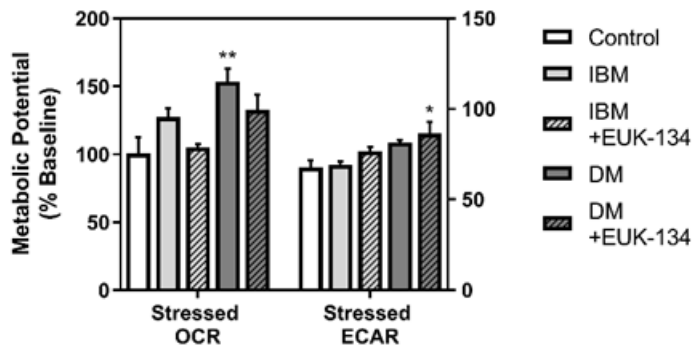


Figure 5.4 Energy phenotype of IBM and DM-derived cells. A) Bioenergetic profile expressed as OCR versus ECAR measured under basal conditions. Statistical analysis of (B) OCR and ECAR ratio, (C) OCR and ECAR baseline phenotype, (D) OCR and ECAR stressed phenotype, and (E) metabolic potential. Data were normalised to total protein content. Data represent mean \pm S.E.M. ($n=2-3$), * $p \leq 0.05$, ** $p < 0.01$, *** $p < 0.001$ compared to control or otherwise stated.

The mitochondrial function parameters of IBM and DM-derived primary cells in presence or absence of EUK-134 (Figure 5.6) were calculated from the bioenergetic profile as generated from the sequential addition of mitochondrial respiration inhibitors oligomycin (ATP synthase inhibitor) and rotenone/antimycin A mixture (complex I and III inhibitors, respectively), as well as the mitochondrial oxidative phosphorylation uncoupler FCCP (Figure 5.5). As previously discussed, both IBM and DM samples showed an overall increase in non-mitochondrial and mitochondrial OCR (Figure 5.6A), with DM cells reaching statistical significance in all mitochondrial parameters – basal, maximal, and ATP-linked respiration, spare respiratory capacity, and proton leak – compared to control healthy cells (Figure 5.6A–F). Specifically, non-mitochondrial respiration, maximal respiration, proton leak, and ATP production were significantly greater in DM compared to IBM (Figure 5.6A, C, E, and F). Furthermore, treatment with the antioxidant EUK-134 in both IBM and DM presented an overall decrease in OCR compared to non-treated patient cells, which was closer to control levels (Figure 5.5). This OCR decrease in response to EUK-134 was statistically significant compared to non-treated cells under maximal respiration and ATP production IBM (Figure 5.6C and F). However, it should be

noted that maximal-linked OCR and proton leak in DM cells were significantly increased compared to control even in presence of EUK-134 (**Figure 5.6C and E**). Lastly, phosphorylating respiration was decreased, with DM showing statistical significance ($p=0.02$ compared to control), while other control flux ratios were unaffected (**Figure 5.7**).

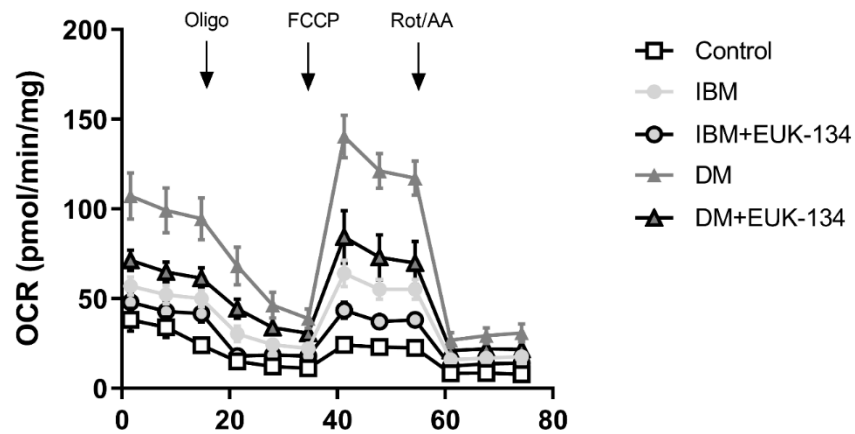
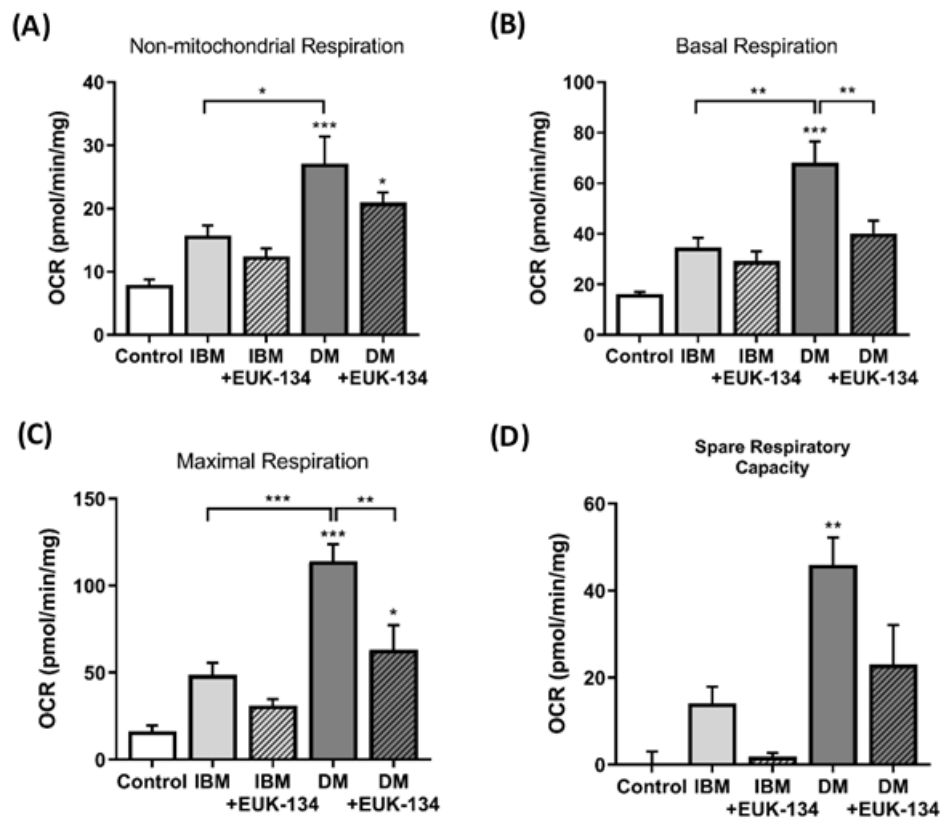


Figure 5.5 Bioenergetic profile of IBM and DM-derived cells. Real-time measurements of oxygen consumption rate (OCR) following the sequential injection of oligomycin, FCCP, and a mixture of rotenone/antimycin A ($n=2-3$).



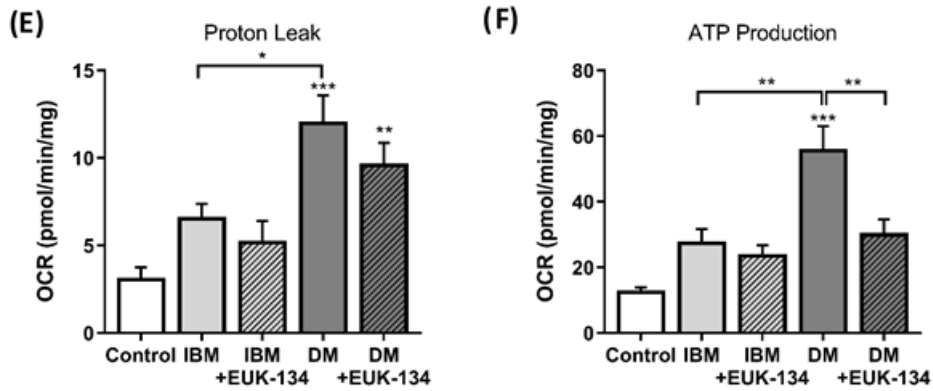


Figure 5.6 Individual mitochondrial parameters calculated from the bioenergetic profile.

(A–F) Mitochondrial parameters – non-mitochondrial respiration, basal respiration, maximal respiration, spare respiratory capacity, proton leak, and ATP production – per mg of protein, in IBM and DM cells in presence or absence of EUK-134. Data represent mean \pm S.E.M. ($n=2-3$), * $p \leq 0.05$, ** $p < 0.01$, *** $p < 0.001$ compared to control or otherwise stated.

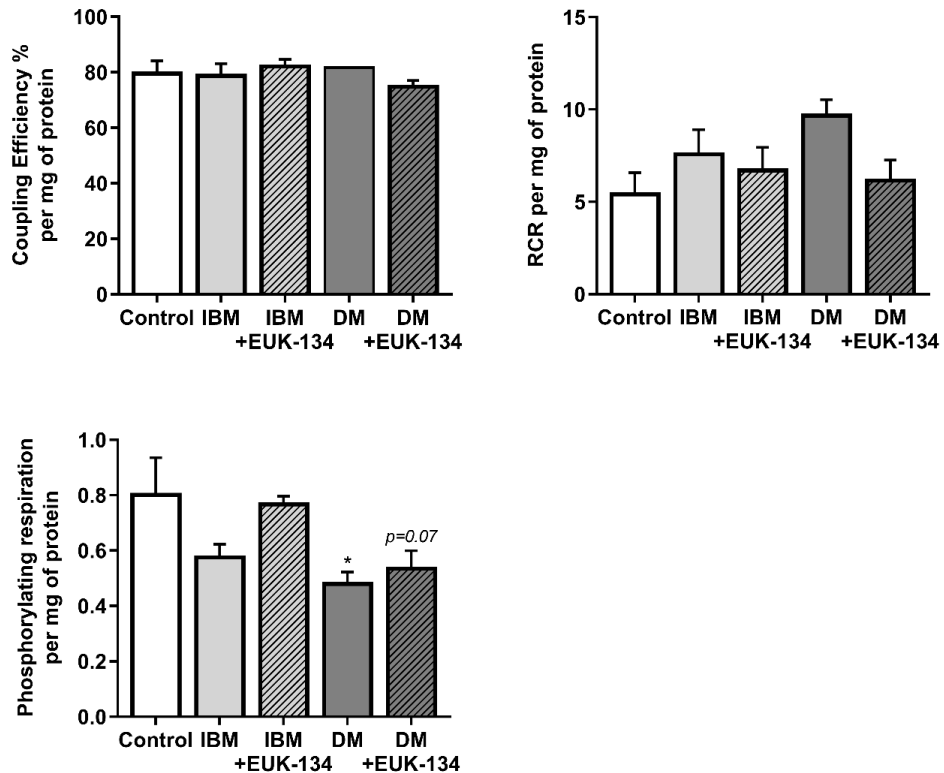
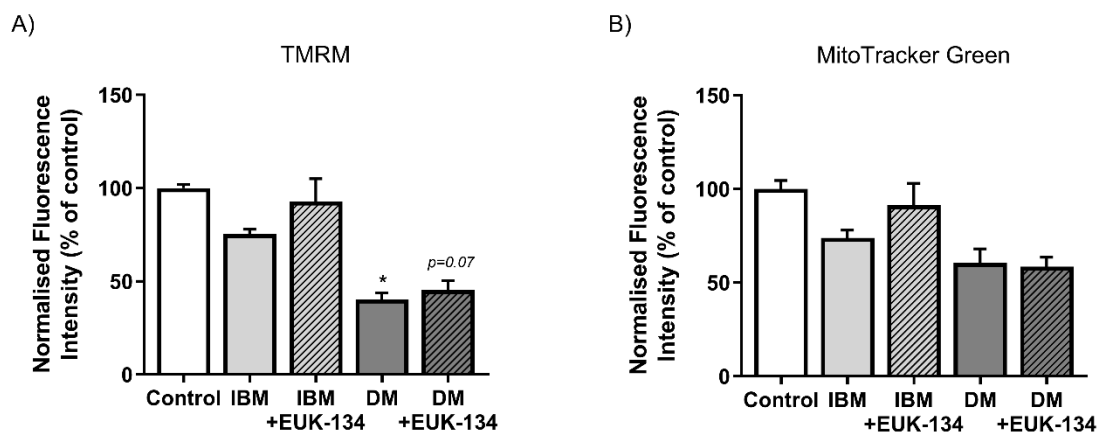


Figure 5.7 Normalised respiratory flux control ratios. Coupling efficiency (%), respiratory control ratio (RCR), and phosphorylating respiration per mg of protein in IBM and DM

cells in presence or absence of EUK-134, calculated from individual mitochondrial parameters. Data represent mean \pm S.E.M., * $p \leq 0.05$ compared to control.

5.3.4 Mitochondrial mass and membrane potential

TMRM fluorophore was used to assess changes in mitochondrial membrane potential in IBM and DM-derived myoblasts in presence or absence of EUK-134. Mitochondrial membrane potential was reduced in both IBM (~30%) and DM (~70%) samples, as seen by a decreased TMRM fluorescence intensity normalised to protein content, with DM showing statistical significance ($p=0.02$) (**Figure 5.8A**). Even though EUK-134 was able to increase TMRM fluorescence intensity of IBM myoblast close to the control level, no changes were seen in DM myoblast ($p=0.07$) (**Figure 5.8A**). A small decrease in MitoTracker Green normalised fluorescence intensity, indicative of mitochondrial mass, was also seen in both IBM and DM (~10% and 20%, respectively) (**Figure 5.8B**). Therefore, TMRM normalisation to mitochondrial mass showed no change in mitochondrial membrane potential in IBM sample, whereas it was statistically significant decreased in DM sample (**Figure 5.8C**).



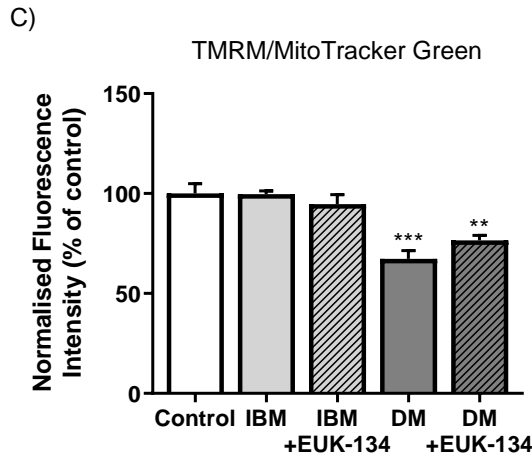


Figure 5.8 Mitochondrial membrane potential and mass. Relative change (%) in **(A)** TMRM fluorescence intensity (mitochondrial membrane potential), **(B)** MitoTracker Green fluorescence intensity (mitochondrial mass), and **(C)** TMRM fluorescence intensity normalised to MitoTracker Green. Data were normalised to protein content and represent mean \pm S.E.M. ($n=2-3$), * $p \leq 0.05$, ** $p < 0.01$, *** $p < 0.001$ compared to control.

5.3.5 RONS generation

In regards to ROS generation, no significant changes were seen in the % of MitoSOX Red fluorescence intensity, indicative of mitochondrial superoxide levels, in either IBM or DM myoblasts compared to healthy control myoblasts (**Figure 5.9A**). Interestingly though, MitoSOX Red normalised to MitoTracker Green fluorescence intensity (% of control), presented a substantial increase in DM myoblasts (**Figure 5.9B**). IBM and DM myoblasts displayed no changes in mitochondrial hydroxyl radical as seen by OH580 probe fluorescent radical. Amplex Red hydrogen peroxide/peroxidase assay showed elevated hydrogen peroxide levels in IBM sample that was almost statistically significant ($p = 0.08$) compared to control; particularly, drastic statistical increase was seen in IBM compared to DM sample. This hydrogen peroxide elevation was not altered by the presence of EUK-134; in contrast, EUK-134 induced a significant increase in hydrogen peroxide compared to both IBM and DM samples (**Figure 5.9E**). A decreased trend was found in NO production (DAF-FM DA fluorescence intensity) in both samples, with IBM showing even higher reduction in presence of EUK-134 (**Figure 5.9D**).

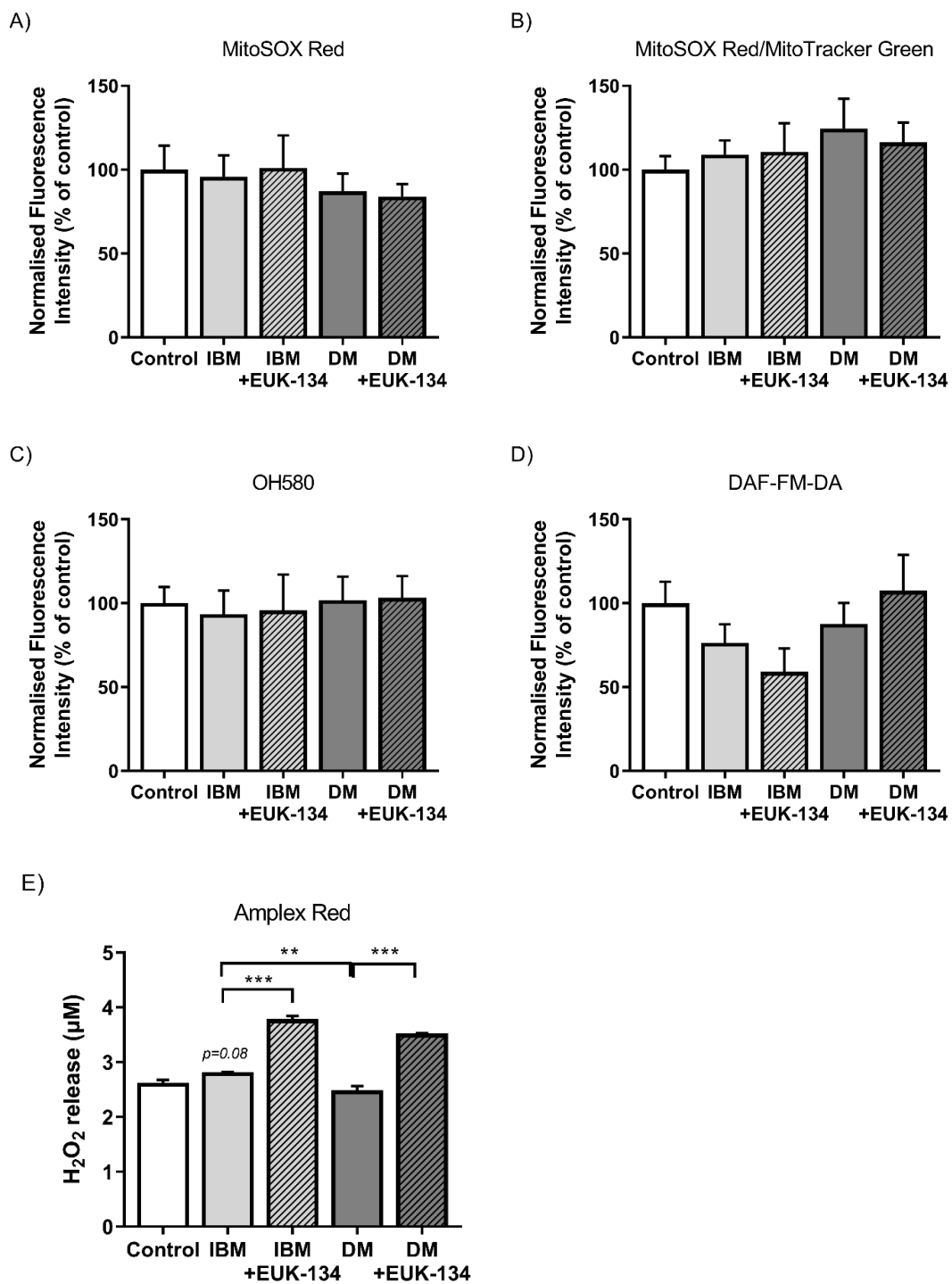


Figure 5.9 RONS generation. Relative change (% of control) in **(A)** mitochondrial superoxide (MitoSOX Red), **(B)** mitochondrial superoxide (MitoSOX Red) normalised to mitochondrial mass (MitoTracker Green), **(C)** mitochondrial hydroxyl radical (OH580), and **(D)** NO (DAF-FM-DA), as well as **(E)** hydrogen peroxide release (μM). Data were normalised to protein content and represent mean \pm S.E.M. ($n=3$), ** $p<0.01$, *** $p<0.001$ compared to control or otherwise stated.

5.4. Discussion

Mitochondrial alterations have been commonly displayed in various myositic muscles at histological and to a lesser degree molecular level, highlighting the potential role of mitochondrial damage in the disease pathology (Basualto-Alarcón *et al.*, 2020). However, less is known about the involvement of mitochondrial dysfunction and ROS generation at a functional or molecular level. Furthermore, evidence remain scarce considering the rarity of the disease as well as its broad subcategorisation that has been fully individually described or compared yet in the context of mitochondrial functionality. Given this gap in the literature, the present study aimed to provide further insight into mitochondrial function and RONS generation using primary human derived myoblasts from patients with IBM and DM cultured with or without the superoxide dismutase and catalase mimetic EUK-134. The major finding of this chapter is the observed changes in mitochondrial respiration in diseased myoblasts compared to control, which seem to be drastically greater in DM myoblasts than in IBM myoblasts, while the presence of EUK-134 can mostly alleviate them.

MHC-I expression is a prominent feature in myositis muscle (Das *et al.*, 2013) that has shown promising evidence of its contribution to non-immune mediated mechanisms of myositis pathogenesis (Nagaraju *et al.*, 2005; Fréret *et al.*, 2013). Therefore, following track of primary cells growth and confirmation of myogenic cells isolation (MyoD-positive cells) from the human muscle biopsy samples, MHC/HLA class I expression was assessed using immunostaining. As expected, elevated HLA class I fluorescence intensity staining was evident in myositis myoblasts compared to control. A clear observation was the higher levels of HLA class I fluorescence intensity in DM myoblasts compared to IBM. Numerous early studies have previously examined MHC-I detection as a diagnostic tool in IIMs and showed 100% positivity on MHC-I staining in both IBM and DM (Das *et al.*, 2013; Sundaram *et al.*, 2008; Jain *et al.*, 2007). However, consistently with this chapter's data, Sundaram *et al.* (2008) reported a weak staining intensity in sIBM muscle fibers along sarcolemma, whereas intense cytoplasmic staining was present in perifascular regenerating fibers in DM. It is also of interest that stronger MHC-II staining has been suggested in IBM compared to DM (Das *et al.*, 2013; Rigolet *et al.*, 2019).

This study shows that both IBM and DM myoblasts have an increased metabolic potential under both baseline and stressed conditions, also displaying an ability to increase both oxygen consumption (oxidative phosphorylation) and extracellular acidification (glycolysis). Overall, mitochondrial respiration was increased in both DM and IBM; this increase might be seen as a compensatory machinery, potentially in response to augmented bioenergetic demand in the myositis cells that are subject to stress, as well as decreased mitochondrial efficiency as seen by increases in proton leak and reduction in phosphorylating respiration and mitochondrial membrane potential. An increase in mitochondrial respiration has been previously reported as an adaptive response to stresses, including ER stress and ROS production (Knupp *et al.*, 2019), a widely accepted mechanism in myositis pathogenesis (Nagaraju *et al.*, 2005). However, current results suggest that even though myositic myoblasts have increased metabolic potential, mitochondria seem to be dysfunctional in other aspects, with DM sample showing depolarised mitochondria. Interestingly, changes in mitochondrial function parameters and respiratory flux control ratios seem to be drastic in DM myoblasts, showing statistically significant difference not only compared to healthy control myoblasts, but also to IBM myoblasts. These differential findings in the degree of mitochondrial respiration alterations between DM and IBM myoblasts are consistent with a previous study that reported a different pattern of mitochondrial complexes deficits in DM and IBM muscle (Meyer *et al.*, 2017).

To the best of our knowledge, only two, recently published, studies have provided data on real time mitochondrial respiration measurement, with one examining DM/IMNM myoblasts (showing grouped data) (Basualto-Alarcón *et al.*, 2020) and the other one sIBM myoblasts (Oikawa *et al.*, 2020). In contrast to our data, Oikawa *et al.* (2020) showed decreased basal, maximal, and ATP-linked respiration in all three cases of sIBM examined, while other parameters of mitochondrial respiration were not described. It should be noted that female and older sIBM individuals ($n=2$, ≥ 84 years old) showing higher oxygen consumption depletion compared to the male sIBM individual ($n=1$, 71 years old), whose biopsy showed no COX negative-fibers either. Another element of consideration is the years between the age of onset/diagnosis and the age of examination, ranging from 6–9 years (Oikawa *et al.*, 2020), whereas in the present study, both IBM and DM biopsy

samples were collected for diagnosis purposes; in other words, their examination would probably be performed at an early disease stage. Basualto-Alarcón *et al.* (2020) also showed decreased basal and ATP-linked respiration in male DM/IMNM myoblasts ($n=2/3$ each), which is contractory to the data seen in female DM myoblasts in this study. However, proton leak was notably increased in DM/IMNM myoblasts compared to control myoblast, a finding that was also seen in the present study. Furthermore, an interesting finding in the study performed by Basualto-Alarcón *et al.* (2020) was that when myoblasts were grown in galactose instead of glucose media conditions, as a 'force' for higher mitochondrial workload, DM/IMNM myoblasts showed an ability to increase oxygen consumption, implying their efficiency in adapting to stress, which is consistent to the increases in metabolic potential observed in the current study, especially in DM myoblasts.

In this study, the antioxidant EUK-134 was used to assess the impact of ROS generation in myositic muscle cells. In respect to mitochondrial bioenergetics, the presence of EUK-134 prevented the observed increase in reserve capacity, basal, maximal, and ATP-linked respiration. This potentially implies that myositic myoblasts were partially rescued from stress, but still significantly at some aspects, and consequently, increases in mitochondrial respiration were not required to promote cell survival. In addition, in IBM myoblasts, EUK-134 was able to ameliorate reductions in mitochondrial mass, further supporting its contribution to the prevention of stress-associated mitochondrial effects. The importance of targeting oxidative stress to prevent or cure myositis has been previously highlighted by Boyer *et al.* (2018) in a study that demonstrated the partially preventive effects of the antioxidant *N-acetylcysteine* in a novel animal myositis model characterised by free radical emission, hydrogen peroxide-associated muscle atrophy, as well as impaired oxygen consumption and mitochondrial genes/proteins regulation. Besides mitochondrial respiration, data demonstrated increases in non-mitochondrial respiration that can be attributable to elevated ROS generation (Hill *et al.*, 2012). This change was statistically significant in DM myoblasts and was substantially ameliorated in the presence of EUK-134, even though control levels were not reached. The present study also displayed a tendency of elevated mitochondrial superoxide generation, a value that was normalised to mitochondrial mass, in DM myoblasts, as well as hydrogen peroxide in

IBM myoblasts, further supporting the potential role of ROS generation in IIMs pathophysiology.

To conclude, the present study provides evidence of the ability of myositic myoblasts, especially DM, to respond to stress by increasing their metabolic potential at early disease stages. However, mitochondrial dysfunction remains a prominent feature that needs further investigation using molecular and functional techniques. Lastly, it turns the attention to the better understanding of ROS emission and whether their scavenging can be a novel therapeutic strategy for myositis disease.

CHAPTER 6:

Effect of the muscle secretome from myositis patient-derived myoblasts on mitochondrial function and ROS generation

6.1 Introduction

The presence of immune cell-derived cytokines is a prominent feature in IIM, which however, seem not to be correlated with disease-associated muscle weakness, where immunosuppressive treatments are often ineffective (Carstens and Schmidt, 2014). Given the existing evidence of skeletal muscle acting as an endocrine organ (Schnynder and Handschin, 2015), attention has been given to the role of muscle-released cytokines, termed myokines, in skeletal muscle mass/function and disease. Myokines refer to cytokines, chemokines, or peptides that are generated and released by muscle cells upon contraction or other stimuli (Lightfoot and Cooper, 2016). A wide range of myokines have been detected the last decade, and to date, there are several reviews examining studies on the role of myokines in normal and diseased muscle, with only a few focusing on myokines in myositis (Mageriu *et al.*, 2020).

Several cytokines have been detected to be upregulated or downregulated in IIMs muscle cells and serum (Salomonsson and Lundberg, 2006), and suggested to play a role in myositis pathology, highlighting their potential significance as a therapeutic target in myositis. Among other, IL6 is a commonly detected myokine in myositis, but still not well-defined in the aspect of IIMs pathology. Specifically, dual roles of IL6 have been proposed, with pro-inflammatory activity as a cytokine and anti-inflammatory activity as a myokine (Mageriu *et al.*, 2020). A number of studies though have showed increased IL6 serum levels in DM patients (Bilgic *et al.*, 2009) as well as IIM patients with interstitial lung disease (Gono *et al.*, 2014). In addition to IL-6, IL-15, IL-18, CXCL10, CCL2/MCP-1, and CCL4/MIP1b have been proposed to be overexpressed in IIMs (Civatte *et al.*, 2005; Sanner *et al.*, 2014; De Paepe *et al.*, 2005; Helmers *et al.*, 2018; Sugiura *et al.*, 2002). On the other hand, another study introduced Insl6 as a downregulated myokine seen in muscle of patients with PM and DM, even though, upregulated Insl6 has been seen in murine models of myositis and cardiotoxin injury. Therefore, this differential observation between samples suggests potential different response mechanisms in short-term and chronic disease, and consequently highlights the importance of investigating the muscle secretome in human myositic muscle samples. In turn, the study showed that Insl6 deficiency in a mouse experimental model of autoimmune myositis led to a worsened

myositis phenotype characterised by CD5 and CD8 T-cells infiltration and elevated inflammatory cytokines expression (Zeng *et al.*, 2014).

As a hallmark of myositis, MHC-I overexpression has been assessed whether it displays a chemotactic activity by inducing the release of pro-inflammatory cytokines in absence of inflammation (Lightfoot *et al.*, 2015). Specifically, Lightfoot *et al.* (2015) demonstrated that MHC class I overexpression induces ER stress pathway activation, which in turn, stimulates the release of IL-6, CCL2/MCP-1, CCL4/MIP1b, and CCL5/RANTES in a murine skeletal muscle cell model. These findings are in support with other studies showing MHC class I-induced activation of the ER stress response and ER overload response, initiating NF-Kb pathway and its downstream activation of pro-inflammatory cytokines (Nagaraju *et al.*, 2005; Kim *et al.*, 2015). Therefore, it has been suggested that myokines release in muscle may be involved in inflammation maintenance, as well as muscle weakness in absence of immune cells (Nagaraju *et al.*, 2005; Mageriu *et al.*, 2020). However, the existing evidence of downregulated myokines seen in myositis patients show that both myokine upregulation and deficiency might play a pathological role in myositis.

Even though assumptions have been made regarding the pathological role of aberrant myokine release in IIM based upon the evidence of cytokines effects on skeletal muscle, the repertoire of myokines-induced alterations has not yet been characterised. In particular, to our knowledge, this is the first study dedicated to the effects of myositis secretome on myogenesis and mitochondrial function.

6.1.2 Aims of this chapter

1. Assess the impact of myositis muscle-derived secretome on myogenesis, MHC-I overexpression, mitochondrial function and ROS generation
2. Further explore the role of ROS generation on myositis secretome-associated changes in mitochondrial function using the antioxidant EUK-134.
3. Characterise the myokines repertoire of primary human myositis skeletal muscle cell line derived from patient biopsy samples with IBM and DM.

6.2 Methods

6.2.1 Cell culture, conditioned media, and treatments

Immortalised human skeletal muscle cells were grown in culture under as previously described in **Section 2.1.1**, and treated with conditioned media collected from human primary cells derived from patients with IBM and DM, as well as a healthy individual, for 48 hours; once collected, the media was stored at -80°C . Cells were also treated with EUK-134 for 24 hours, as explained in **Section 2.1.4**.

6.2.2 Immunostaining

Muscle cells were fixed using 4% paraformaldehyde, permeabilised using 0.5% (v/v) Triton X-100, and blocked using 3% goat serum supplemented with 0.05% Tween-20, as described in **Section 2.5.2**. Then, cells were incubated with primary antibody anti-HLA class I antibody at 4°C overnight, followed by incubation with goat anti-mouse IgG (H+L) Alexa Fluor 488 and DAPI for 1 hour. Stained cells were imaged using LEICA DMI6000 B inverted microscope.

6.2.3. Quantification of differentiation parameters

Cells exposed to different percentages of conditioned media (25%, 50%, and 100%), were differentiated into mature myotubes over 72 hours in differentiation media to determine optimal conditioned media percentage and their effect on muscle atrophy. Following immunostaining as described in **Section 2.5.2.3**, differentiation parameters were quantified using NIH ImageJ(**Section 2.5.2.3.1**).

6.2.4 Assessment of cellular respiration using Seahorse Extracellular Flux Analyser

Mitochondrial function and glycolytic activity were measured with an XFp Extracellular Flux Analyser, as explained in **Section 2.4.1**. Human skeletal muscle cells were seeded in an 8-well XFp plate at a density of 6×10^3 cells/well in growth media, and treated with conditioned media in presence or absence of EUK-134. OCR and ECAR were quantified using the Seahorse XFp Mito Stress Test (Agilent Technologies, UK), and normalised to total protein concentration using the Pierce™ BCA Protein Assay as previously explained in **Section 2.3.1**.

4.2.5 Assessment of mitochondrial membrane potential and mass

Human skeletal muscle myoblasts were seeded at 7×10^3 cells/well in a black-sided, clear-bottom 96-well plate, and treated as described above. TMRM was used to assess mitochondrial membrane potential ($\Delta\Psi_m$) that was normalised to mitochondrial mass using MitoTracker Green as described in **Section 2.7.2 and 2.7.4**.

6.2.6 Measurement of RONS

To quantify total cellular and mitochondrial superoxide, as well as mitochondrial hydroxyl radical generation, cells incubated with conditioned media with or without EUK134, were exposed to the following fluorophores, respectively: DHE (5 μ M, 20 minutes, 37°C), MitoSOX™ Red (5 μ M, 30 minutes, 37°C) and OH580 probe (1 hour, 37°C) as described in Section 2X. Following incubation, cells were maintained in phenol red-free DMEM and endpoint fluorescence was measured with the following excitation and emission wavelengths: DHE, 320/40 and 460/40 nm; MitoSOX™ Red, 360/40 and 590/35 nm; and OH580 probe, 530/25 and 590/35 nm, respectively. Measurements were normalised to total protein content.

6.2.7 Luminex multiplex assay

A human premixed multiplex kit was used to quantify the concentration of a number of cytokines, chemokines and growth factors in cell culture media of IBM, DM, and a healthy control individual in presence or absence of EUK-134, as described in **Section 2.3.5**. Myokines that were not falling within the assay standard curve were excluded from analysis.

6.2.8 Statistical analysis

GraphPad Prism version 8 was used to assess normally distributed data using one-way ANOVA followed by Tukey's test, and non-normally distributed data using Dunn's test. A p -value ≤ 0.05 was considered to be statistically significant.

6.3 Results

6.3.1 Conditioned media optimisation and assessment of differentiation parameters

Initially, conditioned media was prepared in normal growth media at 1:3 (25%), 1:1 (50%), or neat (100% conditioned media) to investigate conditioned media toxicity following 48 hours of exposure. In parallel, myoblast differentiation was examined in all conditioned media samples under the same conditions. As seen in **Figures 6.1, 6.2, and 6.3** showing exposure to the different dilutions conditioned media in growth media, no clear effects were noticeable on nuclei number or myoblast differentiation by any conditioned media percentage or sample. Further quantitative analysis was not performed because of limited sample availability.

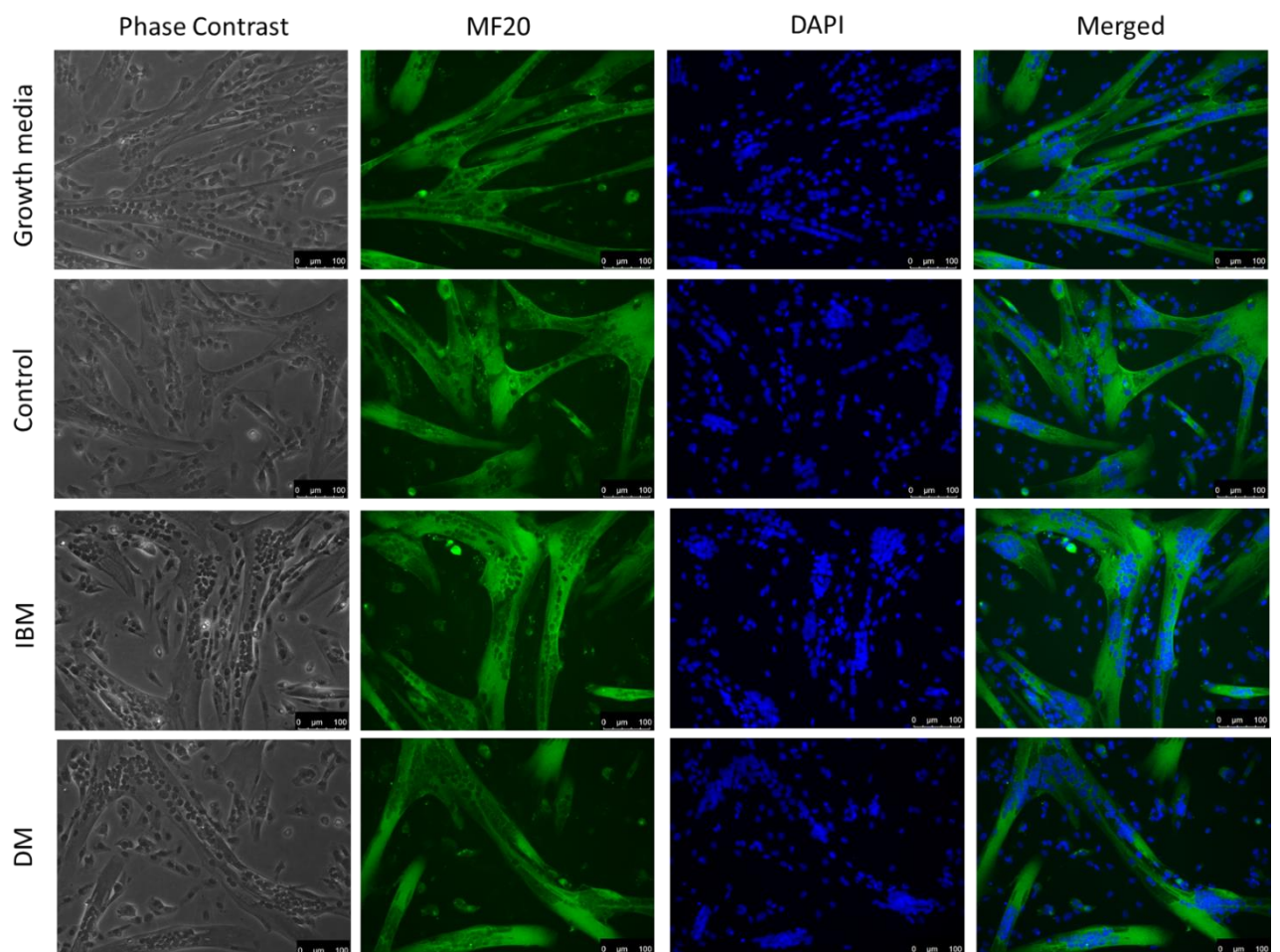


Figure 6.1 Muscle differentiation upon 1:3 conditioned media. Representative images of myotubes stained for MF20 (green fluorescence) and DAPI (blue fluorescence) following exposure to 1:3 conditioned media from primary (healthy) control, DM- and IBM-derived primary cells, or neat growth media. Images captured at 20× magnification. Scale bar = 100 μm.

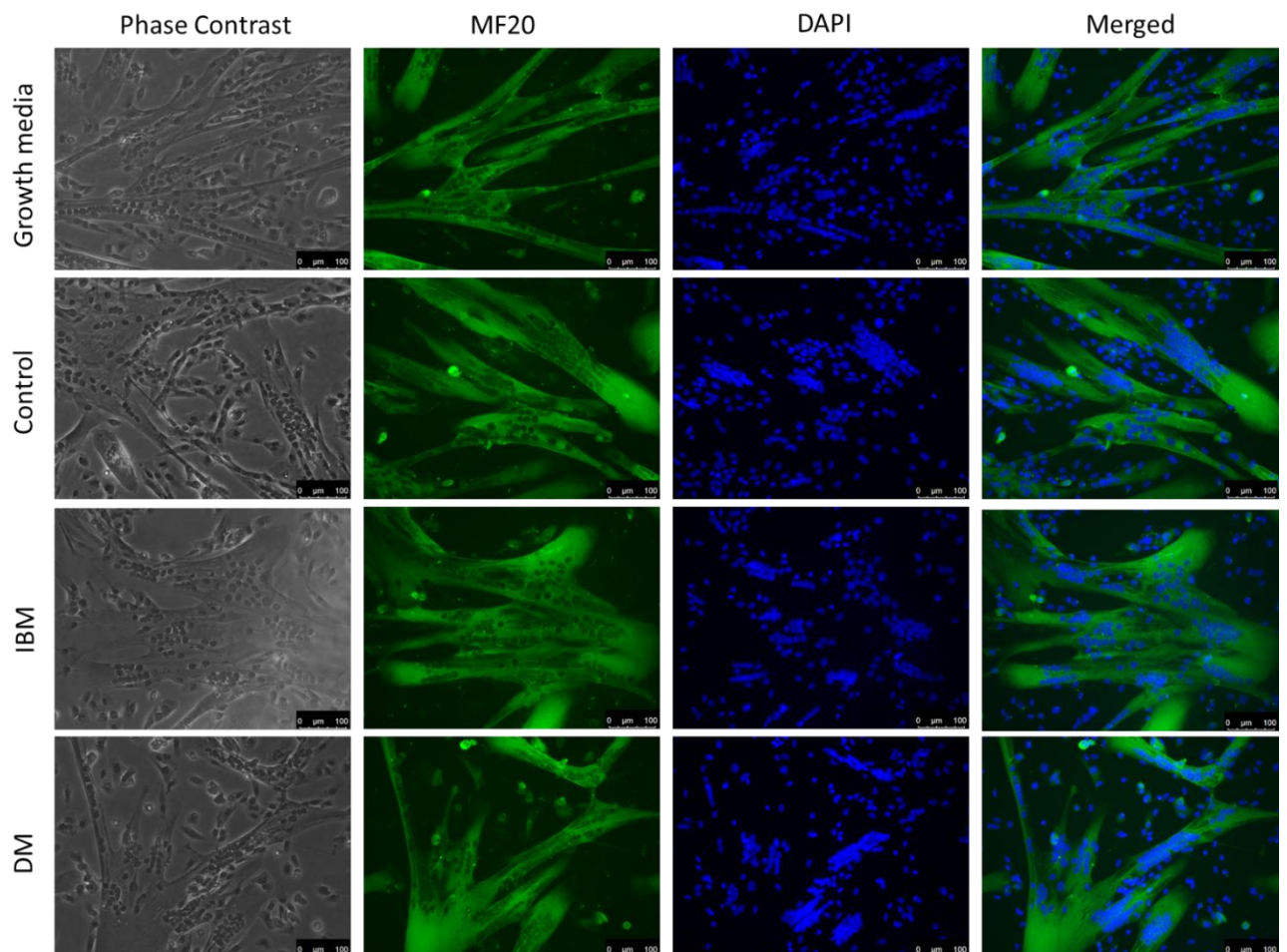


Figure 6.2 Muscle differentiation upon 1:2 conditioned media. Representative images of myotubes stained for MF20 (green fluorescence) and DAPI (blue fluorescence) following exposure to 1:2 conditioned media from primary (healthy) control, DM- and IBM-derived primary cells, or neat growth media. Images captured at 20× magnification. Scale bar = 100 μm.

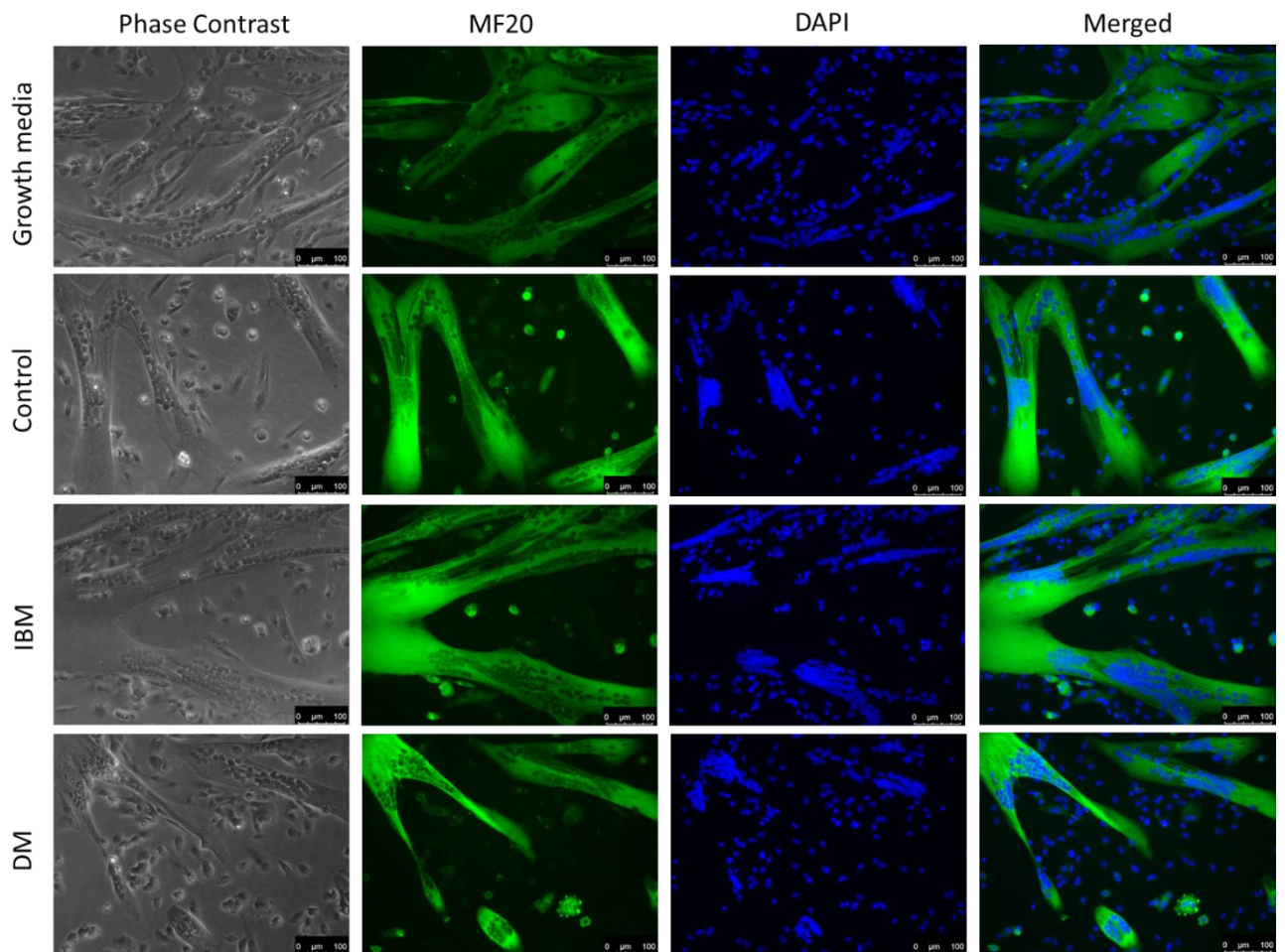


Figure 6.3 Muscle differentiation upon neat conditioned media. Representative images of myotubes stained for MF20 (green fluorescence) and DAPI (blue fluorescence) following exposure to neat conditioned media from primary (healthy) control, DM- and IBM-derived primary cells, or neat growth media. Images captured at 20× magnification. Scale bar = 100 μm.

6.3.2 Expression of HLA class I

The expression of HLA class I was also assessed via immunostaining in myoblasts grown in fresh growth media, as well as conditioned media derived from healthy control, IBM, and DM primary myoblasts. Qualitative analysis demonstrated no noticeable changes in

HLA class I fluorescence intensity between samples, while myoblasts viability seemed to be unaffected by conditioned media, as well (**Figure 6.4**).

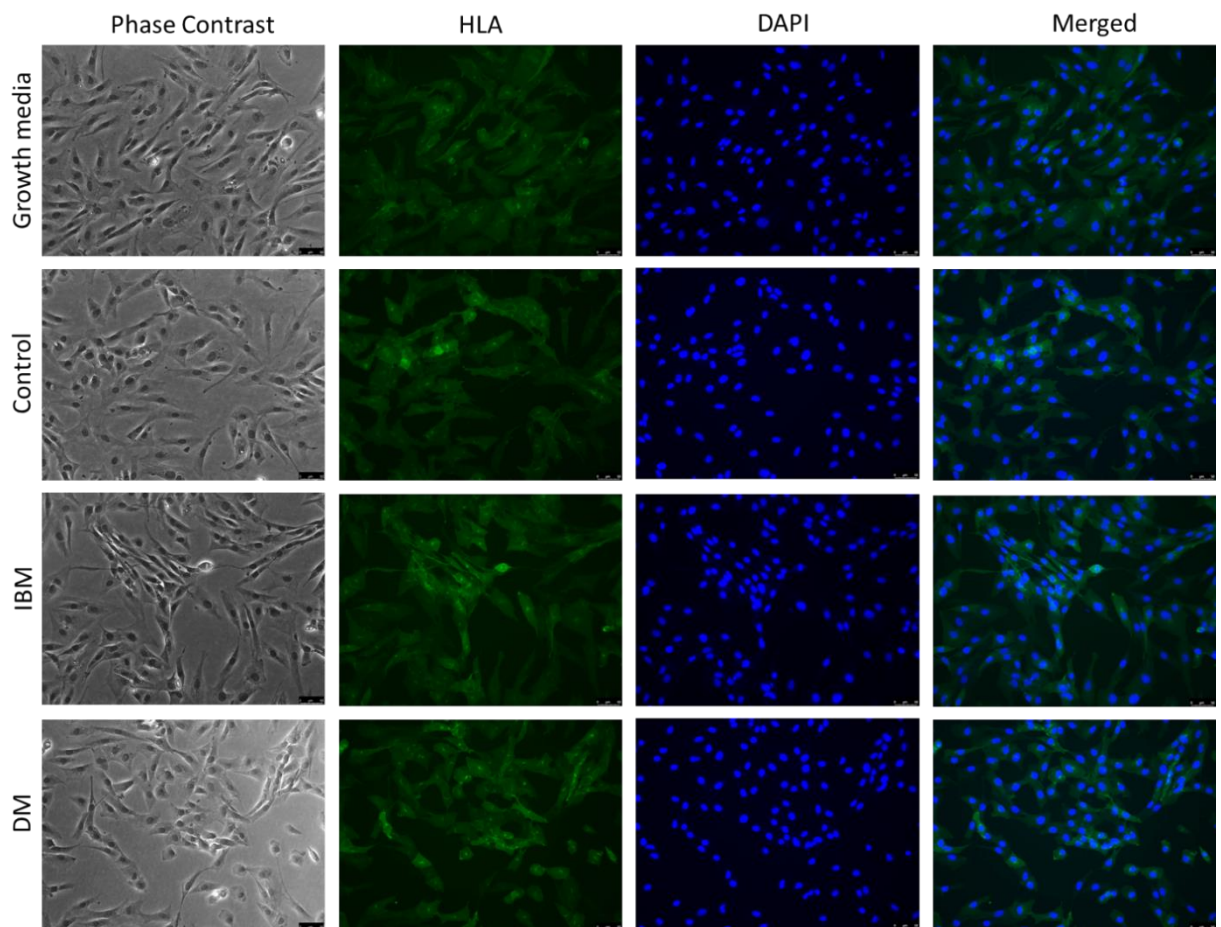
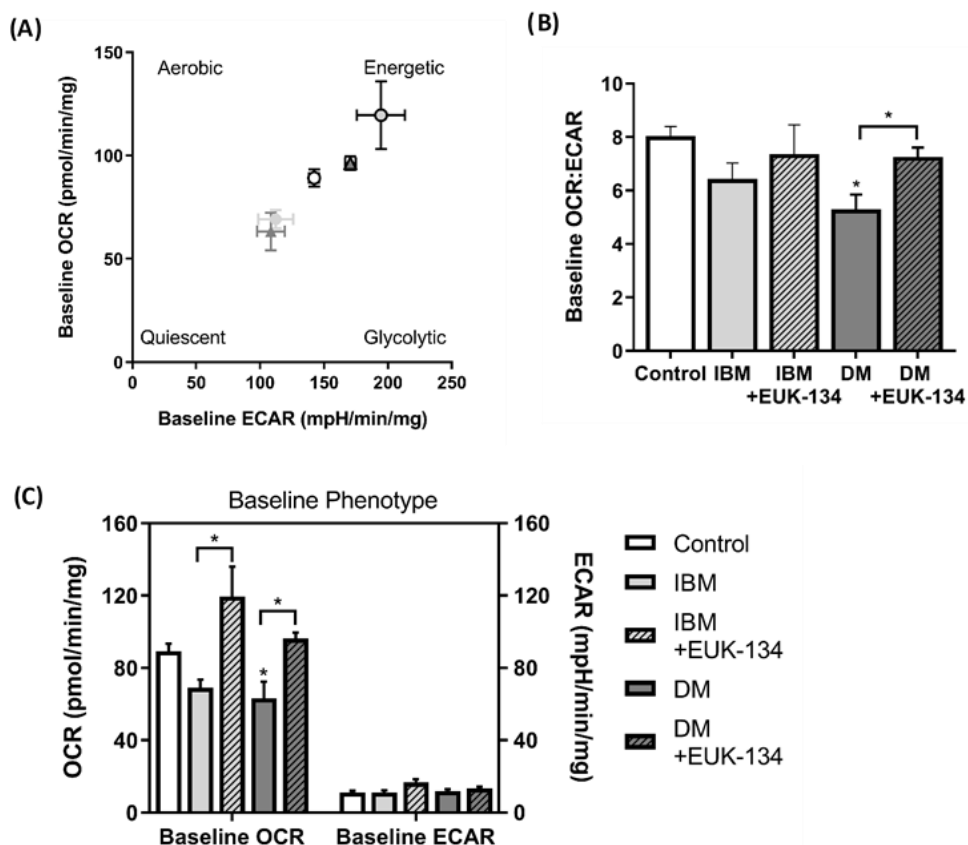


Figure 6.4 Expression of HLA class I upon neat conditioned media. Representative images of human immortalised myoblast treated with neat conditioned media from primary (healthy) control, DM- and IBM-derived primary cells, or neat growth media. Cells were stained with anti-HLA class I (green) and DAPI (blue). Images captured at 20× magnification. Scale bar = 50 μ m. Brightness was adjusted equally in each image to enhance visualisation.

6.3.3 Mitochondrial bioenergetic profile

The energy phenotype under baseline and stressed conditions, as well as the metabolic potential of myoblasts exposed to DM and IBM conditioned media (**Figure 6.5**) was defined using Seahorse extracellular flux analyser. According to **Figure 6.5A**, both IBM and DM conditioned media evoked a shifted metabolic status towards quiescent,

compared to control conditioned media, which did not occur in presence of EUK-134. Baseline OCR:ECAR ratio also shows that myoblasts exposed to IBM and DM conditioned media are potentially reliant on glycolysis, since lower ratio was found under those conditions compared to control (~10% and 35% of decrease, respectively, compared to control). In particular, statistical significance was reached by DM compared to control ($p=0.01$) and this was statistically prevented by EUK134 ($p=0.04$) (**Figure 6.5B**). Similar findings were seen by quantifying baseline and stressed phenotypes, with myoblasts incubated in IBM or DM conditioned media having reduced baseline and stress oxidative phosphorylation phenotype, while their glycolytic phenotype was not affected; DM conditioned media induced significant deficits, whereas EUK-134 was able to increase OCR phenotypes back to control levels when added to both IBM and DM conditioned media (**Figure 6.5C and D**). Interestingly, both IBM and DM conditioned media presented significantly reduced metabolic potential in respect to glycolytic flux, which was prevented by EUK-134, whereas no effects were seen in respect to oxidative phosphorylation, compared to control, indicating their overall inability to meet increasing energy demand, especially via glycolysis (**Figure 6.5E**).



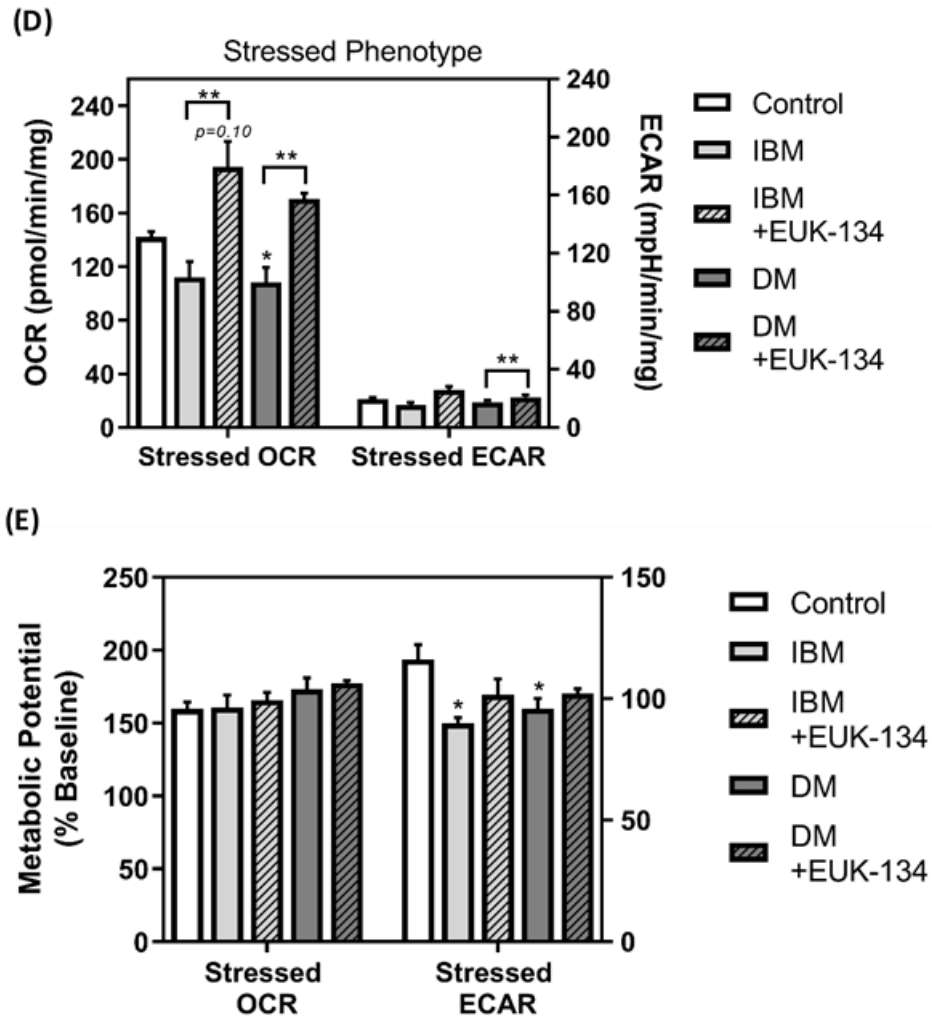


Figure 6.5 Energy phenotype of immortalized human skeletal myoblasts incubated with IBM and DM conditioned media. (A) Bioenergetic profile expressed as OCR versus ECAR measured under basal conditions. Statistical analysis of **(B)** baseline OCR to ECAR ratio, **(C)** OCR and ECAR baseline phenotype, **(D)** OCR and ECAR stressed phenotype, and **(E)** metabolic potential. Data were normalised to total protein content. Data represent mean \pm S.E.M ($n=3$), $**p \leq 0.05$, $**p < 0.01$ compared to control or otherwise stated.

According to the real-time OCR trace, representing the cells' bioenergetic profile, both IBM and DM conditioned media induced an overall increase in OCR compared to the healthy control conditioned media at basal conditions as well as followed by the addition of various metabolic modulators. Furthermore, EUK-134 treatment restored OCR to control levels (**Figure 6.6**).

The bioenergetic profile was used to calculate the individual mitochondrial function parameters of IBM and DM conditioned media in presence or absence of EUK-134 (**Figure 6.6**). All immortalised human skeletal muscle cells exposed to IBM conditioned media presented a trend of decrease in non-mitochondrial, basal, and maximal, leak and ATP-linked respiration, as well as spare respiratory capacity, even though none of them showed statistical significance (**Figure 6.7**). The presence of EUK-134 induced an increase in respiration compared to IBM that was close to statistical significance under basal and maximal conditions ($p=0.06$ and $p=0.13$, respectively) (**Figure 6.7B and C**). It should also be noted that IBM conditioned media in presence of EUK-134 produced a statistically significant increase in proton leak compared to IBM conditioned media only (**Figure 6.7E**). Cells incubated with DM conditioned media also showed decreased OCR, reaching statistical significance in basal, maximal, and ATP-linked respiration, while the decrease in spare respiratory capacity reached a p value of 0.06, compared to those incubated with control (**Figure 6.7**). EUK-134 was able to restore OCR to control levels in all mitochondrial function parameters (**Figure 6.6 and 6.7**).

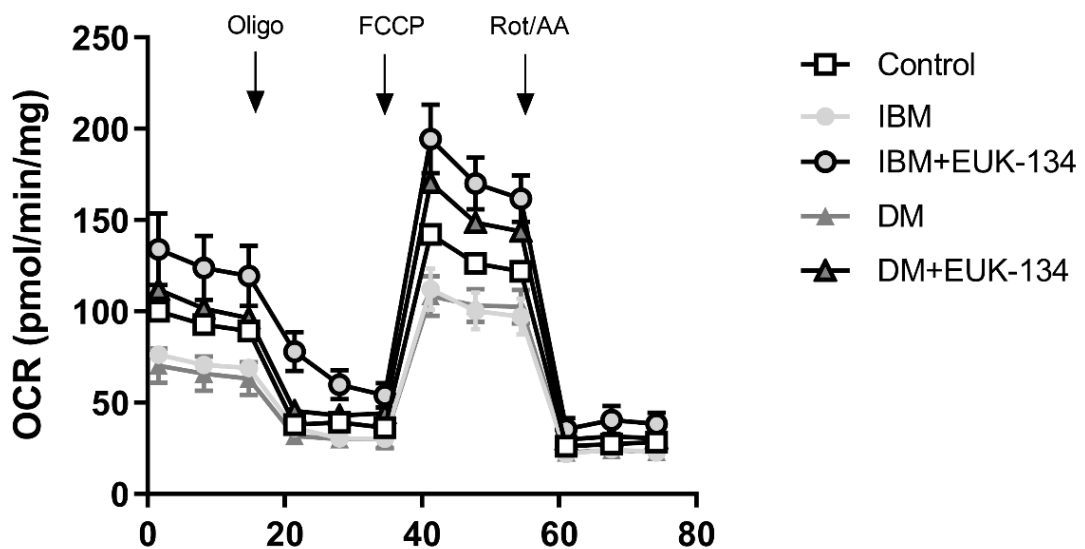


Figure 6.6 Bioenergetic profile of immortalized human skeletal myoblasts incubated with IBM and DM conditioned media. Real-time measurements of oxygen consumption rate (OCR) following the sequential injection of oligomycin, FCCP, and a mixture of rotenone/antimycin A ($n=3$).

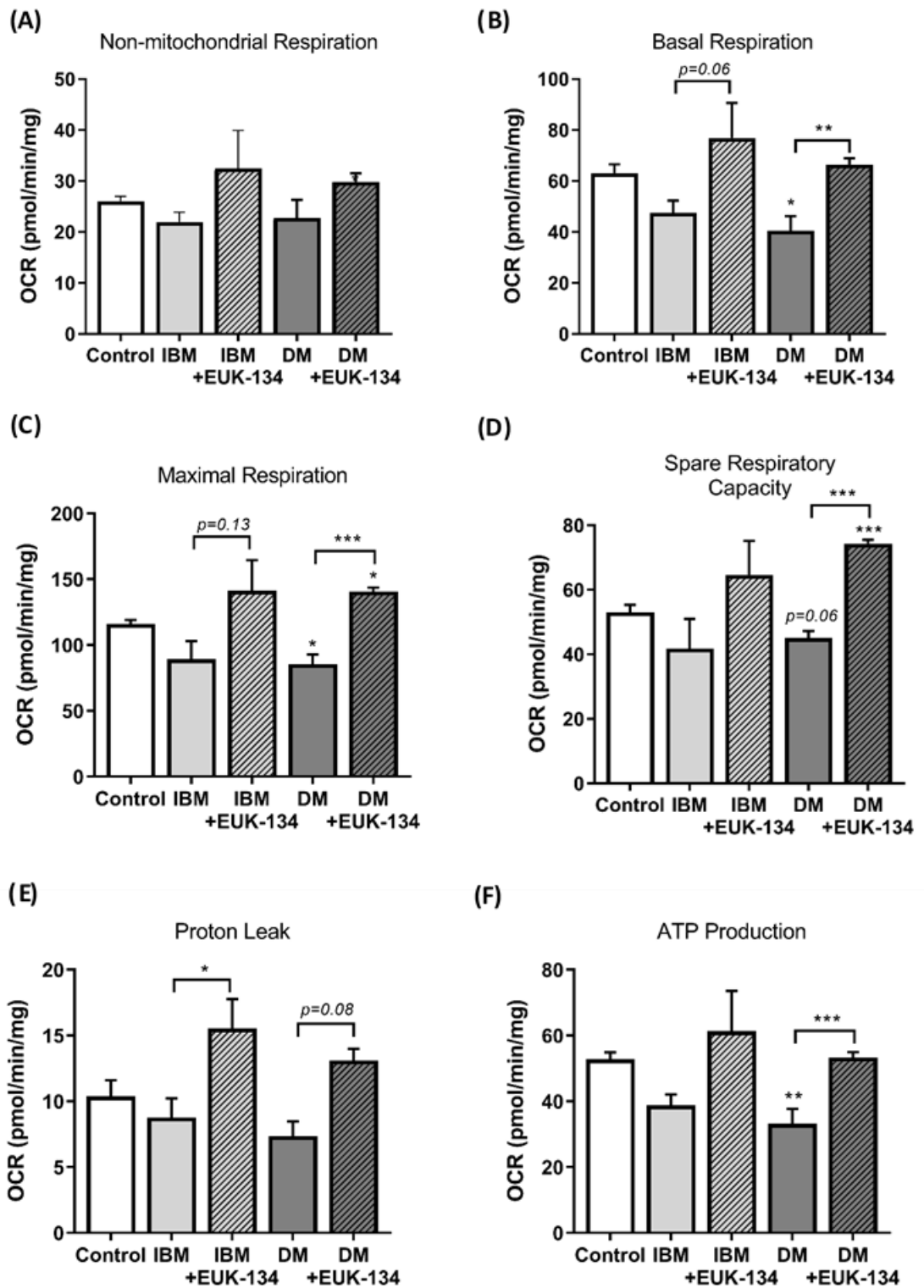


Figure 6.7 Individual mitochondrial parameters calculated from the bioenergetic profile. (A–F) Mitochondrial parameters – non-mitochondrial respiration, basal respiration, maximal respiration, spare respiratory capacity, proton leak, and ATP production – per mg of protein, in myoblasts treated with 100% condition media from primary (healthy)

control, DM- and IBM-derived primary cells, in presence or absence of EUK-134. Data are normalised to protein content and represent mean \pm S.E.M. ($n=3$), * $p \leq 0.05$, ** $p < 0.01$, *** $p < 0.001$ compared to primary control conditioned media.

Further analysis on mitochondrial function also presented a defect in phosphorylating respiration induced by DM conditioned media, which was unable to be restored by EUK-134 (Figure 6.8). No statistical significance was seen in coupling efficiency (%) or respiratory control ratio in neither IBM nor DM conditioned media compared to control conditioned media (Figure 6.8).

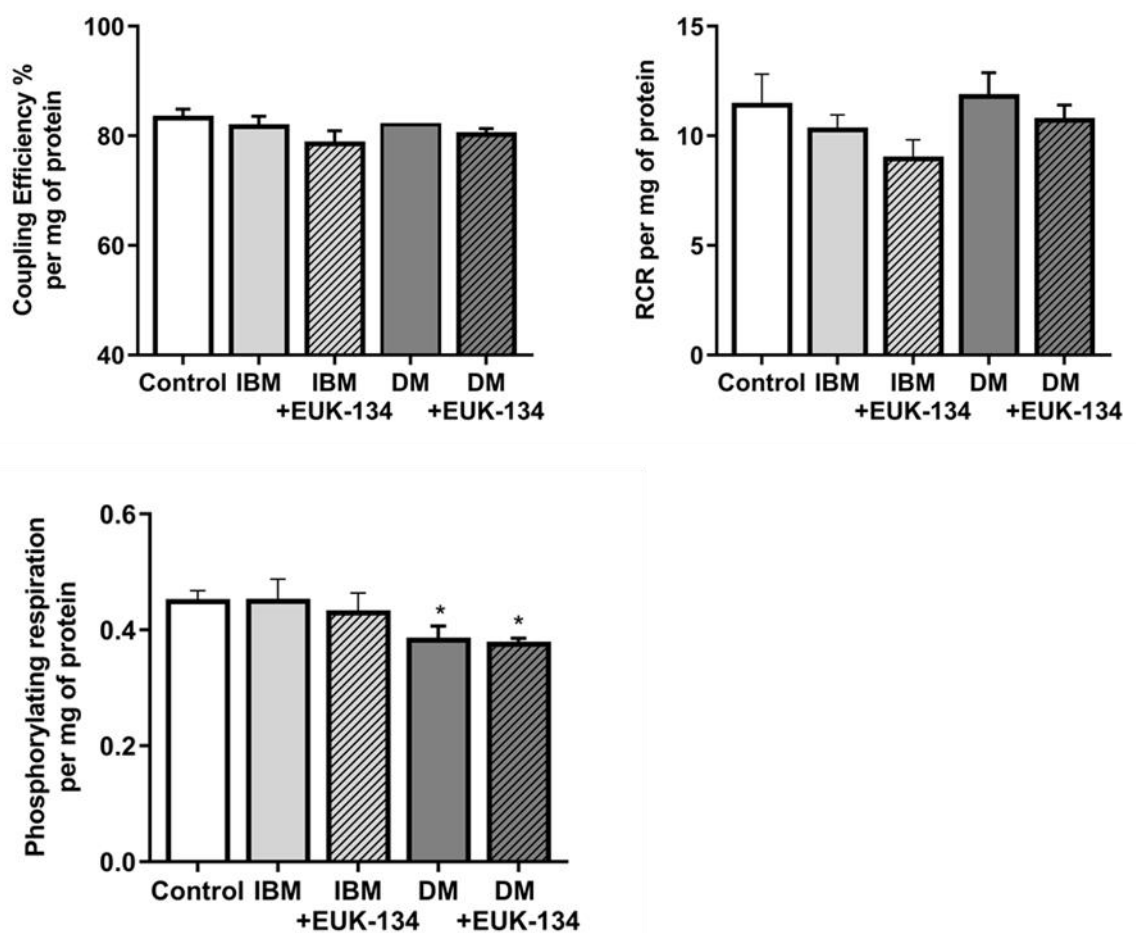
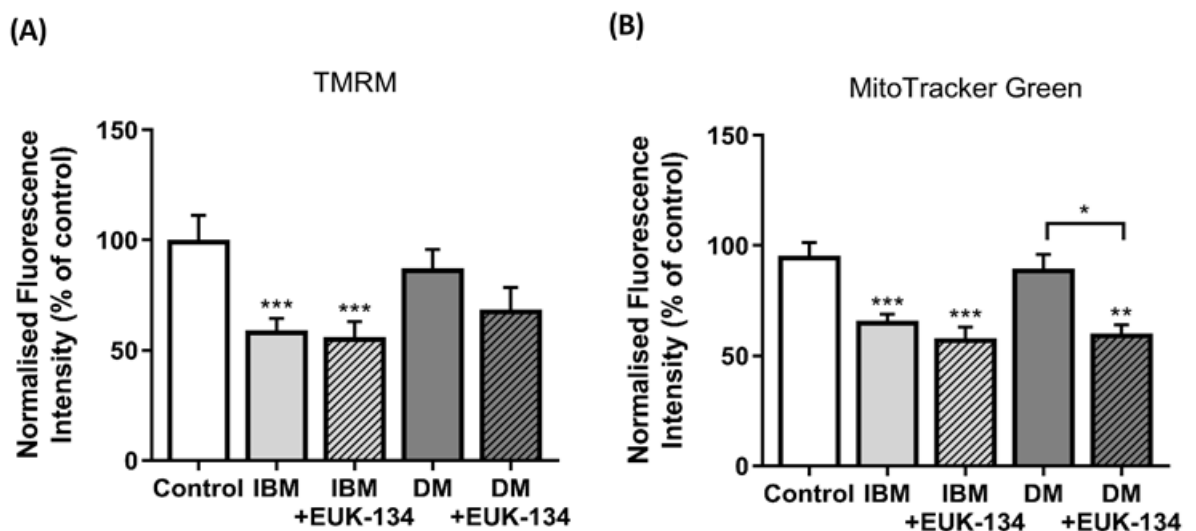


Figure 6.8 Normalised respiratory flux control ratios. Coupling efficiency (%), respiratory control ratio (RCR), and phosphorylating respiration per mg of protein in immortalised human skeletal myoblast incubated with IBM and DM conditioned media in presence or

absence of EUK-134, calculated from individual mitochondrial parameters. Data represent mean \pm S.E.M. ($n=3$), $*p \leq 0.05$ compared to control.

6.3.4 Mitochondrial mass and membrane potential

To further examine mitochondrial dysfunction under myositic conditioned media compared to control conditioned media, mitochondrial membrane potential was assessed using TMRM fluorophore. Initial TMRM data interpretation showed significantly depleted TMRM fluorescence intensity in myoblasts exposed to IBM conditioned media in presence or absence of EUK-134 ($p < 0.001$) (**Figure 6.9A**). As previously suggested by (Perry *et al.*, 2005), TMRM fluorescence intensity was normalised to MitoTracker Green fluorescence, indicative of mitochondrial mass. Data showed that IBM conditioned media can induce a significant decrease in MitoTracker Green fluorescence when added with or without EUK-134 (**Figure 6.9B**); therefore, the IBM conditioned media-induced reduction in TMRM fluorescence intensity was ameliorated when normalised to MitoTracker Green fluorescence intensity (**Figure 6.9C**). Surprisingly though, EUK-134 treatment also led to significantly reduced MitoTracker Green fluorescence intensity compared to both DM and control conditioned media (**Figure 6.9B**).



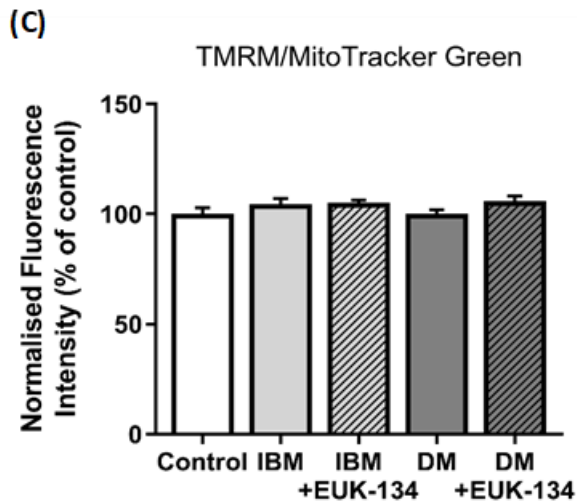


Figure 6.9 Mitochondrial membrane potential and mass. Relative change (%) in **(A)** TMRM fluorescence intensity (mitochondrial membrane potential), **(B)** MitoTracker Green fluorescence intensity (mitochondrial mass), and **(C)** TMRM fluorescence intensity normalised to MitoTracker Green. Data were normalised to protein content and represent mean \pm S.E.M. ($n=3$), * $p \leq 0.05$, ** $p < 0.01$, *** $p < 0.001$ compared to control or otherwise stated.

6.3.5 ROS generation

Different aspects of ROS generation in response to myotoc conditioned media were assessed. MitoSOX Red measurement, used to assess mitochondrial superoxide, showed a substantial increase in MitoSOX Red fluorescence intensity by DM conditioned media ($p=0.08$), which was attenuated by EUK-134 treatment ($\sim 40\%$ of decrease). In contrast, no changes were seen in MitoSOX Red fluorescence intensity induced by IBM conditioned media in presence or absence of EUK-134 (**Figure 6.10A**). Mitochondrial superoxide levels were also normalised to mitochondrial mass using MitoTracker Green. As expected, normalised MitoSOX Red fluorescence intensity levels were still substantially increased by DM conditioned media ($p=0.08$), but the decrease by EUK-134 was less ($\sim 10\%$ of decrease) (**Figure 6.10B**). Interestingly, decreased OH580 and DHE fluorescence intensity levels was seen by both IBM and DM conditioned media in presence or absence of EUK-134 compared to control conditioned media (**Figure 6.10C and D**). In particular, a p value

of 0.07 was seen by IBM conditioned media, with statistical significance being produced in presence of EUK-134 (**Figure 6.10D**).

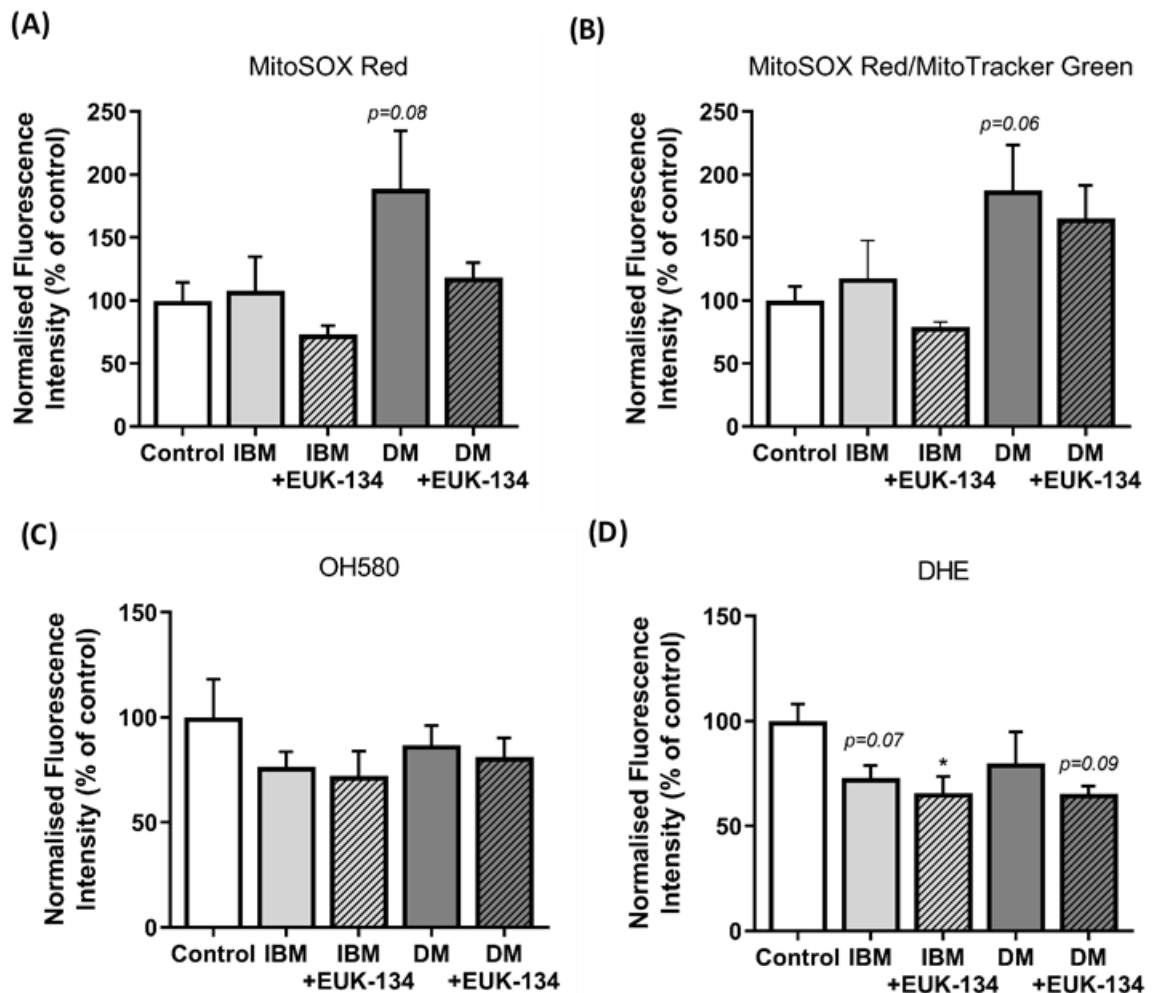
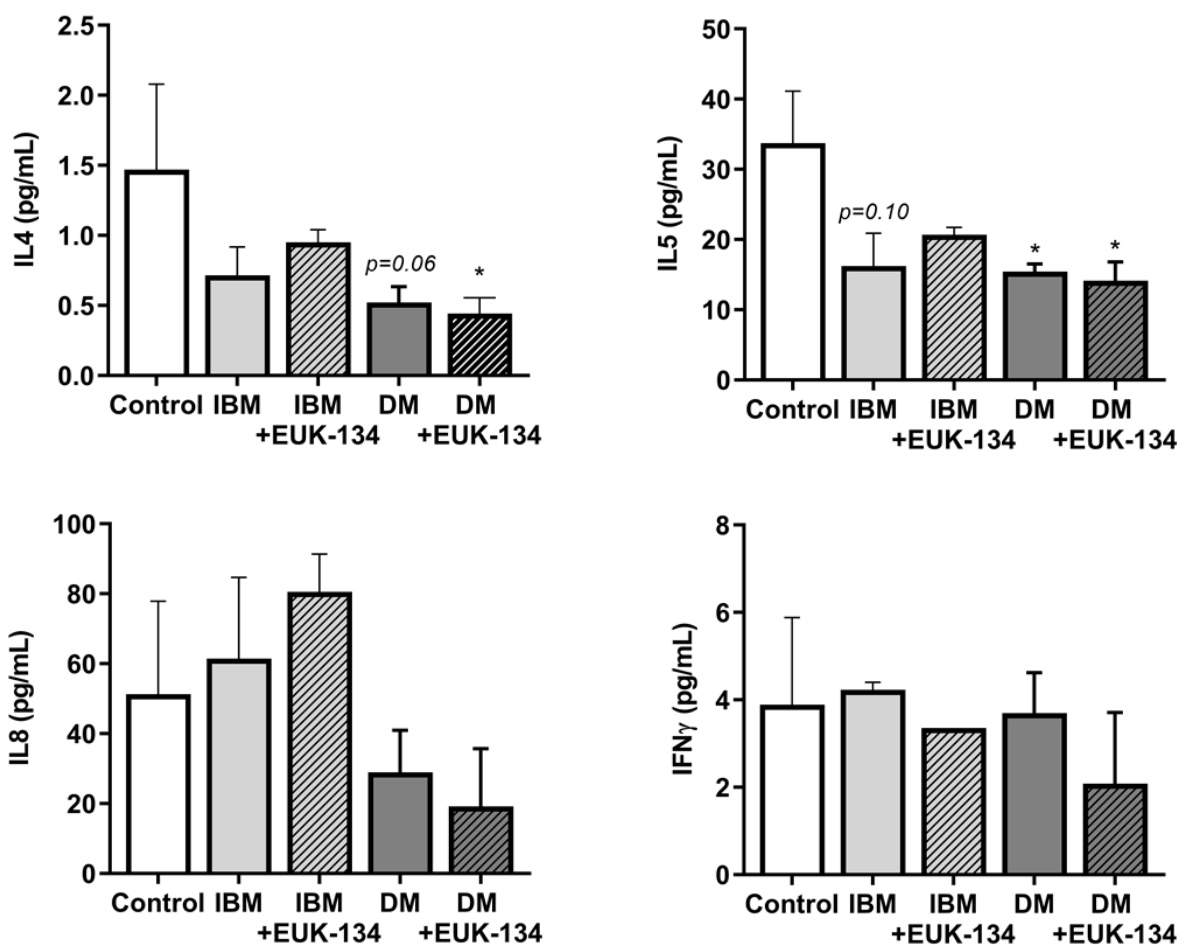


Figure 6.10 ROS generation. Relative change (% of control) in **(A)** mitochondrial superoxide (MitoSOX Red), **(B)** mitochondrial superoxide (MitoSOX Red) normalised to mitochondrial mass (MitoTracker Green), **(C)** mitochondrial hydroxyl radical (OH580), and **(D)** total cellular superoxide levels (DHE). Data were normalised to protein content and represent mean \pm S.E.M. ($n=3-4$), $*p \leq 0.05$ compared to control or otherwise stated.

6.3.6 Myokines secretome of IBM and DM myoblasts

According to **Figure 6.11**, Luminex multiplex assay analysis of human cytokines and chemokines revealed reduced levels (mean \pm S.E.M., pg/mL) of IL4 (0.52 ± 0.11 , $p=0.06$), IL5

(15.43 ± 1.09 , $p \leq 0.05$), and IL8 (28.94 ± 12.03) in DM conditioned media compared to healthy control conditioned media (1.47 ± 0.61 , 33.74 ± 7.40 , and 51.28 ± 26.63 , respectively), with EUK-134 treatment being unable to ameliorate their decline; instead, statistically significant depletion was also seen in IL4 (0.95 ± 0.09) and IL5 (14.13 ± 2.69) levels in presence of EUK-134. Similarly, IL4 (0.72 ± 0.20) and IL5 (16.24 ± 4.67 , $p = 0.10$) levels were decreased in IBM conditioned media compared with control conditioned media, an effect that was slightly prevented by EUK-134. In contrast, CCL5/RANTES levels were substantially elevated in both IBM (5.13 ± 1.02) and DM (6.46 ± 2.55) conditioned media compared to control conditioned media (2.86 ± 0.97), an increase that was inhibited by EUK-134 (1.89 and 1.63 ± 0.86 , respectively). Last but not least, no changes were noticeable in IFN γ and CCL2/MCP-1 levels in IBM and DM conditioned media; a slight decrease was induced though by EUK-134, especially in CCL2/MCP-1 levels (**Figure 6.11**).



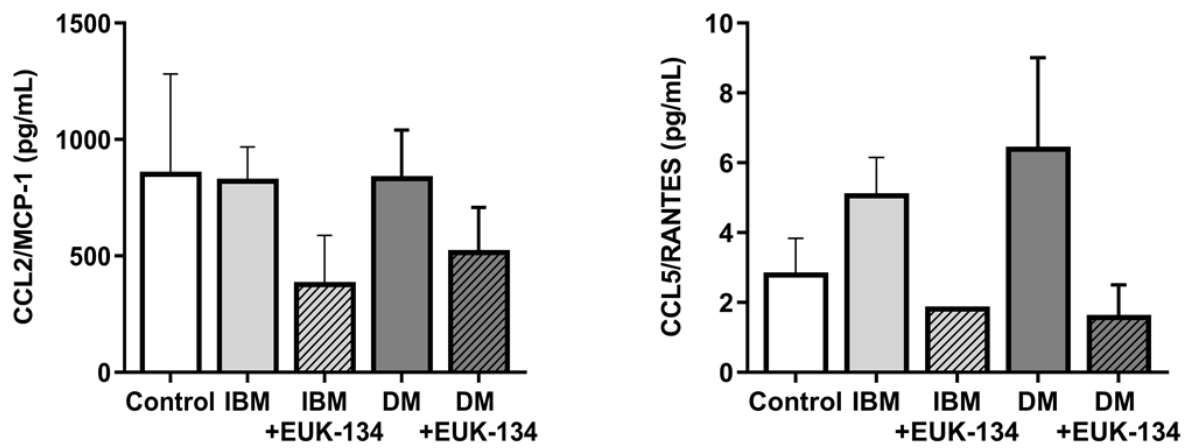


Figure 6.11 IBM and DM myokines secretome. IL4, IL5, IL8, IFN γ , CCL2/MCP-1, CCL5/RANTES levels (pg/mL) released by skeletal myoblasts isolated from individuals with IBM and DM, and treated with or without EUK-134 for 24 hours. Data represent mean \pm S.E.M. ($n=2-4$), $*p \leq 0.05$ compared to control.

6.4 Discussion

Given the paracrine and endocrine capabilities of skeletal muscle, the role of its secreted factors, the so-called myokines, has gained a great attention in respect to muscle health and disease. Myokines secretome has emerged as a new era of investigation in myositis pathogenesis, with however, limited evidence existing on the pathogenic effect of myositis-associated myokines and their underlying pathomechanisms (Mageriu *et al.*, 2020; Lightfoot and Cooper, 2016). The focus of this study was aimed at gaining an insight into the myositic myokines secretome and its effects on muscle atrophy, MHC-I expression, and mitochondrial bioenergetics, and ROS generation, parameters that have been suggested to play a prominent role in myositis pathogenesis (Nagaraju *et al.*, 2005; Basualto-Alarcón *et al.*, 2020).

Muscle atrophy is characterised by inhibited myoblast differentiation and/or impaired muscle morphology (Al-Dabbagh *et al.*, 2015). Initially, three conditioned media dilutions in normal growth media were used to assess any effect on myoblast differentiation in parallel to cells viability. Qualitative analyses showed that the morphology and differentiation capacity of myoblasts exposed to conditioned media derived from DM or IBM primary cells remained unaffected with elongated, branched, and multinucleated myotubes being evident. Thus, these data suggest no direct effect of myositic myokines secretome on disease-associated muscle atrophy; however, it should be noted that further in-depth quantitative analysis should be established involving longer time points to make any conclusive statements. Similarly, MHC class I expression in myoblasts was not altered by myositic conditioned media compared to healthy control conditioned media or normal growth media, indicating that the observed surface overexpression of MHC class I in myositic muscle (Vattemi *et al.*, 2014) might not be mediated by the myositic secretome.

To our knowledge, this is the first study examining the role of myositic myokines secretome in mitochondrial impairments. A major finding of the present study was the myositic (both IBM and DM) secretome-induced deficit in mitochondrial respiration and a trend towards a quiescent state; these deficits were evident under both basal and stressed conditions. In particular, significant depletion was seen in basal, maximal, and ATP-linked respiration, accompanying by reduced phosphorylating respiration capacity

induced by the DM myokines secretome. Furthermore, data showed that even though cells were potentially reliant on glycolysis when coupled for oxygen consumption and energy production via complex V activity under basal conditions, they presented inability to increase glycolytic flux to compensate for energy demands under stressed conditions, as seen by the depressed ECAR metabolic potential.

Another interesting finding of this study was the reduced mitochondrial mass observation in response to IBM conditioned media exposure, but not DM conditioned media. A reduction in mitochondrial mass could be resulted by upregulated mitophagy, pointing out a potential mechanism of IBM myokines secretome, (Benischke *et al.*, 2017). Furthermore, low number of mitochondrial DNA copy has been previously reported in sIBM, which however, has not been consistent (Brady *et al.*, 2018; Bhatt *et al.*, 2019). Thus, further investigation is needed in mitophagy processes in IBM.

The differential effects of IBM and DM conditioned media on mitochondrial biogenesis or mitophagy and mitochondrial respiratory processes in skeletal muscle recommends a differential myokine secretome between those myositis types. This hypothesis is in accordance with an early study that suggested the differential expression of chemokines in IIMs (De Bleecker *et al.*, 2002). Based on this, myokines secretome in IBM and DM conditioned media was quantified using Luminex multiplex assay of human cytokines, chemokines, and growth factors. Overall, data showed similar levels of IL4, IL5, IFN γ , CCL2/MCP-1, and CCL5/RANTES levels, whereas only IL8 seemed to be differentially expressed between IBM and DM conditioned media. In particular, IL4, IL5, and IL8 were reduced in both samples, with stronger depletion being evident in DM sample. In contrast, IL8 was overstimulated in IBM, accompanying by increased levels of CCL5 in both IBM and DM samples.

So far, most of the studies have suggested the potential role of myokines release, acting as pro-inflammatory cytokines, in myositis, such as CCL2, CCL3, CCL4, and MCP-1 (Lightfoot *et al.*, 2015; Civatte *et al.*, 2005; Bartoli *et al.*, 2001). In this study, CCL5 seemed to be increased in both IBM and DM samples. This finding is in controversy with a previous study showing that CCL5 mRNA expression in IIMs muscle biopsy samples (PM, IBM, and DM) was no different compared to normal muscle control sample (Civatte *et al.*, 2005). However, in another study, exercise was proposed to induce a reduction in CCL5 as seen

via a cytokines assay, ELISA and qPCR following electric-pulse stimulation of C2C12 myotubes, as well as mouse experiments of voluntary wheel-running exercise (Ishiuchi *et al.*, 2018); this reduction was explained as a mechanism of inflammation attenuation since CCL5 is known to have a chief role in stimulating immune cells recruitment in inflammation (Ishiuchi *et al.*, 2018). In general, less evidence is known on potentially depleted myokines levels in healthy or diseased muscle. In myositis particularly, InsI6 has been found to be downregulated in PM and DM muscle, even though, overstimulated InsI6 has been evident in a mouse myositic model (Zeng *et al.*, 2014). In that case, Zeng *et al.* (2014) suggested that the opposite findings might rely on the potentially different mechanisms induced in short-term and chronic study disease models. It is undoubtable though that further research is strongly required on deriving conclusions on myokines secretome and its related effects.

Finally, this chapter emphasises the potential role of ROS generation in myokines secretome-associated mitochondrial respiration deficits in DM and IBM, even though ROS generation analysis showed only IBM conditioned media-induced elevation in mitochondrial superoxide, whereas mitochondrial hydroxyl peroxide and total cellular superoxide levels were unaffected. Targeting ROS generation using EUK-134 was able to increase mitochondrial respiration compared to DM and IBM conditioned media, serving a strong foundation for future research on the involvement of ROS generation downstream myositic myokines secretome.

Overall, adding to the current myositic myokines research, the present study suggests the potential downregulation of IL4, IL5, and IL8, specifically in DM disease, and upregulation of CCL5. The observed myokines secretome-induced depletion in mitochondrial respiration also provides evidence of the association of myokines with non-immuned mediated mechanisms involved in myositis pathogenesis. Therefore, deriving an understanding of the myokines secretome, its downstream non-immune mediated mechanisms in skeletal muscle, and its contribution to muscle atrophy and weakness in myositis disease could help point to novel therapeutic approaches.

CHAPTER 7:

General discussion and Future directions

7.1 Major findings and general discussion

Mitochondrial perturbations have been a putative mechanism involved in myositis pathogenesis, even though the foundation for their initiation and perpetuation has not been fully defined, with the literature lacking adequate evidence at a molecular and functional level. Thus, the overarching aim of this research was to assess changes in mitochondrial function upon different stimulus that have shown a crucial contribution to myositis pathogenesis, as well. This also explains this thesis' hypothesis that different intrinsic mechanisms, potentially both immune and non-immune mediated, overlap and operate synergistically and/or independently in persisting muscle damage in myositis disease. Therefore, this thesis also focused on the development of *in vitro* human skeletal muscle models for investigating those mechanisms. The main findings of this study on each model are as following:

Pharmacological cell model of ER stress using tunicamycin

1. ER stress activation inhibits myoblast differentiation and contributes to muscle atrophy; effects that are partially ameliorated by targeting ROS generation.
2. Myoblasts under ER stress rely mostly on oxidative phosphorylation, while they present decreased glycolytic metabolic potential.
3. ER stress activation induces altered bioenergetic profile, which is prevented by targeting ROS generation. This is characterised by increased mitochondrial oxygen consumption, potentially as an attempt to compensate to energetic deficits, as decreased reserve capacity, and ATP-linked respiration, coupling efficiency, RCR, and phosphorylating respiration, as well as increased proton leak are observed. All these aspects of mitochondrial bioenergetic parameters were significantly prevented in presence of EUK-134.
4. ER stress activation increases mitochondrial biogenesis and alters mitochondrial morphology in a ROS-mediated manner. The findings of elevated mitochondrial interconnectivity and elongation, as well as increased *MFN2* mRNA expression reflect ER stress-associated mitochondrial fusion processes, while increases in mitochondrial

perimeter and area, accompanying by upregulated *FIS1* and *DRP1* mRNA expression, indicate high propensity for mitochondrial fission processes.

Genetically modified cell model of an immortalised human skeletal muscle cell line overexpressing MHC-I and treated with or without type I IFNs

1. Type I IFNs have differential effects on MHC-I regulation, mitochondrial respiration, and ROS generation in human skeletal myoblast. Data suggest that IFN α induces mitochondrial alternations potentially via MHC-I overexpression, whereas IFN β can also act independently to MHC-I overexpression, directly inducing stronger effects than IFN α on its own.
2. MHC-I overexpression in myoblasts leads to an overall depleted energetic phenotype in relation to both oxidative phosphorylation and glycolytic flux, as well as mitochondrial membrane potential. This depletion is exacerbated by IFN α or IFN β exposure, showing their strong combinational effects with MHC-I overexpression.
3. MHC-I overexpression and type I IFNs evoke distinct segregated effects on RONS generation, with MHC-I overexpression showing contribution to NO emission, whereas type I IFNs present inhibitory NO effects.

Clinical cell model of IBM and DM-derived primary human skeletal muscle cell line

1. Both IBM and DM primary cells showed an overall increase in mitochondrial respiratory and glycolytic flux, as well as increased metabolic potential, with DM exerting stronger respiratory effects compared to IBM, indicative of their attempt to adapt to stress. However, mitochondrial dysfunction was evident by elevated proton leak, as well as depleted phosphorylating respiration, and mitochondrial membrane potential.
2. EUK-134 intervention in myositis primary cells prevented mitochondrial alterations, suggesting that targeting ROS generation could potentially rescue myoblasts from stress, and therefore, respiratory adaptation was not required for cell survival maintenance.
3. The role of ROS generation in myositis primary cells mechanisms was further supported by a trend towards mitochondrial superoxide generation in DM myoblasts and hydrogen peroxide in IBM myoblasts.

Characterisation of myositic muscle secretome mechanisms

1. Myositic myokines secretome led to impaired energetic phenotype, with an observed deficit in oxidative phosphorylation, described by decreased basal, maximal, and ATP-linked respiration, as well as reserve capacity. Those effects were stronger by DM myokines secretome, further enhancing the differential pattern of mitochondrial-associated impairments in DM and IBM muscle.
2. Myositic myokines secretome-induced mitochondrial alterations seemed to be ROS-mediated, as EUK-134 treatment was able to prevent most of them.
3. The myositic secretome was described by reduced IL5 and IL4 levels in both DM and IBM samples, with DM presenting a greater degree of reduction, as well as that of IL8. In contrast, CCL5/RANTES seemed to be stimulated in both DM and IBM secretomes.

In summary, these studies offer an insight into new pathological mechanisms and therapeutic targets in myositis disease, which can be further examined in the suggested novel myositis human *in vitro* models to enable their translation into clinical practice. It is of great interest that this thesis not only provides segregated effects of the different study models, downstream to the various stimulus, but also a proportion of accordance between models.

ER stress activation following pharmacological intervention using tunicamycin, provided evidence of an overall increase in mitochondrial oxygen consumption, which however, was not attributable to fully functional mitochondria. Specifically, disrupted mitochondria function was evident by reduced normalised respiratory flux control ratios, accompanying by elevated proton leak and mitochondrial membrane depolarisation (Chapter 3). Consistently, this trend of dysfunctional mitochondria besides the increase in overall mitochondrial oxygen consumption, was also seen in primary skeletal muscle cells derived from individuals with IBM and DM; in particular, DM was able to induce more drastic effects in mitochondrial function compared to IBM (Chapter 5). The observation of promoted mitochondrial respiration has been previously reported as an adaptive response to stress, to meet increasing energetic demand, especially when cells present inability in increasing glycolytic flux (Jackisch *et al.*, 2016; Knupp *et al.*, 2019). Elevated levels of ER stress activation markers have been previously found in both DM and IBM muscle biopsy samples (Nagaraju *et al.*, 2005; Nogalska *et al.*, 2015). Even though

ER stress induction in human primary myositis myoblasts was not assessed in this case, these findings further support a possible link between ER stress-induced mitochondrial abnormalities.

MHC-I overexpression following transfection with HLA-A2/K^b vector presented a different pattern of mitochondrial respiratory alterations compared to the *in vitro* ER stress model. Instead, MHC-I overexpression was associated with an overall reduction in mitochondrial respiration, which was exacerbated in presence of type I IFNs, a characteristic feature in individuals with DM (Chapter 4). Overall, data suggested their strong combinational effects derived through their synergistic but also independent activity. Furthermore, these findings highlight the importance of considering and studying the combinational effects of the various mechanisms involved in a disease to gain a better understanding of their mechanisms of action. Nagaraju *et al.* (2005) suggested that MHC-I overexpression was an early characteristic of myositis that seems to induce ER stress activation, which can further upregulate endogenous MHC class I expression, generating a self-sustaining loop that leads to muscle atrophy, as also seen in our *in vitro* ER stress model. However, in this case, ER stress-associated MHC-I expression was not assessed that makes the interpretation more challenging; it can be suggested that endogenous MHC-I upregulation is a late effect of ER stress activation, which might not be apparent at the early stages of myositis disease either. The strong effects of extensive MHC-I upregulation are further supported by the finding that DM-derived primary myoblasts showed a striking mitochondrial respiratory depression and a higher MHC-I upregulation compared to IBM-derived primary myoblasts.

Similar to MHC-I-induced mitochondrial abnormalities, the muscle secretome of IBM and DM myoblasts evoked an overall reduction in mitochondrial respiration, with striking findings being seen by DM muscle secretome. IBM and DM muscle secretome was characterised by decreased IL4 and IL5 levels, and increased CCL5 levels (Chapter 6). Decreases in myokines levels were not expected, considering that so far, much attention has been given on elevated myokines levels under pathological conditions. Interestingly though, Zeng *et al.* (2014) introduced the potential role of depleted myokines in myositis, pointing out their finding of downregulated InsI6 in PM and DM muscle, which however, had been previously found to be upregulated in a mouse myositic model. This, along with

this thesis' findings, emphasise the importance of investigating myokines secretome in clinical models that exert chronic effects over any short-term *in vitro* models. In addition to those cytokines, it would be interesting to measure type I IFNs levels that have been suggested as a potential biomarker of DM (Rigolet et al., 2019), as well as IL6 that has presented dual roles under physiological versus pathological conditions. IL-6 was among the initial myokines found to be produced at a high level in skeletal muscle following intense exercise (Ostrowski *et al.*, 1998), that showed to induce antioxidant defense system in response to oxidative stress (Sacheck *et al.*, 2006). IL6 is acting as a pro-inflammatory cytokine in several conditions, but as an anti-inflammatory cytokine when released from muscle, showing an important role in metabolism (Mageriu *et al.*, 2020). As Mageriu *et al.* suggested in a recent review (2020), it is of high importance to consider the role of IL6 as both a myokine and cytokine when assessing and targeting IL6, but also other myokines/cytokines.

The trend of DM-associated detrimental effects over IBM was also seen in MHC-I overexpressing myoblasts in presence of type I IFNs over in absence of type I IFNs, which enabled the representation of a more accurate study model of DM. Furthermore, an interesting observation was that those effects as a result of IBM and DM muscle secretome was not associated with MHC-I overexpression, suggesting their independent mechanism of action. Consistent with this finding, type I IFN β -associated mitochondrial impairments seemed to be non-mediated by MHC-I overexpression. These findings support the potential involvement of multiple factors in myositis pathogenesis, providing an insight into the potential importance of the development of combinational therapies, targeting multiple factors.

Lastly, this thesis has offered a great foundation on the potential beneficial effects of quenching ROS generation. Treatment with the antioxidant EUK-134 provided major evidence of its ability to ameliorate aspects of mitochondrial dysfunction upon ER stress activation. It should be noted here that EUK-134 treatment in presence of tunicamycin showed persistent increase in the fluorescence and protein levels of chaperones, GRP78 and GRP94, respectively. An explanation for this observation could be the potential protective role of GRPs chaperones, which have been previously shown to prevent ER stress-mediated cell damage and death (Dey *et al.*, 2006). In particular, Dey *et al.* (2006)

showed that treatment with Trolox and N-acetylcysteine, a vitamin E analogue and an antioxidant, respectively, resulted in increased protein expression of GRPs in a thapsigargin-induced ER stress model in HepG2 liver cells, showing consistency with our findings. However, it is also possible that EUK-134 could present ER-independent effects on mitochondrial function and/or ROS generation. Last but not least, future studies on EUK-134 pre-treatment compared to co- and post-treatment would enable assessment of the prophylactic capability of EUK-134 compared to its capability to prevent and cure/reverse an effect, respectively. Interestingly, several studies have demonstrated promising findings following EUK-134 pre-treatment on oxidative stress and mitochondrial homeostasis (Peugnet *et al.*, 2021; Purushothaman and Nair, 2016).

EUK-134 treatment showed beneficial effects in IBM and DM muscle secretome conditions, as well as in IBM- and DM-derived primary cells; thus, these findings suggest that mitochondrial dysfunction in myositis is highly mediated by ROS accumulation. Further enhancing this hypothesis, Boyer *et al.* (2018) reported the beneficial effect of the antioxidant *N-acetylcysteine* in amending myositis pathophysiology. In addition, EUK-134 has previously been found to attenuate markers of muscle damage, as well as proinflammatory phenotype in a murine model of Duchenne muscular dystrophy (Kim and Lawler, 2012). Furthermore, ROS generation was assessed in the various myositic models, with the experimental procedures performed in these studies overall suggesting ROS generation in myositis disease. Specifically, ER stress induced elevated total cellular ROS levels, including cellular superoxide. Furthermore, mitochondrial superoxide generation was suggested to be induced by type I IFNs, hallmarks of DM, but not by MHC-I overexpression, which actually seemed to be associated with increased peroxynitrite levels. These findings are in agreement with a previous study in DM/IMNM myoblasts showing increased intracellular superoxide levels, which however, has not investigated whether mitochondria are responsible for this effect (Basualto-Alarcón *et al.*, 2020), as well as elevated NOS expression in sIBM muscle fibres and to a much lesser degree in DM and PM samples (Schmidt *et al.*, 2012). Interestingly, in this study, DM primary myoblasts showed a tendency towards increased mitochondrial superoxide, with no changes in peroxynitrite, hydrogen peroxide or hydroxyl radical levels, whereas IBM primary myoblasts presented elevated hydrogen peroxide levels. Differences in mitochondrial

superoxide levels across models could be attributable to the early stage of disease, the quick rate of conversion to hydrogen peroxide, or the specific myositis cases. Further highlighting the involvement of mitochondrial ROS generation in myositis, an early study in sIBM showed downregulated complex I expression (Rygiel *et al.*, 2015), which has been historically linked with elevated superoxide levels (Leipnitz *et al.*, 2018; Pitkanen *et al.*, 1996). Indeed, assessing this link, as well as the involvement of other ROS sources in myositis, such as other mitochondrial complexes, ER, or NOS, could further facilitate the development of targeted therapeutic interventions. It cannot be ignored that further assessment is required to gain a better characterisation of the oxidative stress involved in myositis disease. In addition, an investigation on the antioxidant activity in myositis would be a great contribution to the field as it could provide further support on the importance of antioxidant treatment as a therapeutic approach. Interestingly, differential findings exist between sIBM and PM/DM in regards to antioxidants activity; however, evidence seem to be limited (Catalán-García *et al.*, 2020; Shabrokh *et al.*, 2014; Basualto-Alarcón *et al.*, 2020).

The very low number of myositis biopsy samples collected and assessed in this research is considered a limitation that does not allow definite conclusions to be made. IIMs have a low prevalence, ranging from 15 to 17.4 cases per 100,000 individuals in the USA (Cavazzana *et al.*, 2017), that makes the study of these conditions extremely challenging, especially in terms of identifying each subtype's specific and segregated effects. Furthermore, the heterogeneity of IIMs, as well as the slow age of onset in several subtypes, can slow down the diagnosis, as well as research in those samples. For example, in this case a higher number of biopsy samples were collected from individuals who were involved in a skeletal muscle biopsy procedure for diagnostic purposes; however, diagnosis was not definite for a number of those, while others were diagnosed with non-myositis condition (e.g., metabolic myopathies). In addition, the collection and receipt of diagnosis, as well as growth of primary cells required a long period of time, which actually lasted through the first three years of my PhD. Lastly, even though Chapter 6 results assessed the effects on mitochondrial function in an immortalised human skeletal muscle cell line exposed to conditioned media derived from primary DM and IBM skeletal muscle cells cultured *in vitro* compared to conditioned media derived from healthy

control cells, it should be noted that the primary skeletal muscle cells growth media differed from the immortalised cell line growth media. In particular, the immortalised cell line growth media contained an array of growth factors that were absent from the primary cells conditioned media, serving as a potential limitation of this experimental approach – indeed, in this study, healthy primary cells conditioned media was compared to healthy immortalised conditioned media showing no effects on the differentiation capacity or HLA fluorescence intensity.

7.2 Future directions

The present study has provided some novel data on mitochondrial impairments in IBM and DM primary human skeletal myoblasts, as well as in response to different mechanisms that had been previously suggested to be involved in myositis pathogenesis, including ER stress, MHC-I overexpression, type I IFNs, and myositic myokines secretome. In addition, it highlighted the role of ROS generation and suggested the potential beneficial effects of ROS-targeted interventions in myositis disease. This thesis has offered a foundation on myositis-associated mitochondrial abnormalities, which needs, to be extended in future research.

It is undoubtable that longer sample size is required to completely define IBM and DM-specific mitochondrial respiratory abnormalities. A promising future work would be the stratification of IIMs based on their mitochondrial and/or other non-immune mediated abnormalities to enable the development of a precision therapeutic approach in the different types of myositis, an approach being recently explored in sporadic Parkinson's disease, as well (Carling *et al.*, 2020) – however, this will require a large sample size, age- and sex-matched healthy controls. Such a study would be enhanced by the assessment of the serology of the patients with IIM and identify whether certain antibodies confer differential pathological observations and associated mechanisms. Furthermore, additional experiments, such as individual mitochondrial complexes levels and activity would enable us to further characterise and identify the specific cause of any mitochondrial respiratory deficits. In addition, other facilities, such as large size high-content live-cell imaging would enable a better and more accurate interpretation of mitochondrial membrane potential and ROS generation using the various live-cell assay fluorophores.

Assessing stem cell fate, including regenerative, proliferative and differentiation capacity, and its link to mitochondrial changes, has gained a great attention, especially for skeletal muscle, given its high capability to maintain normal muscle physiology following injury (Bhattacharya and Scimè, 2020). The present thesis used myoblasts cultured *in vitro*. Consistent with this study, previous studies investigating mitochondrial bioenergetics in myositis used myoblasts cells over myotubes (Catalán-García *et al.*, 2020; Oikawa *et al.*, 2020; Basualto-Alarcón *et al.*, 2020). Interestingly, a recent study on the effects of simvastatin in myopathies, showed that C2C12 myoblasts presented higher susceptibility to simvastatin toxicity, leading to impaired myoblast proliferation and differentiation, as well as more severe cellular ATP deficit, compared to C2C12 myotubes, whereas similarly reduced oxygen consumption rates were seen in both myoblasts and myotubes (Sanvee *et al.*, 2021). However, there is a lack of evidence on the mitochondrial phenotype in differentiating myotubes in myositis, highlighting the need for further research. Therefore, it would be of great importance to assess the three models developed in this thesis, *in vitro* ER stress model, MHC-I-overexpressing model, and clinical cell model, as well as myokines secretome in fully differentiated myotubes.

Appendix

Appendix 1. Chapter 3 western blots

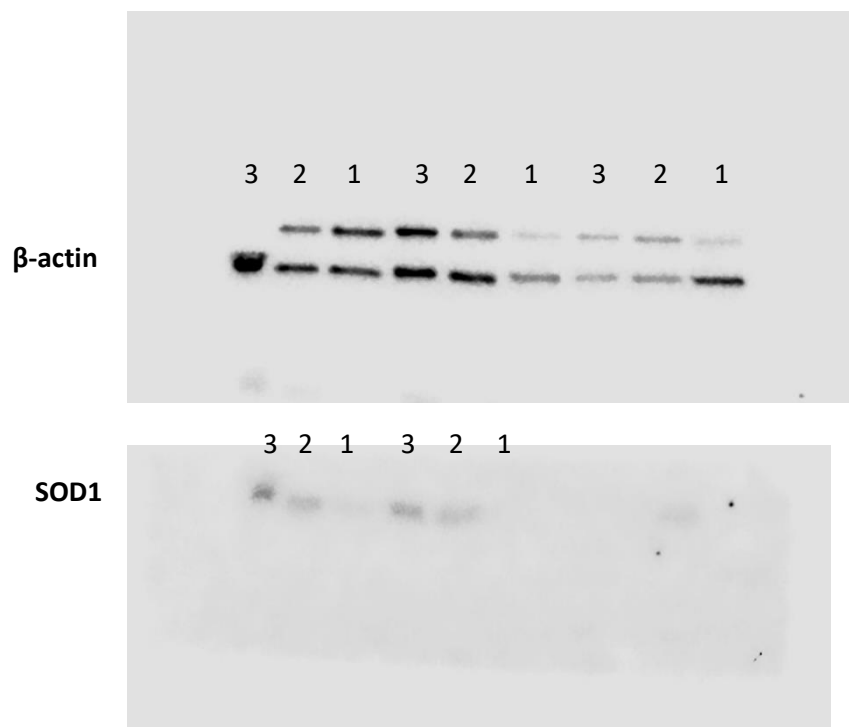
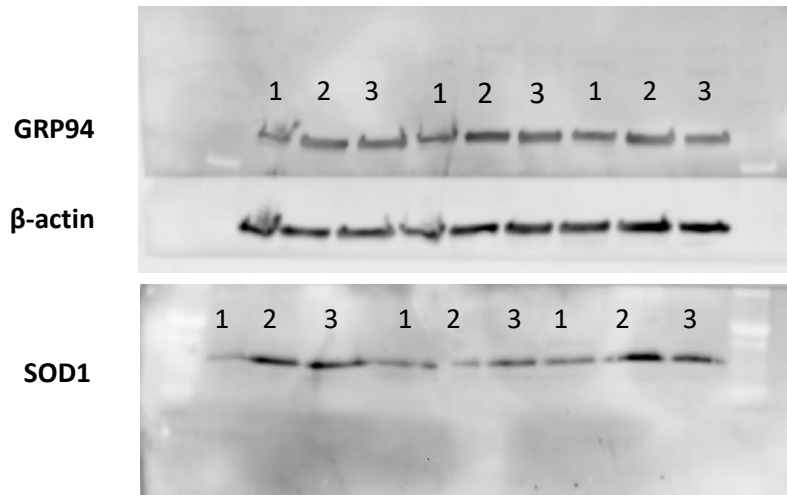


Figure 7.1 Full images of western blots for GRP94 and SOD1 with the relevant loading control (β -actin); Samples arranged as: 1, Control; 2, tunicamycin; 3, tunicamycin + EUK-134

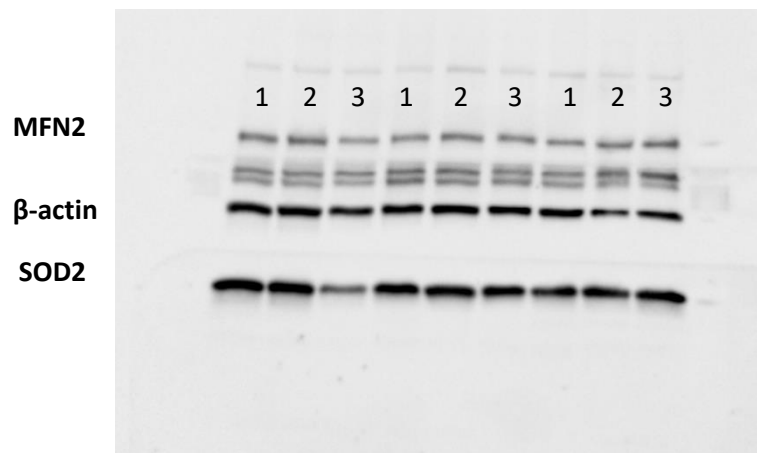


Figure 7.2 Full images of western blots for MFN2 and SOD2 with the relevant loading control (β -actin); 1, Control; 2, tunicamycin; 3, tunicamycin + EUK-134

References

Acosta-Alvear, D., Zhou, Y., Blais, A., Tsikitis, M., Lents, N.H., Arias, C., Lennon, C.J., Kluger, Y. and Dynlacht, B.D., 2007. XBP1 controls diverse cell type-and condition-specific transcriptional regulatory networks. *Molecular cell*, 27(1), pp.53-66.

Adams, C.J., Kopp, M.C., Larburu, N., Nowak, P.R. and Ali, M.M., 2019. Structure and molecular mechanism of ER stress signaling by the unfolded protein response signal activator IRE1. *Frontiers in molecular biosciences*, 6, p.11.

Aeschlimann, F.A., Frémond, M.L., Duffy, D., Rice, G.I., Charuel, J.L., Bondet, V., Saire, E., Neven, B., Bodemer, C., Balu, L. and Gitiaux, C., 2018. A child with severe juvenile dermatomyositis treated with ruxolitinib. *Brain*, 141(11), pp.e80-e80.

Aggarwal, R., Rockette, H., Venturupalli, S., Marder, G., Dimachkie, M., Gazeley, D., Ernste, F.C., Crofford, L., Moghadam-Kia, S., Koontz, D. and Zhu, L., 2020, October. Tocilizumab in myositis: results of a phase IIb double-blind randomized controlled trial. In *ARTHRITIS & RHEUMATOLOGY* (Vol. 72). 111 RIVER ST, HOBOKEN 07030-5774, NJ USA: WILEY.

Agilent. (2021) *Seahorse FluxPaks | Agilent*. [Online] [Accessed 2 September 2021] https://www.agilent.com/en/product/cell-analysis/real-time-cell-metabolic-analysis/xf-sensor-cartridges-cell-culture-microplates/seahorse-fluxpaks-740883?fbclid=IwAR3keKR5l65QPADJlKnNUQpYTPkdwIqs2n87cyarBlml5CGsijLV7qU_Js0

Akira, S., Takeda, K. and Kaisho, T., 2001. Toll-like receptors: critical proteins linking innate and acquired immunity. *Nature immunology*, 2(8), p.675.

Alam, S., Abdullah, C.S., Aishwarya, R., Orr, A.W., Traylor, J., Miriyala, S., Panchatcharam, M., Pattillo, C.B. and Bhuiyan, M., 2017. Sigmar1 regulates endoplasmic reticulum stress-induced C/EBP-homologous protein expression in cardiomyocytes. *Bioscience reports*, 37(4).

Al-Dabbagh, S., McPhee, J.S., Murgatroyd, C., Butler-Browne, G., Stewart, C.E. and Al-Shanti, N., 2015. The lymphocyte secretome from young adults enhances skeletal muscle

proliferation and migration, but effects are attenuated in the secretome of older adults. *Physiological reports*, 3(11), p.e12518.

Alhatou, M.I., Sladky, J.T., Bagasra, O. and Glass, J.D., 2004. Mitochondrial abnormalities in dermatomyositis: characteristic pattern of neuropathology. *Journal of molecular histology*, 35(6), pp.615-619.

Alter, J. and Bengal, E., 2011. Stress-induced C/EBP homology protein (CHOP) represses MyoD transcription to delay myoblast differentiation. *PloS one*, 6(12), p.e29498.

Andersson, D.C., Betzenhauser, M.J., Reiken, S., Meli, A.C., Umanskaya, A., Xie, W., Shiomi, T., Zalk, R., Lacampagne, A. and Marks, A.R., 2011. Ryanodine receptor oxidation causes intracellular calcium leak and muscle weakness in aging. *Cell metabolism*, 14(2), pp.196-207.

Arahata, K. and Engel, A.G., 1984. Monoclonal antibody analysis of mononuclear cells in myopathies. I: Quantitation of subsets according to diagnosis and sites of accumulation and demonstration and counts of muscle fibers invaded by T cells. *Annals of neurology*, 16(2), pp.193-208.

Arshanapalli, A., Shah, M., Veerula, V. and Somani, A.K., 2015. The role of type I interferons and other cytokines in dermatomyositis. *Cytokine*, 73(2), pp.319-325.

Baker, K., Marcus, C.B., Huffman, K., Kruk, H., Malfroy, B. and Doctrow, S.R., 1998. Synthetic combined superoxide dismutase/catalase mimetics are protective as a delayed treatment in a rat stroke model: a key role for reactive oxygen species in ischemic brain injury. *Journal of Pharmacology and Experimental Therapeutics*, 284(1), pp.215-221.

Bankapalli, K., Vishwanathan, V., Susarla, G., Sunayana, N., Saladi, S., Peethambaram, D. and D'Silva, P., 2020. Redox-dependent regulation of mitochondrial dynamics by DJ-1 paralogs in *Saccharomyces cerevisiae*. *Redox biology*, 32, p.101451.

Baraka, E. and Ahmed, I., 2015. Toll-like receptors 4 and 9 expression in systemic lupus erythematosus and dermatomyositis: relation to clinical status and disease activity. *The Egyptian Journal of Biochemistry and Molecular Biology*, 33(1-2), pp.68-81.

Baron, P., Galimberti, D., Meda, L., Prat, E., Scarpini, E., Conti, G., Moggio, M., Prella, A. and Scarlato, G., 2000. Synergistic effect of β -amyloid protein and interferon gamma on nitric oxide production by C2C12 muscle cells. *Brain*, 123(2), pp.374-379.

Barone, R., Macaluso, F., Sangiorgi, C., Campanella, C., Gammazza, A.M., Moresi, V., Coletti, D., de Macario, E.C., Macario, A.J., Cappello, F. and Adamo, S., 2016. Skeletal muscle Heat shock protein 60 increases after endurance training and induces peroxisome proliferator-activated receptor gamma coactivator 1 α 1 expression. *Scientific reports*, 6(1), pp.1-18.

Bartoli, C., Civatte, M., Pellissier, J. and Figarella-Branger, D., 2001. CCR2A and CCR2B, the two isoforms of the monocyte chemoattractant protein-1 receptor are up-regulated and expressed by different cell subsets in idiopathic inflammatory myopathies. *Acta neuropathologica*, 102(4), pp.385-392.

Basualto-Alarcón, C., Urra, F.A., Bozán, M.F., Jaña, F., Trangulao, A., Bevilacqua, J.A. and Cárdenas, J.C., 2020. Idiopathic inflammatory myopathy human derived cells retain their ability to increase mitochondrial function. *PloS one*, 15(11), p.e0242443.

Benischke, A.S., Vasanth, S., Miyai, T., Katikireddy, K.R., White, T., Chen, Y., Halilovic, A., Price, M., Price, F., Liton, P.B. and Jurkunas, U.V., 2017. Activation of mitophagy leads to decline in Mfn2 and loss of mitochondrial mass in Fuchs endothelial corneal dystrophy. *Scientific reports*, 7(1), pp.1-11.

Betteridge, Z. and McHugh, N., 2016. Myositis-specific autoantibodies: an important tool to support diagnosis of myositis. *Journal of internal medicine*, 280(1), pp.8-23.

Bhandary, B., Marahatta, A., Kim, H.R. and Chae, H.J., 2013. An involvement of oxidative stress in endoplasmic reticulum stress and its associated diseases. *International journal of molecular sciences*, 14(1), pp.434-456.

Bhatt, P.S., Tzoulis, C., Balafkan, N., Miletic, H., Tran, G.T.T., Sanaker, P.S. and Bindoff, L.A., 2019. Mitochondrial DNA depletion in sporadic inclusion body myositis. *Neuromuscular Disorders*, 29(3), pp.242-246.

Bhattacharya, D. and Scimè, A., 2020. Mitochondrial function in muscle stem cell fates. *Frontiers in Cell and Developmental Biology*, 8, p.480.

Bilgic, H., Ytterberg, S.R., Amin, S., McNallan, K.T., Wilson, J.C., Koeth, T., Ellingson, S., Newman, B., Bauer, J.W., Peterson, E.J. and Baechler, E.C., 2009. Interleukin-6 and type I interferon-regulated genes and chemokines mark disease activity in dermatomyositis. *Arthritis & Rheumatism: Official Journal of the American College of Rheumatology*, 60(11), pp.3436-3446.

Blume, G., Pestronk, A., Frank, B. and Johns, D.R., 1997. Polymyositis with cytochrome oxidase negative muscle fibres. Early quadriceps weakness and poor response to immunosuppressive therapy. *Brain: a journal of neurology*, 120(1), pp.39-45.

Boehler, J.F., Horn, A., Novak, J.S., Li, N., Ghimbovsi, S., Lundberg, I.E., Alexanderson, H., Alemo Munters, L., Jaiswal, J.K. and Nagaraju, K., 2019. Mitochondrial dysfunction and role of harakiri in the pathogenesis of myositis. *The Journal of pathology*, 249(2), pp.215-226.

Bohnert, K.R., McMillan, J.D. and Kumar, A., 2018. Emerging roles of ER stress and unfolded protein response pathways in skeletal muscle health and disease. *Journal of cellular physiology*, 233(1), pp.67-78.

Boyer, O., Meyer, A., Boitard, C. and Abad, C., 2018. FRI0403 Mitochondrial dysfunction and oxidative stress in myositis: a central pathogenic pathway from mouse to man.

Bradshaw, E.M., Orihuela, A., McArdel, S.L., Salajegheh, M., Amato, A.A., Hafler, D.A., Greenberg, S.A. and O'Connor, K.C., 2007. A local antigen-driven humoral response is present in the inflammatory myopathies. *The Journal of Immunology*, 178(1), pp.547-556.

Brady, S., Wang, E., Carver, J., Hofer, M., Diot, A., Hilton, D., Hilton-Jones, D., Poulton, J. and Fratter, C., 2018. Low mitochondrial DNA copy number suggests abnormal mitophagy in inclusion body myositis. *Neuromuscular Disorders*, 28, p.S30.

Bravo, R., Gutierrez, T., Paredes, F., Gatica, D., Rodriguez, A.E., Pedrozo, Z., Chiong, M., Parra, V., Quest, A.F., Rothermel, B.A. and Lavandero, S., 2012. Endoplasmic reticulum: ER stress regulates mitochondrial bioenergetics. *The international journal of biochemistry & cell biology*, 44(1), pp.16-20.

Bravo, R., Vicencio, J.M., Parra, V., Troncoso, R., Munoz, J.P., Bui, M., Quiroga, C., Rodriguez, A.E., Verdejo, H.E., Ferreira, J. and Iglewski, M., 2011. Increased ER-

mitochondrial coupling promotes mitochondrial respiration and bioenergetics during early phases of ER stress. *Journal of cell science*, 124(13), pp.2143-2152.

Brunn, A., Zornbach, K., Hans, V.H., Haupt, W.F. and Deckert, M., 2012. Toll-like receptors promote inflammation in idiopathic inflammatory myopathies. *Journal of Neuropathology & Experimental Neurology*, 71(10), pp.855-867.

Buie, J.J., Renaud, L.L., Muise-Helmericks, R. and Oates, J.C., 2017. IFN- α negatively regulates the expression of endothelial nitric oxide synthase and nitric oxide production: implications for systemic lupus erythematosus. *The Journal of Immunology*, 199(6), pp.1979-1988.

Cao, S.S. and Kaufman, R.J., 2014. Endoplasmic reticulum stress and oxidative stress in cell fate decision and human disease. *Antioxidants & redox signaling*, 21(3), pp.396-413.

Carling, P.J., Mortiboys, H., Green, C., Mihaylov, S., Sandor, C., Schwartzenruber, A., Taylor, R., Wei, W., Hastings, C., Wong, S. and Lo, C., 2020. Deep phenotyping of peripheral tissue facilitates mechanistic disease stratification in sporadic Parkinson's disease. *Progress in Neurobiology*, 187, p.101772.

Carstens, P.O. and Schmidt, J., 2014. Diagnosis, pathogenesis and treatment of myositis: recent advances. *Clinical & Experimental Immunology*, 175(3), pp.349-358.

Catalán-García, M., García-García, F.J., Moreno-Lozano, P.J., Alcarraz-Vizán, G., Tort-Merino, A., Milisenda, J.C., Cantó-Santos, J., Barcos-Rodríguez, T., Cardellach, F., Lladó, A. and Novials, A., 2020. Mitochondrial Dysfunction: A Common Hallmark Underlying Comorbidity between sIBM and Other Degenerative and Age-Related Diseases. *Journal of clinical medicine*, 9(5), p.1446.

Catalán-García, M., Garrabou, G., Morén, C., Guitart-Mampel, M., Hernando, A., Díaz-Ramos, À., González-Casacuberta, I., Juárez, D.L., Bañó, M., Enrich-Bengo, J. and Emperador, S., 2016. Mitochondrial DNA disturbances and deregulated expression of oxidative phosphorylation and mitochondrial fusion proteins in sporadic inclusion body myositis. *Clinical Science*, 130(19), pp.1741-1751.

Cavazzana, I., Fredi, M., Selmi, C., Tincani, A. and Franceschini, F., 2017. The clinical and histological spectrum of idiopathic inflammatory myopathies. *Clinical reviews in allergy & immunology*, 52(1), pp.88-98.

Chad, D.A., 2003. Neuromuscular Disorders, Overview. *Encyclopedia of the Neurological Sciences*, pp.494-500

Chariot, P., Ruet, E., Authier, F.J., Labes, D., Poron, F. and Gherardi, R., 1996. Cytochrome c oxidase deficiencies in the muscle of patients with inflammatory myopathies. *Acta neuropathologica*, 91(5), pp.530-536.

Chatterjee, P.K., Patel, N.S., Kvale, E.O., Brown, P.A., Stewart, K.N., Mota-Filipe, H., Sharpe, M.A., Di Paola, R., Cuzzocrea, S. and Thiemermann, C., 2004. EUK-134 reduces renal dysfunction and injury caused by oxidative and nitrosative stress of the kidney. *American journal of nephrology*, 24(2), pp.165-177.

Chen, Z., Su, Z., Pang, W., Huang, Y., Lin, J., Ding, Z., Wu, S., Xu, S., Quan, W., Zheng, J. and Chen, H., 2017. Antioxidant status of serum bilirubin and uric acid in patients with polymyositis and dermatomyositis. *International Journal of Neuroscience*, 127(7), pp.617-623.

Civatte, M., Bartoli, C., Schleinitz, N., Chetaille, B., Pellissier, J.F. and Figarella-Branger, D., 2005. Expression of the β chemokines CCL3, CCL4, CCL5 and their receptors in idiopathic inflammatory myopathies. *Neuropathology and applied neurobiology*, 31(1), pp.70-79.

Coirault, C., Guellich, A., Barbry, T., Samuel, J.L., Riou, B. and Lecarpentier, Y., 2007. Oxidative stress of myosin contributes to skeletal muscle dysfunction in rats with chronic heart failure. *American Journal of Physiology-Heart and Circulatory Physiology*, 292(2), pp.H1009-H1017.

Coley, W., Rayavarapu, S., Pandey, G.S., Sabina, R.L., Van der Meulen, J.H., Ampong, B., Wortmann, R.L., Rawat, R. and Nagaraju, K., 2012. The molecular basis of skeletal muscle weakness in a mouse model of inflammatory myopathy. *Arthritis & Rheumatism*, 64(11), pp.3750-3759.

Connolly, N.M., Theurey, P., Adam-Vizi, V., Bazan, N.G., Bernardi, P., Bolaños, J.P., Culmsee, C., Dawson, V.L., Deshmukh, M., Duchen, M.R. and Düssmann, H., 2018.

Guidelines on experimental methods to assess mitochondrial dysfunction in cellular models of neurodegenerative diseases. *Cell Death & Differentiation*, 25(3), pp.542-572.

Cooper, G.M., 2000. *The Cell: A Molecular Approach* 2nd edition Boston University. Sunderland (MA): Sinauer Associates.

Cortese-Krott, M.M., Rodriguez-Mateos, A., Kuhnle, G.G., Brown, G., Feelisch, M. and Kelm, M., 2012. A multilevel analytical approach for detection and visualization of intracellular NO production and nitrosation events using diaminofluoresceins. *Free Radical Biology and Medicine*, 53(11), pp.2146-2158.

Cruz-Tapias, P., Castiblanco, J. and Anaya, J.M., 2013. Major histocompatibility complex: antigen processing and presentation. In *Autoimmunity: From Bench to Bedside [Internet]*. El Rosario University Press.

D'Agostino, C., Nogalska, A., Cacciottolo, M., Engel, W.K. and Askanas, V., 2011. Abnormalities of NBR1, a novel autophagy-associated protein, in muscle fibers of sporadic inclusion-body myositis. *Acta neuropathologica*, 122(5), pp.627-636.

Dagda R.K., Cherra S.J., Kulich S.M., Tandon A., Park D., Chu C.T. Loss of PINK1 function promotes mitophagy through effects on oxidative stress and mitochondrial fission. *J. Biol. Chem.* 2009;284:13843–13855.

Das, L., Blumbergs, P.C., Manavis, J. and Limaye, V.S., 2013. Major histocompatibility complex class I and II expression in idiopathic inflammatory myopathy. *Applied Immunohistochemistry & Molecular Morphology*, 21(6), pp.539-542.

De Bleecker, J.L., De Paepe, B., Vanwalleghem, I.E. and Schröder, J.M., 2002. Differential expression of chemokines in inflammatory myopathies. *Neurology*, 58(12), pp.1779-1785.

de Brachène, A.C., Dos Santos, R.S., Marroqui, L., Colli, M.L., Marselli, L., Mirmira, R.G., Marchetti, P. and Eizirik, D.L., 2018. IFN- α induces a preferential long-lasting expression of MHC class I in human pancreatic beta cells. *Diabetologia*, 61(3), pp.636-640.

De Paepe, B., De Keyser, K., Martin, J.J. and De Bleecker, J.L., 2005. Alpha-chemokine receptors CXCR1–3 and their ligands in idiopathic inflammatory myopathies. *Acta Neuropathologica*, 109(6), pp.576-582.

Debaud C., Salga M., Begot L., Holy X., Chedik M., De l'Escalopier N., Torossian F., Levesque J.P., Lataillade J.J., Le Bousse-Kerdiles M.C., et al. Peripheral denervation participates in heterotopic ossification in a spinal cord injury model. *PLoS ONE*. 2017;12:e0182454.

Deldicque, L., Bertrand, L., Patton, A., Francaux, M. and Baar, K., 2011. ER stress induces anabolic resistance in muscle cells through PKB-induced blockade of mTORC1. *PLoS one*, 6(6), p.e20993.

Dey, A., Kessova, I.G. and Cederbaum, A.I., 2006. Decreased protein and mRNA expression of ER stress proteins GRP78 and GRP94 in HepG2 cells over-expressing CYP2E1. *Archives of biochemistry and biophysics*, 447(2), pp.155-166.

Ding, Y., Huang, B., Wang, Y., Hou, J., Chi, Y., Zhou, Z. and Li, J., 2021. Janus kinase inhibitor significantly improved rash and muscle strength in juvenile dermatomyositis. *Annals of the rheumatic diseases*, 80(4), pp.543-545.

Dorph, C., Englund, P., Nennesmo, I. and Lundberg, I.E., 2006. Signs of inflammation in both symptomatic and asymptomatic muscles from patients with polymyositis and dermatomyositis. *Annals of the rheumatic diseases*, 65(12), pp.1565-1571.

Dott, W., Mistry, P., Wright, J., Cain, K. and Herbert, K.E., 2014. Modulation of mitochondrial bioenergetics in a skeletal muscle cell line model of mitochondrial toxicity. *Redox biology*, 2, pp.224-233.

Dugan, E.M., Huber, A.M., Miller, F.W. and Rider, L.G., 2009. Photoessay of the cutaneous manifestations of the idiopathic inflammatory myopathies. *Dermatology online journal*, 15(2).

Dugdale, H.F., Hughes, D.C., Allan, R., Deane, C.S., Coxon, C.R., Morton, J.P., Stewart, C.E. and Sharples, A.P., 2018. The role of resveratrol on skeletal muscle cell differentiation and myotube hypertrophy during glucose restriction. *Molecular and Cellular Biochemistry*, 444(1), pp.109-123.

Duksin, D. and Mahoney, W.C., 1982. Relationship of the structure and biological activity of the natural homologues of tunicamycin. *Journal of Biological Chemistry*, 257(6), pp.3105-3109.

- Ellgaard, L., Sevier, C.S. and Balleid, N.J., 2018. How are proteins reduced in the endoplasmic reticulum?. *Trends in biochemical sciences*, 43(1), pp.32-43.
- Englund, P., Lindroos, E., Nennesmo, I., Klareskog, L. and Lundberg, I.E., 2001. Skeletal muscle fibers express major histocompatibility complex class II antigens independently of inflammatory infiltrates in inflammatory myopathies. *The American journal of pathology*, 159(4), pp.1263-1273.
- Fan, X., Hussien, R. and Brooks, G.A., 2010. H₂O₂-induced mitochondrial fragmentation in C2C12 myocytes. *Free Radical Biology and Medicine*, 49(11), pp.1646-1654.
- Frenette, J., St-Pierre, M., Côté, C.H., Mylona, E. and Pizza, F.X., 2002. Muscle impairment occurs rapidly and precedes inflammatory cell accumulation after mechanical loading. *American Journal of Physiology-Regulatory, Integrative and Comparative Physiology*, 282(2), pp.R351-R357.
- Fréret, M., Drouot, L., Obry, A., Ahmed-Lacheheb, S., Dauly, C., Adriouch, S., Cosette, P., Authier, F.J. and Boyer, O., 2013. Overexpression of MHC class I in muscle of lymphocyte-deficient mice causes a severe myopathy with induction of the unfolded protein response. *The American Journal of Pathology*, 183(3), pp.893-904.
- Girolamo, F., Lia, A., Amati, A., Strippoli, M., Coppola, C., Virgintino, D., Roncali, L., Toscano, A., Serlenga, L. and Trojano, M., 2013. Overexpression of autophagic proteins in the skeletal muscle of sporadic inclusion body myositis. *Neuropathology and applied neurobiology*, 39(7), pp.736-749.
- Gomes, L.C., Di Benedetto, G. and Scorrano, L., 2011. During autophagy mitochondria elongate, are spared from degradation and sustain cell viability. *Nature cell biology*, 13(5), pp.589-598.
- Gono, T., Kaneko, H., Kawaguchi, Y., Hanaoka, M., Kataoka, S., Kuwana, M., Takagi, K., Ichida, H., Katsumata, Y., Ota, Y. and Kawasumi, H., 2014. Cytokine profiles in polymyositis and dermatomyositis complicated by rapidly progressive or chronic interstitial lung disease. *Rheumatology*, 53(12), pp.2196-2203.
- Greenberg, S.A., 2019. Inclusion body myositis: clinical features and pathogenesis. *Nature Reviews Rheumatology*, 15(5), pp.257-272.

Greenberg, S.A., Bradshaw, E.M., Pinkus, J.L., Pinkus, G.S., Burleson, T., Due, B., Bregoli, L.S., O'Connor, K.C. and Amato, A.A., 2005. Plasma cells in muscle in inclusion body myositis and polymyositis. *Neurology*, 65(11), pp.1782-1787.

Greenberg, S.A., Higgs, B.W., Morehouse, C., Walsh, R.J., Kong, S.W., Brohawn, P., Zhu, W., Amato, A., Salajegheh, M., White, B. and Kiener, P.A., 2012. Relationship between disease activity and type 1 interferon-and other cytokine-inducible gene expression in blood in dermatomyositis and polymyositis. *Genes & Immunity*, 13(3), pp.207-213.

Guha, P., Kaptan, E., Gade, P., Kalvakolanu, D.V. and Ahmed, H., 2017. Tunicamycin induced endoplasmic reticulum stress promotes apoptosis of prostate cancer cells by activating mTORC1. *Oncotarget*, 8(40), p.68191.

Güttsches, A.K., Jacobsen, F., Schreiner, A., Mertens-Rill, J., Tegenthoff, M., Marcus, K., Vorgerd, M. and Kley, R.A., 2020. Chaperones in sporadic inclusion body myositis— Validation of proteomic data. *Muscle & nerve*, 61(1), pp.116-121.

Hassan, R.H., Hainault, I., Vilquin, J.T., Samama, C., Lasnier, F., Ferre, P., Foufelle, F. and Hajduch, E., 2012. Endoplasmic reticulum stress does not mediate palmitate-induced insulin resistance in mouse and human muscle cells. *Diabetologia*, 55(1), pp.204-214.

Helmers, S.B., Bruton, M., Loell, I., Ulfgren, A.K., Gracie, A.J., McInnes, I.B. and Lundberg, I.E., 2018. Expression of interleukin-18 in muscle tissue of patients with polymyositis or dermatomyositis and effects of conventional immunosuppressive treatment. *Rheumatology*, 57(12), pp.2149-2157.

Hidalgo, C., Donoso, P. and Carrasco, M.A., 2005. The ryanodine receptors Ca²⁺ release channels: cellular redox sensors?. *IUBMB life*, 57(4-5), pp.315-322.

Hill, B.G., Benavides, G.A., Lancaster, J.R., Ballinger, S., Dell'Italia, L., Zhang, J. and Darley-Usmar, V.M., 2012. Integration of cellular bioenergetics with mitochondrial quality control and autophagy. *Biological chemistry*, 393(12), pp.1485-1512.

Himori, K., Abe, M., Tatebayashi, D., Lee, J., Westerblad, H., Lanner, J.T. and Yamada, T., 2017. Superoxide dismutase/catalase mimetic EUK-134 prevents diaphragm muscle weakness in monocrotalin-induced pulmonary hypertension. *PloS one*, 12(2), p.e0169146.

Hotamisligil, G.S., 2010. Endoplasmic reticulum stress and the inflammatory basis of metabolic disease. *Cell*, 140(6), pp.900-917.

Huxley, A.F. and Niedergerke, R., 1954. Structural changes in muscle during contraction: interference microscopy of living muscle fibres. *Nature*, 173(4412), pp.971-973.

Huxley, H. and Hanson, J., 1954. Changes in the cross-striations of muscle during contraction and stretch and their structural interpretation. *Nature*, 173(4412), pp.973-976.

Hyatt, H.W. and Powers, S.K., 2021. Mitochondrial dysfunction is a common denominator linking skeletal muscle wasting due to disease, aging, and prolonged inactivity. *Antioxidants*, 10(4), p.588.

Hyatt, H.W., Ozdemir, M., Yoshihara, T., Nguyen, B.L., Deminice, R. and Powers, S.K., 2021. Calpains play an essential role in mechanical ventilation-induced diaphragmatic weakness and mitochondrial dysfunction. *Redox Biology*, 38, p.101802.

Iqbal, S. and Hood, D.A., 2014. Oxidative stress-induced mitochondrial fragmentation and movement in skeletal muscle myoblasts. *American Journal of Physiology-Cell Physiology*, 306(12), pp.C1176-C1183.

Irrcher, I., Ljubcic, V. and Hood, D.A., 2009. Interactions between ROS and AMP kinase activity in the regulation of PGC-1 α transcription in skeletal muscle cells. *American Journal of Physiology-Cell Physiology*, 296(1), pp.C116-C123.

Irwin, M.J., Heath, W.R. and Sherman, L.A., 1989. Species-restricted interactions between CD8 and the alpha 3 domain of class I influence the magnitude of the xenogeneic response. *The Journal of experimental medicine*, 170(4), pp.1091-1101.

Ishiuchi, Y., Sato, H., Komatsu, N., Kawaguchi, H., Matsuwaki, T., Yamanouchi, K., Nishihara, M. and Nedachi, T., 2018. Identification of CCL5/RANTES as a novel contraction-reducible myokine in mouse skeletal muscle. *Cytokine*, 108, pp.17-23.

Jackisch, L., Murphy, A., Al-Daghri, N., McTernan, P., Randeve, H. and Tripathi, G., 2016, October. Tunicamycin-induced ER stress mediates mitochondrial dysfunction in human adipocytes. In *Endocrine Abstracts* (Vol. 44, p. P193). Society for Endocrinology.

- Jadiya, P. and Tomar, D., 2020. Mitochondrial protein quality control mechanisms. *Genes*, 11(5), p.563.
- Jain, A., Sharma, M.C., Sarkar, C., Bhatia, R., Singh, S. and Handa, R., 2007. Major histocompatibility complex class I and II detection as a diagnostic tool in idiopathic inflammatory myopathies. *Archives of pathology & laboratory medicine*, 131(7), pp.1070-1076.
- Jakubaszek, M., Kwiatkowska, B. and Maślińska, M., 2015. Polymyositis and dermatomyositis as a risk of developing cancer. *Reumatologia*, 53(2), p.101.
- Ji, L.L., GOMEZ-CABRERA, M.C. and Vina, J., 2006. Exercise and hormesis: activation of cellular antioxidant signaling pathway. *Annals of the New York Academy of Sciences*, 1067(1), pp.425-435.
- Jia, H., Thelwell, C., Dilger, P., Bird, C., Daniels, S. and Wadhwa, M., 2018. Endothelial cell functions impaired by interferon in vitro: Insights into the molecular mechanism of thrombotic microangiopathy associated with interferon therapy. *Thrombosis research*, 163, pp.105-116.
- Jones, D., Round, J. and De Haan, A., 2004. *Skeletal muscle: from molecules to movement*. Edinburgh.
- Jørgensen, A.N., Aagaard, P., Frandsen, U., Boyle, E. and Diederichsen, L.P., 2018. Blood-flow restricted resistance training in patients with sporadic inclusion body myositis: a randomized controlled trial. *Scandinavian journal of rheumatology*, 47(5), pp.400-409.
- Joshi, P.R., Vetterke, M., Hauburger, A., Tacik, P., Stoltenburg, G. and Hanisch, F., 2014. Functional relevance of mitochondrial abnormalities in sporadic inclusion body myositis. *Journal of Clinical Neuroscience*, 21(11), pp.1959-1963.
- Khadilkar, S.V. and Dhamne, M.C., 2020. What is new in idiopathic inflammatory myopathies: Mechanisms and therapies. *Annals of Indian Academy of Neurology*, 23(4), p.458.

Kim, G.T., Cho, M.L., Park, Y.E., Yoo, W.H., Kim, J.H., Oh, H.J., Kim, D.S., Baek, S.H., Lee, S.H., Lee, J.H. and Kim, H.Y., 2010. Expression of TLR2, TLR4, and TLR9 in dermatomyositis and polymyositis. *Clinical rheumatology*, 29(3), pp.273-279.

Kim, J.H. and Lawler, J.M., 2012. Amplification of proinflammatory phenotype, damage, and weakness by oxidative stress in the diaphragm muscle of mdx mice. *Free Radical Biology and Medicine*, 52(9), pp.1597-1606.

Kim, J.H. and Lawler, J.M., 2012. Amplification of proinflammatory phenotype, damage, and weakness by oxidative stress in the diaphragm muscle of mdx mice. *Free Radical Biology and Medicine*, 52(9), pp.1597-1606.

Kim, S., Joe, Y., Kim, H.J., Kim, Y.S., Jeong, S.O., Pae, H.O., Ryter, S.W., Surh, Y.J. and Chung, H.T., 2015. Endoplasmic reticulum stress–induced IRE1 α activation mediates cross-talk of GSK-3 β and XBP-1 To regulate inflammatory cytokine production. *The Journal of Immunology*, 194(9), pp.4498-4506.

Kissig, M., Ishibashi, J., Harms, M.J., Lim, H.W., Stine, R.R., Won, K.J. and Seale, P., 2017. PRDM16 represses the type I interferon response in adipocytes to promote mitochondrial and thermogenic programming. *The EMBO journal*, 36(11), pp.1528-1542.

Knupp, J., Arvan, P. and Chang, A., 2019. Increased mitochondrial respiration promotes survival from endoplasmic reticulum stress. *Cell Death & Differentiation*, 26(3), pp.487-501.

Kondo, M., Murakawa, Y., Matsumura, T., Matsumoto, O., Taira, M., Moriyama, M., Sumita, Y. and Yamaguchi, S., 2014. A case of overlap syndrome successfully treated with tocilizumab: a hopeful treatment strategy for refractory dermatomyositis?. *Rheumatology*, 53(10), pp.1907-1908.

Kurasawa, K., Arai, S., Namiki, Y., Tanaka, A., Takamura, Y., Owada, T., Arima, M. and Maezawa, R., 2018. Tofacitinib for refractory interstitial lung diseases in anti-melanoma differentiation-associated 5 gene antibody-positive dermatomyositis. *Rheumatology*, 57(12), pp.2114-2119.

Kurtzman, D.J., Wright, N.A., Lin, J., Femia, A.N., Merola, J.F., Patel, M. and Vleugels, R.A., 2016. Tofacitinib citrate for refractory cutaneous dermatomyositis: an alternative treatment. *JAMA dermatology*, 152(8), pp.944-945.

Ladislau, L., Suárez-Calvet, X., Toquet, S., Landon-Cardinal, O., Amelin, D., Depp, M., Rodero, M.P., Hathazi, D., Duffy, D., Bondet, V. and Preusse, C., 2018. JAK inhibitor improves type I interferon induced damage: proof of concept in dermatomyositis. *Brain*, 141(6), pp.1609-1621.

Lawler, J.M., Kunst, M., Hord, J.M., Lee, Y., Joshi, K., Botchlett, R.E., Ramirez, A. and Martinez, D.A., 2014. EUK-134 ameliorates nNOS μ translocation and skeletal muscle fiber atrophy during short-term mechanical unloading. *American Journal of Physiology-Regulatory, Integrative and Comparative Physiology*.

Le Moal, E., Pialoux, V., Juban, G., Groussard, C., Zouhal, H., Chazaud, B. and Mounier, R., 2017. Redox control of skeletal muscle regeneration. *Antioxidants & redox signaling*, 27(5), pp.276-310.

Lebeau, J., Saunders, J.M., Moraes, V.W., Madhavan, A., Madrazo, N., Anthony, M.C. and Wiseman, R.L., 2018. The PERK arm of the unfolded protein response regulates mitochondrial morphology during acute endoplasmic reticulum stress. *Cell reports*, 22(11), pp.2827-2836.

Lee, J.H. and Jun, H.S., 2019. Role of myokines in regulating skeletal muscle mass and function. *Frontiers in physiology*, 10, p.42.

Leipnitz, G., Mohsen, A.W., Karunanidhi, A., Seminotti, B., Roginskaya, V.Y., Markantone, D.M., Grings, M., Mihalik, S.J., Wipf, P., Van Houten, B. and Vockley, J., 2018. Evaluation of mitochondrial bioenergetics, dynamics, endoplasmic reticulum-mitochondria crosstalk, and reactive oxygen species in fibroblasts from patients with complex I deficiency. *Scientific reports*, 8(1), pp.1-14.

Li, C.K., Varsani, H., Holton, J.L., Gao, B., Woo, P., Wedderburn, L.R. and Juvenile Dermatomyositis Research Group, 2004. MHC Class I overexpression on muscles in early juvenile dermatomyositis. *The Journal of rheumatology*, 31(3), pp.605-609.

Li, C.K.C., Knopp, P., Moncrieffe, H., Singh, B., Shah, S., Nagaraju, K., Varsani, H., Gao, B. and Wedderburn, L.R., 2009. Overexpression of MHC class I heavy chain protein in young skeletal muscle leads to severe myositis: implications for juvenile myositis. *The American journal of pathology*, 175(3), pp.1030-1040.

Li, J., Yin, C., Okamoto, H., Jaffe, H., Oldfield, E.H., Zhuang, Z., Vortmeyer, A.O. and Rushing, E.J., 2006. Proteomic analysis of inclusion body myositis. *Journal of Neuropathology & Experimental Neurology*, 65(8), pp.826-833.

Li, K., Pu, C., Huang, X., Liu, J., Mao, Y. and Lu, X., 2014. Proteomic study of sporadic inclusion body myositis. *Proteome science*, 12(1), pp.1-8.

Li, R., Jia, Z. and Trush, M.A., 2016. Defining ROS in biology and medicine. *Reactive oxygen species (Apex, NC)*, 1(1), p.9.

Lightfoot, A., Jackson, M., McArdle, A. and Cooper, R., 2014. Endoplasmic Reticulum (ER) Stress-Induced Mitochondrial Dysfunction and Atrophy Can be Prevented By Pharmacological Upregulation of Heat Shock Protein 70 (HSP) in Cultured Murine Myotubes.: 2218. *Arthritis & Rheumatology*, 66.

Lightfoot, A.P., Goljanek-Whysall, K., Cotton, C.V., Earl, K.E., McArdle, A. and Cooper, R.G., 2015. O42. Is muscle a chemotactic organ in the idiopathic inflammatory myopathies (IIM)? Overexpression of MHC I (H-2Kb) in C2C12 myotubes results in release of pro-inflammatory cytokines. *Rheumatology*, 54(suppl_1), pp.i43-i43.

Lightfoot, A.P., McArdle, A., Jackson, M.J. and Cooper, R.G., 2015. In the idiopathic inflammatory myopathies (IIM), do reactive oxygen species (ROS) contribute to muscle weakness?. *Annals of the Rheumatic Diseases*, 74(7), pp.1340-1346

Lightfoot, A.P., Nagaraju, K., McArdle, A. and Cooper, R.G., 2015. Understanding the origin of non-immune cell-mediated weakness in the idiopathic inflammatory myopathies—potential role of ER stress pathways. *Current opinion in rheumatology*, 27(6), pp.580-585.

Lim, J., Eftimov, F., Verhamme, C., Brusse, E., Hoogendijk, J.E., Saris, C.G., Raaphorst, J., De Haan, R.J., van Schaik, I.N., Aronica, E. and de Visser, M., 2021. Intravenous

immunoglobulins as first-line treatment in idiopathic inflammatory myopathies: a pilot study. *Rheumatology*, 60(4), pp.1784-1792.

Lindgren, U., Roos, S., Oldfors, C.H., Moslemi, A.R., Lindberg, C. and Oldfors, A., 2015. Mitochondrial pathology in inclusion body myositis. *Neuromuscular Disorders*, 25(4), pp.281-288.

Loaiza-Félix, J., Moreno-Ramírez, M., Pérez-García, F.L., Jiménez-Rojas, V., Sánchez-Muñoz, F. and Amezcua-Guerra, M.L., 2017. Serum levels of adipokines in patients with idiopathic inflammatory myopathies: a pilot study. *Rheumatology international*, 37(8), pp.1341-1345.

Lundberg, I., Kratz, A.K., Alexanderson, H. and Patarroyo, M., 2000. Decreased expression of interleukin-1 α , interleukin-1 β , and cell adhesion molecules in muscle tissue following corticosteroid treatment in patients with polymyositis and dermatomyositis. *Arthritis & Rheumatism: Official Journal of the American College of Rheumatology*, 43(2), pp.336-348.

Lundberg, I., Ulfgren, A.K., Nyberg, P., Andersson, U. and Klareskog, L., 1997. Cytokine production in muscle tissue of patients with idiopathic inflammatory myopathies. *Arthritis & Rheumatism: Official Journal of the American College of Rheumatology*, 40(5), pp.865-874.

Lundberg, I.E., 2016. New ways to subclassify patients with myositis. *Journal of internal medicine*, 280(1), pp.4-7.

Lundberg, I.E., Miller, F.W., Tjärnlund, A. and Bottai, M., 2016. Diagnosis and classification of idiopathic inflammatory myopathies. *Journal of internal medicine*, 280(1), pp.39-51

Lundberg, I.E., Tjärnlund, A., Bottai, M., Werth, V.P., Pilkington, C., de Visser, M., Alfredsson, L., Amato, A.A., Barohn, R.J., Liang, M.H. and Singh, J.A., 2017. EULAR/ACR classification criteria for adult and juvenile idiopathic inflammatory myopathies and their major subgroups. *Arthritis & rheumatology (Hoboken, NJ)*, 69(12), p.2271.

Madreiter-Sokolowski, C.T., Waldeck-Weiermair, M., Bourguignon, M.P., Villeneuve, N., Gottschalk, B., Klec, C., Stryeck, S., Radulovic, S., Parichatikanond, W., Frank, S. and Madl,

- T., 2019. Enhanced inter-compartmental Ca²⁺ flux modulates mitochondrial metabolism and apoptotic threshold during aging. *Redox biology*, 20, pp.458-466.
- Mageriu, V., Manole, E., Bastian, A.E. and Staniceanu, F., 2020. Role of Myokines in Myositis Pathogenesis and Their Potential to be New Therapeutic Targets in Idiopathic Inflammatory Myopathies. *Journal of Immunology Research*, 2020.
- Malik, A., Hayat, G., Kalia, J.S. and Guzman, M.A., 2016. Idiopathic inflammatory myopathies: clinical approach and management. *Frontiers in neurology*, 7, p.64.
- Mamchaoui, K., Trollet, C., Bigot, A., Negroni, E., Chaouch, S., Wolff, A., Kandalla, P.K., Marie, S., Di Santo, J., St Guily, J.L. and Muntoni, F., 2011. Immortalized pathological human myoblasts: towards a universal tool for the study of neuromuscular disorders. *Skeletal muscle*, 1(1), pp.1-11.
- Marino Gammazza, A., Macaluso, F., Di Felice, V., Cappello, F. and Barone, R., 2018. Hsp60 in skeletal muscle fiber biogenesis and homeostasis: From physical exercise to skeletal muscle pathology. *Cells*, 7(12), p.224.
- Marroqui, L., Dos Santos, R.S., de Brachène, A.C., Marselli, L., Marchetti, P. and Eizirik, D.L., 2017. Interferon- α mediates human beta cell HLA class I overexpression, endoplasmic reticulum stress and apoptosis, three hallmarks of early human type 1 diabetes. *Diabetologia*, 60(4), pp.656-667.
- Marvi, U., Chung, L. and Fiorentino, D.F., 2012. Clinical presentation and evaluation of dermatomyositis. *Indian journal of dermatology*, 57(5), p.375.
- Mason, S. and Wadley, G.D., 2014. Skeletal muscle reactive oxygen species: a target of good cop/bad cop for exercise and disease. *Redox Report*, 19(3), pp.97-106.
- Meyer, A., Laverny, G., Allenbach, Y., Grelet, E., Ueberschlag, V., Echaniz-Laguna, A., Lannes, B., Alsaleh, G., Charles, A.L., Singh, F. and Zoll, J., 2017. IFN- β -induced reactive oxygen species and mitochondrial damage contribute to muscle impairment and inflammation maintenance in dermatomyositis. *Acta neuropathologica*, 134(4), pp.655-666.

Michaelson, L.P., Iler, C. and Ward, C.W., 2013. ROS and RNS signaling in skeletal muscle: critical signals and therapeutic targets. *Annual review of nursing research*, 31(1), pp.367-387.

Munters, L.A., Loell, I., Ossipova, E., Raouf, J., Dastmalchi, M., Lindroos, E., Chen, Y.W., Esbjörnsson, M., Korotkova, M., Alexanderson, H. and Nagaraju, K., 2016. Endurance exercise improves molecular pathways of aerobic metabolism in patients with myositis. *Arthritis & rheumatology*, 68(7), pp.1738-1750.

Nagaraju, K., Casciola-Rosen, L., Lundberg, I., Rawat, R., Cutting, S., Thapliyal, R., Chang, J., Dwivedi, S., Mitsak, M., Chen, Y.W. and Plotz, P., 2005. Activation of the endoplasmic reticulum stress response in autoimmune myositis: potential role in muscle fiber damage and dysfunction. *Arthritis & Rheumatism*, 52(6), pp.1824-1835.

Narazaki, M., Hagihara, K., Shima, Y., Ogata, A., Kishimoto, T. and Tanaka, T., 2011. Therapeutic effect of tocilizumab on two patients with polymyositis. *Rheumatology*, 50(7), pp.1344-1346.

Nemes, R., Koltai, E., Taylor, A.W., Suzuki, K., Gyori, F. and Radak, Z., 2018. Reactive oxygen and nitrogen species regulate key metabolic, anabolic, and catabolic pathways in skeletal muscle. *Antioxidants*, 7(7), p.85.

Nogalska, A., D'Agostino, C., Engel, W.K., Cacciottolo, M., Asada, S., Mori, K. and Askanas, V., 2015. Activation of the unfolded protein response in sporadic inclusion-body myositis but not in hereditary GNE inclusion-body myopathy. *Journal of Neuropathology & Experimental Neurology*, 74(6), pp.538-546.

Nogalska, A., D'Agostino, C., Terracciano, C., Engel, W.K. and Askanas, V., 2010. Impaired autophagy in sporadic inclusion-body myositis and in endoplasmic reticulum stress-provoked cultured human muscle fibers. *The American journal of pathology*, 177(3), pp.1377-1387.

Nogalska, A., Engel, W.K., McFerrin, J., Kokame, K., Komano, H. and Askanas, V., 2006. Homocysteine-induced endoplasmic reticulum protein (Herp) is up-regulated in sporadic inclusion-body myositis and in endoplasmic reticulum stress-induced cultured human muscle fibers. *Journal of neurochemistry*, 96(5), pp.1491-1499.

Nogalska, A., Wojcik, S., Engel, W.K., McFerrin, J. and Askanas, V., 2007. Endoplasmic reticulum stress induces myostatin precursor protein and NF- κ B in cultured human muscle fibers: relevance to inclusion body myositis. *Experimental neurology*, 204(2), pp.610-618.

Nyberg, P.E.R.N.I.L.L.A., Wikman, A.L., Nennesmo, I.N.G.E.R. and Lundberg, I.N.G.R.I.D., 2000. Increased expression of interleukin 1 α and MHC class I in muscle tissue of patients with chronic, inactive polymyositis and dermatomyositis. *The Journal of rheumatology*, 27(4), pp.940-948.

O'Connor, A., Mulhall, J., Harney, S., Ryan, J., Murphy, G., Henry, M., Annis, P. and Ryan, A., 2016. Should the Use of the Extended Myositis Antibody (EMA) Panel Be Part of the Routine Work-Up in Suspected Myositis?(P5. 038).

O'Connor, A., Mulhall, J., Harney, S.M., Ryan, J.G., Murphy, G., Henry, M.T., Annis, P., Tormey, V. and Ryan, A., 2017. Investigating idiopathic inflammatory myopathy; initial cross speciality experience with use of the extended myositis antibody panel. *Clinics and practice*, 7(2), pp.64-66.

Oddis, C.V. and Aggarwal, R., 2018. Treatment in myositis. *Nature Reviews Rheumatology*, 14(5), pp.279-289.

Oh, T.H., Brumfield, K.A., Hoskin, T.L., Kasperbauer, J.L. and Basford, J.R., 2008. Dysphagia in inclusion body myositis: clinical features, management, and clinical outcome. *American journal of physical medicine & rehabilitation*, 87(11), pp.883-889.

Oikawa, Y., Izumi, R., Koide, M., Hagiwara, Y., Kanzaki, M., Suzuki, N., Kikuchi, K., Matsushashi, T., Akiyama, Y., Ichijo, M. and Watanabe, S., 2020. Mitochondrial dysfunction underlying sporadic inclusion body myositis is ameliorated by the mitochondrial homing drug MA-5. *PloS one*, 15(12), p.e0231064.

Okiyama, N., Sugihara, T., Iwakura, Y., Yokozeki, H., Miyasaka, N. and Kohsaka, H., 2009. Therapeutic effects of interleukin-6 blockade in a murine model of polymyositis that does not require interleukin-17A. *Arthritis & Rheumatism: Official Journal of the American College of Rheumatology*, 60(8), pp.2505-2512.

- Oldfors, A., Moslemi, A.R., Fyhr, I.M., Holme, E., Larsson, N.G. and Lindberg, C., 1995. Mitochondrial DNA deletions in muscle fibers in inclusion body myositis. *Journal of Neuropathology & Experimental Neurology*, 54(4), pp.581-587.
- Oldroyd, A., Lilleker, J. and Chinoy, H., 2017. Idiopathic inflammatory myopathies—a guide to subtypes, diagnostic approach and treatment. *Clinical Medicine*, 17(4), p.322.h
- Ono, Y. and Sakamoto, K., 2017. Lipopolysaccharide inhibits myogenic differentiation of C2C12 myoblasts through the Toll-like receptor 4-nuclear factor- κ B signaling pathway and myoblast-derived tumor necrosis factor- α . *PLoS One*, 12(7), p.e0182040.
- Osowski, C.M. and Urano, F., 2011. Measuring ER stress and the unfolded protein response using mammalian tissue culture system. *Methods in enzymology*, 490, pp.71-92.
- Ostrowski, K., Hermann, C., Bangash, A., Schjerling, P., Nielsen, J.N. and Pedersen, B.K., 1998. A trauma-like elevation of plasma cytokines in humans in response to treadmill running. *The Journal of physiology*, 513(3), pp.889-894.
- Ostrowski, K., Rohde, T., Zacho, M., Asp, S. and Pedersen, B.K., 1998. Evidence that interleukin-6 is produced in human skeletal muscle during prolonged running. *The Journal of physiology*, 508(3), pp.949-953.
- Ott, M., Gogvadze, V., Orrenius, S. and Zhivotovsky, B., 2007. Mitochondria, oxidative stress and cell death. *Apoptosis*, 12(5), pp.913-922.
- Ott, M., Gogvadze, V., Orrenius, S. and Zhivotovsky, B., 2007. Mitochondria, oxidative stress and cell death. *Apoptosis*, 12(5), pp.913-922.
- Paik, J.J., Casciola-Rosen, L., Shin, J.Y., Albayda, J., Tiniakou, E., Leung, D.G., Gutierrez-Alamillo, L., Perin, J., Florea, L., Antonescu, C. and Leung, S.G., 2021. Study of Tofacitinib in Refractory Dermatomyositis: An Open-Label Pilot Study of Ten Patients. *Arthritis & Rheumatology*, 73(5), pp.858-865.
- Papadopoulou, C., Hong, Y., Omoyinmi, E., Brogan, P.A. and Eleftheriou, D., 2019. Janus kinase 1/2 inhibition with baricitinib in the treatment of juvenile dermatomyositis. *Brain*, 142(3), pp.e8-e8.

Pauly, M., Angebault-Prouteau, C., Dridi, H., Notarnicola, C., Scheuermann, V., Lacampagne, A., Matecki, S. and Fauconnier, J., 2017. ER stress disturbs SR/ER-mitochondria Ca²⁺ transfer: Implications in Duchenne muscular dystrophy. *Biochimica et Biophysica Acta (BBA)-Molecular Basis of Disease*, 1863(9), pp.2229-2239.

Pearson, T., Kabayo, T., Ng, R., Chamberlain, J., McArdle, A. and Jackson, M.J., 2014. Skeletal muscle contractions induce acute changes in cytosolic superoxide, but slower responses in mitochondrial superoxide and cellular hydrogen peroxide. *PloS one*, 9(5), p.e96378.

Pearson, T., McArdle, A. and Jackson, M.J., 2015. Nitric oxide availability is increased in contracting skeletal muscle from aged mice, but does not differentially decrease muscle superoxide. *Free Radical Biology and Medicine*, 78, pp.82-88.

Perry, S.W., Norman, J.P., Barbieri, J., Brown, E.B. and Gelbard, H.A., 2011. Mitochondrial membrane potential probes and the proton gradient: a practical usage guide. *Biotechniques*, 50(2), pp.98-115.

Perry, S.W., Norman, J.P., Litzburg, A., Zhang, D., Dewhurst, S. and Gelbard, H.A., 2005. HIV-1 transactivator of transcription protein induces mitochondrial hyperpolarization and synaptic stress leading to apoptosis. *The Journal of Immunology*, 174(7), pp.4333-4344.

Peugnet, V., Chwastyniak, M., Lancel, S., Bultot, L., Fourny, N., Beseme, O., Loyens, A., Heyse, W., Amouyel, P., Bertrand, L. and Pinet, F., 2021. Restore mitophagy is essential to prevent cardiac oxidative stress during hypertrophy. *bioRxiv*.

Phaniendra, A., Jestadi, D.B. and Periyasamy, L., 2015. Free radicals: properties, sources, targets, and their implication in various diseases. *Indian journal of clinical biochemistry*, 30(1), pp.11-26.

Pitkanen, S. and Robinson, B.H., 1996. Mitochondrial complex I deficiency leads to increased production of superoxide radicals and induction of superoxide dismutase. *The Journal of clinical investigation*, 98(2), pp.345-351.

Plant, D.R., Lynch, G.S. and Williams, D.A., 2000. Hydrogen peroxide modulates Ca²⁺-activation of single permeabilized fibres from fast-and slow-twitch skeletal muscles of rats. *Journal of Muscle Research & Cell Motility*, 21(8), pp.747-752.

Powers, S.K., Duarte, J., Kavazis, A.N. and Talbert, E.E., 2010. Reactive oxygen species are signalling molecules for skeletal muscle adaptation. *Experimental physiology*, 95(1), pp.1-9.

Purushothaman, S. and Nair, R.R., 2016. Mitoprotective antioxidant EUK-134 stimulates fatty acid oxidation and prevents hypertrophy in H9C2 cells. *Molecular and Cellular Biochemistry*, 420(1), pp.185-194.

Quan, X., Wang, J., Liang, C., Zheng, H. and Zhang, L., 2015. Melatonin inhibits tunicamycin-induced endoplasmic reticulum stress and insulin resistance in skeletal muscle cells. *Biochemical and biophysical research communications*, 463(4), pp.1102-1107.

R&DSystem. (2021) *Luminex Assay Principle*. UK: R&D System. [Online] [Accessed on 05 Sept 2021] <https://www.rndsystems.com/resources/technical/luminex-assay-principle>

Raju, R., Vasconcelos, O., Granger, R. and Dalakas, M.C., 2003. Expression of IFN- γ -inducible chemokines in inclusion body myositis. *Journal of neuroimmunology*, 141(1-2), pp.125-131.

Rayavarapu, S., Coley, W., Kinder, T.B. and Nagaraju, K., 2013. Idiopathic inflammatory myopathies: pathogenic mechanisms of muscle weakness. *Skeletal muscle*, 3(1), pp.1-13.

Regnier, M., Lorenz, R.R. and Sieck, G.C., 1992, February. EFFECTS OF OXYGEN RADICAL SCAVENGERS ON FORCE PRODUCTION IN SINGLE LIVING FROG SKELETAL-MUSCLE FIBERS. In *FASEB JOURNAL* (Vol. 6, No. 5, pp. A1819-A1819). 9650 ROCKVILLE PIKE, BETHESDA, MD 20814-3998 USA: FEDERATION AMER SOC EXP BIOL.

Reid, M.B., Khawli, F.A. and Moody, M.R., 1993. Reactive oxygen in skeletal muscle. III. Contractility of unfatigued muscle. *Journal of applied physiology*, 75(3), pp.1081-1087.

Rigolet, M., Hou, C., Amer, Y.B., Aouizerate, J., Periou, B., Gherardi, R.K., Lafuste, P. and Authier, F.J., 2019. Distinct interferon signatures stratify inflammatory and dysimmune myopathies. *RMD open*, 5(1), p.e000811.

Rygiel, K.A., Miller, J., Grady, J.P., Rocha, M.C., Taylor, R.W. and Turnbull, D.M., 2015. Mitochondrial and inflammatory changes in sporadic inclusion body myositis. *Neuropathology and applied neurobiology*, 41(3), pp.288-303.

Rygiel, K.A., Miller, J., Grady, J.P., Rocha, M.C., Taylor, R.W. and Turnbull, D.M., 2015. Mitochondrial and inflammatory changes in sporadic inclusion body myositis. *Neuropathology and applied neurobiology*, 41(3), pp.288-303.

Saborido, A., Naudí, A., Portero-Otín, M., Pamplona, R. and Megías, A., 2011. Stanazolol treatment decreases the mitochondrial ROS generation and oxidative stress induced by acute exercise in rat skeletal muscle. *Journal of applied physiology*, 110(3), pp.661-669.

Sachdev, R., Kappes-Horn, K., Paulsen, L., Duernberger, Y., Pleschka, C., Denner, P., Kundu, B., Reimann, J. and Vorberg, I., 2018. Endoplasmic reticulum stress induces myostatin high molecular weight aggregates and impairs mature myostatin secretion. *Molecular neurobiology*, 55(11), pp.8355-8373.

Sacheck, J.M., Cannon, J.G., Hamada, K., Vannier, E., Blumberg, J.B. and Roubenoff, R., 2006. Age-related loss of associations between acute exercise-induced IL-6 and oxidative stress. *American Journal of Physiology-Endocrinology and Metabolism*, 291(2), pp.E340-E349.

Sahlin, K., Shabalina, I.G., Mattsson, C.M., Bakkman, L., Fernström, M., Rozhdestvenskaya, Z., Enqvist, J.K., Nedergaard, J., Ekblom, B. and Tonkonogi, M., 2010. Ultraendurance exercise increases the production of reactive oxygen species in isolated mitochondria from human skeletal muscle. *Journal of applied physiology*, 108(4), pp.780-787.

Sakellariou, G.K., Jackson, M.J. and Vasilaki, A., 2014. Redefining the major contributors to superoxide production in contracting skeletal muscle. The role of NAD (P) H oxidases. *Free radical research*, 48(1), pp.12-29.

Salajegheh, M., Pinkus, J.L., Amato, A.A., Morehouse, C., Jallal, B., Yao, Y. and Greenberg, S.A., 2010. Permissive environment for B-cell maturation in myositis muscle in the absence of B-cell follicles. *Muscle & nerve*, 42(4), pp.576-583.

Salomonsson, S. and Lundberg, I.E., 2006. Cytokines in idiopathic inflammatory myopathies. *Autoimmunity*, 39(3), pp.177-190.

Sanner, H., Schwartz, T., Flatø, B., Vistnes, M., Christensen, G. and Sjaastad, I., 2014. Increased levels of eotaxin and MCP-1 in juvenile dermatomyositis median 16.8 years after disease onset; associations with disease activity, duration and organ damage. *PLoS One*, 9(3), p.e92171.

Santorelli, F.M., Sciacco, M., Tanji, K., Shanske, S., Vu, T.H., Golzi, V., Griggs, R.C., Mendell, J.R., Hays, A.P., Bertorini, T.E. and Pestronk, A., 1996. Multiple mitochondrial DNA deletions in sporadic inclusion body myositis: a study of 56 patients.

Sanvee, G.M., Bouitbir, J. and Krähenbühl, S., 2021. C2C12 myoblasts are more sensitive to the toxic effects of simvastatin than myotubes and show impaired proliferation and myotube formation. *Biochemical Pharmacology*, 190, p.114649.

Schmidt, J., 2018. Current classification and management of inflammatory myopathies. *Journal of neuromuscular diseases*, 5(2), pp.109-129.

Schmidt, J., Barthel, K., Zschüntzsch, J., Muth, I.E., Swindle, E.J., Hombach, A., Sehmisch, S., Wrede, A., Lühder, F., Gold, R. and Dalakas, M.C., 2012. Nitric oxide stress in sporadic inclusion body myositis muscle fibres: inhibition of inducible nitric oxide synthase prevents interleukin-1 β -induced accumulation of β -amyloid and cell death. *Brain*, 135(4), pp.1102-1114.

Schreiner, B., Voss, J., Wischhusen, J., Dombrowski, Y., Steinle, A., Lochmüller, H., Dalakas, M., Melms, A. and Wiendl, H., 2006. Expression of toll-like receptors by human muscle cells in vitro and in vivo: TLR3 is highly expressed in inflammatory and HIV myopathies, mediates IL-8 release and up-regulation of NKG2D-ligands. *The FASEB journal*, 20(1), pp.118-120.

Sciorati, C., Monno, A., Doglio, M.G., Rigamonti, E., Ascherman, D.P., Manfredi, A.A. and Rovere-Querini, P., 2018. Exacerbation of murine experimental autoimmune myositis by Toll-like receptor 7/8. *Arthritis & Rheumatology*, 70(8), pp.1276-1287.

Scuderi, F., Mannella, F., Marino, M., Provenzano, C. and Bartoccioni, E., 2006. IL-6-deficient mice show impaired inflammatory response in a model of myosin-induced experimental myositis. *Journal of Neuroimmunology*, 176(1-2), pp.9-15.

- Senft, D. and Ze'ev, A.R., 2015. UPR, autophagy, and mitochondria crosstalk underlies the ER stress response. *Trends in biochemical sciences*, 40(3), pp.141-148.
- Seo, A.Y., Joseph, A.M., Dutta, D., Hwang, J.C., Aris, J.P. and Leeuwenburgh, C., 2010. New insights into the role of mitochondria in aging: mitochondrial dynamics and more. *Journal of cell science*, 123(15), pp.2533-2542.
- Shabrokh, E., Kavanaugh, J., McMillan, R.P., Pittman, J., Hulver, M.W. and Frisard, M., 2014. Mitochondrial dysregulation in skeletal muscle from patients diagnosed with Alzheimer's disease and sporadic inclusion body myositis.
- Shirihai, O.S., Song, M. and Dorn, G.W., 2015. How mitochondrial dynamism orchestrates mitophagy. *Circulation research*, 116(11), pp.1835-1849.
- Sivandzade, F., Bhalerao, A. and Cucullo, L., 2019. Analysis of the mitochondrial membrane potential using the cationic JC-1 dye as a sensitive fluorescent probe. *Bio-protocol*, 9(1).
- Soriano-Arroquia, A., Clegg, P.D., Molloy, A.P. and Goljanek-Whysall, K., 2017. Preparation and culture of myogenic precursor cells/primary myoblasts from skeletal muscle of adult and aged humans. *Journal of visualized experiments: JoVE*, (120).
- Sriram, S., Subramanian, S., Sathiakumar, D., Venkatesh, R., Salerno, M.S., McFarlane, C.D., Kambadur, R. and Sharma, M., 2011. Modulation of reactive oxygen species in skeletal muscle by myostatin is mediated through NF- κ B. *Aging cell*, 10(6), pp.931-948.
- Sugiura, T., Harigai, M., Kawaguchi, Y., Takagi, K., Fukasawa, C., Ohsako-Higami, S., Ohta, S., Tanaka, M., Hara, M. and Kamatani, N., 2002. Increased IL-15 production of muscle cells in polymyositis and dermatomyositis. *International Immunology*, 14(8), pp.917-924.
- Sundaram, C., Uppin, M.S. and Meena, A.K., 2008. Major histocompatibility complex class I expression can be used as a diagnostic tool to differentiate idiopathic inflammatory myopathies from dystrophies. *Neurology India*, 56(3), p.363.
- Terasawa, H., Tsang, K.Y., Gulley, J., Arlen, P. and Schlom, J., 2002. Identification and characterization of a human agonist cytotoxic T-lymphocyte epitope of human prostate-specific antigen. *Clinical Cancer Research*, 8(1), pp.41-53.

Tews, D.S. and Goebel, H.H., 1998. Cell death and oxidative damage in inflammatory myopathies. *Clinical immunology and immunopathology*, 87(3), pp.240-247.

Thoma, A., Lyon, M., Al-Shanti, N., Nye, G.A., Cooper, R.G. and Lightfoot, A.P., 2020. Eukarion-134 attenuates endoplasmic reticulum stress-induced mitochondrial dysfunction in human skeletal muscle cells. *Antioxidants*, 9(8), p.710.

Torres-Ruiz, J., Carrillo-Vazquez, D.A., Padilla-Ortiz, D.M., Vazquez-Rodriguez, R., Nuñez-Alvarez, C., Juarez-Vega, G. and Gomez-Martin, D., 2020. TLR expression in peripheral monocyte subsets of patients with idiopathic inflammatory myopathies: association with clinical and immunological features. *Journal of translational medicine*, 18(1), pp.1-12.

Tournadre, A., Lenief, V. and Miossec, P., 2010. Expression of toll-like receptor 3 and toll-like receptor 7 in muscle is characteristic of inflammatory myopathy and is differentially regulated by Th1 and Th17 cytokines. *Arthritis & Rheumatology*, 62(7), pp.2144-2151.

Trnka, J., Elkalaf, M. and Anděl, M., 2015. Lipophilic triphenylphosphonium cations inhibit mitochondrial electron transport chain and induce mitochondrial proton leak. *PLoS one*, 10(4), p.e0121837.

Vasilaki, A., Mansouri, A., Van Remmen, H., Van Der Meulen, J.H., Larkin, L., Richardson, A.G., McArdle, A., Faulkner, J.A. and Jackson, M.J., 2006. Free radical generation by skeletal muscle of adult and old mice: effect of contractile activity. *Aging cell*, 5(2), pp.109-117.

Vattemi, G., Engel, W.K., McFerrin, J. and Askanas, V., 2004. Endoplasmic reticulum stress and unfolded protein response in inclusion body myositis muscle. *The American journal of pathology*, 164(1), pp.1-7.

Vattemi, G., Mirabella, M., Guglielmi, V., Lucchini, M., Tomelleri, G., Ghirardello, A. and Doria, A., 2014. Muscle biopsy features of idiopathic inflammatory myopathies and differential diagnosis. *Autoimmunity Highlights*, 5(3), pp.77-85.

Walsh, R.J., Kong, S.W., Yao, Y., Jallal, B., Kiener, P.A., Pinkus, J.L., Beggs, A.H., Amato, A.A. and Greenberg, S.A., 2007. Type I interferon-inducible gene expression in blood is present and reflects disease activity in dermatomyositis and polymyositis. *Arthritis &*

Rheumatism: Official Journal of the American College of Rheumatology, 56(11), pp.3784-3792.

Walter, P. and Ron, D., 2011. The unfolded protein response: from stress pathway to homeostatic regulation. *science*, 334(6059), pp.1081-1086.

Walter, P. and Ron, D., 2011. The unfolded protein response: from stress pathway to homeostatic regulation. *science*, 334(6059), pp.1081-1086.

Walter, P. and Ron, D., 2011. The unfolded protein response: from stress pathway to homeostatic regulation. *Science*, 334(6059), pp.1081-1086.

Wang, J., Tan, J., Qi, Q., Yang, L., Wang, Y., Zhang, C., Hu, L., Chen, H. and Fang, X., 2018. MiR-487b-3p suppresses the proliferation and differentiation of myoblasts by targeting IRS1 in skeletal muscle myogenesis. *International journal of biological sciences*, 14(7), p.760.

Westrate L.M., Drocco J.A., Martin K.R., Hlavacek W.S., MacKeigan J.P. Mitochondrial morphological features are associated with fission and fusion events. *PLoS ONE*. 2014;9:e95265.

Win, S., Than, T.A., Fernandez-Checa, J.C. and Kaplowitz, N., 2014. JNK interaction with Sab mediates ER stress induced inhibition of mitochondrial respiration and cell death. *Cell death & disease*, 5(1), pp.e989-e989.

Wredenberg, A., Wibom, R., Wilhelmsson, H., Graff, C., Wiener, H.H., Burden, S.J., Oldfors, A., Westerblad, H. and Larsson, N.G., 2002. Increased mitochondrial mass in mitochondrial myopathy mice. *Proceedings of the National Academy of Sciences*, 99(23), pp.15066-15071.

Xiang, C., Wang, Y., Zhang, H. and Han, F., 2017. The role of endoplasmic reticulum stress in neurodegenerative disease. *Apoptosis*, 22(1), pp.1-26.

Xiao, T., Liang, X., Liu, H., Zhang, F., Meng, W. and Hu, F., 2020. Mitochondrial stress protein HSP60 regulates ER stress-induced hepatic lipogenesis. *Journal of molecular endocrinology*, 64(2), pp.67-75.

Yamada, T., Abe, M., Lee, J., Tatebayashi, D., Himori, K., Kanzaki, K., Wada, M., Bruton, J.D., Westerblad, H. and Lanner, J.T., 2015. Muscle dysfunction associated with adjuvant-induced arthritis is prevented by antioxidant treatment. *Skeletal muscle*, 5(1), pp.1-10.



Zeng, L., Maruyama, S., Nakamura, K., Parker-Duffen, J.L., Adham, I.M., Zhong, X., Lee, H.K., Querfurth, H. and Walsh, K., 2014. The injury-induced myokine insulin-like 6 is protective in experimental autoimmune myositis. *Skeletal muscle*, 4(1), pp.1-14.

Zhang, H., He, F., Shi, M., Wang, W., Tian, X., Kang, J., Han, W., Wu, R., Zhou, L., Hu, M. and Li, X., 2017. Toll-like receptor 4–myeloid differentiation primary response gene 88 pathway is involved in the inflammatory development of polymyositis by mediating interferon- γ and interleukin-17A in humans and experimental autoimmune myositis mouse model. *Frontiers in neurology*, 8, p.132.

Zygmunt D.A., Singhal N., Kim M.L., Cramer M.L., Crowe K.E., Xu R., Jia Y., Adair J., Y Valenzuela I.M.P., Akaaboune M., et al. Deletion of Pofut1 in mouse skeletal myofibers induces muscle aging-related phenotypes in cis and in trans. *Mol. Cell. Biol.* 2017;37:e00426-16.

Article

Eukarion-134 Attenuates Endoplasmic Reticulum Stress-Induced Mitochondrial Dysfunction in Human Skeletal Muscle Cells

Anastasia Thoma¹, Max Lyon², Nasser Al-Shanti¹, Gareth A. Nye³ , Robert G. Cooper² and Adam P. Lightfoot^{1,*} 

¹ Musculoskeletal Science & Sports Medicine Research Centre, Department of Life Sciences, Faculty of Science & Engineering, Manchester Metropolitan University, Manchester M1 5GD, UK; anastasia.thoma@stu.mmu.ac.uk (A.T.); n.al-shanti@mmu.ac.uk (N.A.S.)

² Department of Musculoskeletal Biology, Institute of Ageing and Chronic Disease, Faculty of Health and Life Sciences, University of Liverpool, Liverpool L7 8TX, UK; max.lyon@nbt.nhs.uk (M.L.); robert.cooper@liverpool.ac.uk (R.G.C.)

³ Chester Medical School, University of Chester, Chester CH1 4BJ, UK; g.nye@chester.ac.uk

* Correspondence: A.Lightfoot@mmu.ac.uk

Received: 19 June 2020; Accepted: 31 July 2020; Published: 5 August 2020



Abstract: Maladaptive endoplasmic reticulum (ER) stress is associated with modified reactive oxygen species (ROS) generation and mitochondrial abnormalities; and is postulated as a potential mechanism involved in muscle weakness in myositis, an acquired autoimmune neuromuscular disease. This study investigates the impact of ROS generation in an *in vitro* model of ER stress in skeletal muscle, using the ER stress inducer tunicamycin (24 h) in the presence or absence of a superoxide dismutase/catalase mimetic Eukarion (EUK)-134. Tunicamycin induced maladaptive ER stress, which was mitigated by EUK-134 at the transcriptional level. ER stress promoted mitochondrial dysfunction, described by substantial loss of mitochondrial membrane potential, as well as a reduction in respiratory control ratio, reserve capacity, phosphorylating respiration, and coupling efficiency, which was ameliorated by EUK-134. Tunicamycin induced ROS-mediated biogenesis and fusion of mitochondria, which, however, had high propensity of fragmentation, accompanied by upregulated mRNA levels of fission-related markers. Increased cellular ROS generation was observed under ER stress that was prevented by EUK-134, even though no changes in mitochondrial superoxide were noticeable. These findings suggest that targeting ROS generation using EUK-134 can amend aspects of ER stress-induced changes in mitochondrial dynamics and function, and therefore, in instances of chronic ER stress, such as in myositis, quenching ROS generation may be a promising therapy for muscle weakness and dysfunction.

Keywords: ER stress; mitochondria; reactive oxygen species; antioxidant; EUK-134

1. Introduction

The endoplasmic reticulum (ER) is a specialised organelle, which is the key site of protein folding in the cell. The reducing environment of the ER contributes to the high fidelity needed to correctly fold newly synthesised peptides and proteins into their biological active conformation [1,2]. The accumulation of misfolded or aggregated proteins within the ER, termed ER stress, initiates the unfolded protein response (UPR), a ubiquitously expressed network of cellular processes, responsible for restoring protein homeostasis [3]. The UPR induces ER-associated degradation via the ubiquitin proteasome pathway (26S proteasome) to facilitate clearance of misfolded proteins, inhibits protein assembly via translation attenuation, and increases protein folding capacity via chaperones release

(glucose-regulated protein (GRP) 78 and 94). However, failure of establishing protein homeostasis and sustained ER stress lead to UPR-induced cell death, through caspase 12 (autophagy) and cholesterol oxidase-peroxidase C/EBP homologous protein (CHOP) activation (apoptosis) [4,5].

It is well established that chronic or prolonged activation of the ER stress response is implicated in a wide range of diseases, such as neurodegenerative diseases (e.g., Alzheimer's disease), chronic metabolic diseases (e.g., diabetes), and muscle diseases (e.g., Duchenne muscular dystrophy and myositis) [6–9]. The observation that aberrant activation of the ER stress pathway in the muscles of patients with myositis, a rare neuromuscular disorder of autoimmune origin, has directed our research interest at the understanding of the downstream mechanisms of ER stress in skeletal muscle.

The close approximation of ER and mitochondria permits bi-directional crosstalk via the mitochondrial-associated ER membranes and Ca^{2+} signalling, and highlights the potential impact of the sarcoplasmic reticulum (ER in skeletal muscle) on mitochondrial function. Reactive oxygen species (ROS) are generated as an upstream and a downstream component of the UPR pathway. Hydrogen peroxide (H_2O_2) is generated via the thiol/disulphide (-SH/-SS) exchange mechanism during protein folding in the ER, as well as from superoxide ($\text{O}_2^{\bullet-}$) generated from mitochondrial complexes I and III following Ca^{2+} influx. In addition to H_2O_2 , peroxynitrite (ONOO^-) is also generated as a by-product of the reaction between $\text{O}_2^{\bullet-}$ and nitric oxide (NO), and its generation depends on Ca^{2+} -stimulated nitric oxide synthase [5,10]. Prolonged activation of the ER stress response can influence mitochondrial function, resulting in aberrant ROS generation, from both the ER lumen and mitochondria, and oxidative damage [10,11].

Numerous studies have focused on the impact of acute/chronic ER stress on mitochondria bioenergetics, but less is known about the mediators of this ER–mitochondrial crosstalk [12–14]. In this study, we aimed to investigate the role of ROS accumulation in ER stress-induced changes in mitochondrial bioenergetics, biogenesis, and biodynamics, as described by mitochondrial respiration, mass/volume, and morphology. We examined those changes and the impact of ROS generation in human skeletal muscle myoblasts using the ER stress inducer tunicamycin and a synthetic antioxidant, Eukarion (EUK)-134, which has both superoxide dismutase and catalase activity [15].

2. Materials and Methods

2.1. Cell Culture and Treatments

An immortalised human skeletal muscle cell line (donor age, 25 years; sex, male) was provided as a gift to our group from the Institute of Myology, Paris [16]. Skeletal muscle cells were cultured in growth medium containing Dulbecco's modified eagles medium (DMEM, Lonza, Nottingham, UK) and Medium-199 with Earle's BSS (1:5, v/v) (Sigma-Aldrich, Dorset, UK), supplemented with 20% (v/v) heat inactivated foetal bovine serum (Gibco, Loughborough, UK), 1% (v/v) penicillin/streptomycin, 1% (v/v) L-glutamine (Lonza, Nottingham, UK), 10 $\mu\text{g}/\text{mL}$ gentamicin, 25 ng/mL fetuin from foetal bovine serum, 0.2 $\mu\text{g}/\text{mL}$ dexamethasone, 5 $\mu\text{g}/\text{mL}$ recombinant human insulin (Sigma-Aldrich, Dorset, UK), 0.5 ng/mL recombinant human basic fibroblast growth factor, 5 ng/mL recombinant human epidermal growth factor, and 2.5 ng/mL recombinant human hepatocyte growth factor (Gibco, Loughborough, UK). Skeletal muscle myoblasts were incubated at 37 °C in a humidified atmosphere of 5% CO_2 until 80% confluence, and sub-cultured using 0.05% Trypsin/0.53 mM EDTA (1×) (Lonza, Nottingham, UK). Myoblasts were treated with the pharmaceutical ER stress inducer tunicamycin (0.1 $\mu\text{g}/\text{mL}$) in the absence or presence of EUK-134 (10 μM) for 24 h. Data from our laboratory (not shown) and others have determined a dose of 10 μM EUK-134 and 0.1 $\mu\text{g}/\text{mL}$ tunicamycin (24 h) to show efficacy in the absence of apoptosis/cell death—therefore, these concentrations were chosen for this study [17].

2.2. RNA Isolation and Quantitative Real-Time Polymerase Chain Reaction (PCR)

Following 24 h of treatment, myoblasts were harvested using Dulbecco's Phosphate-Buffered Saline (Lonza, Nottingham, UK) and stored at -80 °C. RNA of treated cells was isolated using EZ-RNA

isolation kit (Biological Industries, Beit Haemek, Israel) and cDNA was synthesised using iScript cDNA synthesis kit (Bio-Rad, Watford, UK). Real-time qPCR analyses were performed on a StepOnePlus™ real-time PCR system (Applied Biosystems, Warrington, UK) using QuantiNova SYBR Green PCR Kit (QIAGEN, Manchester, UK); 10 ng of cDNA per reaction was used in a total volume of 10 µL PCR reaction mixture. Three amplifications, consisted of an initial denaturation cycle at 95 °C for 2 min, followed by 40 cycles of 20 s at 95 °C (denaturation), 20 s at optimal annealing temperature, and 20 s at 72 °C (extension), were performed for each primer, followed by a melt curve analysis. Threshold cycle for each target gene of interest was normalised to the housekeeping gene 18S (annealing temperature, 55.7 °C), which has been extensively used in muscle [18–20], and analysed using the delta-delta ($2^{-\Delta\Delta Ct}$) method [21]. The sequences and annealing temperature of all mitochondrial- and ER stress pathway-associated primers used are provided in Tables 1 and 2, respectively.

Table 1. The sequences and annealing temperature of mitochondrial-associated primers.

Target mRNA	Annealing Temperature (°C)	Forward Primer Sequence (5'-3')	Reverse Primer Sequence (5'-3')
MFN2	58	AGTTGGAGCGGAGACTTAGC	ATCGCCTTCTTAGCCAGCAC
HSP60	58	GAACAGCTAACTCCAAGTCAGA	CAGCCGCTCTGAGAACTCA
TFAM	58	CTGCACTCTGTCCCTCACTC	GGGTAACCGAAGCATTCTGC
DRP1	58	TCACCCGGAGACCTCTCATT	TCTGCTTCCACCCCATTTTCT
Citrate Synthase	58	TGATGAGGGCATCCGTTTCC	GTCTTCCCCACCCCTAGCC
FIS1	58	AGGCCTTAAAGTACGTCCGC	TGCCACGAGTCCATCTTTC
UCP3	55.7	GGGTCAACCTGGGATGTAGC	TCCCTAACCCCTCCCCATCAG
HSPA9	58	AGAAGACCGCGAAAGAAGG	TGTTGCACCTATCAGCAGGT

Abbreviations: MFN1, mitofusin 2; HSP60, heat shock protein 60; TFAM, transcription factor A, mitochondrial precursor; DRP1, dynamin-related protein 1; FIS1, fission 1; UCP-3, uncoupling protein 3; and HSPA9, heat shock protein family A member 9.

Table 2. The sequences and annealing temperature of endoplasmic reticulum stress-associated primers.

Target mRNA	Annealing Temperature (°C)	Forward Primer Sequence (5'-3')	Reverse Primer Sequence (5'-3')
GRP78	59.3	TGACATTGAAGACTTCAAAGCT	CTGCTGTATCCTCTTACCAGT
Total XBP1	59.3	GGCATCCTGGCTTGCCTCCA	GCCCCCTCAGCAGGTGTTCC
ERDJ4	59.3	TCCGCATCAGAGCCCAAATCA	ACCACCTAGTAAAAGCACTGTGTCCAAG
CHOP	59.3	GGAGCATCAGTCCCCCACTT	TGTGGGATTGAGGGTCACATC
GADD34	59.3	CCCAGAAACCCCTACTCATGATC	GCCCAGACAGCCAGGAAAT

Abbreviations: GRP78, glucose-regulated protein 78 kDa; total XBP1, total X-box-binding protein 1; ERDJ4, ER-DnaJ-like 4; CHOP, cholesterol oxidase-peroxidase C/EBP homologous protein; and GADD34, growth arrest and DNA damage-inducible gene 34.

2.3. Measurement of Mitochondrial Bioenergetics Using Seahorse Extracellular Flux Analyser

Real-time oxygen consumption rate (OCR) in skeletal muscle myoblasts was measured with a Seahorse XFp Extracellular Flux Analyser (Agilent Technologies, Manchester, UK). Cells were seeded in an 8-well XFp cell culture microplate at a density of 7×10^3 cells/well in 100 µL growth medium, and after adhesion, myoblasts were incubated with TN+/-EUK-134 under standard conditions. The Seahorse XFp Mito Stress Test was performed according to manufacturer's instructions. Specifically, 1 h prior the experiment, growth medium was replaced with unbuffered DMEM (pH 7.4) supplemented with 1 mM pyruvate, 2 mM L-glutamine, and 10 mM glucose, and the plate was equilibrated at 37 °C in a non-CO₂ incubator. Parameters of the cell bioenergetic phenotype were determined following the sequential addition of oligomycin (1 µM), carbonyl cyanide 4-(trifluoromethoxy) phenylhydrazone (FCCP, 2 µM), and rotenone/antimycin (0.5 µM). OCR and extracellular acidification rates, normalised using the bovine gamma globulin assay, were automatically calculated by Seahorse XFp software version 2.2.0.

2.4. Quantification of Mitochondrial Morphology Parameters Using Confocal Microscopy

Skeletal muscle myoblasts were seeded on a 35 mm glass-bottom μ -Dish (ibidi®, Martinsried, Germany), treated as previously described, incubated with the cell-permeant MitoTracker Red CMXRos (5 μ M, 30 min, 37 °C) (Molecular Probes, Invitrogen, Paisley, UK) selective for living mitochondria, and fixed in 4% paraformaldehyde. Nuclei were counter-stained with 4',6'-diamidino-2-phenylindole dihydrochloride (DAPI; 1/5000) (Sigma-Aldrich, Dorset, UK). Imaging was performed on a Leica TCS SP5 confocal microscope (Leica Microsystems, Milton Keynes, UK), using a 63 \times /1.4 oil immersion objective. Parameters of mitochondrial morphology were quantified using a macro on NIH ImageJ, created by Dagda et al. (2009) [22]. Briefly, following background subtraction and local contrast enhancement, region of interest (individual cell) was selected, and macro was activated to subject the images to threshold and transform them to binary.

2.5. Measurement of ROS Generation and Oxidative Damage Markers

To quantify ROS generation and oxidative damage, skeletal muscle cells were seeded at 7×10^3 cells/well in a black, clear bottom microplate (96 wells) and cultured in growth medium. After 24 h treatment with TN \pm /EUK-134, myoblasts were washed once with warm DPBS and incubated with different fluorophores in phenol red-free DMEM medium, in the dark at 37 °C. Total intracellular ROS were determined using 2,7-dichlorofluorescein diacetate (DCFH-DA, 10 μ M, 30 min) (Sigma-Aldrich, Dorset, UK). Intracellular and mitochondrial superoxide generation was measured using dihydroethidium (DHE, 5 μ M, 20 min) (Sigma-Aldrich, Dorset, UK) and MitoSOX Red mitochondrial superoxide indicator (5 μ M, 30 min) (Molecular Probes, Invitrogen, Paisley, UK), respectively. Following incubation with fluorophores, myoblasts were washed three times with DPBS and maintained in Seahorse assay medium. Endpoint fluorescence was measured using a Synergy™ multi-detection microplate reader (BioTek Instruments, Swindon, UK) with the following excitation and emission wavelength: DCFH-DA, 485/20 and 590/35 nm; DHE, 320/40 and 460/40 nm; and MitoSOX Red, 530/25 and 590/35 nm. Total protein thiols (sulphydryl) were quantified as per the manufacturer's guidelines (Abcam, Cambridge, UK). Briefly, treated myoblasts were incubated with Thiol Blue sensor for 30 min on a shaker and samples were run through spin column. Absorbance was measured using a microplate reader at A280 and A680 nm.

For each experiment, the mean value derived from blank wells was subtracted to correct for background fluorescence/absorbance. All microplate reader measurements were normalised to total protein content per sample using the Pierce™ BCA Protein Assay and Bovine Gamma Globulin assay (Thermo scientific, Loughborough, UK).

2.6. Assessment of Mitochondrial Membrane Potential

Mitochondrial membrane potential ($\Delta\Psi_m$) was interrogated using the JC-1 fluorophore (5,5',6,6'-tetrachloro-1,1',3,3'-tetraethylbenzimidazolylcarbocyanine iodide; 5 μ M, 30 min, 37 °C) (Abcam, Cambridge, UK), MitoTracker Red CMXRos (5 μ M, 30 min, 37 °C) (Molecular Probes, Invitrogen, Paisley, UK), or TMRM (Tetramethylrhodamine, methyl ester; 10 nM, 37 °C) (Molecular Probes, Invitrogen, Paisley, UK). Following treatment, myoblasts were incubated with and maintained in TMRM solution, and endpoint fluorescence was read at excitation 530/25 and emission 590/35 nm. JC-1 normally forms red fluorescent aggregates. Red to green fluorescent shift occurs when mitochondrial membrane potential decreases, because of the presence of the green fluorescent monomeric form of JC-1 [23]. Following washing with DPBS, myoblasts were maintained in Seahorse assay medium and endpoint fluorescence from aggregate and monomer form was recorded on the microplate reader at excitation 530/25 and 485/20 nm, respectively, and emission 590/35 nm. Similarly, for MitoTracker Red CMXRos fluorescence staining, myoblasts were maintained in Seahorse assay medium and endpoint fluorescence was read at excitation 590/20 and emission 645/40 nm. Measurements were normalised to total protein content per sample using the Pierce™ BCA Protein Assay and Bovine Gamma Globulin assay.

2.7. Measurement of Mitochondrial Mass/Volume

Human skeletal muscle myoblasts were incubated with 100 nM MitoTracker Green FM (Molecular Probes, Invitrogen, Paisley, UK) prepared in a phenol red-free DMEM and incubated for 30 min at 37 °C. Then, cells were washed once with DPBS and read by a fluorescence microplate reader (excitation 485/20 and emission 528/20 nm) or imaged using a LEICA DMI6000 B inverted microscope at 40× magnification (CTR6000 laser, Leica Microsystems). Fluorescence intensity was normalised to total protein content or nuclei number (using DAPI staining), respectively.

2.8. Immunofluorescence Staining

Human skeletal muscle myoblasts were washed twice with DPBS and fixed using 4% (*w/v*) paraformaldehyde. After 15 min fixation at room temperature, cells were washed and permeabilised using 0.5% (*v/v*) Triton X-100 for 15 min at room temperature. Then, cells were washed and blocked with 3% (*v/v*) goat serum supplemented with 0.05% (*v/v*) Tween-20 for 1 h at room temperature. After washing, cells were incubated with rabbit anti-GRP78 (1/1000) (ab213258; Abcam, Cambridge, UK) at 4 °C overnight. Secondary antibody conjugated with Alexa Fluor 488 (goat anti-rabbit IgG; 1/800; Invitrogen, Paisley, UK) and DAPI (1/5000; Sigma-Aldrich, Dorset, UK) were added to the cells for 1 h at room temperature in the dark. Cells were maintained in DPBS and images were taken using a LEICA DMI6000 B inverted microscope at 20× magnification (CTR6000 laser, Leica Microsystems).

2.9. Western Blotting

Human skeletal muscle myoblasts were lysed using RIPA buffer protease/phosphatase inhibitors and the total protein in each sample was quantified using the Bovine Gamma Globulin assay. Twenty micrograms of protein were separated by 4–15% Mini-PROTEAN TGX Precast Gels (PAGE) (Bio-Rad, Hertfordshire, UK) and transferred to a nitrocellulose membrane. The membranes were blocked with 5% (*w/v*) fat free milk dissolved in Tris-phosphate buffer with 0.0125% (*v/v*) Tween 20 for 1 h and incubated with primary antibodies anti-GRP94 (ab3674), anti-MFN2 (ab56889), anti-SOD1 (ab13498), and anti-SOD2 (ab13533) (1/1000), as well as anti-β-actin (ab8226) (1/5000) as a loading control, at 4 °C overnight. Secondary antibodies were added for 1 h at room temperature and visualised using chemiluminescent substrate (Thermo scientific, Loughborough, UK) and LI-COR Odyssey Fc Imaging System (LI-COR Biosciences, Cambridge, UK).

2.10. Statistical Analyses

Data were assessed for normality of distribution by Shapiro–Wilk test. Data assessed to be normally distributed were analysed using one-way ANOVA, with Tukey post hoc test. Data not normally distributed were analysed using Kruskal–Wallis test, where appropriate. Data were analysed using GraphPad Prism version 8. A *p*-value ≤ 0.05 was considered to be statistically significant.

3. Results

3.1. ER Stress Pathway Activation

Significantly increased expression (fold change) of the UPR genes, *GRP78*, growth arrest and DNA damage-inducible gene 34 (*GADD34*), total X-box-binding protein 1 (*XBPI*), cholesterol oxidase-peroxidase C/EBP homologous protein (*CHOP*), and ER-DnaJ-like 4 (*ERDJ4*), were observed in human skeletal muscle myoblasts treated with tunicamycin, as expected. Combination treatment with EUK-134 resulted in significantly attenuated expression of all genes, except *GADD34* (Figure 1A). ER stress activation following tunicamycin treatment was further confirmed by significantly increased protein levels of GRP94, which, however, were not inhibited by EUK-134 (Figure 1B). GRP78 fluorescence intensity increased upon ER stress activation. However, there was no change in the presence of EUK-134 (Figure 1C,D).

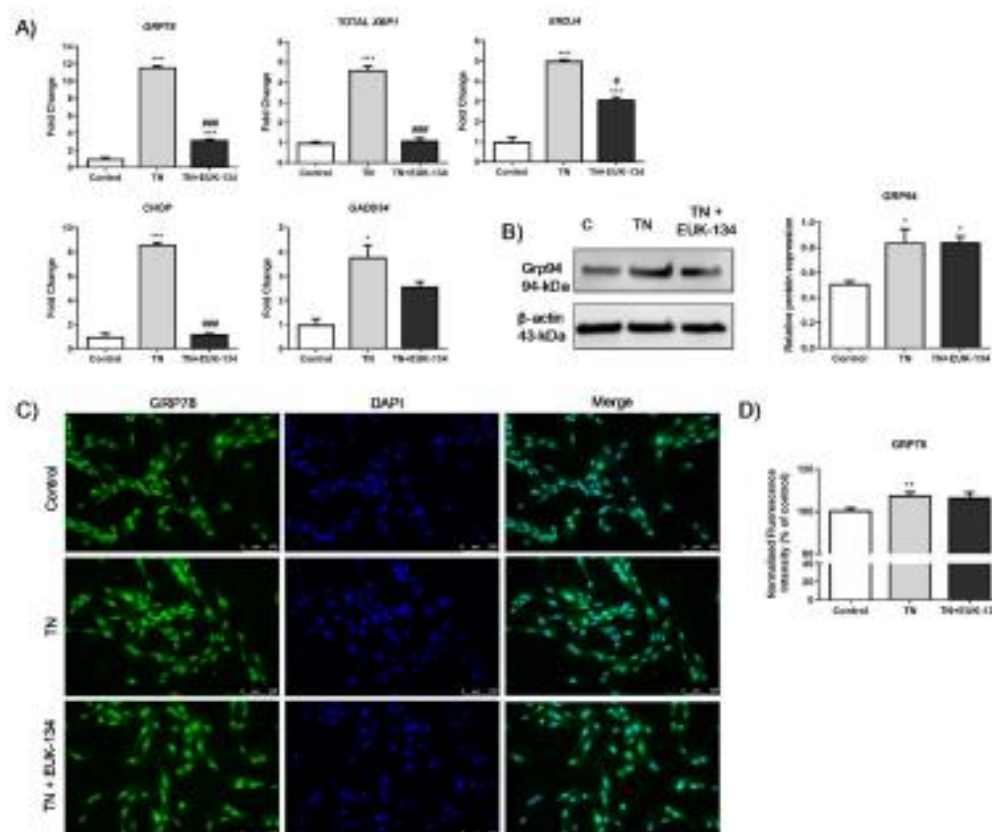


Figure 1. ER stress activation in tunicamycin-treated cells with or without EUK-134. **(A)** Relative fold changes in gene expression for ER stress markers. Data represent the mean fold change normalised to 18S housekeeper gene \pm SEM of Δ Ct values ($n = 3$). **(B)** Cropped representative Western blot image and quantification of GRP94 protein levels relative to β -actin (loading control). Data represent the mean \pm SEM ($n = 3$). **(C)** Representative images of human skeletal muscle myoblast stained for GRP78 (green) and DAPI (blue). Images captured at 20 \times magnification. Scale bar = 100 μ m. Brightness was adjusted equally in each image to enhance visualisation. **(D)** Quantification of total GRP78 fluorescence intensity normalised to nuclei number, relative to control (%). Data represent the mean \pm SEM ($n = 26$). * $p \leq 0.033$, ** $p < 0.002$, and *** $p < 0.001$ against vehicle control or tunicamycin alone (#).

3.2. Mitochondrial Oxygen Consumption and Mitochondrial Unfolded Protein Response

Tunicamycin-induced ER stress showed an overall increase in mitochondrial and non-mitochondrial respiration, which was attenuated in the presence of the antioxidant EUK-134 (Figure 2A,D). Basal OCR values were plotted versus the ECAR values to distinguish the metabolic profile of tunicamycin-treated myocytes in the presence or absence of EUK-134, showing significantly increased basal OCR levels compared to the control group, with no change in basal ECAR levels (Figure 2A,B) [24]. EUK-134 was able to significantly inhibit tunicamycin-induced increase in basal respiration (Figure 2B). Decreased spare respiratory capacity (%), also called as reserve capacity) observed after ER stress induction was significantly increased following EUK-134 treatment, even compared to the vehicle control (Figure 2E). Consistently, depressed ATP-linked OCR was observed following tunicamycin treatment, (Figure 2F), which was further enhanced by a substantial increase in leak respiration, with more than half of oxygen consumed not being used for ATP production (Figure 2G). Importantly, ER stress-induced proton leak was inhibited by EUK-134 treatment.

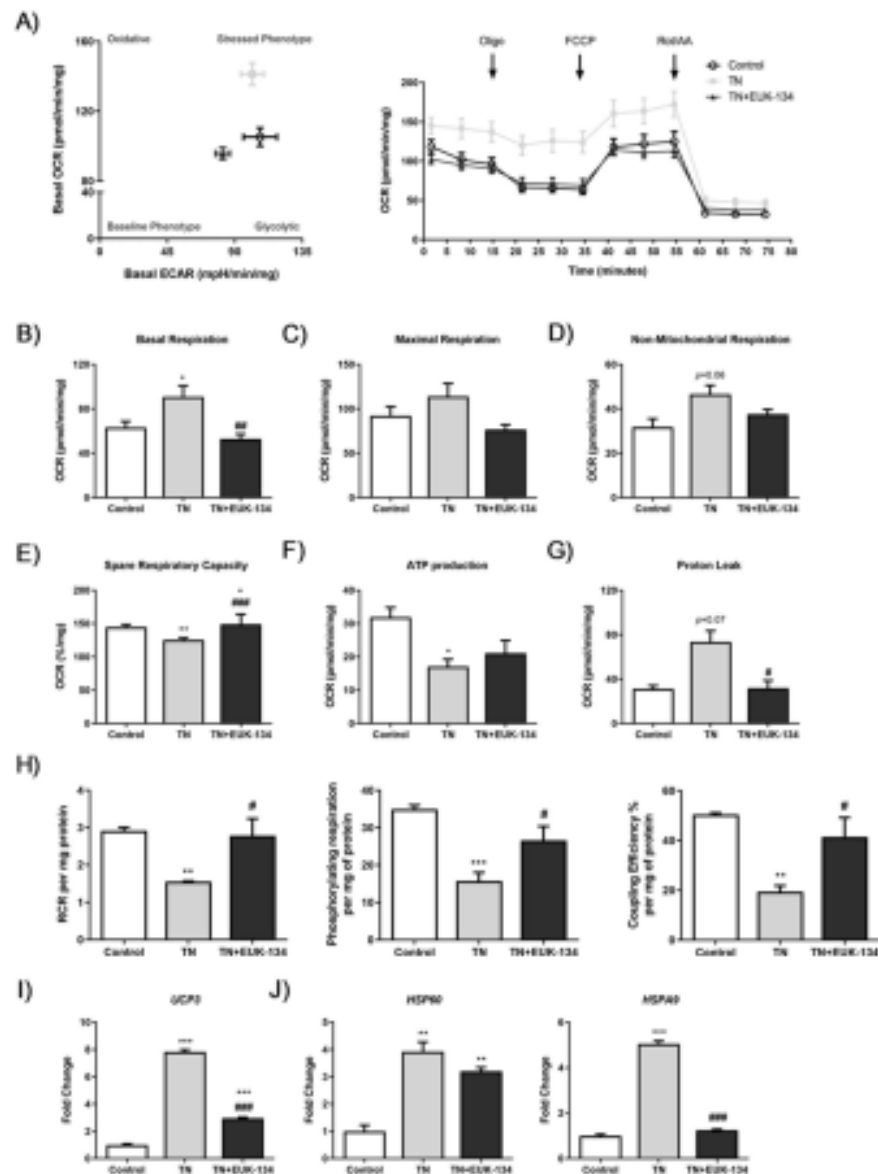


Figure 2. Cellular bioenergetics of tunicamycin-treated cells with or without EUK-134. **(A)** Bioenergetic status presented by basal oxygen consumption rate versus basal extracellular acidification rate, and real-time oxygen consumption rate measured under basal conditions followed by the sequential addition of oligomycin, FCCP, and rotenone/antimycin A mix. **(B–G)** Individual parameters of mitochondrial function; basal respiration, maximal respiration, non-mitochondrial respiration, spare respiratory capacity, ATP production, and proton leak, normalised to protein content. **(H)** Normalised respiratory flux control ratios, respiratory control ratio, phosphorylating respiration, and coupling efficiency (%), derived from the individual mitochondrial parameters. Data represent the mean \pm SEM ($n = 5$). * $p \leq 0.033$, ** $p < 0.002$, and *** $p < 0.001$ against vehicle control or tunicamycin alone (#). **(I)** Relative fold change in mRNA expression of *UCP3*. **(J)** Relative fold changes in mRNA expression of mitochondrial unfolded protein response markers, *HSP60* and *HSPA9*. Data represent the mean fold change normalised to 18S housekeeper gene \pm SEM of Δ Ct values, ($n = 3$). * $p \leq 0.033$, ** $p < 0.002$, and *** $p < 0.001$ against vehicle control or tunicamycin alone (#). OCR, oxygen consumption rate; ECAR, extracellular acidification rate; RCR, respiratory control ratio.

To further evidence ER stress-induced mitochondrial dysfunction and investigate the impact of EUK-134, normalised respiratory flux control ratios were determined using the six parameters of mitochondrial function [24]. A significant decline was found in respiratory control ratio (RCR), phosphorylating respiration, and coupling efficiency under ER stress, which were inhibited by antioxidant treatment (Figure 2H). ER stress impaired the efficiency of mitochondrial respiration and decreased the potential ATP turnover leading to proton leak, and these effects were ROS-mediated. ROS-mediated decreased coupling efficiency and increased leak respiration, both indicative of proton leak-driven oxygen consumption, were also attributable to changes in the expression of the mitochondrial uncoupling protein 3 (*UCP3*), which were significantly decreased by EUK-134, but not to control levels (Figure 2I).

ER stress-induced activation of the mitochondrial unfolded protein response was also evident. Real-time qPCR results showed an ROS-dependent increase in heat shock protein (HSP) Family A Member 9 (*HSPA9*) following tunicamycin treatment, but also ER stress-induced *HSP60* expression, which was upregulated in the presence of EUK-134, as well (Figure 2J).

3.3. Mitochondrial Membrane Potential and Mitochondrial Mass

Changes in mitochondrial membrane potential following ER stress induction in the presence or absence of EUK-134, as an additional marker of mitochondrial dysfunction, were next examined using different fluorophores. MitoTracker Red showed TN-induced hyperpolarisation, which was significantly inhibited by EUK-134 (Figure 3A). These results were also seen when assessing the accumulation of JC-1 polymers (red signal), indicative of increased number of hyperpolarised mitochondria (Figure 3B). Interestingly, JC-1 polymers to monomers ratio (red to green signal), showed TN-induced depolarisation which was prevented by EUK-134. This may be due to changes in mitochondrial mass or the existence of a pre-autophagic pool following asymmetrical mitochondrial fission [25,26]. To examine whether the increase in MitoTracker Red and JC-1 polymers fluorescence intensity was attributable to a rise in mitochondrial mass/volume, TMRM was employed with or without MitoTracker Green to normalise to mitochondrial mass/volume. Indeed, TMRM showed mitochondrial hyperpolarisation after tunicamycin treatment (Figure 3D), while mitochondrial content normalisation produced a substantial loss of mitochondrial membrane potential by tunicamycin with no changes observed in the presence of EUK-134 (Figure 3E). In other words, tunicamycin induced increase in mitochondrial mass/volume that seems to have affected our initial interpretation; importantly this effect was inhibited by EUK-134 (Figure 4A,B). These results were further confirmed by increased expression (fold change) of *Citrate Synthase* and transcription factor A and mitochondrial precursor (*TFAM*), the initial enzyme of the citric acid cycle and a regulator of mitochondrial DNA transcription, respectively; both prevented by EUK-134. (Figure 4C,D). Collectively, data suggest that biogenesis is induced in response to ER and mitochondrial stress to compensate for changes in energetic demand.

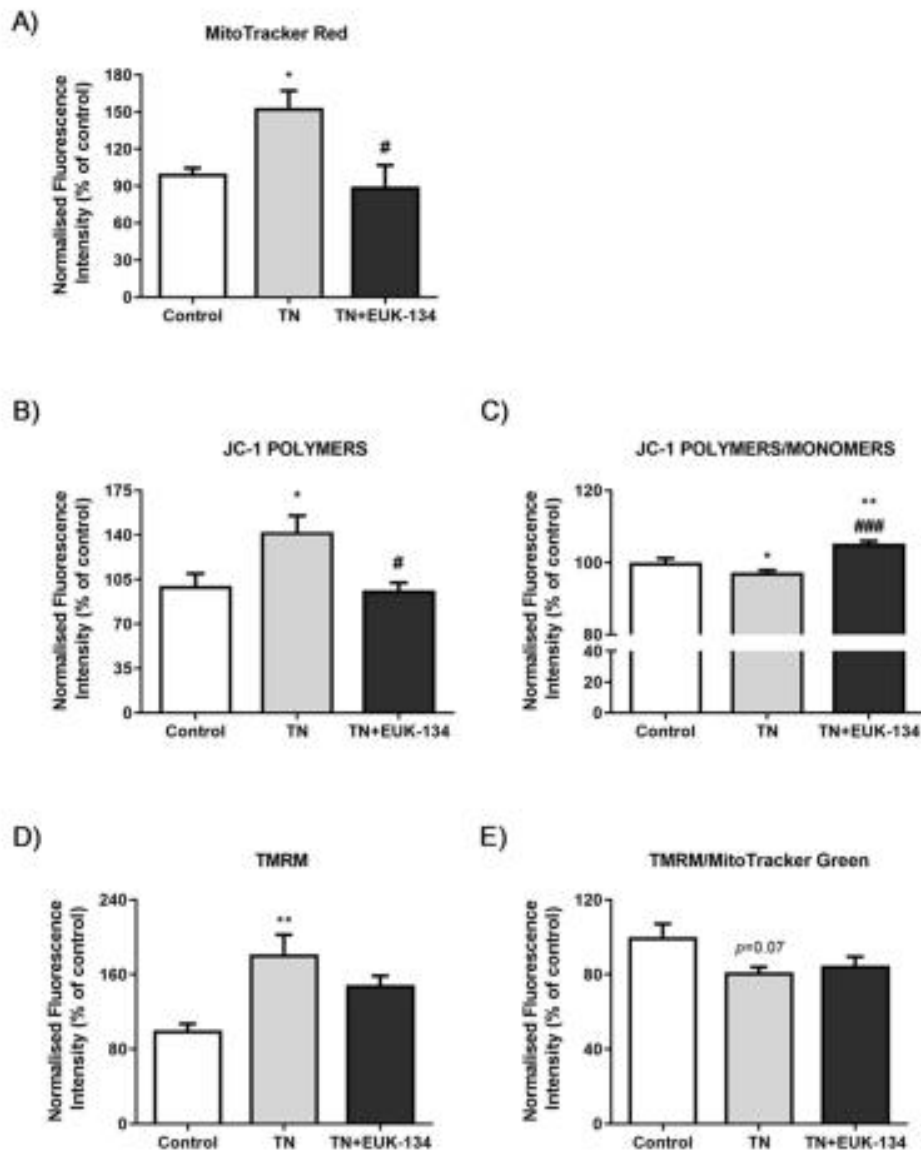


Figure 3. Mitochondrial membrane potential of tunicamycin-treated cells with or without EUK-134. Relative change (%) in (A) MitoTracker Red CMXRos fluorescence intensity ($n = 4$), (B) JC-1 red fluorescence (polymers) intensity ($n = 8$), (C) JC-1 red to green fluorescence (polymers/monomers) intensity ($n = 8$), (D) TMRM fluorescence intensity ($n = 4$), and (E) TMRM per MitoTracker Green (mitochondrial mass/volume) fluorescence intensity ($n = 4$), normalised to protein content. Data represent the mean \pm SEM, * $p \leq 0.033$, ** $p < 0.002$, and *** $p < 0.001$ against vehicle control or tunicamycin alone (#).

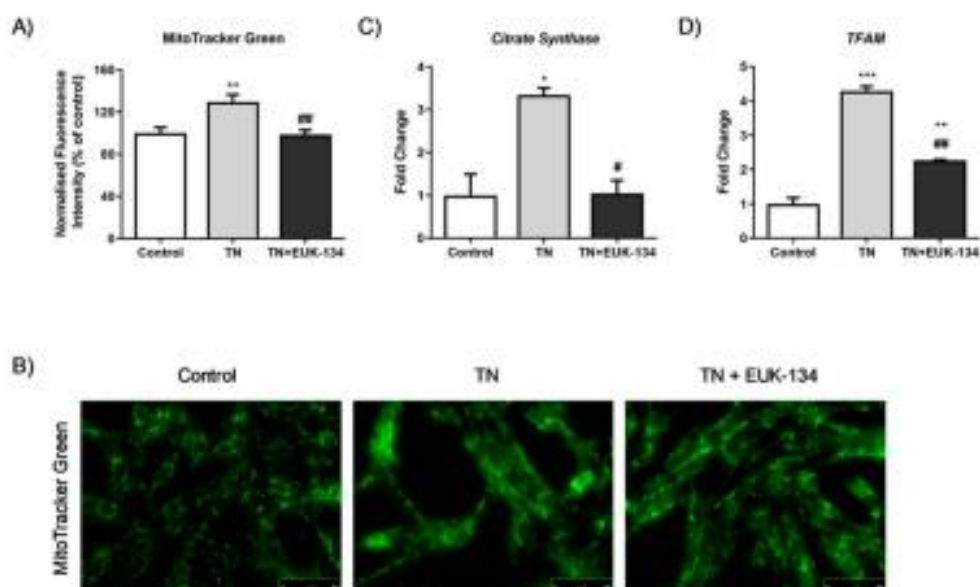


Figure 4. Mitochondrial biogenesis of tunicamycin-treated cells with or without EUK-134. (A) Representative graph of mitochondrial mass/volume showing the relative change (%) in MitoTracker Green fluorescence intensity, normalised to protein content. Data represent the mean \pm SEM ($n = 12$). * $p \leq 0.033$, ** $p < 0.002$, against vehicle control or tunicamycin alone (#). (B) Representative images of mitochondrial staining in human skeletal muscle myoblast using MitoTracker Green acquired under cell culture conditions. Images captured at 40 \times magnification. Scale bar = 75 μ m. Brightness was adjusted equally in each image to enhance visualisation. (C,D) Relative fold changes in mRNA expression of *Citrate Synthase* and *TFAM*. Data represent the mean fold change normalised to 18S housekeeper gene \pm SEM of Δ Ct values, ($n = 3$). * $p \leq 0.033$, ** $p < 0.002$, and *** $p < 0.001$ against vehicle control or tunicamycin alone (#).

3.4. Mitochondrial Morphology: Fusion and Fission Events

Mitochondrial network structure was visualised using MitoTracker Red to explore mitochondrial dynamics, including fusion and fission processes, in response to ER stress and antioxidant intervention. Tunicamycin induced a significant increase in mitochondrial interconnectivity and elongation, indicative of mitochondrial fusion events, which can be associated with increased mitochondrial mass [27,28]. These results were accompanying with an increase in the percentage of cytosol occupied by mitochondria. EUK-134 was able to drop TN-induced changes in mitochondrial interconnectivity and content to control levels, but not in elongation (Figure 5A,B). These findings were further confirmed by tunicamycin-induced upregulation of mitofusin-2 (*MFN2*), a gene associated with mitochondrial fusion; even though EUK-134 substantially decreased *MFN2* expression compared to tunicamycin treatment, it was still significantly upregulated compared to the control (Figure 6A).

It has been described that mitochondrial perimeter and area are positively correlated with mitochondria about to undergo a fission event, which can result in increased mitochondrial number [27,29]. MitoTracker Red staining showed increased tunicamycin-induced average mitochondrial perimeter and area, which were inhibited by EUK-134 (Figure 5C). These results are indicative of ROS-mediated fragmentation propensity in response to ER stress. This finding was further supported by increased expression changes in fission protein 1 (*FIS1*) and dynamin-related protein 1 (*DRP1*) genes, which are fission mediators. Overall, those results suggest that although the cell attempts to respond to ER stress-induced mitochondria dysfunction by increasing mitochondrial mass/volume, cells retain a propensity for fission.

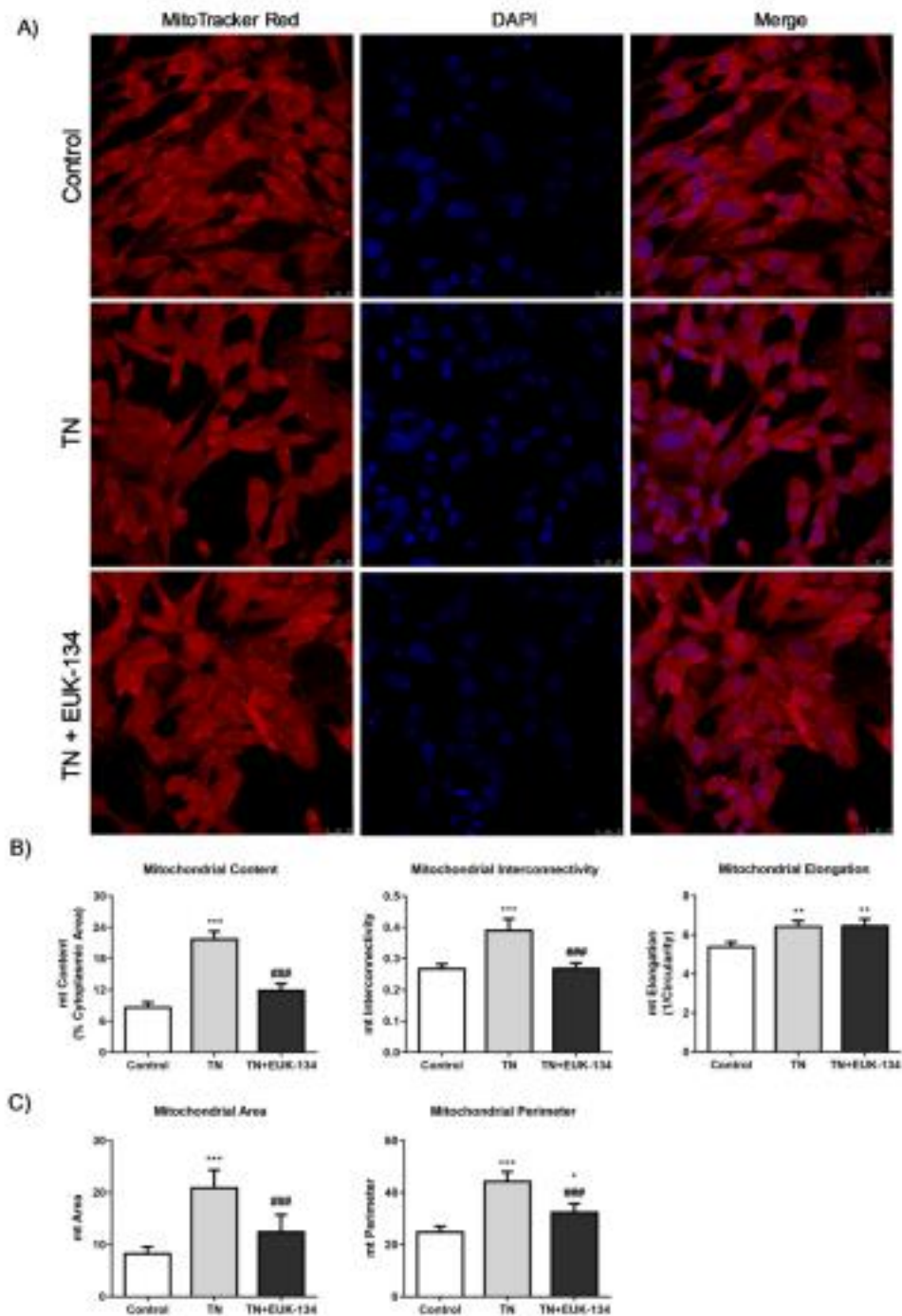


Figure 5. Mitochondrial morphological parameters of tunicamycin-treated cells with or without EUK-134. (A) Representative images of fixed human skeletal muscle myoblast stained with MitoTracker Red CMXRos. Images captured using 63×/1.4 oil immersion objective. Scale bar = 25 μ m. (B) Mitochondrial content as % of cytoplasmic area, mitochondrial interconnectivity expressed by the ratio of mitochondrial area/perimeter, and mitochondrial elongation expressed by $1/\text{circularity}$. (C) Mitochondrial fragmentation propensity described by mitochondrial area and perimeter. Data represent the mean \pm SEM ($n = 100$ cells per group). * $p \leq 0.033$, ** $p < 0.002$, and *** $p < 0.001$ against vehicle control or tunicamycin alone (#).

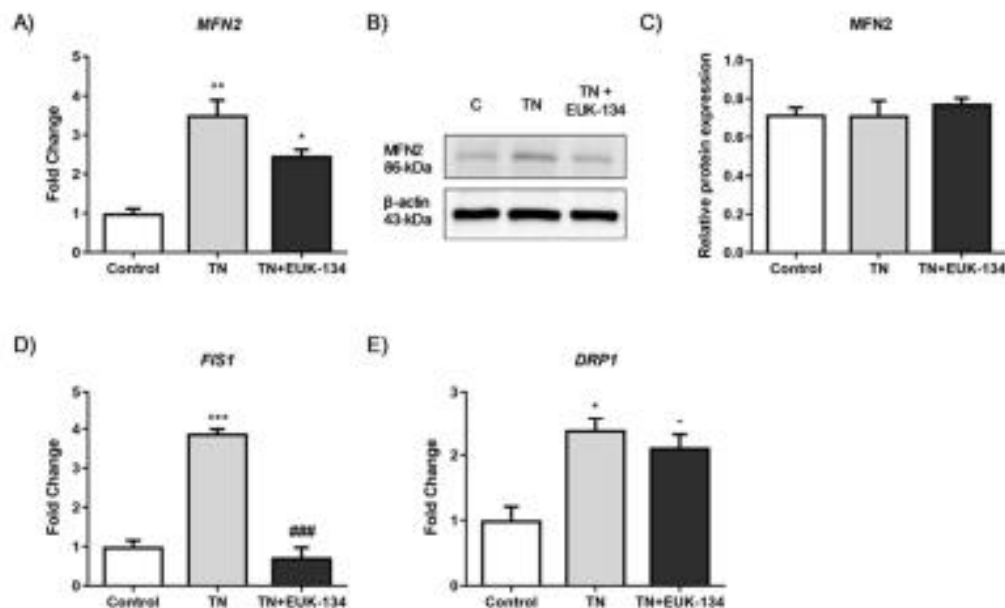


Figure 6. Mitochondrial dynamics of tunicamycin-treated cells with or without EUK-134. (A) Relative fold changes in mRNA expression of *MFN2* fusion-associated gene. Data represent the mean fold change normalised to 18S housekeeper gene \pm SEM of Δ Ct values ($n = 3$). * $p \leq 0.033$, ** $p < 0.002$ against vehicle control or tunicamycin alone (#). (B,C) Cropped representative Western blot image and quantification of *MFN2* protein levels relative to β -actin (loading control). Data represent the mean \pm SEM ($n = 3$). (D,E) Relative fold changes in mRNA expression of *FIS1* and *DRP1* fission-associated gene. Data represent the mean fold change normalised to 18S housekeeper gene \pm SEM of Δ Ct values ($n = 3$). * $p \leq 0.033$, ** $p < 0.002$, and *** $p < 0.001$ against vehicle control or tunicamycin alone (#).

3.5. ROS Generation

Since previous findings emphasised the importance of ROS in ER stressed-induced mitochondrial dysfunction, we aimed to further investigate ROS generation in our model. TN-treated cells exhibited higher levels of total cellular ROS (DCFH-DA fluorescence intensity) (Figure 7A) and specifically, superoxide levels (DHE fluorescence intensity), compared to the control group, which were decreased by EUK-134 treatment (Figure 7B). However, no changes were found on mitochondrial superoxide levels in the presence of tunicamycin (Figure 7C), which might be because of its rapid conversion to hydrogen peroxide or peroxynitrite [10,30,31]. The observation of decreased thiols content is also indicative of elevated ROS generation and specifically, hydrogen peroxide release in the ER lumen through GSH oxidation to GSSG; EUK-134 was able to restore thiols levels (Figure 7D). We also examined the protein levels of superoxide dismutase (SOD) 1 and 2 as markers of ROS generation (Figure 7E). Results showed that tunicamycin induced a substantial increase in SOD1 as an adaptive response to ROS generation, but no changes observed in SOD2 protein levels (Figure 7F,G).

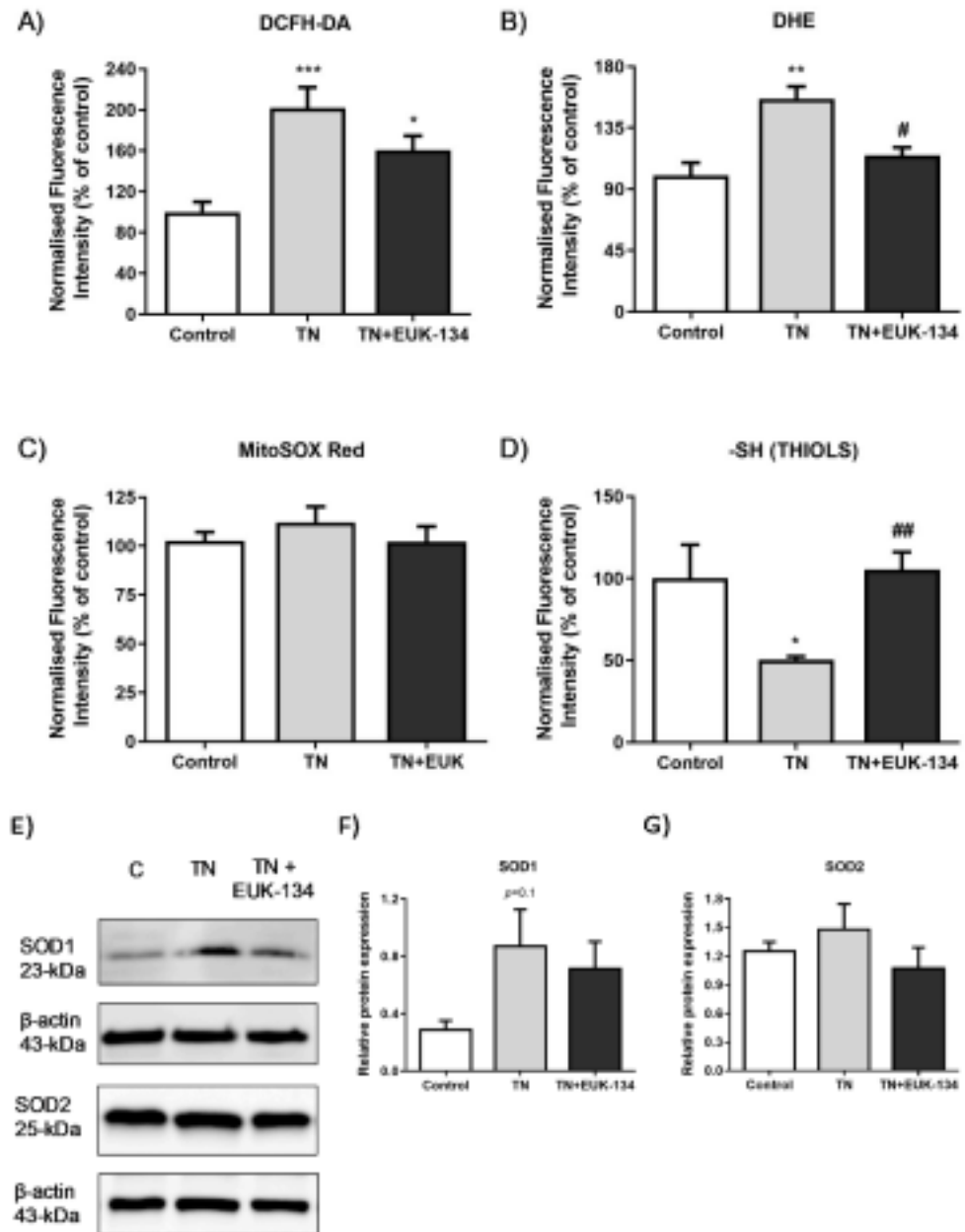


Figure 7. Markers of ROS generation in tunicamycin-treated cells with or without EUK-134. Relative change (%) in (A) total cellular ROS levels (DCFH-DA, $n = 8$), (B) total cellular superoxide levels (DHE, $n = 4$), (C) mitochondrial superoxide levels (MitoSOX Red, $n = 20$), and (D) total thiol content ($n = 6$), normalised to protein content. Data represent the mean \pm SEM, * $p \leq 0.033$, ** $p < 0.002$, and *** $p < 0.001$ against vehicle control or tunicamycin alone (#). (E–G) Cropped representative Western blot image and quantification of SOD1 and SOD2 protein levels relative to β -actin (loading control). Data represent the mean \pm SEM ($n = 3$ –5).

4. Discussion

Crosstalk between ER and mitochondria is a key cellular process and there is a strong link between chronic ER stress and mitochondrial dysfunction [10]. Based on the existing evidence of ER

stress activation as a mechanism involved in skeletal muscle weakness in patients with myositis [9], and the little knowledge on the role of ROS generation on ER stress downstream effects, this study aimed to determine the impact of the antioxidant EUK-134 in an in vitro model of ER stress-induced mitochondrial dysfunction in skeletal muscle, focusing on various aspects including mitochondrial function, biogenesis, and dynamics. EUK-134 was selected in the present study as it has been previously reported to exert beneficial effects on muscle atrophy and dysfunction induced by oxidative stress [32–35].

Tunicamycin is an inhibitor of the n-glycosylation step of protein folding, leading to accumulation of unfolded glycans within the ER [36]. Tunicamycin has been extensively used in numerous studies to activate the ER stress pathway in mouse and human skeletal muscle cells [37–39]. In this study, tunicamycin-induced ER stress, validated by an increase in UPR pathway markers, was partially ameliorated by EUK-134, with inhibitory effects on mRNA levels of *GRP78*, *ERDJ4*, and *total XBP1*. Even though the dose of tunicamycin was relatively lower compared to other studies [12,39,40], the 24 h incubation has been used to induce later phase of ER stress [12,41], and the expression of *CHOP*, a pro-apoptotic transcription factor, as a marker of prolonged/maladaptive ER stress [42]. Importantly, this study showed that EUK-134 diminished ER stress-induced upregulation of *CHOP* mRNA expression, protecting the cells from apoptosis initiation.

Previous studies have reported an increase in mitochondrial respiration and mass as an adaptive response to ER stress, which, when unresolved, leads to mitochondrial dysfunction and cell death [12,28,41]. A major finding of this study is that prolonged tunicamycin administration induced impaired mitochondrial function that was mediated by ROS generation. In agreement with previous findings, prolonged tunicamycin treatment promoted basal mitochondrial respiration upon ER stress [13], which can be considered as an attempt of the cell to meet ATP demand [43], as they showed inability to shift to glycolysis. However, elevations in OCR were not correlated with ATP production, as previously described, with total cellular ATP levels substantially reduced under prolonged ER stress (20 h, 0.5 µg/mL) compared to early ER stress (1–4 h) and the control group [12]. Diminished ATP turnover and impaired oxidative phosphorylation were also evident by suppression of reserve capacity, coupling efficiency, RCR, and phosphorylating respiration induced by prolonged ER stress, showing the inability of the cell to respond to energetic demands. Importantly, those changes induced by ER stress were mitigated by EUK-134, highlighting the important role of ROS generation in ER stress-induced mitochondrial dysfunction. Increased basal respiration can also be associated with other sources of oxygen consumption, including ROS generation [43]. In accordance with this, the present study showed substantial rise in non-mitochondrial OCR upon ER stress, which was further supported by elevated changes in the markers of oxidative stress. Specifically, tunicamycin increased total cellular ROS generation, including superoxide levels, and reduced thiol content, which were inhibited by EUK-134. However, no changes were noticeable in mitochondrial superoxide levels. This finding can be likely explained by the presence of nitric oxide production that has been previously shown to compete with superoxide dismutase and reduce superoxide availability to produce peroxynitrite [30,44]. Further supporting this hypothesis, a study on prostate cancer cells revealed that prolonged ER stress induced by tunicamycin is highly correlated with endothelial nitric oxide synthase upregulation and nitric oxide production [45]. A previous study has shown that EUK-134 can reduce nitric oxide, and subsequently, peroxynitrite production in proximal tubular cell injury [46]. It is also known that thiols are oxidised by peroxynitrite into disulphide bonds [47]. Consistently with these findings, the present study showed that EUK-134 increased thiol content under ER stress conditions, potentially by inhibiting peroxynitrite production.

Mitochondrial dysfunction with noticeable increase in proton leak, as observed in the current study, has been correlated with changes in mitochondrial membrane potential [48]. Initial investigation showed tunicamycin-induced mitochondrial membrane hyperpolarisation. However, a previous study has emphasised the importance of normalising this parameter to not only protein content, but also, mitochondrial content [26]. Normalisation to mitochondrial mass/volume showed mitochondrial

membrane depolarisation under ER stress, supporting its effects on mitochondrial biogenesis. Specifically, this study showed stimulation of mitochondrial biogenesis by tunicamycin as a response to increased ATP demands induced by ER stress, which was not noticeable in the presence of EUK-134. This finding was consistent with another study showing increased mitochondrial mass in an animal model of mitochondrial myopathy, induced by respiratory chain deficiency [49].

Mitochondrial biogenesis has also been associated with an increase in HSP60 levels in skeletal muscle [50]. Specifically, HSP60 showed to upregulate proliferator-activated receptor gamma coactivator 1 α 1 expression, a chief regulator in mitochondrial biogenesis process [51,52]. Furthermore, ER UPR has been suggested to activate mitochondrial UPR [53,54]. These findings are in agreement with our study that showed tunicamycin-associated increases in mitochondrial mass, as well as in the expression of HSP60 and HSPA9 mitochondrial UPR mediators, with HSPA9 being completely inhibited by EUK-134. However, it should be noted that HSP60 and HSPA9 upregulation might be attributable to the increased tunicamycin-mediated mitochondrial mass to further support mitochondrial protein translocation, folding, and refolding [50].

Previous studies have shown a distinct impact of oxidative stress on mitochondrial structural network. In consistent with our study, high respiration rates but decreased reserve capacity, as well as loss of mitochondrial membrane potential were induced by hydrogen peroxide and preceded mitochondrial fragmentation in mouse skeletal muscle myocytes [55]. Specifically, it has been found that prior to mitochondrial fragmentation, mitochondria elongate and fuse as an adaptive response to cellular insults, including ER stress and ROS generation [28,56]. Changes in mitochondrial structure have shown to determine cell fate when autophagy is stimulated, with elongated mitochondria being able to escape from degradation and maintain cell viability [57]. Similarly, in our model, it was found that 24 h incubation with tunicamycin maintained fusion processes, which were partially suppressed by EUK-134. Fusion processes were described by elongated and interconnected mitochondria, which can be positively correlated with increased mitochondrial mass [27]. Even though MFN2 mRNA expression was upregulated under ER stress conditions, protein expression levels remained unchanged. This finding might indicate (a) that increased mitochondrial mass/volume, interconnectivity, and elongation are potentially MFN1-dependent, with outer mitochondrial membrane fusion occurring mostly through the homotypic MFN1-MFN1 manner, or (b) the activation of other processes that require MFN2 protein expression, including Parkin-mediated mitophagy [25]. Taken together, these findings suggest ROS-mediated increase in mitochondrial fusion events, which are MFN2 independent, and accumulation of dysfunctional mitochondrial mass under maladaptive ER stress conditions.

Since it is known that mitochondrial dysfunction precedes mitochondrial fragmentation, we examined the propensity of mitochondria to fragment in our ER stress model, as suggested by Westrate et al. [29]. Tunicamycin increased morphological parameters predictive of future mitochondrial fragmentation, including perimeter, the most prominent one, as well as mitochondrial area. These results were further supported by our findings of increased changes in mRNA levels of fission markers, FIS1 and DRP1. Importantly, those events were mitigated by EUK-134, indicating that ER stress-associated fragmentation events are mediated by ROS. Further supporting this finding, in mouse skeletal muscle myoblasts, ROS induced mitochondrial depolarisation and fragmentation, resulting in stimulation of the ER UPR [54].

This study presents novel findings on the role of ROS in ER stress-induced mitochondrial dysfunction. However, some limitations should be noted and further examined. Firstly, even though this study examines mitochondrial fusion and fission processes through investigating mitochondrial morphological parameters and changes in mRNA expression levels, it lacks analysis on potential changes in MFN1, FIS1, and DRP1 protein expression levels, which would provide further insights into the physiological changes induced by tunicamycin. Secondly, the present study was conducted using a single immortalised human myoblast cell line, which represents an appropriate cell line in relation to the properties of the model. However, we acknowledge the importance of evaluating other myoblast cell lines and primary cells when considering the wider applicability of these findings.

5. Conclusions

EUK-134 can protect against aspects of ER stress-induced mitochondrial dysfunction, biodynamics, and biogenesis in human skeletal muscle cells, highlighting a role of ROS in instances of prolonged ER stress, such as in myositis. Overall, this work provides a possibility of quenching ROS generation as an avenue for beneficial impact for ER stress-related diseases.

Author Contributions: Conceptualisation, A.P.L. and R.G.C.; methodology, A.P.L. and A.T.; validation, A.T.; formal analysis, A.T. and M.L.; investigation, A.T. and M.L.; resources, A.P.L., R.G.C. and N.A.-S.; data curation, A.T.; writing—original draft preparation, A.T.; writing—review and editing, A.P.L., G.A.N. and N.A.-S.; visualisation, A.T.; supervision, A.P.L.; project administration, A.T. and A.P.L.; funding acquisition, A.P.L.; R.G.C. All authors have read and agreed to the published version of the manuscript.

Funding: This study was funded by a Faculty PhD Studentship awarded to AT by The Manchester Metropolitan University.

Acknowledgments: The authors gratefully acknowledge the gift of an immortalised human skeletal muscle cell line from the Institute of Myology, Paris.

Conflicts of Interest: The authors declare no conflict of interest.

References

- Walter, P.; Ron, D. The unfolded protein response: From stress pathway to homeostatic regulation. *Science* **2011**, *334*, 1081–1086. [\[CrossRef\]](#) [\[PubMed\]](#)
- Ellgaard, L.; Sevier, C.S.; Bulleid, N.J. How are proteins reduced in the endoplasmic reticulum? *Trends Biochem. Sci.* **2018**, *43*, 32–43. [\[CrossRef\]](#) [\[PubMed\]](#)
- Sicari, D.; Igarria, A.; Chevet, E. Control of protein homeostasis in the early secretory pathway: Current status and challenges. *Cells* **2019**, *8*, 1347. [\[CrossRef\]](#) [\[PubMed\]](#)
- Senft, D.; Ze'ev, A.R. UPR, autophagy, and mitochondria crosstalk underlies the ER stress response. *Trends Biochem. Sci.* **2015**, *40*, 141–148. [\[CrossRef\]](#) [\[PubMed\]](#)
- Bhandary, B.; Marahatta, A.; Kim, H.R.; Chae, H.J. An involvement of oxidative stress in endoplasmic reticulum stress and its associated diseases. *Int. J. Mol. Sci.* **2012**, *14*, 434–456. [\[CrossRef\]](#)
- Xiang, C.; Wang, Y.; Zhang, H.; Han, F. The role of endoplasmic reticulum stress in neurodegenerative disease. *Apoptosis* **2017**, *22*, 1–26. [\[CrossRef\]](#)
- Pauly, M.; Angebault-Prouteau, C.; Dridi, H.; Notarnicola, C.; Scheuermann, V.; Lacampagne, A.; Matecki, S.; Fauconnier, J. ER stress disturbs SR/ER-mitochondria Ca²⁺ transfer: Implications in Duchenne muscular dystrophy. *Biochim. Biophys. Acta Mol. Basis Dis.* **2017**, *1863*, 2229–2239. [\[CrossRef\]](#)
- Hotamisligil, G.S. Endoplasmic reticulum stress and the inflammatory basis of metabolic disease. *Cell* **2010**, *140*, 900–917. [\[CrossRef\]](#)
- Nagaraju, K.; Casciola-Rosen, L.; Lundberg, I.; Rawat, R.; Cutting, S.; Thapliyal, R.; Chang, J.; Dwivedi, S.; Mitsak, M.; Chen, Y.W.; et al. Activation of the endoplasmic reticulum stress response in autoimmune myositis: Potential role in muscle fiber damage and dysfunction. *Arthritis Rheum.* **2005**, *52*, 1824–1835. [\[CrossRef\]](#)
- Cao, S.S.; Kaufman, R.J. Endoplasmic reticulum stress and oxidative stress in cell fate decision and human disease. *Antioxid. Redox Signal.* **2014**, *21*, 96–113. [\[CrossRef\]](#)
- Bravo, R.; Gutierrez, T.; Paredes, F.; Gatica, D.; Rodriguez, A.E.; Pedrozo, Z.; Chiong, M.; Parra, V.; Quest, A.F.; Rothermel, B.A.; et al. Endoplasmic reticulum: ER stress regulates mitochondrial bioenergetics. *Int. J. Biochem. Cell Biol.* **2012**, *44*, 16–20. [\[CrossRef\]](#) [\[PubMed\]](#)
- Bravo, R.; Vicencio, J.M.; Parra, V.; Troncoso, R.; Munoz, J.P.; Bui, M.; Quiroga, C.; Rodriguez, A.E.; Verdejo, H.E.; Ferreira, J.; et al. Increased ER-mitochondrial coupling promotes mitochondrial respiration and bioenergetics during early phases of ER stress. *J. Cell Sci.* **2011**, *124*, 2143–2152. [\[CrossRef\]](#) [\[PubMed\]](#)
- Jackisch, L.; Murphy, A.; Al-Daghri, N.; McTernan, P.; Randevara, H.; Tripathi, G. Tunicamycin-induced ER stress mediates mitochondrial dysfunction in human adipocytes. In Proceedings of the Society for Endocrinology BES 2016, Brighton, UK, 7–9 November 2016; Endocrine Abstracts: Bristol, UK, 2016; Volume 44, p. 193. [\[CrossRef\]](#)

14. Madreiter-Sokolowski, C.T.; Waldeck-Weiermair, M.; Bourguignon, M.P.; Villeneuve, N.; Gottschalk, B.; Klec, C.; Stryeck, S.; Radulovic, S.; Parichatikanond, W.; Frank, S.; et al. Enhanced inter-compartmental Ca^{2+} flux modulates mitochondrial metabolism and apoptotic threshold during aging. *Redox Biol.* **2019**, *20*, 458–466. [CrossRef]
15. Baker, K.; Marcus, C.B.; Huffman, K.; Kruk, H.; Malfroy, B.; Doctrow, S.R. Synthetic combined superoxide dismutase/catalase mimetics are protective as a delayed treatment in a rat stroke model: A key role for reactive oxygen species in ischemic brain injury. *J. Pharmacol. Exp. Ther.* **1998**, *284*, 215–221. [PubMed]
16. Mamchaoui, K.; Trollet, C.; Bigot, A.; Negroni, E.; Chaouch, S.; Wolff, A.; Kandalla, P.K.; Marie, S.; Di Santo, J.; St Guily, J.L.; et al. Immortalized pathological human myoblasts: Towards a universal tool for the study of neuromuscular disorders. *Skelet. Muscle* **2011**, *1*, 34. [CrossRef]
17. Wedgwood, S.; Black, S.M. Combined superoxide dismutase/catalase mimetics alter fetal pulmonary arterial smooth muscle cell growth. *Antioxid. Redox Signal.* **2004**, *6*, 191–197. [CrossRef] [PubMed]
18. Zygmunt, D.A.; Singhal, N.; Kim, M.L.; Cramer, M.L.; Crowe, K.E.; Xu, R.; Jia, Y.; Adair, J.; Valenzuela, I.M.P.; Akaaboune, M.; et al. Deletion of Pofut1 in mouse skeletal myofibers induces muscle aging-related phenotypes in cis and in trans. *Mol. Cell. Biol.* **2017**, *37*, e00426–16. [CrossRef]
19. Wang, J.; Tan, J.; Qi, Q.; Yang, L.; Wang, Y.; Zhang, C.; Hu, L.; Chen, H.; Fang, X. MiR-487b-3p suppresses the proliferation and differentiation of myoblasts by targeting IRS1 in skeletal muscle myogenesis. *Int. J. Biol. Sci.* **2018**, *14*, 760–774. [CrossRef]
20. Debaud, C.; Salga, M.; Begot, L.; Holy, X.; Chedik, M.; De l'Escalopier, N.; Torossian, F.; Levesque, J.P.; Lataillade, J.J.; Le Bousse-Kerdiles, M.C.; et al. Peripheral denervation participates in heterotopic ossification in a spinal cord injury model. *PLoS ONE* **2017**, *12*, e0182454. [CrossRef]
21. Livak, K.J.; Schmittgen, T.D. Analysis of relative gene expression data using real-time quantitative PCR and the 2- $\Delta\Delta CT$ method. *Methods* **2001**, *25*, 402–408. [CrossRef]
22. Dagda, R.K.; Cherra, S.J.; Kulich, S.M.; Tandon, A.; Park, D.; Chu, C.T. Loss of PINK1 function promotes mitophagy through effects on oxidative stress and mitochondrial fission. *J. Biol. Chem.* **2009**, *284*, 13843–13855. [CrossRef] [PubMed]
23. Sivandzade, F.; Bhalerao, A.; Cucullo, L. Analysis of the mitochondrial membrane potential using the cationic JC-1 dye as a sensitive fluorescent probe. *Bio Protoc.* **2019**, *9*, e3128. [CrossRef] [PubMed]
24. Dott, W.; Mistry, P.; Wright, J.; Cain, K.; Herbert, K.E. Modulation of mitochondrial bioenergetics in a skeletal muscle cell line model of mitochondrial toxicity. *Redox Biol.* **2014**, *2*, 224–233. [CrossRef] [PubMed]
25. Shirihai, O.S.; Song, M.; Dorn, G.W. How mitochondrial dynamism orchestrates mitophagy. *Circ. Res.* **2015**, *116*, 1835–1849. [CrossRef] [PubMed]
26. Perry, S.W.; Norman, J.P.; Litzburg, A.; Zhang, D.; Dewhurst, S.; Gelbard, H.A. HIV-1 transactivator of transcription protein induces mitochondrial hyperpolarization and synaptic stress leading to apoptosis. *J. Immunol.* **2005**, *174*, 4333–4344. [CrossRef]
27. Seo, A.Y.; Joseph, A.M.; Dutta, D.; Hwang, J.C.; Aris, J.P.; Leeuwenburgh, C. New insights into the role of mitochondria in aging: Mitochondrial dynamics and more. *J. Cell Sci.* **2010**, *123*, 2533–2542. [CrossRef]
28. Bankapalli, K.; Vishwanathan, V.; Susarla, G.; Sunayana, N.; Saladi, S.; Peethambaram, D.; D'Silva, P. Redox-dependent regulation of mitochondrial dynamics by DJ-1 paralogs in *Saccharomyces cerevisiae*. *Redox Biol.* **2020**, *32*, 101451. [CrossRef]
29. Westrate, L.M.; Drocco, J.A.; Martin, K.R.; Hlavacek, W.S.; MacKeigan, J.P. Mitochondrial morphological features are associated with fission and fusion events. *PLoS ONE* **2014**, *9*, e95265. [CrossRef]
30. Pearson, T.; Kabayo, T.; Ng, R.; Chamberlain, J.; McArdle, A.; Jackson, M.J. Skeletal muscle contractions induce acute changes in cytosolic superoxide, but slower responses in mitochondrial superoxide and cellular hydrogen peroxide. *PLoS ONE* **2014**, *9*, e96378. [CrossRef]
31. Ott, M.; Gogvadze, V.; Orrenius, S.; Zhivotovsky, B. Mitochondria, oxidative stress and cell death. *Apoptosis* **2007**, *12*, 913–922. [CrossRef]
32. Kim, J.H.; Lawler, J.M. Amplification of proinflammatory phenotype, damage, and weakness by oxidative stress in the diaphragm muscle of mdx mice. *Free Radic. Biol. Med.* **2012**, *52*, 1597–1606. [CrossRef] [PubMed]
33. Lawler, J.M.; Kunst, M.; Hord, J.M.; Lee, Y.; Joshi, K.; Botchlett, R.E.; Ramirez, A.; Martinez, D.A. EUK-134 ameliorates nNOS μ translocation and skeletal muscle fiber atrophy during short-term mechanical unloading. *Am. J. Physiol. Regul. Integr. Comp. Physiol.* **2014**, *306*, R470–R482. [CrossRef] [PubMed]

34. Yamada, T.; Abe, M.; Lee, J.; Tatebayashi, D.; Himori, K.; Kanzaki, K.; Wada, M.; Bruton, J.D.; Westerblad, H.; Lanner, J.T. Muscle dysfunction associated with adjuvant-induced arthritis is prevented by antioxidant treatment. *Skelet. Muscle* **2015**, *5*, 20. [[CrossRef](#)] [[PubMed](#)]
35. Himori, K.; Abe, M.; Tatebayashi, D.; Lee, J.; Westerblad, H.; Lanner, J.T.; Yamada, T. Superoxide dismutase/catalase mimetic EUK-134 prevents diaphragm muscle weakness in monocrotalin-induced pulmonary hypertension. *PLoS ONE* **2017**, *12*, e0169146. [[CrossRef](#)] [[PubMed](#)]
36. Duksin, D.; Mahoney, W.C. Relationship of the structure and biological activity of the natural homologues of tunicamycin. *J. Biol. Chem.* **1982**, *257*, 3105–3109.
37. Win, S.; Than, T.A.; Fernandez-Checa, J.C.; Kaplowitz, N. JNK interaction with Sab mediates ER stress induced inhibition of mitochondrial respiration and cell death. *Cell Death Dis.* **2014**, *5*, e989. [[CrossRef](#)]
38. Quan, X.; Wang, J.; Liang, C.; Zheng, H.; Zhang, L. Melatonin inhibits tunicamycin-induced endoplasmic reticulum stress and insulin resistance in skeletal muscle cells. *Biochem. Biophys. Res. Commun.* **2015**, *463*, 1102–1107. [[CrossRef](#)]
39. Hassan, R.H.; Hainault, I.; Vilquin, J.T.; Samama, C.; Lasnier, F.; Ferre, P.; Fougere, E.; Hajdouch, E. Endoplasmic reticulum stress does not mediate palmitate-induced insulin resistance in mouse and human muscle cells. *Diabetologia* **2012**, *55*, 204–214. [[CrossRef](#)]
40. Deldicque, L.; Bertrand, L.; Patton, A.; Francaux, M.; Baar, K. ER stress induces anabolic resistance in muscle cells through PKB-induced blockade of mTORC1. *PLoS ONE* **2011**, *6*, e20993. [[CrossRef](#)]
41. Knupp, J.; Arvan, P.; Chang, A. Increased mitochondrial respiration promotes survival from endoplasmic reticulum stress. *Cell Death Differ.* **2019**, *26*, 487–501. [[CrossRef](#)]
42. Alam, S.; Abdullah, C.S.; Aishwarya, R.; Orr, A.W.; Traylor, J.; Miriyala, S.; Panchatcharam, M.; Pattillo, C.B.; Bhuiyan, M. Sigmar1 regulates endoplasmic reticulum stress-induced C/EBP-homologous protein expression in cardiomyocytes. *Biochem. Biophys. Res. Commun.* **2017**, *37*, BSR20170898. [[CrossRef](#)]
43. Hill, B.G.; Benavides, G.A.; Lancaster, J.R.; Ballinger, S.; Dell'Italia, L.; Zhang, J.; Darley-Usmar, V.M. Integration of cellular bioenergetics with mitochondrial quality control and autophagy. *Biol. Chem.* **2012**, *393*, 1485–1512. [[CrossRef](#)] [[PubMed](#)]
44. Pearson, T.; McArdle, A.; Jackson, M.J. Nitric oxide availability is increased in contracting skeletal muscle from aged mice, but does not differentially decrease muscle superoxide. *Free Radic. Biol. Med.* **2015**, *78*, 82–88. [[CrossRef](#)] [[PubMed](#)]
45. Guha, P.; Kaptan, E.; Gade, P.; Kalvakolanu, D.V.; Ahmed, H. Tunicamycin induced endoplasmic reticulum stress promotes apoptosis of prostate cancer cells by activating mTORC1. *Oncotarget* **2017**, *8*, 68191–68207. [[CrossRef](#)]
46. Chatterjee, P.K.; Patel, N.S.; Kvale, E.O.; Brown, P.A.; Stewart, K.N.; Mota-Filipe, H.; Sharpe, M.A.; Di Paola, R.; Cuzzocrea, S.; Thiemermann, C. EUK-134 reduces renal dysfunction and injury caused by oxidative and nitrosative stress of the kidney. *Am. J. Nephrol.* **2004**, *24*, 165–177. [[CrossRef](#)] [[PubMed](#)]
47. Daiber, A.; Daub, S.; Bachschmid, M.; Schildknecht, S.; Oelze, M.; Steven, S.; Schmidt, P.; Megner, A.; Wada, M.; Tanabe, T.; et al. Protein tyrosine nitration and thiol oxidation by peroxynitrite—Strategies to prevent these oxidative modifications. *Int. J. Mol. Sci.* **2013**, *14*, 7542–7570. [[CrossRef](#)] [[PubMed](#)]
48. Trnka, J.; Elkalaf, M.; Anděl, M. Lipophilic triphenylphosphonium cations inhibit mitochondrial electron transport chain and induce mitochondrial proton leak. *PLoS ONE* **2015**, *10*, e0121837. [[CrossRef](#)]
49. Wredenberg, A.; Wibom, R.; Wilhelmsson, H.; Graff, C.; Wiener, H.H.; Burden, S.J.; Oldfors, A.; Westerblad, H.; Larsson, N.G. Increased mitochondrial mass in mitochondrial myopathy mice. *Proc. Natl Acad. Sci. USA* **2002**, *99*, 15066–15071. [[CrossRef](#)]
50. Jadya, P.; Tomar, D. Mitochondrial Protein Quality Control Mechanisms. *Genes* **2020**, *11*, 563. [[CrossRef](#)]
51. Marino Gammazza, A.; Macaluso, F.; Di Felice, V.; Cappello, F.; Barone, R. Hsp60 in skeletal muscle fiber biogenesis and homeostasis: From physical exercise to skeletal muscle pathology. *Cells* **2018**, *7*, 224. [[CrossRef](#)]
52. Barone, R.; Macaluso, F.; Sangiorgi, C.; Campanella, C.; Gammazza, A.M.; Moresi, V.; Coletti, D.; De Macario, E.C.; Macario, A.J.; Cappello, F.; et al. Skeletal muscle Heat shock protein 60 increases after endurance training and induces peroxisome proliferator-activated receptor gamma coactivator 1 α expression. *Sci. Rep.* **2016**, *6*, 19781. [[CrossRef](#)]
53. Xiao, T.; Liang, X.; Liu, H.; Zhang, F.; Meng, W.; Hu, F. Mitochondrial stress protein HSP60 regulates ER stress-induced hepatic lipogenesis. *J. Mol. Endocrinol.* **2020**, *64*, 67–75. [[CrossRef](#)] [[PubMed](#)]

54. Iqbal, S.; Hood, D.A. Oxidative stress-induced mitochondrial fragmentation and movement in skeletal muscle myoblasts. *Am. J. Physiol. Cell Physiol.* **2014**, *306*, C1176–C1183. [[CrossRef](#)] [[PubMed](#)]
55. Fan, X.; Hussien, R.; Brooks, G.A. H₂O₂-induced mitochondrial fragmentation in C₂C₁₂ myocytes. *Free Radic. Biol. Med.* **2010**, *49*, 1646–1654. [[CrossRef](#)] [[PubMed](#)]
56. Lebeau, J.; Saunders, J.M.; Moraes, V.W.; Madhavan, A.; Madrazo, N.; Anthony, M.C.; Wiseman, R.L. The PERK arm of the unfolded protein response regulates mitochondrial morphology during acute endoplasmic reticulum stress. *Cell Rep.* **2018**, *22*, 2827–2836. [[CrossRef](#)]
57. Gomes, L.C.; Di Benedetto, G.; Scorrano, L. During autophagy mitochondria elongate, are spared from degradation and sustain cell viability. *Nat. Cell Biol.* **2011**, *13*, 589–598. [[CrossRef](#)]



© 2020 by the authors. Licensee MDPI, Basel, Switzerland. This article is an open access article distributed under the terms and conditions of the Creative Commons Attribution (CC BY) license (<http://creativecommons.org/licenses/by/4.0/>).